LEVEL ²ᴵᴵ

CERAMIC PIEZOELECTRIC TRANSDUCERS

Period January 1, 1978 to December 31, 1978

Contract N00014-76-C-0515

Project No. 3203

Sponsored by

ADVANCED RESEARCH PROJECTS AGENCY (DOD)

ARPA ORDER NO. 3203

OFFICE OF NAVAL RESEARCH

Contract N00014-76-C-0515

MONITORED BY ONR

L. E. Cross
J. V. Biggers
R. E. Newnham

D D C
RECEIVED
JUL 25 1979
RECEIVE
D

MATERIALS RESEARCH LABORATORY

THE PENNSYLVANIA STATE UNIVERSITY

UNIVERSITY PARK, PENNSYLVANIA 16802

79 07 23 073

REPORT DOCUMENTATION PAGE		READ INSTRUCTIONS BEFORE COMPLETING FORM
1. REPORT NUMBER	2. GOVT ACCESSION NO.	3. RECIPIENT'S CATALOG NUMBER
4. TITLE *(and Subtitle)* CERAMIC PIEZOELECTRIC TRANSDUCERS		5. TYPE OF REPORT & PERIOD COVERED FINAL REPORT Jan. 1, 1978 to Dec. 31, 1978
		6. PERFORMING ORG. REPORT NUMBER
7. AUTHOR(s) L.E. Cross, J.V. Biggers, R.E. Newnham		8. CONTRACT OR GRANT NUMBER(s) N00014-76-C-0515, DARPA Order-3203
9. PERFORMING ORGANIZATION NAME AND ADDRESS Materials Research Laboratory The Pennsylvania State University University Park, PA 16802		10. PROGRAM ELEMENT, PROJECT, TASK AREA & WORK UNIT NUMBERS Project No. 3203 DARPA
11. CONTROLLING OFFICE NAME AND ADDRESS R.C. Pohanka, Office of Naval Research Ballston Tower, 800 N. Quincy St. Arlington, VA 22217		12. REPORT DATE June 1, 1979
		13. NUMBER OF PAGES 342
14. MONITORING AGENCY NAME & ADDRESS*(if different from Controlling Office)*		15. SECURITY CLASS. *(of this report)* Unclassified
		15a. DECLASSIFICATION/DOWNGRADING SCHEDULE

16. DISTRIBUTION STATEMENT *(of this Report)*

> **DISTRIBUTION STATEMENT A**
> Approved for public release;
> Distribution Unlimited

17. DISTRIBUTION STATEMENT *(of the abstract entered in Block 20, if different from Report)*

Final rept. 1 Jan - 31 Dec 78;

18. SUPPLEMENTARY NOTES

342 p.   1 Jun 79

19. KEY WORDS *(Continue on reverse side if necessary and identify by block number)*

Transducers, ferroelectrics, piezoelectrics, dielectrics, electrostriction, composites, crystal growth, ceramic processing, electroceramic materials

20. ABSTRACT *(Continue on reverse side if necessary and identify by block number)*

The work described in this report was carried out in the Materials Research Laboratory of The Pennsylvania State University over the period January 1, 1978 to December 31, 1978. The period is the final year of a joint DARPA:ONR sponsored three-year contract effort directed towards the development of new and improved piezoceramic materials for electromechanical transducers.

DD FORM 1473 EDITION OF 1 NOV 65 IS OBSOLETE
1 JAN 73
S/N 0102-014-6601

A major success of the program has been the development of new composite transducers with unusually high piezoelectric $g_{(h)}$ coefficients. Theoretical considerations had suggested that by paying proper attention to material and device symmetries and to the mode of phase interconnection (connectivity), elastic and electric "fluxes" could be distributed so as to give coupled properties outside the range available in either single phase of the composite. The theory was confirmed using PZT:polymer composites fabricated by the replamineform replication techniques and has been further elucidated by work on macrocomposites with similar controlled connectivity which have been carried through at NRL.

A second important advance has been the development of a new family of electrostrictive materials based on the ferroelectric relaxor $Pb_3MgNb_2O_9$ (PMN). In PMN:lead titanate solid solutions, materials have been developed which permit very large anhysteretic strains ($1,000 \times 10^{-6}$), have zero aging and very low coefficients of thermal expansion. Taking advantage of multilayer integrated electrodes to reduce the terminal voltages required, these ceramics would appear to offer significant advantage over conventional PZTs for some micropositioning and mirror support applications.

Sophisticated computer aided graphics techniques have been used to develop a phenomenological Gibbs function for the PZT solid solution family. This treatment permits for the first time a complete interrelation of the thermoelasto-dielectric properties across the whole temperature and composition field of the single cell perovskite structure. The function reproduces the feature of morphotropy in the phase diagram and gives a promising method for the separation of intrinsic single domain and extrinsic domain wall and phase boundary contributions to the measured ceramic properties.

In support of these major efforts, a considerable amount of detailed work has been done to develop the processing capabilities which were required to assemble the many different ceramics and composites which have been the topics of study. New work has been performed on the zirconia problem, on the preparation and fabrication of multilayers from different material combinations, with and without interleaving electrodes, on extruded macrostructures, and on the replication techniques necessary for replamineform processing.

A small additional effort was committed to the growth of single crystals and of oriented polycrystals of the ferroelectric antimony sulphur iodide (SbSI). These crystals were supplied for fabrication and hot-forging studies at the Naval Research Laboratories.

CERAMI PIEZOELECTRIC TRANSDUCERS

Period January 1, 1978 to December 31, 1978

Contract N00014-76-C-0515

Project No. 3203

Sponsored by

ADVANCED RESEARCH PROJECTS AGENCY (DOD)

ARPA ORDER NO. 3203

OFFICE OF NAVAL RESEARCH

Contract N00014-76-C-0515

MONITORED BY ONR

APPROVED FOR PUBLIC RELEASE--DISTRIBUTION UNLIMITED

Reproduction in whole or in part is permitted for
any purpose of the United States Government

L. E. Cross
J. V. Biggers
R. E. Newnham

D D C

JUL 25 1979

D

CONTENTS

APPENDICES

1. Electrostriction in $Pb(Zn_{1/3}Nb_{2/3})O_3$.

2. Large Electrostrictive Effects in Relaxor Ferroelectrics.

3. The Electrostriction Effects in Ceramic $Pb(Mg_{1/3}Nb_{2/3})O_3$:$PbTiO_3$ Solid Solutions.

4. Al_2O_3-PZT Tape-Cast Composite Materials.

5. Piezoelectric Properties of $Pb_5Ge_3O_{11}$ Bonded PZT Composites.

6. Piezoelectric Properties of Internally Electroded PZT Multilayer.

7. Electromechanical Behavior of Antiferroelectric-Ferroelectric Multi-Layer PZT Based Composites.

8. A Phenomenological Gibbs Function for the $PbZrO_3$:$PbTiO_3$ Solid Solution System.

9. Solid State Reactions in the System PbO-TiO_2-ZrO_2.

10. Reactivity of Chemically Prepared Lead Zirconate-Lead Titanate Solid Solutions.

11. Hot-Isostatic Pressing of PZT Materials.

12. A Study of Acentricity in Complex Perovskites Based on Tellurium Oxide Using Optical Second Harmonic Generation (SHG).

13. RF Sputtering of $Sr_2Nb_2O_7$.

14. Electro Mechanical Behavior of Single Domain Single Crystals of Bismuth Titanate ($Bi_4Ti_3O_{12}$).

15. Electrostatic Measurements of Unusually Large Secondary Pyroelectricity in Partially Clamped $LiNbO_3$.

16. Electrostatic Measurements of Tertiary Pyroelectricity in Partially Clamped $LiNbO_3$.

17. Crystal Growth of Antimony Sulphur Iodide.

18. Crystal Growth and Characterization of Lithium Metasilicate.

1. INTRODUCTION

This report describes work carried out in the Materials Research Laboratory at The Pennsylvania State University over the period January 1, 1978 to December 31, 1978 under joint DARPA:ONR sponsorship. The period is the final year of a three year contract effort directed towards the development of new and improved piezoceramic materials for electromechanical transducers.

Undoubtedly the major success of this program has been the development of a new approach to the design of two-phase composite materials which optimize coupled properties such as the electromechanical coupling in piezoelectric transducers. The idea that new composites with uniquely advantageous coupled properties could be engineered by combining already known single phases if proper attention is paid to material and device symmetries and the mode of phase interconnection (connectivity) in the composite has been unequivocally confirmed in the PZT:polymer composites fabricated by the replamineform replication technique. The unusually high hydrostatic piezoelectric voltage coefficient (g_h) achieved in this material has been confirmed by measurements at NUSC, New London, and the basic principles of the composite forms further elucidated by work on macrocomposites with similar controlled connectivities carried through at NRL.

The principles established theoretically and experimentally on this program are now being applied to the fabrication of new pyroelectric materials, and to the construction of systems in which both the scale and geometry of the microstructure of the composite can be more closely controlled.

A second important advance has been the development of a new family of electrostrictive materials based on the ferroelectric relaxor $Pb_3MgNb_2O_9$ (PMN). In the solid solution system between PMN and lead titanate (PT) materials have been developed which permit very large anhysteretic strain amplitudes (up to .001) and near zero thermal expansion. The frequency response can be tailored over a limited range and rather unexpectedly the materials exhibit stable displacements under DC field. These ceramics would appear to offer significant advantage over conventional PZT piezoelectrics for some micropositioner and mirror support type applications.

Of longer range importance has been the development using sophisticated computer graphic techniques of a phenomenological elastic Gibbs function for the PZT solid solution family. This treatment permits for the first time a complete interrelation of dielectric, elastic and piezoelectric properties across the whole temperature range and composition field of the single cell perovskite structure.

In support of these major thrusts an immense amount of detailed work has been done to develop the processing capabilities which were required to assemble and fabricate the many different ceramic material combinations required in these studies. New work was performed on the zirconia problem, on the preparation and fabrication of multilayers of different material combinations, on extruded macrostructures and on the replication techniques necessary for the replamineform processing.

A small effort was committed to the growth of single crystals and of oriented polycrystals of antimony sulphur iodide which were required for hot-forging studies at the Naval Research Laboratory.

Over the present contract year, the following papers have been presented at national meetings:

Papers Presented

J.V. Biggers, S. Venkataramani, D. Hankey. Reactivity Diagrams for PZT Ceramics. 80th Annual Meeting, American Ceramic Society, Detroit, MI, May 6, 1978.

L.J. Bowen, T.A. Shrout, W.A. Schulze, J.V. Biggers. Piezoelectric Properties of PZT Multilayers. 80th Annual Meeting, American Ceramic Society, Detroit, MI, May 6, 1978.

D.P. Skinner, R.E. Newnham, L.E. Cross. Piezoelectric PZT Polymer Composites. 80th Annual Meeting American Ceramic Society, Detroit, MI, May 6, 1978.

S. Jang, S. Nomura, L.E. Cross. Electrostriction Transducers. 80th Annual Meeting, American Ceramic Society, Detroit, MI, May 6, 1978.

L.J. Bowen, W.A. Schulze, J.V. Biggers. Hot Isostatic PRessing of Lamellar Heterogeneous Piezoelectric Devices. Electronics Division and IEEE Ferroelectrics Subcommittee, Fall Meeting, Dallas, Texas, Sept. 17, 1978.

W.A. Schulze, J.V. Biggers. $Pb_5Ge_3O_{11}$-Bonded PZT Ceramics. Electronics Division and IEEE Ferroelectrics Subcommittee, Fall Meeting, Dallas, TX, Sept. 17, 1978.

T.A. Shrout, W.A. Schulze, J.V. Biggers. Lamellar Heterogeneous Piezo-electric Devices. Electronics Division and IEEE Ferroelectrics Subcommittee, Fall Meeting, Dallas, TX, Sept. 17, 1978.

T.W. Cline, L.E. Cross. Domain Contributions to the Dielectric Response in Single Crystal $Pb_5Ge_3O_{11}$ and $Sr_{0.5}Ba_{0.5}Nb_2O_6$. Electronics Division and IEEE Ferroelectrics Subcommittee, Fall Meeting, Dallas, TX, Sept. 17, 1978.

R.E. Newnham, D.P. Skinner, L.E. Cross. Multiphase Piezoelectrics. Electronics Division and IEEE Ferroelectrics Subcommittee, Fall Meeting, Dallas, TX, Sept. 17, 1978.

L.E. Cross, D. Skinner. Coupled Properties in Diphasic Systems. Electronics Division and IEEE Ferroelectrics Subcommittee, Fall Meeting, Dallas, TX, Sept. 17, 1978.

A. Bhalla, L.E. Cross, R.E. Newnham. Fibrous Ferroics. Electronics Division and IEEE Ferroelectrics Subcommittee, Fall Meeting, Dallas, TX, Sept. 17, 1978.

J.W. Laughner, T.W. Cline, R.E. Newnham, L.E. Cross. Electrical and Acoustic Effects of Ferrobielastic Switching in Quartz. Electronics Division and IEEE Ferroelectrics Subcommittee, Fall Meeting, Dallas, TX, Sept. 17, 1978.

A. Amin, R.E. Newnham, L.E. Cross, H. McKinstry. Thermal Expansion Coefficients for $PbZrO_3$:$PbTiO_3$ Piezoelectrics. American Crystallographic Association Winter Meeting, Norman, OK, March 1978.

A.S. Bhalla, L. Tongson, L.E. Cross, I.S.T. Tsong. Characterization of the Films Deposited by Chemical Reaction on Ferroelectric-Ferroelastic Gadolinium Molybdate (GMO) Surfaces. International Conference on Metallurgical Coatings, San Francisco, June 1978.

The following papers have been published in refereed journals:

R.E. Newnham, D.P. Skinner, L.E. Cross. Connectivity and Piezoelectric-Pyroelectric Composites. Mat. Res. Bull. 13, 525 (1978).

D.P. Skinner, R.E. Newnham, L.E. Cross. Flexible Composite Transducers. Mat. Res. Bull. 13, 599 (1978).

W.A. Schulze, J.V. Biggers, L.E. Cross. Aging of the Dielectric Dispersion in PLZT Relaxor Ceramics. J. Am. Ceram. Soc. 61, 46 (1978).

I.S.T. Tsong, A.S. Bhalla. Hydrogen and Fluorine Profiles in GdF_3 Films Measured by Sputter Induced Optical Emission. Appl. Phys. Letters 31(6) 381 (1978).

T. Cline, M. Liu, L.E. Cross. Dielectric Behavior of Strontium Barium Niobate ($Sr_{0.5}Ba_{0.5}Nb_2O_6$) Crystals. J. Appl. Phys. 49(7) 4298 (1978).

J.V. Biggers, S. Venkataramani. Preparation and Reactivity of Lead Zirconate Titanate Solid Solutions Produced by Precipitation from Aqueous Solutions. Mat. Res. Bull. 12, 717 (1978).

A.S. Bhalla, L.E. Cross, D.A. Payne. Thermal Optical and Elastic Properties of Isopropyl Ammonium Chloroplatinate and Chlorostannate. Phys. Stat. Sol. (a) 50, 661 (1978).

A.S. Bhalla, L.E. Cross, R.E. Newnham. Polar Domains in Lithium Metasilicate and Metagermanate. J. Cryst. Growth 46, 262 (1979).

A.S. Bhalla, L. Tongson, L.E. Cross, I.S.T. Tsong. Characterization of the Films Deposited by Chemical Reaction on the Ferroelectric:Ferroelastic Gadolinium Molybdate (GMO) Surfaces. J. Thin Solid Films 53, 55 (1978).

A.S. Bhalla, K.E. Spear, L.E. Cross. Single Crystal Growth of Antimony Sulphur Iodide. Mat. Res. Bull. 14, 423 (1979).

A.S. Bhalla, L.E. Cross, K. Vedam. Unusual White Light Conoscopic Figure in Single Crystal Lithium Metagermanate. Appl. Optics 17, 3339 (1978).

L.E. Cross, A.S. Bhalla. Domain 'Decoration' in $Gd_2(MoO_4)_3$. Phys. Stat. Sol. (a) 48, 431 (1978).

The following papers have been accepted for publication:

J.V. Biggers, T.R. Shrout, W.A. Schulze. Densification of PZT Cast Tape by Pressing. Bull. Am. Ceram. Soc.

J.M. Bind, J.V. Biggers. Classification and Particle Size Measurement of Metal Powders. Proc. Powder Conf., Rosemont, IL (1978).

J.V. Biggers, D.L. Hankey, L. Tarhay. The Role of ZrO_2 Powder in Microstructural Development of PZT Ceramics. Proc. Conf. Ceramic Processing, Raleigh, NC (1977).

J.V. Biggers, S. Venkataramani. Reactivity of Zirconia in Calcining of Lead Zirconate:Lead Titanate Compositions Prepared from Mixed Oxides. Bull. Am. Ceram. Soc.

L.B. Schein, P.J. Cressman, L.E. Cross. Electrostatic Measurements of Primary and Secondary Pyroelectricity in Partially Clamped $LiNbO_3$. Ferroelectrics.

L.B. Schein, P.J. Cressman, L.E. Cross. Electrostatic Measurement of Tertiary Pyroelectricity in Partially Clamped $LiNbO_3$. Ferroelectrics.

S. Nomura, S.J. Jang, L.E. Cross, R.E. Newnham. Structure and Dielectric Properties of Materials in the Solid Solution System $Pb(Mg_{1/3}Nb_{2/3})O_3$: $Pb(W_{1/2}Mg_{1/2})O_3$. J. Am. Ceram. Soc.

Degrees Granted:

D. Skinner. PhD Solid State Science. Nov. 1978. "Piezoelectric Composites."

A. SaNeto. PhD Solid State Science. Sept. 1978. "High Curie Temperature Ferroelectrics for Piezoelectric Applications."

J. Hauris. M.S. Solid State Science. Dec. 1978. "A Sensitive Capacitance Dilatometer for Electromechanical Strain Measurements."

K. Klicker. M.S. Solid State Science. March 1979. "Control of the PbO Partial Pressure During the Sintering of PZT Ceramics."

The report is organized into seven sections: Introduction, Electrostriction Materials, Piezoelectric Composites, Phenomenological Studies, Ceramic Processing, Related Areas, and Crystal Growth. Since most of the studies have been completed and written up for publication only a brief connecting narrative is given in each section. More detailed results are presented in the set of technical appendices.

2. ELECTROSTRICTION MATERIALS

2.1 Introduction

The rationale for reconsidering possible application of the phenomenon of electrostriction for certain types of transducer applications was given in our previous annual report (Annual Summary Report 1977-78). Monolithic multilayer technology, which makes it possible to achieve high electric fields over large volumes at low applied voltages by integrating electrodes into the body of the ceramic, has been demonstrated for larger multi-electrode electrostrictors under separate contract (Final Report on Contract N00014-77-C-0445). This work showed quite clearly that in $BaTiO_3$, PZT, and $Pb(Mg_{1/3}Nb_{2/3})O_3$ based systems internal electrodes do not have any major deleterious effect on the electroelastic response, and can be used with any of these materials to bring the voltage and current requirements to convenient levels.

It has been the major task on this contract to explore in detail the electrostrictive response of bulk samples fabricated in a number of relaxor ferroelectric compositions based on $Pb_3(Mg_{1/3}Nb_{2/3})O_3$ (PMN). Initial work on the PMN:$Pb(Mg_{1/2}W_{1/2})O_3$ (PMN:PMW) solid solution was described in the last summary report (Appendix 1) and this paper has now been accepted for publication in the September/October issue of the Journal of the American Ceramic Society. Studies of the electrostriction behavior in pure PMN in the earlier summary report indicated clearly that for higher sensitivity slow-speed applications there would be a real advantage in raising the Curie range of the PMN.

Attempts to form solid solutions with the higher temperature relaxor $Pb(Zn_{1/3}Nb_{2/3})O_3$, however, proved abortive due to the formation of a stable pyrochlore structure modification which could not be eradicated by our processing methods. However, joint work with Dr. S. Nomura clearly demonstrates that the pure PZnN has relaxor character above the higher temperature Curie range (Appendix 1).

A more successful approach to mimic the relaxor:relaxor solid solution in the complex solid solution family $Pb(Mg_{1/3}Nb_{2/3})O_3$:$PbTiO_3$:$Ba(Zn_{1/3}Nb_{2/3})O_3$ (PMN)(PT)(BaZnN) demonstrated that dual relaxor character could be preserved in ceramics of this form, leading to new high permittivity bodies with flat

temperature response over a wide temperature range.

The major part of our efforts over the last year have, however, been concerned with compositions in the solid solution system $Pb(Mg_{1/3}Nb_{2/3})O_3$: $PbTiO_3$ (PMN:PT) and with the evaluation of the electrostriction behavior as a function of composition and temperature in solid solutions in the family.

2.2 Electrostriction Behavior in the PMN:PT Solid Solution Ceramics

An outline of the initial studies on this system, indicating the property combinations which are considered of importance and some of the areas of practical applicability for materials in the 0 to 10 mole% PT composition range has been written up and submitted for publication in the journal Ferroelectrics. A copy of this manuscript is included as Appendix 2.

A more detailed paper delineating the dielectric, electrostrictive, and thermoelastic behavior has been prepared for submission to Journal of Applied Physics and is included as Appendix 3.

In very brief summary: The PMN:PT solid solution family encompasses relaxor dielectrics in which the temperature and width of the Curie range can be adjusted by composition change to give

(a) Pure quadratic electrostrictive response at room temperature, with anhysteretic behavior up to 100 kHz.

(b) Higher sensitivity slower response with maximum strains up to 1000×10^{-6} without hysteresis at frequencies of 1 Hz.

(c) Zero remanence and no aging.

(d) DC stability of the induced strain for periods up to at least eight hours.

(e) Very low thermal expansion coefficients over a wide temperature range in the relaxation region.

We believe that these practical aspects of the performance of the relaxor based materials make them of considerable interest for applications in micropositioners for optical and for other types of systems.

Basically an interesting new finding is that the polarization related electrostriction constants for the pure relaxor compositions appear to be almost an order of magnitude smaller than the corresponding $\bar{Q}_{ij}$ constants

in the ferroelectric perovskites. Further studies on other relaxors would be desirable to confirm whether this is a general rule, but it does appear that this low level of elasto-electric coupling may be critical in destabilizing the macro-domain structures in the relaxor families.

In pure $Pb_3MgNb_2O_9$, though the polarizability (dielectric permittivity) is considerably larger than in the corresponding paraelectric perovskites based on $BaTiO_3$, the strain sens vity is quite comparable reflecting this lower intrinsic electrostric ve coupling. For the PMN:PT solid solutions, as the PT content increases, the Q_{11} and Q_{12} values also increase and the relaxation range narrows. It is in these materials at compositions close to 10 mole% PT that the largest anhysteretic strains are possible (about $1,000 \times 10^{-6}$).

3. PIEZOELECTRIC COMPOSITES

3.1 Introduction

The simple theoretical considerations which lead to the expectation that two-phase composites could be designed in such a manner as to strongly optimize coupled parameters such as piezoelectricity was discussed in Appendix II of our previous annual report, and the work has now been published in the Materials Research Bulletin [MRB (3.1)]. This paper delineates the important roles which are played by the symmetry and by the mode of phase interconnection (connectivity) in optimizing the coupling in two-phase composites. From this work it became apparent that even for the simple linear systems new two-phase composites could be conceived which would have very high effective piezoelectric g coefficients, and that in particular the symmetry constraint which rigorously limits the possible hydrostatic sensitivity of the conventional PZT ceramic piezoelectric could be broken by using the appropriate composite structure.

Realization of the advantages possible for a hydrophone type material was demonstrated using an adaptation of the replamineform ceramic technology which had been evolved earlier in MRL for prosthetic bone implant materials. This replamine work was described in the earlier report (Appendix III) and has now also been published in MRB (3.2). A much more detailed account of the processing has also now been given in the PhD dissertation on "Piezoelectric Composites" by Dr. D. Skinner (3.3).

In very brief summary, Skinner's work has shown that by using a modification of the lost wax casting technique the three-dimensionally porous macrostructure of a natural coral template can be replicated in a PZT composition. Because of the full three-dimensional interconnection of the resulting PZT, it can be poled to saturation remanence from simple surface electrodes. If the PZT is backfilled with a soft elastomer second phase it can be processed to achieve a very flexible composite with exceedingly high g_{33} and g_h coefficients.

Over the last year of the current contract, the replamine studies were phased out from the present contract and were taken up under new longer term ONR funding. Here the emphasis has shifted to a new approach to the task of replication which seeks to develop artificial template structures

of dominantly 3:1 connection which can be repeatedly used for many replication steps.

A number of limited studies of alternative composite structures have been completed on the present contract. Following the work of Lester et al. (3.4) a number of attempts were made to fabricate fiber-reinforced composites in 3:1 connection using Al_2O_3 fibers or whiskers suitably dispersed in a PZT matrix. A second short study was also carried through to explore the influence of additions of a low melting $Pb_5Ge_3O_{11}$ phase on the densification and poling behavior of a soft PZT ceramic.

Two studies were also completed on lamellar heterogeneous materials fabricated by tape casting techniques. In the first experiments monolithic structures with implanted noble metal electrodes were fabricated to test the possibilities for modifying the strain sensitivity and impedance level of both static and resonant structures. In a second set of studies, techniques were developed which permitted the fabrication of lamellar structures incorporating both ferroelectric PZT and antiferroelectric PSnZT components. Samples of this type were used to explore the influence of a field forced phase change on the poling and depoling characteristics of the resulting multilayer.

The salient features from each of these studies are briefly summarized in the next section. More detailed accounts of the work are given in appropriate appendices.

3.2 Composite Piezoelectrics: Summary of Current Status

3.2.1 Replicated Macrostructures

We believe that the primary importance of our original replication work has been to demonstrate for piezoelectric voltage generation requirements the very clear advantages of composite structures of appropriate composition and phase connectivity. The established replamine technology provided a good vehicle with which to test the simple original theories and to confirm the expected advantage in the composite.

Representative data for a composite made up from a soft PZT (Ultrasonics 501A) on the template of a porites:porites coral and impregnated with an elastomer is shown in Table 3.1. Present studies which are concerned with modifications toward the development of re-usable artificial templates

TABLE 3.1

Comparison of several transducer materials

Property	PVF$_2$ (Ref. 3)	Homogeneous PZT-501A*	Flexible 3-3 composite
Density x 10^3 Kg/m^3	1.8	7.9	3.3
Compliance	High	Low	High
d_{33} x 10^{-12} C/N	14	400	100
ϵ_R	10	2000	40
g_{33} x 10^{-3} V·m/N	140	20	300

*Ultrasonic Powder, Inc. "Piezosonic Powders" data sheet

in 3:1 connection, and with the direct fabrication of the composites from extruded PZT fibers are discussed in detail elsewhere (Annual Report 1978, Contract N00014-78-C-0291).

3.2.2 Fiber and Whisker Reinforced PZTs

Efforts to fabricate a high density PZT reinforced by high strength alumina fiber or whiskers have not been successful. Even under the most gentle firing conditions there is a significant interaction between the Al_2O_3 and the mixed oxides of the PZT so that densification by conventional sintering proved impossible. A most bothersome feature of the study was the clear evidence that local reactions with the components of the PZT produce strong local "sticking" around the fibers so that voids are always present.

It appears that a local liquid phase which would promote densification at lower temperatures and help lubricate the fibers will be necessary to exploit this approach.

Details of these studies are given in Appendix 4.

3.2.3 Lead Germanate Composites

Evidence from earlier studies on lead zirconate titanate based capacitor dielectrics had suggested that the low melting $Pb_5Ge_3O_{11}$ ferroelectric germanate might be used to lower the temperatures required for densification and to produce a thin lamellar interface phase which could markedly modify the poling and depoling characteristics of the ceramic piezoelectric. This study demonstrated that it was possible to form dense piezoelectric composites with PZT at temperatures below 1000°C. The composites demonstrated that the ferroelectric component could be poled at elevated temperature and was stabilized against depoling. In this initial study composites were prepared with $d_{33} = 65 \times 10^{-12}$ m/V, permittivity k = 470 which showed stabilization of the polarization at reverse fields up to 40 kv/cm.

Full details are given in appendix 5.

3.2.4 Piezoelectric Properties of Internally Electroded PZT Multilayers

Internally electroded piezoelectric devices have been prepared by screen-printing platinum electrodes onto tape cast PZT, stacking the electroded tapes in appropriate configurations, warm-pressing to form a monolithic unit and then air-sintering in controlled atmosphere to final density. After firing the internal electrodes are exposed where necessary by surface grinding and contacted by external electrodes for poling and driving.

Composites have been made from both hard and soft commercial PZT formulations for both resonant and static strain evaluation.

It has been shown that the dielectric permittivity, dissipation factor, and piezoelectric coefficients are largely unaffected by the presence of the internal electrode and thus that elements which show greatly improved strain:voltage ratios compared to conventional monoliths can be prepared. The internal electrodes have also been shown to have little effect on the frequency constant or the mechanical Q for resonant vibrations.

As an example of one type of device which can be fabricated by this versatile technique, a piezoelectric transformer has been designed and

tested. The multilayer configuration shows considerable improvement in voltage step-up characteristics compared to a conventional single layer design.

A detailed account of these studies has been prepared for publication and is given in Appendix 6.

3.2.5 Electromechanical Properties of Antiferroelectric: Ferroelectric Multilayer PZT Based Composites

In a second example of the tape cast multilayer technology, lamellar devices have been made up which comprise alternating layers of a commercial soft PZT composition and a $PbTiO_3:PbZrO_3:PbSnO_3$ antiferroelectric composition. The objective of this study was to determine whether the antiferroelectric-ferroelectric field forced phase transition in the PbSnZT could be exploited to permit displacement continuity and poling of the interleaving PZT, while the higher transition field at higher temperature could effectively stabilize against depoling under reverse field. The concept is somewhat similar to that attempted with the germanate interleaving phase in 3.2.3 above, but attempts to use an alternative dielectric mechanism to establish displacement continuity in the poling process.

The essential features of the processing required to achieve dense samples and of the resulting properties are given in Appendix 7.

References

3.1 R.E. Newnham, D.P. Skinner, L.E. Cross. Mat. Res. Bull. 13, 525 (1978).

3.2 D.P. Skinner, R.E. Newnham, L.E. Cross. Mat. Res. Bull. 13, 599 (1978).

3.3 D.P. Skinner. "Piezoelectric Composites," PhD Solid State Science, The Pennsylvania State University, November 1978.

3.4 W. Lester. "A New Composite Ceramic Piezoelectric Transducer Material," Technical Memorandum IW 69-20-TM-IU (1970).

4. PHENOMENOLOGICAL STUDIES

4.1 Introduction

Over the contract period work in this area has been focused on the task of developing the programming techniques so that the ADAGE computer graphics system and the associated IBM 370 computer at Penn State can be used for the rapid evaluation of the phenomenological elastic Gibbs functions which can be used to describe the perovskite type simple proper ferroelectrics.

In earlier studies routines were developed which permit the visualization of the polarization surfaces of constant free energy in full three-dimensional form, so that the low energy saddle points which separate the phases at the first order transitions between cubic and tetragonal, tetragonal and orthorhombic, and between orthorhombic and rhombohedral ferroelectric phases can be readily visualized. The programmming was developed using the simple Devonshire function with coefficients chosen to describe $BaTiO_3$ but is of a suitable form that other energy parameters may be used so as to describe any combination of phases possible in the perovskites.

Over the past year a considerable effort has been devoted to the development of a Gibbs function which can be used to describe the full family of thermal, dielectric, elastic, and piezoelectric properties of the unmodified $PbZrO_3$:$PbTiO_3$ crystalline solid solutions which are the basis for most present piezoceramic formulations.

In the following section, a brief summary of the results to date is given. A more complete description of the study is presented in Appendix 8.

4.2 Brief Summary of Results

Parameters in the ΔG function which give a good fitting with the observed phase diagram and which generate a near vertical morphotropic boundary between tetragonal and rhombohedral phases are

$$A = A_o \ (T-\theta)$$
$$\phi = B/C = -1.20 \text{ in } PbZrO_3$$

changing linearly to $+ 0.80$ in $PbTiO_3$.

$$E = 80 \times 10^{-6}$$

$$F = -450 \times 10^{-6} \text{ in } PbZrO_3 \text{ changing to } -200 \times 10^{-6} \text{ in } PbTiO_3.$$

The fitting to the spontaneous polarizations as a function of composition and temperature which have been derived from the spontaneous strain assuming pure electrostriction is quite good, and the striction constants required appear reasonable and as expected do not change significantly with composition. The rather sharper curvatures of P_s calculated at temperatures near T_c in all compositions as compared to the experimental values suggests that the present level of approximation might be improved by either including a first eighth power term in the energy expansion or by imparting a temperature coefficient to the B term. There is evidence from very recent computer runs that a small positive temperature coefficient on B also improves morphotropy near T_c.

Free energy values calculated from the function are in reasonable accord with measured values of the enthalpy, but the present thermal data are not very precise. Using that fitting to derive the Curie constant C gives a value 3.0×10^5 which is not unreasonable. However, again the available experimental data are not of great help, with literature values going from $1.5.10^5$ to 15.10^5.

In making any comparison between the calculated and measured X, d, and g values, it must be remembered that what has been derived are the single domain single crystal values, while what are available experimentally are averaged polycrystal values. For the paraelectric cubic states, the polycrystal orientations make no difference and the calculated X values are towards the lower end of the spectrum of measured values as might be expected. For the g values the calculated values are in general higher than measured g values, but without proper averaging comparison is difficult. In the d values the calculated values are lower, reflecting the lower X values of the ferroelectric single domain states.

In the influence of mechanical stress the calculations give probably the first reliable evidence of how the composition at which morphotropy occurs will be shifted by internal stresses. The manner in which the boundary moves under compression and tension agrees with earlier estimates made by Henning (4.1).

It should be realized that the phenomenological analysis which has

been completed essentially establishes a reasonable framework to inter-relate all aspects of the bulk elasto-dielectro-thermal behavior of the PZT system. As additional experimental evidence in any of these areas becomes available, the refinement of the function can be improved and the consequences on other apparently only indirectly related parameters ascertained.

The present analysis suggests immediately two areas where refined data could be of great help:

(1) High temperature, high frequency dielectric measurements are required at temperatures above T_c to better delineate the Curie Weiss behavior in the cubic phase. Careful specimen preparation and characterization are required before such measurements are carried through to be sure that the data are not perturbed by grain boundary phases or Maxwell Wagner effects.

(2) With modern calorimetry it should now be possible to refine the thermal data and thus provide a check on the dielectric Curie Weiss parameter.

With the basic relations now established for the pure PZTs, a second area which can be very effectively carried through is the study of the effects of various doping ions on the intrinsic properties. This would give a clearer quantitative indication of the extrinsic modifications which such doping schemes engender.

Developments from the present study could also include:

(1) Extension to the single cell compositions in the PLZT and PSnZT families.

(2) Incorporation of the Kittell:Cross two-sublattice formalism to encompass the antiferroelectric phase compositions.

(3) Inclusion of the nonferroelectric oxygen octahedron rotation order parameters and their coupling coefficients to polarization and strain so as to describe the canted octahedra multicell phases in the PZT and PLZT families.

Certainly, an immense amount of work has been carried out already to develop modified PZT-like compositions. Perhaps a major criticism which could be leveled at much of this work is that in very few cases has it been possible to separate modifications which have been made to the intrinsic single domain properties of the ferroelectric from those which

have been made simultaneously to the extrinsic domain and phase boundary contributions to the measured properties. Yet without such clear separation a proper scientific attack on the problem is not strictly possible.

We believe that the automated phenomenological analysis provides the necessary correlation between some simply measured properties and the single domain characteristics, which will permit such a separation and thus a much better understanding of this and of many other comparable perovskite and tungsten bronze solid solution ferroelectric systems.

It should be stressed that the phenomenology is not a theory, but merely a rather sophisticated way of describing and inter-relating the thermo-elasto-electric properties of these complex polarizable deformable solids. The functional description involves a level of approximation which can always be improved by expansion of the function, as new and more precise experimental data become available and thus is a continuing task. Since, however, there is very clear evidence in ferroelectric solid solutions that the energy function parameters mutate slowly and continuously with composition change, it does have the very strong merit that the time invested in generating a proper and adequate function to describe the present experimental information on the pure PZTs will be a firm base from which to develop relations for the practical transducer ceramics, the PLZTs and other comparable solution systems.

Reference

4.1   K.H. Härdtl, D. Hennings.   Science of Ceramics 6A, 298 (1973).

5. CERAMIC PROCESSING

5.1 Introduction

Over the earlier period of this contract a substantial effort was required to equip the group with the background and techniques for processing a very broad range of piezoceramic materials by both conventional and some less conventional methods. New equipment for powder preparation both from mixed oxides and from organic precursors has been installed, including new jet and attritor mills. A Donaldson classifier was acquired and brought into operation with the MRL CESEMI system for automatic particle shape and size analysis. For forming, an automatic rotary pellet press was installed and new equipment for tape casting of PZTs brought into operation. During the three year period all processing furnaces have been placed on automatic program control using Research Inc. controllers and data track programming. Gas isostatic hot pressing equipment was designed, fabricated and placed into operation.

Utilizing this equipment, studies have been completed on preparation and reactivity of lead zirconate:lead titanate solid solutions prepared by precipitation from aqueous solutions (5.1); the densification of PZT cast tape by pressing (5.2); the role of ZrO_2 powder in microstructure development in PZT ceramics (5.3), and the reactivity of zirconia (5.4).

During the current year studies on the solid state reactions in the $PbO-TiO_2-ZrO_2$ system, on the reactivity of chemically prepared PZT solid solutions, and on the hot isostatic pressing of PZT materials have been completed. A very brief description of these works are given in the next section; full reports are included as appendices.

5.2 Solid State Reactions in the $PbO-TiO_2-ZrO_2$ System

The reaction sequences which can occur in the formation of PZT solid solutions by thermal processing of mixed oxide powders have been studied. The method of analysis of the complex reaction sequence was to place the charge in a closed Al_2O_3 crucible which was inserted into a preheated calcining furnace for a fixed interval of time ranging from 2 to 24 hours. After heating the crucible was air quenched and the powders analyzed for phase content by x-ray powder methods. DTA and TGA were also carried out

on the powders. A wet chemical analysis technique was also used to determine the amount of uncombined PbO in each calcined powder.

To account for the observed sequence of phases, a three-step reaction sequence involving initial formation of $PbTiO_3$ followed by its reaction with PbO and ZrO_2 to form a PbO solid solution phase, the final PZT being formed by the PbO solid solution phase reacting with uncombined ZrO_2 and $PbTiO_3$ (Appendix 9).

5.3 Reactivity of Chemically Prepared Lead Zirconate:Lead Titanate Solid Solutions

The sequence of reactions leading to the formation of the final PZT phase from precipitated alkoxides of zirconium and titanium and lead oxide have been studied for compositions $PbZr_xTi_{1-x}O_3$ with x = 0.5, 0.52, 0.55, and 0.60. The techniques of analysis were similar to those used in the mixed oxide compositions above, i.e. x-ray diffraction for phase identification, wet chemical analysis for unreacted PbO and DTA and TGA for phase changes.

It appears from these studies that the reaction sequence is much simpler in the alkoxide prepared system than in the mixed oxides. The precipitated complex is already a PZT hydroxide which directly decomposes into the homogeneous PZT. There is no evidence of intermediate lead titanate or lead oxide solid solution phases. Clearly the chemical preparation method should give a more homogeneous stoichiometric PZT. However, the densification of this powder will certainly be different from conventional mixed oxide sintering where the intermediates may play a very important role (Appendix 10).

5.4 Hot Isostatic Pressing (HIP)

A study has been made of the parameters for a single step hot isostatic pressing process for PZT piezoceramics. It is shown that the time required to reach high densities is considerably shorter than in conventional sintering. The small porosity reduction which the HIP does effect does not make any significant change in the relative permittivity piezo-electric coefficients or elastic compliance of the PZTs tested, but does make a significant improvement in the dielectric breakdown strength.

Densification of the PZT during the HIP processing is believed to take place largely by a mechanism involving particle deformation, even for the materials where a liquid second phase appears to be present at the HIP temperature (Appendix 11).

References

5.1 J.V. Biggers, S. Venkataramani. Mat. Res. Bull. _12_, 717 (1978).

5.2 J.V. Biggers, T.R. Shrout, W.A. Schulze. Bull. Amer. Ceram. Soc. (in press).

5.3 J.V. Biggers, D.L. Hankey, L. Tarhay, Proc. Conf. Ceramic Processing, Raleigh, NC (1977).

5.4 J.V. Biggers, S. Venkataramani. Bull. Amer. Ceram. Soc. (in press).

6. RELATED AREAS

6.1 Introduction

Over the period of this contract, a number of studies which are closely related to the primary objectives have received full or partial support from contract funds. In this section these projects will be briefly discussed, the aims and objectives of the studies outlined and in each case the important results reviewed. A more complete account of each area is given in the attached Appendices 12, 13, 14, 15, and 16.

6.2 Complex Perovskites Containing TeO$_6$ Groups

Politova and Venevtsev (6.1, 6.2) have reported data on a wide family of compounds in the perovskite structure on the general formula $A^{+2} (B_{0.5}^{+2} Te_{0.5}^{+6}) O_3$ where the A^{+2} cations are Sr, Ca, or Cd and the B^{+2} cations are Mg, Co, Zn, Cd, Sr, Ca, or Mn. Many were reported to have high temperature phase transitions into a distorted monoclinic form and to be of potential interest as high Curie temperature "strong" ferroelectrics. Since such materials are clearly of interest for potential piezoelectrics, either alone or as components in other perovskite solid solutions, it was decided to investigate the family. Unfortunately, from the simple structural and dielectric studies of the Russian workers, it was not possible to distinguish whether the distorted phases were ferroelectric or whether they were antiferroelectric or ferroelastic.

To clarify the nature of the distorted phases appearing at room temperature in these tellurate perovskites, it was decided to apply the method of second harmonic optical analysis using simple powder samples. By this method it is possible to separate in the distorted perovskites acentric (ferroelectric) species from centric (antiferroelectric and ferroelastic) distorted structures.

For 19 of the compounds studied, only 4 showed any harmonic signal at all, and in all of these the activity was less than 2% of quartz, suggesting probably even in these compounds an extrinsic, perhaps an impurity, effect. Thus it appears that in spite of the very high suggested polarizability of the TeO$_6$ octahedron, these compounds still appear to follow the general rule that for (B^{2+}, B^{6+}) systems cation ordering

usually occurs and gives rise to dominantly antiferroelectric displacement structures.

In view of the focus of our work on potential piezoceramics, the optical SHG results saved much time by eliminating these tellurates from further study.

6.3 Studies of Strontium Pyroniobate Sr₂Nb₂O₇

Recent studies in Japan (6.3) have shown $Sr_2Nb_2O_7$ to be a strong ferroelectric with one of the highest Curie temperatures known (1352°C). Initial studies in our laboratory on ceramic samples confirmed exceedingly strong optical harmonic generation and thus a strongly acentric structure, but it proved impossible to pole the ceramics to a bulk piezoelectric response.

The study was then transferred to exploring the possibility of generating very thin stoichiometric films of the pyroniobate by RF sputtering. The reasons for adopting this approach were (1) to ascertain whether the amorphous $Sr_2Nb_2O_7$ films themselves might retain a measure of ferroelectric activity, as had been suggested by Lines (6.4) in $LiNbO_3$, and (2) if the noncrystalline films were not ferroelectric, to recrystallize the specimens by thermal annealing and delineate the evolution of the ferroelectric behavior with increasing crystallite size.

The initial task of generating stoichiometric pinhole-free films of the correct pyroniobate composition proved more challenging then anticipated. The problem was eventually traced to an anomalously high resputtering rate from the substrate which we believe may prove to be a problem common to the fabrication of all high permittivity insulator films made by the RF sputtering method.

The $Sr_2Nb_2O_7$ composition was formed by sputtering from a nonstoichiometric target with suitable adjusted $SrO:Nb_2O_5$ ratio. In the noncrystalline form the films proved to be nonferroelectric, and to have linear dielectric properties and a relative permittivity ∿20.

Attempts to use the sputtered films to study the effects of recrystallization on the dielectric properties were completely frustrated by the unusual thermal annealing kinetics. It appeared that once initiated crystallization proceeded very rapidly but was accompanied by total disruption of the film.

6.4 Piezoelectricity in Bismuth Titanate

With the evolution of new techniques which may permit the economical production of strongly grain oriented ceramics, the highly anisotropic ferroelectrics in the bismuth oxide layer structure family are becoming of considerable interest as candidate materials for piezoceramic applications.

Unfortunately, at present very little is known about the electromechanical coupling in any of these bismuth oxide layer structure cyrstals. Since we were very fortunate in having already a rather large suite of bismuth titanate ($Bi_4Ti_3O_{12}$) single crystals, several of which had already been electrically poled into the single domain form, it appeared useful to measure the piezoelectric response in these single domain crystals.

In bismuth titanate, the ferroelectric phase is in point group m and the d_{ij} matrix has the components

$$\begin{matrix} d_{11} & d_{12} & d_{13} & 0 & d_{15} & 0 \\ 0 & 0 & 0 & d_{24} & 0 & d_{26} \\ d_{31} & d_{32} & d_{33} & 0 & d_{35} & 0 \end{matrix}$$

For experimental study, the Berlincourt d_{33} meter was used to measure d_{11}, d_{22}, d_{33} on small rectangular crystals cut from single domain sections. To compare to these measured data, d values were derived phenomenologically on the assumption that $Bi_4Ti_3O_{12}$ is a simple proper ferroelectric.

Comparing the measured and calculated values, there is excellent agreement for d_{11} and d_{22}, but for d_{33} theory and experiment differ by more than one order of magnitude. The data show clearly that the simple Devonshire type phenomenology is inadequate for $Bi_4Ti_3O_{12}$ and suggest a triggered phase change in which the spontaneous polarization triggers an instability in a second symmetry unrelated order parameter.

6.5 Electrostatic Measurements of Unusually Large Secondary Pyroelectricity and of Tertiary Pyroelectricity in Partially Clamped $LiNbO_3$ Single Crystals

In a cooperative study with L.B. Schein and P.J. Cressman at Xerox Corporation pyroelectric signals were observed from single domain crystals

of lithium niobate under conditions of partial radial clamping. The appropriate boundary conditions were produced by the use of local laser heating to generate a temperature change in the central spot of a larger diameter circular disk.

The observations using a non-contact electrometer to map the potential distribution permitted the effective separation of primary and secondary pyroelectricity, and the observation in a ?-cut crystal (the 2 or y axis normal to the plane of the disk) of a very large secondary signal where components along the 1 and 3 axes map the radial and tangential components of the thermal stresses.

In a second study, the neutral axis which exists when the 1 or x axis is normal to the plane of the sheet was used to map what appears to be the first observations of true tertiary pyroelectricity.

References

6.1 E.D. Politova, Yu. N. Venetsev. Soviet Phys. Dokl. _18_, 264 (1973).

6.2 E.D. Politova, Yu. N. Venetsev. Mat. Res. Bull. _10_, 319 (1975).

6.3 S. Nanamatsu, M. Kimura, T. Kowamura. J. Phys. Soc. Japan _38_, 817 (1975).

6.4 M.E. Lines. Phys. Rev. B_15_, 388 (1977).

7. CRYSTAL GROWTH

7.1 Antimony Sulphur Iodide

During the second year of this work, a restricted effort was initiated to grow single crystals of the ferroelectric antimony sulphur iodide (SbSI). This crystal has the highest known d_{33} in any ferroelectric, but it is mechanically unsuitable for direct application. The prototypic symmetry is mmm (orthorhombic) and the bonding highly anisotropic with strong covalent bonding along the polar 'c' axis of the ferroelectric phase, but only very weak Van der Waals forces perpendicular to this direction. In practice the crystals tend to grow in fibrous bundles which open like the pages of a book under shearing forces.

The objective of the present study was to grow single crystals or tightly intergrown crystal bundles which could then be hot forged to study the influence of the forging technique on the mechanical strength and piezoelectric response of the resulting polycrystal.

In view of the need for crystalline material in rather large quantity on a rather short time scale, it was decided to use a flux growth method with SbI_3 as the flux. The studies which were accomplished are summarized in Appendix 17.

It was observed that the morphology of the crystals grown could be controlled by choosing suitable combinations of growth parameters primarily the $Sb_2S_3:SbI_3$ ratio, the temperature gradient, and the rate at which the crucible was lowered through the gradient. A number of batches with crystals more than several centimeters in length, and ranging from large platey crystals to lightly intergrown fiber boules were supplied to NRL for forging studies.

7.2 Lithium Metasilicate

The Czochralski pulling technique was used to study the growth of single crystals of lithium metasilicate Li_2SiO_3 which is an interesting polar crystal having potential for applications in piezoelectric and electrooptic systems. Crystalline Li_2SiO_3 has an orthorhombic structure in space group Cmc2, with $(Si_2O_6)_\infty$ chains oriented parallel to the polar c axis. The compound melts congruently at 1201°C, but Czochralski growth

is complicated by the very high viscosity of the melt at the growth temperature. Good quality crystals with crack-free areas up to 5mm x 5mm normal to the 'c' axis were eventually grown. In all cases, however, the crystals exhibited a lamellar structure of closely spaced antipolar twins which were revealed by etching. Attempts to modify this twin structure by doping and by growth in an electric field were not successful.

We believe that a more thorough investigation of the conditions required for producing larger crack-free crystals will be required before the antipolar twinning can be successfully tackled. In very recent studies of the recrystallization of lithium metasilicate from lithium silicate glasses, we have found that excellent crystal alignment can be achieved by recrystallizing in a very high temperature gradient. Thus it may be that by careful control of the gradient at the crystal-melt interface, the polar twinning can also be controlled in the single crystal.

Details of this work are given in Appendix 18.

APPENDIX 1

Electrostriction in $Pb(Zn_{1/3}Nb_{2/3})O_3$

S. Nomura, J. Kuwata, S.J. Jang,
L.E. Cross and R.E. Newnham

ELECTROSTRICTION IN $Pb(Zn_{1/3}Nb_{2/3})O_3$

S. Nomura and J. Kuwata
Department of Physical Electronics
Tokyo Institute of Technology
Ookayama, Meguro-Ku, Tokyo 152

S.J. Jang, L.E. Cross and R.E. Newnham
Materials Research Laboratory
The Pennsylvania State University
University Park, Pennsylvania 16802

ABSTRACT

The electrostriction in $Pb(Zn_{1/3}Nb_{2/3})O_3$ crystals has been investigated using a strain gauge method. In the ferroelectric phase below 140 C, the strain vs the electric field shows a hysteresis, which is ascribed to the effect of ferroelectric domains. A quadratic relation holds between the strain x and the electric polarization P as $x = QP^2$ above about 170 C in the paraelectric phase. Values of the electrostrictive Q coefficients are determined from the measurements near 190 C, as $Q_{11} = 1.6 \cdot 10^{-2} m^4/C^2$, $Q_{12} = -0.86 \cdot 10^{-2} m^4/C^2$, and $Q_{44} = 0.85 \cdot 10^{-2} m^4/C^2$.

Introduction

Lead zinc niobate $Pb(Zn_{1/3}Nb_{2/3})O_3$ is a ferroelectric of the perovskite type exhibiting a diffuse phase transition. The structure is rhombohedral at room temperature and undergoes the phase transition to cubic at about 140 C. Many studies have been done on the dielectric properties (1,2,3), on the optical properties (3,4,5,6), on the domain structure (7), and also on the thermal dilatation (8).

One of the fundamental properties of a ferroelectric is electrostriction, which gives rise to a strain proportional to the square of an applied electric field. Yet no work has been reported so far on the electrostriction in $Pb(Zn_{1/3}Nb_{2/3})O_3$ crystal while applying electric field in the temperature region of the diffuse phase transition, where the regions of ferroelectric and paraelectric phases coexist.

This paper is concerned with the electrostriction in $Pb(Zn_{1/3}Nb_{2/3})O_3$ single crystals using a strain gauge. The induced strain was measured as a function of applied electric field, or the electric polarization from room temperature to 200 C.

Experimental

Our investigation was made using flux-grown crystals of $Pb(Zn_{1/3}Nb_{2/3}O_3)$ (2). The specimens used in the measurement of the electrostriction were rectangular plates oriented parallel to (111) and to (100), and ranging from 2.5 ~ 3.7 mm on edge and from 0.35 to 3.75 mm thick. Silver electrodes were evaporated onto the faces, and a polymid foil strain gauge (Kyowa, KFH-02-350) was bonded with a cement (Kyowa, PC-6) on the face of the crystal as shown in Fig. 1.

In the cubic structure of perovskite type, the electrostrictive coefficient tensor Q_{ij} is defined by the following equation

$$\begin{pmatrix} x_{11} \\ x_{22} \\ x_{33} \\ x_{23} \\ x_{13} \\ x_{12} \end{pmatrix} = \begin{pmatrix} Q_{11} & Q_{12} & Q_{12} & 0 & 0 & 0 \\ Q_{12} & Q_{11} & Q_{12} & 0 & 0 & 0 \\ Q_{12} & Q_{12} & Q_{11} & 0 & 0 & 0 \\ 0 & 0 & 0 & Q_{44} & 0 & 0 \\ 0 & 0 & 0 & 0 & Q_{44} & 0 \\ 0 & 0 & 0 & 0 & 0 & Q_{44} \end{pmatrix} \begin{pmatrix} P_1^2 \\ P_2^2 \\ P_3^2 \\ P_2 P_3 \\ P_1 P_3 \\ P_1 P_2 \end{pmatrix} \quad (1)$$

where x_{ij} represents the strain components and P_1 is a component of the included electric polarization vector (9). In the measurement of the specimen shown in Fig. 1a, the strain is given by

$$x_{11} = Q_{11} P_1^2 \quad (2)$$

For the specimen in Fig. 1b the strain is

$$x_{22} = Q_{12} P_1^2 \quad (3)$$

For the third specimen (Fig. 1c), the strain parallel to the (111) plane denoted by $x_{(111)}$, is measured as a function of the electric polarization P along the [111] direction. Here the relation is

$$x_{(111)} = Q_{(111)} P^2_{[111]}, \quad (4)$$

where

$$Q_{(111)} = (Q_{11} + 2Q_{12} - Q_{44})/3 \quad (5)$$
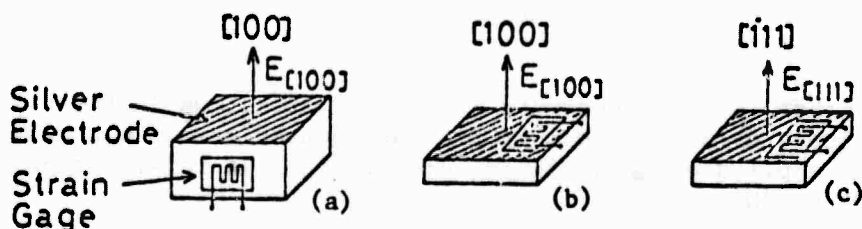
FIG. 1
Specimens with electrodes and strain gauge attached.

3

Thus we were able to determine the values of the electrostrictive coefficients Q_{11}, Q_{12}, and Q_{44}, by measuring the strain with the specimens (a), (b), and (c).

Strain gauge measurements were carried out by an AC method at 180 Hz, using a phase sensitive detector and a double bridge to buck out the residual AC signal. The dummy gauge was bonded on a copper cube mounted inside a copper block together with the sample to ensure uniformity of the temperature. The resolving power was estimated as $\Delta\ell/\ell \sim 3\cdot10^{-7}$. The induced strain was measured step by step with increasing and decreasing applied field at various temperatures. The data were taken about five minutes after the electric field had been applied upon the crystal. The induced electric polarization was measured at 50 Hz using a Sawyer-Tower circuit.

Results

For the specimen (c), in which the electric field was applied along the [111] direction parallel to the spontaneous polarization in the ferroelectric phase, the strain was measured not only in the paraelectric phase but also in the ferroelectric phase, in order to observe the effect of ferroelectric domain. In the cases of the specimens (a) and (b), the measurements were made only in the paraelectric phase, where the quadratic equation (2) or (3) holds.

The curves of strain $x_{(111)}$ vs electric field $E_{[111]}$ taken at various temperatures are shown in Fig. 2. In the ferroelectric phase [(a), (b), and (c)]
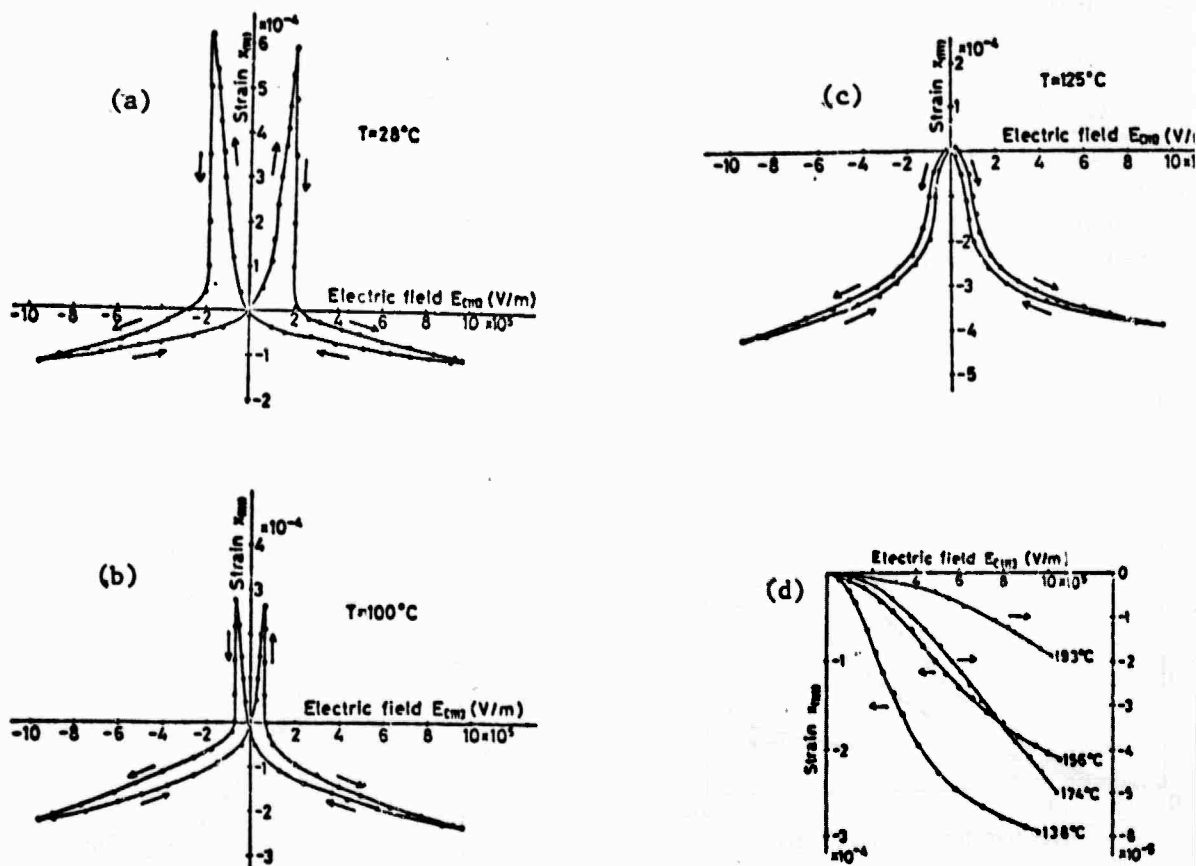
FIG. 2

Strain $x_{(111)}$ vs. electric field $E_{[111]}$. (a) T = 28°C, (b) T = 100°C, (c) T = 125°C, (d) T = 138°C, 156°C, 174°C, and 193°C.

the curve is accompanied by a hysteresis, which is ascribed to the effect of the ferro-electric domains. The coercive field decreases with increasing the temperature, vanishing at about 135 C, which is shown in Fig. 3. The curves of $x_{(111)}$ vs $E_{[111]}$ at temperatures higher than 138 C are shown together in Fig. 2(d). It should be noted that the strain-electric field relation is not quadratic near the average Curie temperature in the paraelectric phase.

The strain x_{11} and x_{22} were measured as a function of electric field E_1 ($\equiv E_{[100]}$) in the paraelectric phase, as shown in Figs. 4 and 5 respectively. The strain x_{11} is positive, while x_{22} is negative. In the measurement of the strain x_{11} [the specimen (a)], the strength of electric field was limited to $3.6 \cdot 10^5$ V/m to protect the specimen and the strain gauge from electric breakdown.

FIG. 3
Coercive field vs temperature
for $Pb(Zn_{1/3}Nb_{2/3})O_3$

To examine the relation between the strain and the polarization, the induced polarization was measured as a function of the electric field at 50 Hz, using a Sawyer-Tower circuit. It was noted that the peak value of the polarization does not vary appreciably with measuring frequency in the paraelectric phase above 170 C. The $P_{[111]}$ vs $E_{[111]}$ curves are shown in Fig. 6. The log-log plot of x_{11}, x_{22}, and $x_{(111)}$ against the polarization at high temperatures are given in Fig. 7, where the quadratic relation $x \propto P^2$ is indicated by a straight line. This confirms the quadratic formulae given by the equations (2), (3), and (4) in the temperature region above 170 C. The values of the electrostrictive coefficients Q_{11}, Q_{12} and $Q_{(111)}$ were determined by a least square method using the data near 190 C as $Q_{11} = 1.6 \cdot 10^{-2}$ m^4/C^2, $Q_{12} = -0.86 \cdot 10^{-2}$ m^4/C^2, and $Q_{(111)} =$
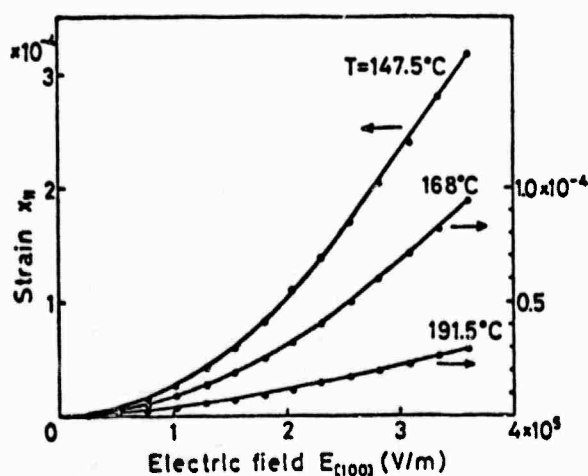
FIG. 4
Strain x_{11} vs electric field $E_{[100]}$
in the paraelectric phase.
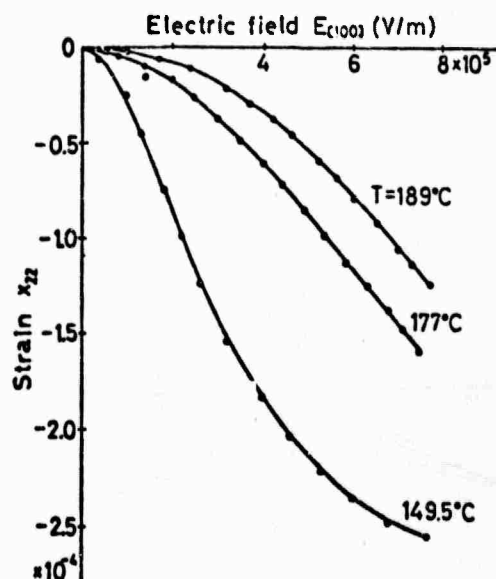
FIG. 5
Strain x_{22} vs electric field $E_{[100]}$ in the paraelectric field.

$-0.32 \cdot 10^{-2}$ m^4/C^2, the errors of which remain less than ten percent. Using the equation (5), the Q_{44} coefficient was calculated as $Q_{44} = 0.85 \cdot 10^{-2}$ m^4/C^2.

Discussion

As an explanation of the diffuse phase transition which occurs in the disordered perovskite compounds, it has been considered that the ferro-electric phase transition is not sim-ultaneous throughout a crystal because of the internal stress and the compo-sition fluctuation. Previously we observed (10) that in the paraelectric phase the quadratic electro-optic g coefficient of Pb(Zn$_{1/3}$Nb$_{2/3}$)O$_3$ quad-ratic with respect to the polarization, increases with decreasing temperature on approaching the average Curie tem-perature. This behavior is attributed to the influence of polar micro-domains, which exist even in the paraelectric phase. We analyzed the data for the electro-optic effect by introducing a temperature-dependent volume fraction of polar regions and found that the true coefficient is nearly temperature-independent and that the volume frac-tion becomes less than five percent in the vicinity of 190 C. In other words, the quadratic formula for the electro-optic effect is approximately correct near 190 C in Pb(Zn$_{1/3}$Nb$_{2/3}$)O$_3$. It is quite reasonable to expect that a sim-ilar situation will hold in the case of electrostriction. As demonstrated in Fig. 7, a quadratic relation holds between the strain and the polarization at the higher temperatures.

In a ferroelectric of the displacive type, derived from centric prototype structures, similar relations between strain and polarization apply regardless of whether the polarization is induced or spontaneous. Therefore one can esti-mate the order of magnitude of the Q coefficients from the values of the spon-taneous strain and the spontaneous polari-zation. The $Q_{(111)}$ coefficient calculated from the values of the spontaneous strain (8) and the spontaneous polarization (10) at room temperature is $-0.322 \cdot 10^{-2}$ m^4/C^2, which agrees with that determined from the measurement in the paraelectric phase.
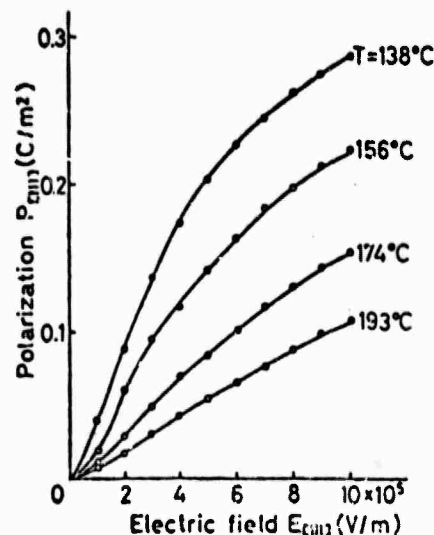

FIG. 6
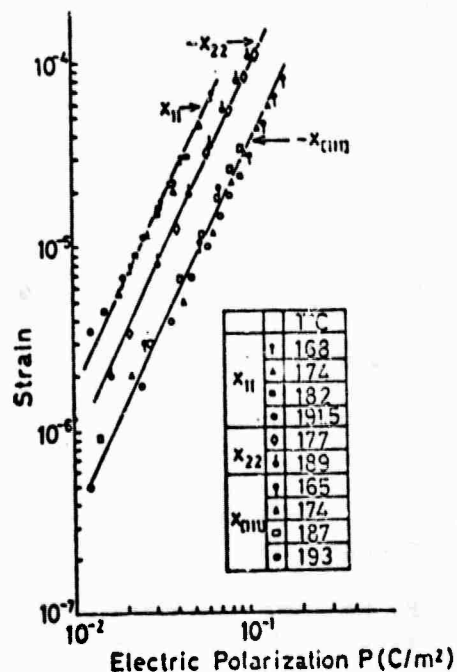Curves of electric polarization $P_{[111]}$ vs electric field $E_{[111]}$ at various temperatures.

FIG. 7
Log-log plot of strain x_{11}, x_{22} and $x_{(111)}$ against polarization in the paraelectric phase. A straight line represents $x \propto P^2$ equation.

According to a phenomenological theory developed by T. Yamada [11], the electrostrictive constants of the perovskite type oxide are nearly constant with the values, $Q_{11} = 0.10$ m^4/C^2, $Q_{12} = 0.034$ m^4/C^2, and $Q_{44} = 0.029$ m^4/C^2. The values we determined on $Pb(Zn_{1/3}Nb_{2/3})O_3$ are smaller in the magnitude, compared with those values. It is interesting to mention that the quadratic electro-optic g coefficients have almost the same value in a number of oxygen-octahedral ferroelectrics, with the exception of those containing highly polarizable Pb^{2+} ions in the perovskite A position. It has been reported that the g coefficient of Pb-containing ferroelectrics are about 1/10 [5]. It is not certain at present whether the similar situation holds for the electrostrictive coefficient. Further understanding awaits experimental data for more perovskite type oxides containing Pb^{2+} ions.

Acknowledgment

References

1. V. A. Bokov and I. E. Myl'nikova, Fozola Tverdogo Tela 2, 2728 (1960); translation: Soviet Physics Solid State 2, 2428 (1961).

2. Y. Yokomizo, T. Takahashi, and S. Nomura: J. Phys. Soc. Japan 28, 1278 (1970).

3. G. A. Smolenskii, Proc. Inst. Meeting of Ferroelectricity, Kyoto, 1969; J. Phys. Soc. Japan 28, Suppl. 26 (1970).

4. G. A. Smolenskii, N. _. Krainik, A. A. Berezhnoi, and I. E. Myl'nikova, Fizika Tverdogo Tela 10, 2675 (1968); translation: Soviet Physics Solid State 10, 2105 (1969).

5. P. D. Thacher, J. Appl. Phys. 41, 4790 (1970).

6. S. Nomura, H. Arima, and F. Kojima, Jap. J. Appl. Phys. 12, 531 (1973).

7. S. Nomura, M. Endo, and F. Kojima, Jap. J. Appl. Phys. 13, 2004 (1974).

8. S. Nomura, M. Abe, F. Kojima, and K. Uchino, Jap. J. Appl. Phys. 14, 1881 (1975).

9. I. S. Zheludev, Physics of Crystalline Dielectrics, Vol. 2, p. 600. Plenum Press (1971).

10. F. Kojima, J. Kuwata, and S. Nomura, Proc. of the 1st Meeting on Ferroelectric Materials and Their Applications, Kyoto, p. 155 (1977).

11. T. Yamada, J. Appl. Phys. 43, 328 (1972).

APPENDIX 2

Large Electrostrictive Effects in Relaxor Ferroelectrics

L.E. Cross, S.J. Jang and R.E. Newnham

LARGE ELECTROSTRICTIVE EFFECTS IN RELAXOR FERROELECTRICS*

L.E. Cross, S.J. Jang and R.E. Newnham

Materials Research Laboratory
The Pennsylvania State University
University Park, Pennsylvania 16802

and

S. Nomura and K. Uchino[†]

Department of Physical Electronics
Tokyo Institute of Technology
Ookayama, Meguro-ku, Tokyo 152, Japan

ABSTRACT

Lead magnesium niobate and other relaxor ferroelectrics are promising transducer materials for use as active elements in adaptive optic systems and similar applications. These ceramics are dominantly in the paraelectric phase, and dimension control is obtained through the high intrinsic quadratic electrostrictive effect. Since stable ferroelectric domain structures do not occur, the problems of dimensional creep and non-reproducibility (aging and de-aging effects) of the conventional poled piezoelectric ceramic are largely eliminated. Suitably chosen compositions in the $Pb_3MgNb_2O_9$-$PbTiO_3$ family give electrostriction strains ten times larger than those of conventional $BaTiO_3$-based ceramics. Low expansion coefficients are an added advantage for thermal stability.

Early in the evolution of piezoelectric ceramics, "soft" low-coercivity ferroelectric ceramics were often used under DC bias for piezoelectric applications. However, with the evolution of the $Pb(Zr,Ti)O_3$, where the effective coercivity could be controlled by suitable dopants, the present generation of poled piezoceramics completely replaced these early electrostrictive devices. Over the past ten years, however, the rapid development of tape-cast multilayer technology, and the ensuing development of new high-permittivity low-saturation anhysteretic capacitor dielectrics has considerably changed the situation.

Foremost among these formulations are a large family of ferroelectrics which exhibit strong relaxation character in their dielectric response near the ferroelectric Curie temperature[1-3]. Lead-magnesium niobate ($Pb_3MgNb_2O_9$) is perhaps the best example for which a wide spectrum of properties has been measured in both single and polycrystal samples. In this crystal, the unusual response has been traced to a statistical inhomogeneity in the distribution of the Mg^{2+} and Nb^{5+} ions in the B-sites of the ABO_3 perovskite structure. This random arrangement leads to a distribution of microvolumes within the sample which have widely different Curie temperatures. Thus on cooling from high temperature, there is a Curie range rather than a distinct Curie point, and within this Curie range the crystal exhibits an intimate mixture of paraelectric and ferroelectric regions.

The point which is of major interest for potential electrostriction applications is that for temperatures within this Curie range, the crystal can be poled into a strongly ferroelectric form, but on removal of the poling field reverts back to a random arrangement of microdomain volumes with no net remanent moment. It is the growth, reorientation and subsequent decay of the microdomains which gives rise to the time-dependent dispersive dielectric response over the Curie region.

High field dielectric measurements at 60 Hz for temperatures just below the Curie range show an apparent normal hysteretic response with large levels of induced polarization[4]. However, low-frequency pyroelectric studies indicate clearly that the apparent remanence is spurious[5] and is associated with the more slowly decaying domain component of the total polarization, thereby causing an S-shaped saturation curve without remanence.

Clearly, then, in the ferroelectric relaxors the possibility exists for utilizing the major poling strain for position control and for generating a high strain device which would be a close dielectric analog of the magnetostrict systems. A critical initial datum required is a measure of the simple electrostriction in a relaxor ferroelectric for some temperature above the Curie range. If the magnitudes of the Q_{ij} constants are similar to those in more normal perov skites such as $BaTiO_3$ then the high induced polarizations in the Curie range wil cause very high strain levels and these systems are obviously of practical inter est for further study.

The thrust of our current studies is to develop materials with large elect strictive response for static of low frequency position control and to explore some of the materials systems in which an electric field-induced phase change may be used to generate and control a highly nonlinear strain response. Appli- cations of current interest include optical interferometers, phase-correction mirrors, and other multiposition optical components[6].

The relaxor ferroelectric chosen for study is $Pb_3MgNb_2O_9$, hereinafter abbreviated PMN. Early optical studies show that above -20°C PMN has no stabl remanent polarization, even though large polarization levels can be field-indu with corresponding high stable quadratic electrooptic response. Clearly, if the quadratic electrostriction constants in this structure are "normal," high stable quadratic electrostriction should also occur. This was shown to be the

case, and PMN itself is superior to modified $BaTiO_3$ in its electrostrictive response. The response can be further improved if the Curie range, which is below room temperature in PMN, could be shifted to slightly higher temperature, and our major effort has been focused on solid solution systems based on PMN which might accomplish this goal. In this paper, we report the results for a composition in the $Pb_3MgNb_2O_9$-$PbTiO_3$ solid solution series, 0.9 PMN - 0.1 PT.

Ceramic samples of 0.9 PMN - 0.1 PT were prepared from reagent grade PbO, MgO, Nb_2O_5 and TiO_2. The constituent oxides were mixed in the appropriate proportions, ball-milled in alcohol, then dried and calcined at 950°C for 15 hours. The calcine was reground and refired twice more under the same conditions to ensure complete reaction. After cold pressing to form disks of the required shape, samples were fired in a closed alumina crucible at 1320°C for two hours, giving a specific gravity of 7.41. X-ray diffractometer patterns recorded at room temperature verified the cubic perovskite structure.

Weak-field dielectric measurements were recorded as a function of temperature using a HP 427A automatic bridge and a model Delta Design 2300 environment control chamber. At 1 kHz, the dielectric constant of 0.9 PMN - 0.1 PT is about 7000 at room temperature. The Curie range extends from about 0 to 40°C.

Electrostrictive strain was measured with a Model 24 DCDT - 050 transducer manufactured by Hewlett Packard which operates as differential transfo: er dilatometer. The transverse contraction S_2 was measured along a thin ceramic rod subject to DC bias fields (E_1) applied in a direction normal to the length of the rod. Figure 1 shows the transverse contraction of polycrystalline 0.9 PMN - 0.1 PT plotted as a function of bias field. The relaxor ceramics are anhysteretic, and retrace the same curve with rising and falling fields.

For comparison the piezoelectric strain of a hard PZT 8 under cyclic fields is also plotted in Fig. 1. This material has often been used in the fabrication

of multi-dither mirrors and other active optical components[6]. Of special
interest in this comparison is the maximum strain and reproducibility under
cyclic drive conditions.

It is in the area of dimensional stability and reproducibility where the
relaxor material compares most favorably with PZT. Using a typical PZT 8
which has a piezoelectric coefficient $d_{31} = -128 \times 10^{-2}$ m/V, with a drive of
14 kV/cm which is required to produce a deformation comparable to the relaxor
ceramics, initial deaging on the first cycles produces a considerable walk-off
in the initial zero position. Field-induced strains in 0.9 PMN - 0.1 PT are
larger than those in PZT and far more reproducible.

Transverse electrictive strain is defined as $S_2 = Q_{12}P_1{}^2$ where Q_{12} is the
polycrystalline (averaged) electrostriction constant and P_1 the electric polari-
zation induced by an electric field E_1. To confirm the electrostrictive nature
of the response in relaxor ferroelectics, S_2 was plotted as a function of $P_1{}^2$
(Fig. 2). The electric polarization was measured using the Sawyer and Tower
method in which dielectric hysteresis loops were generated with a slow wave
sweep of 1 Hz, and the maximum polarization read from the tip of the loop for
each level of applied field. It is evident from Fig. 2 that transverse strain
S_2 is linearly related to $P_1{}^2$ for 0.9 PMN - 0.1 PT ceramics. We have found
the relation to be qualitatively satisfied for other high-permittivity material
as well.

The electrostriction coefficient Q_{12} calculated from the slope of the line
in Fig. 2 is -0.9×10^{-2} m^4/C^2, which is comparable to other perovskites. Ceram
$BaTiO_3$, $SrTiO_3$, $Pb(Zr,Ti)O_3$ and $ITaO_3$ all have Q_{12} values of about -1×10^{-2} m^4
The large electrostrictive strains of PMN and other relaxor ferroelectrics are
not caused by unusually large electrostriction coefficients, but rather by
unusually large induced polarizations. In other words, the strain can be attri-
buted primarily to the large dielectric constant rather than a big coupling
coefficient.

Another interesting property of relaxor ferroelectrics is the very small thermal expansion effect throughout the Curie range. Smolenskii and co-workers reported a linear expansion coefficient of 2×10^{-6}/C for ceramic PMN near room temperature. Figure 3 shows the thermal strain of 0.9 PMN - 0.1 PT plotted as a function of temperature. These measurements were made on a 93% dense ceramic prepared as a rectangular bar 3.5 x 0.6 x 0.6 cm. The sample was mounted in a fused silica holder, and the strain measured with a displacement transducer, Hewlett-Packard Model 24 DCDT-250. After cooling down to liquid nitrogen temperature, the sample was heated at a rate of about 0.5°C/min to 500°C. Calibration was carried out with a barium titanate standard, reproducing previous measurements to better than 5%.

In the temperature range -100 to +100°C, the thermal expansion coefficient of 0.9 PMN - 0.1 PT is less than 1×10^{-6}/C, comparable to the very best low-expansion ceramics. Thermal expansion coefficients of spodumene, petalite, and fused silica are in the range 0.2 to 0.9×10^{-6}. At higher temperatures above 300°C, the expansion coefficient of 0.9 PMN - 0.1 PT increases to 10×10^{-6} which is typical of perovskite oxides. By way of comparison, alumina, zirconia, and most oxide refractories also lie between 5 and 15×10^{-6}.

The thermal strains (Fig. 3) are far smaller than the electrostrictive strains (Fig. 1), which is extremely advantageous for micropositioner applications, since dimension changes caused by temperature variations can easily be compensated electrically. Near room temperature, a ten degree temperature shift produces a strain of about 5×10^{-6}, which could be eliminated by a field change of about 200 V/cm.

In summary, relaxor ferroelectrics offer several advantages over normal piezoelectric transducers: (1) large electrostrictive strains comparable to the best piezoelectric ceramics; (2) excellent positional reproducibility; (3) no poling is required, and (4) very low thermal expansion coefficients.

REFERENCES

1. G.A. Smolenskii, V.A. Isypov, A.I. Agranovskaya, S.N. Popov, Sov. Phys.-Solid State 2, 2584 (1961).

2. V.A. Bokov, I.E. Mylnikova, Sov. Phys.-Solid State 3, 613 (1961).

3. G.A. Smolenskii, Suppl. J. Phys. Soc. Japan 28, 26 (1969).

4. R. Blinc, S. Detroni, I. Levstek, M. Pitas, S. Probesaj, M. Schara, J. Phys. Chem. Solids 20, 187 (1961).

5. J.W. Smith, Ph.D. Thesis, The Pennsylvania State University (July 1967).

6. J. Feinleib, S.G. Lipson and P.F. Cone, Appl. Phys. Lett. 25, 311 (1974).

FIGURE CAPTIONS

Fig. 1. Transverse strain in ceramic specimens of 0.9 PMN - 0.1 PT (a)
and a typical hard PZT 8 piezoceramic (b) under slowly varying
electric fields. Strains are comparable in the two materials but
are far more reproducible in the electrostrictive relaxor because
of de-aging effects in piezoelectric PZT.

Fig. 2. Field-induced transverse strain in polycrystalline 0.9 PMN - 0.1 PT
plotted against the square of the electric polarization. The
linear relationship between these two quantities indicates that
the strain is primarily electrostrictive in origin.

Fig. 3. Thermal strain of polycrystalline 0.9 PMN - 0.1 PT ceramic. The
linear thermal expansion is about 10^{-5} C^{-1} at 400°C and less than
10^{-6} C^{-1} at room temperature.
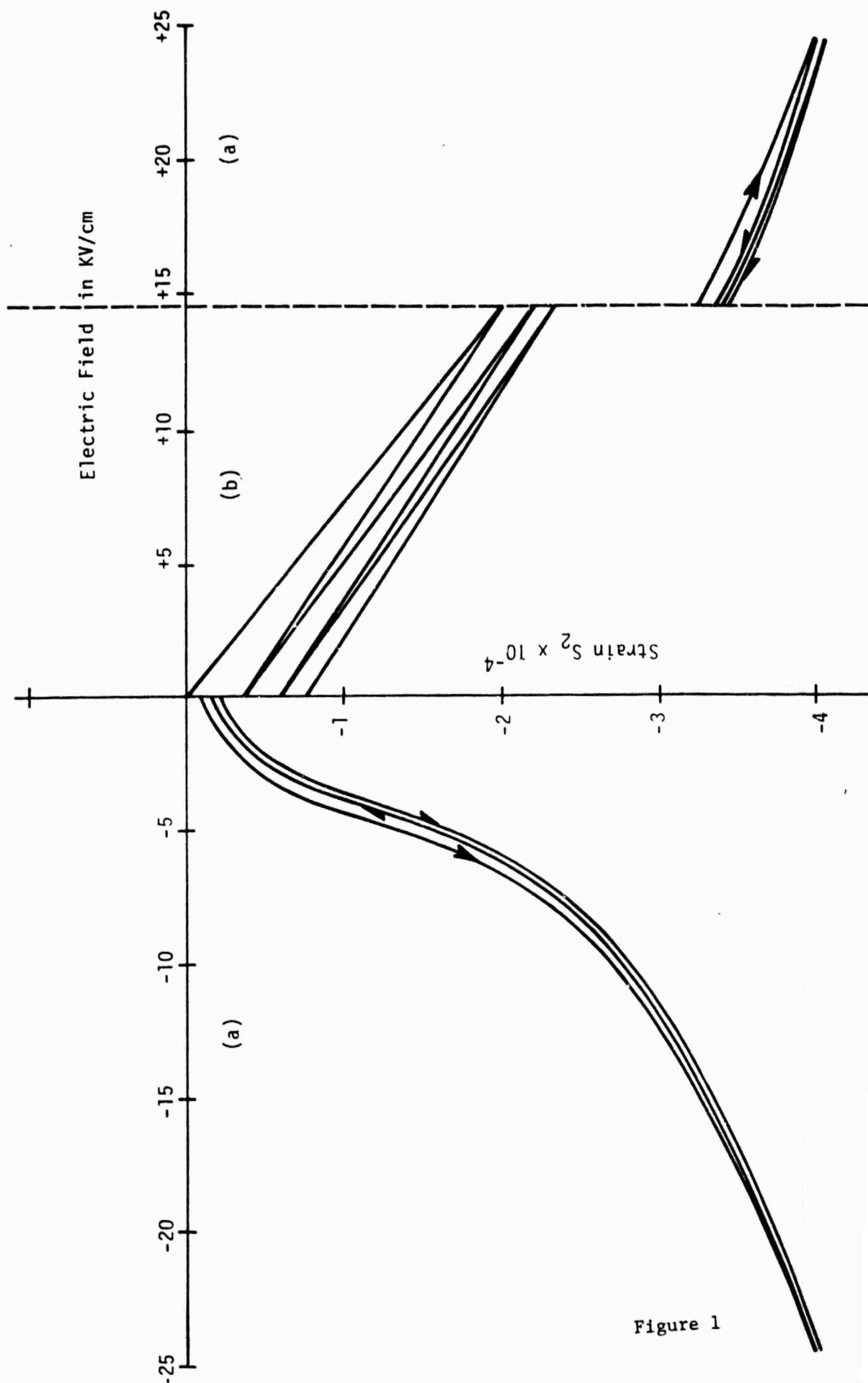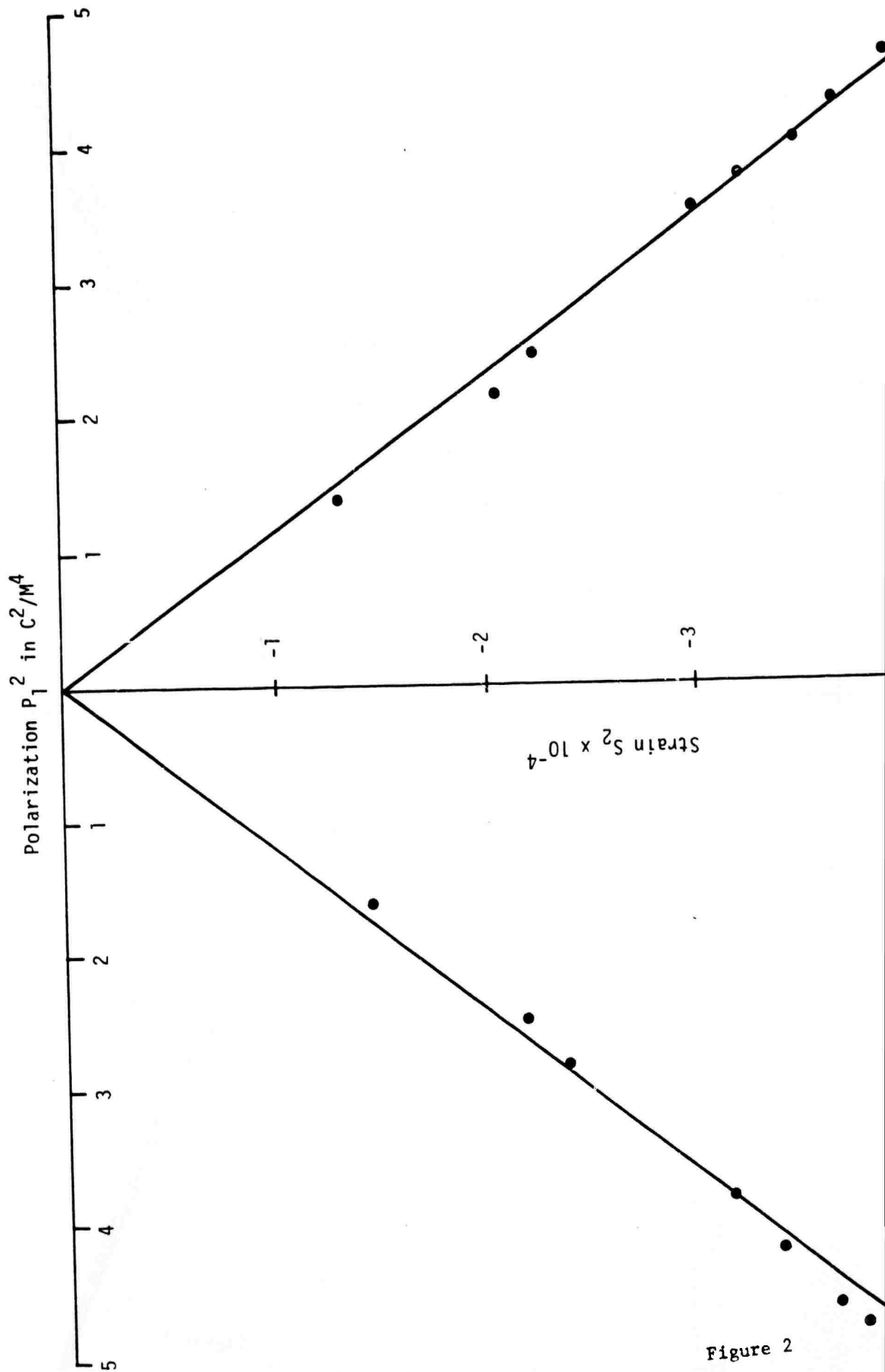
Figure 1

Figure 2
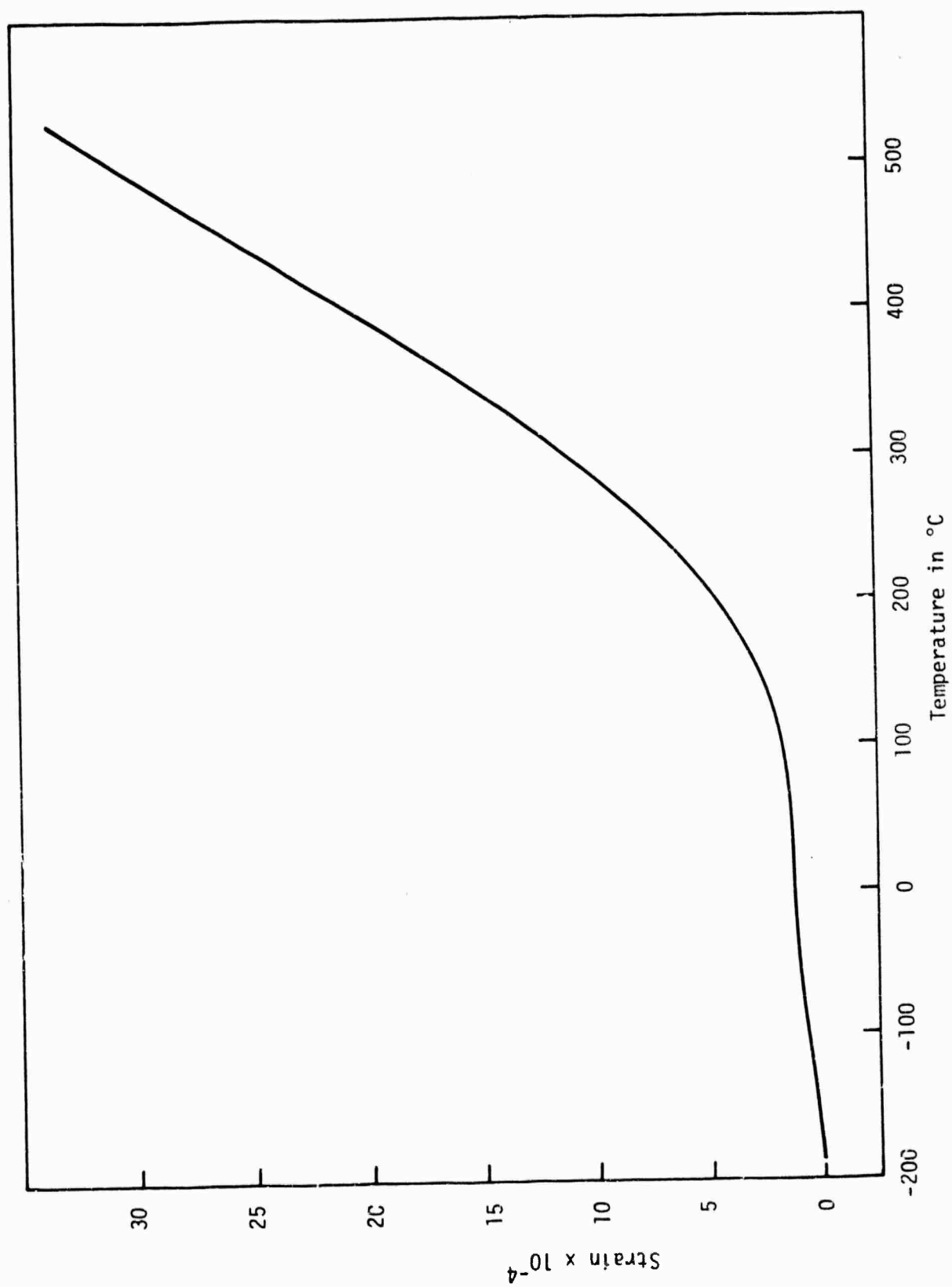
Figure 3

APPENDIX 3

The Electrostriction Effects in Ceramic
$Pb(Mg_{1/3}Nb_{2/3})O_3 : PbTiO_3$ Solid Solutions

S.J. Jang, L.E. Cross, S. Nomura and
K. Uchino

The Electrostriction Effects in Ceramic

$Pb(Mg_{1/3}Nb_{2/3})O_3$:$PbTiO_3$ Solid Solutions

S.J. Jang and L.E. Cross

Materials Research Laboratory

The Pennsylvania State University

University Park, Pennsylvania 16802

and

S. Nomura and K. Uchino

Department of Physical Electronics

Tokyo Institute of Technology

Ookayama, Meguro-Ku, Tokyo 152

ABSTRACT

The dielectric, electromechanical and thermomechanical properties of care-fully characterized ceramic samples in the solid solution system between a ferro electric relaxor ($Pb(Mg_{1/3}Nb_{2/3})O_3$) and a simple perovskite ferroelectric ($PbTiO$ have been investigated. At room temperature compositions in the range from 0 to 10 mole% $PbTiO_3$ exhibit large anhysteretic strains under electric field which have quadratic electrostrictive character. The large induced strains (up to 10^{-3}) are attributed to the mixture of ferroelectric and paraelectric phases in the relaxation range in these materials, and the absence of remanent strain to the instability of the polar domains in the small ferroelectric regions. Elect striction constants $\bar{Q}_{11}$ and $\bar{Q}_{12}$ increase in magnitude with $PbTiO_3$ content and become comparable to those in "normal" ferroelectric perovskites for compositio beyond 13 mole% $PbTiO_3$. Thermal expansion is exceedingly low for all composit at temperatures in the relaxation range, making these materials very interestii for many electromechanical micropositioner-type applications.

I. INTRODUCTION

Lead magnesium niobate, $Pb(Mg_{1/3}Nb_{2/3})O_3$ (PMN) exhibits very
strongly dispersive dielectric properties for measuring frequencies in
the 10 to 10^7 Hz region, and is perhaps one of the most extensively
studied ferroelectric relaxor dielectrics in the perovskite structure
family. An extensive literature exists with papers covering dielec-
tric[1,2], optical[3,4], structural[5,6], electro-optical[7,8], and
nonlinear optical[9] properties for both single crystal and ceramic forms.

Structurally, the material appears cubic to x-ray diffraction
(space group Pm3m) with no evidence of ordering of Mg and Nb in the B
site of the ABO_3 perovskite structure. From very considerable indirect
evidence it has been suggested[10] that the strongly dispersive dielectric
character for temperature below 25 C arises from a diffuse phase transi-
tion into a ferroelectric form giving rise to a very intimate mixture
of paraelectric and ferroelectric microregions over a considerable tem-
perature range. Earlier optical and electro-optical studies on single
crystals[11] have shown that above -20 C PMN has no stable remanent
polarization but that large quadratic electro-optic (Kerr) effects can
be field-induced and are stable under DC field[12].

It is apparent that if the quadratic electrostrictive constants
in this material are at all comparable to those in other perovskites,
then large electrostrictive strains should be possible, and this has
indeed been shown to be the case in pure PMN. For slow-speed applications
the strain response can be further improved by moving the Curie range
to higher temperatures. Solid solution with lead titanate $PbTiO_3$ was
chosen to accomplish this objective, and results are reported for single
phase compositions containing up to 20 mole% $PbTiO_3$.

II. SAMPLE PREPARATION AND CHARACTERIZATION

Ceramic samples were prepared by solid state reaction from the appropriate mixed oxides. Reagent grade PbO, MgO, Nb_2O_5, and TiO_2 were mixed in appropriate proportions, ball milled in alcohol, then dried and calcined in air in a closed alumina crucible. The resulting calcine was cold pressed into disks 2.54 cm diameter, then fired on a platinum setter in air. Calcining and sintering conditions used and calculated and final densities of compounds are given in Table 1.

X-ray powder diffraction patterns, taken at room temperature using Cu-K$_\alpha$ radiation, verified perovskite as the crystal structure of the ceramics. The lattice constants were determined from (200), (211), (220), (310) and (321) reflections, the indices being referred to the primitive perovskite cell. Slow scan techniques were used for a precise measurement of the lattice spacings which are shown in Fig. 1 as a function of composition.

The microstructures of ceramic samples, observed by the scanning electron microscopie, are shown in Fig. 2. Sample surfaces were well polished, then etched for 10 minutes with 5% HCl and 0.5% HF etching solution. The compositions of 15 and 20 mole% PT contents show evidence of a liquid phase sintering. However microprobe analysis showed no evidence of compositional heterogeneity between grain and grain boundary phases. The grain sizes are distributed from 5 to 15 μm as determined by the linear intercept method.

For dielectric measurements, disk-shaped samples were fabricated with dimensions 0.1 x 0.5 x 0.5 cm, and compositions of 0, 5, 10, 13, and 20 mole% $PbTiO_3$. After cleaning and polishing, major faces were

TABLE I. Preparation and densification characteristics of PMN:PT solid solution ceramics.

| Composition (Mole Fraction PMW:FT) | Calcining | | | Sintering 2 hours | Fired density | Calculated density |
	First 15 hours	Second 15 hours	Third 15 hours			
1.0:0.0	850°C	870°C	900°C	1280°C	7.59 gm/cm^3	8.16 gm/cm^3
0.95:0.05	900	920	950	1300	7.45	8.16
0.9:0.1	950	950	950	1300	7.60	8.16
0.87:0.13	950	950	950	1300	7.52	8.17
0.85:0.15	900	920	950	1280	7.45	8.17
8.8:0.2	900	920	950	1260	7.51	8.17

equipped with sputtered gold electrodes and contact leads were attached using air-drying silver. Similar samples were used for the longitudinal electrostriction measurements $(\bar{Q}_{11})$.

Samples for thermal expansion studies were in the form of rectangular bars 3.5 x 0.6 x 0.6 cm, and similar bar samples were used to study transverse electrostriction $(\bar{Q}_{12})$ after the major faces had been equipped with sputtered gold electrodes.

III. DIELECTRIC STUDIES

Dielectric measurements of the weak field permittivity were performed using an HP model 4270A automatic capacitance bridge, and a Delta Design model 2300 environment chamber. Typical permittivity ε' vs T at frequencies of 1, 10, 100 kHz and a measuring field of 10 V/cm for a solid solution of 13% PT in PMN is shown in Fig. 3. The dispersive character is clearly evident. General trends for ε' vs T measured at 100 kHz for several solid solution compositions are shown in Fig. 4.

The continuous increase of the temperature of ε' maximum with increasing PT content is evident. From similar curves taken over the range from 1 kHz to 1 mHz it is evident that the temperature of maximum ε' shifts with frequency, as would be expected in a relaxation dielectric, and the separation of these maximum temperatures as a function of PT content gives a crude measure of the evolution of this relaxation character in the solid solution system (Fig. 6).

Measurements of the saturation of the weak field permittivity under DC bias in this relaxation range show the occurrence of an unusual inverse hysteresis phenomenon. Typical data taken at several temperatures are shown in Fig. 5 for a sample containing 10 mole% PT.

Above 38°C typical anhysteretic paraelectric saturation is evident, at 22°C the inverse hysteresis is clearly evident, at 5°C the sample has reverted again to almost anhysteretic response, and for -12°C and below, the normal hysteretic response associated with a ferroelectric switching phenomenon becomes evident. The approximate range of the inverse hysteresis as a function of composition is also delineated in Fig. 6.

The behavior of the reciprocal susceptibility (dielectric stiffness) for temperatures above the Curie range is shown for several compositions in Fig. 7.

Dielectric hysteresis in these ceramics was measured using the Sawyer and Tower method. Hysteresis loops observed depend strongly on both measuring frequency and temperature. From data taken over the range from 10 Hz to .001 Hz, it is evident that there is almost no true remanence at room temperature for samples containing up to 10 mole% PT. For higher PT content a more normal ferroelectric hysteresis is evident (Fig. 8). A summary of the temperature dependence of the remanent polarization P_R as a function of composition and temperature for all samples measured is given in Fig. 9.

IV. THERMAL EXPANSION

Thermal expansion was measured by a direct dilatometric method from the change in length of sample bars 3.5 cm long which had been sintered to 93% of theoretical density. The measuring head was a Hewlett Packard Model 24DCDT-250 differential transformer. After cooling to liquid nitrogen temperature the sample was warmed at 0.5°C/minute and the strain recorded on an X-Y recorder. Results for several PMN:PT

samples are summarized in Fig. 10. It is evident that a region of very low thermal expansion extends across the relaxation range in each composition, and that as indicated in the dielectric studies the relaxation range shortens and moves to higher temperature with increasing PT content in the solid solution. Over much of the relaxation range the thermal expansion $\alpha < 5 \times 10^{-7}/°C$ comparable to the best known low expansion ceramics. However, above 300°C the coefficient reverts to a value $\alpha \simeq 1 \times 10^{-5}/°C$ typical for other perovskite ceramic oxides.

V. ELECTROSTRICTION

Two systems were used to measure the field-induced strain in these ceramics. At room temperature a direct dilatometric technique was applied, the sample being placed such that the deformation produced a displacement of the push rod of an HP LVDT (Model 24DCDT-050). For temperatures above and below room temperature a bonded strain gauge was used with the arrangement depicted in Fig. 11, and the gauge attachme in Fig. 11a. In transverse measurements where the gauge (Kyowa Co. model KFT-02-C1-11) occupies an equipotential surface, LVDT and gauge measurements of the strain agree to better than ±10%. In the longitudinal measurement where the gauge geometry is more unsuitable the difference is substantial, but the strain curves measured by the gauge exhibit an almost constant fractional error and clearly reproduce the major strain behavior.

Transverse and longitudinal strain at room temperature under DC field is reproduced for several compositions in Fig. 12 and Fig. 13. It may be noted that longitudinal strains larger than 10^{-3} can be induced at field strength of 20 kV/cm in both 10% and 13% PT composition

The anhysteretic behavior of the longitudinal strain under low frequency cyclic fields is also evident in Fig.14.

The dominantly electrostrictive character of the relation between electric polarization and induced strain for transverse effects at room temperature is exhibited in Fig.15. Polarization values corresponding to the DC field levels were obtained from low frequency dielectric hysteresis loops. Electrostriction constants $\bar{Q}_{11}$ and $\bar{Q}_{12}$ were derived from the slopes of the P^2 vs S curves through the relations

$$S_2 = \bar{Q}_{12} \ P_1^2$$

$$S_1 = \bar{Q}_{11} \ P_1^2$$

From data taken as a function of temperature at constant composition, it is evident that $\bar{Q}_{12}$ does not change significantly through the relaxation range (Fig. 16). Data for different compositions, however (Fig. 17), show that both $\bar{Q}_{11}$ and $\bar{Q}_{12}$ increase continuously with PT content up to values close to those found in the paraelectric phases of the normal perovskite oxide ferroelectrics.

An initially surprising feature of the dilatation behavior in the PMN based solid solutions is the stability of the strain under DC field, and the close agreement between electrostrictive behavior observed under DC and cyclic fields. Using the strain gauge techniques the induced transverse strain has been monitored for more than 8 hours, and after that the original relaxation component appears to be quite stable.

VI. DISCUSSION

Perhaps the most widely accepted model for the relaxor ferro-
electrics like PMN is that of Smolenskii et al.[12,13,14]. The basic
postulate is that within the crystal there is a spatial distribution
of Curie temperatures giving rise to a diffuse phase change into the
ferroelectric form, and a rather wide temperature domain over which
ferroelectric and paraelectric microregions coexist. In the Smolenskii
model, this spatial heterogeneity is attributed to statistical fluctua-
tions in the concentrations of Mg^{2+} and Nb^{5+} ions which are disordered
in the B sites of the cubic perovskite ABO_3 structure.

Versions of the model have been proposed[15,16] in which the polari-
zation of the ferroelectric microregions is largely static. In these
cases the dielectric dispersion is attributed to a complex admixture
of both intrinsic and extrinsic polarization processes with contribu-
tions from domain wall motion, phase boundary motion and intrinsic
polarizability. Alternative versions have been proposed in which the
polar microregions are in dynamical equilibrium, with thermal "flipping"
taking place between alternative orientations in a manner analagous
to the magnetization of a superparamagnet.

The electrostrictive measurements can also be qualitatively
described by the Smolenskii model, favoring the static polarization
alternative, but unfortunately again providing no definitive separation.
Certainly, the continuous manner in which the properties change through
the solid solution system with increasing PT content from simple relaxor
to ferroelectric-like rather suggests the continuous change of a
"scale factor" such as the distribution and/or size of the polar micro-
regions. For the dynamical model, it would be expected that if a

major part of the polarizability arose from electric field modulation

of the orientation of the polar vector, that as the microregions become

larger, and the behavior more ferroelectric like the dispersion fre-

quencies should rapidly decrease, leaving only the tail of the size

distribution contributing to polarizability at radio frequencies. Such

a trend is not evident in the measured data.

Two features of the present results provide new information which

may be of considerable importance in the eventual complete interpreta-

tion of the relaxor systems.

A. It is clear from these measurements, and from similar studies

of single crystal $Pb(Zn_{1/3}Nb_{2/3})O_3$ [17] that the polarization related

electrostriction constants Q_{ij} in these relaxor crystals are almost

an order of magnitude smaller than in most normal ferroelectric perov-

skites. From simple Devonshire theory[18] it is evident that, in the

perovskites, electrostrictive coupling is responsible for stabilizing

the polar phase above the Curie Weiss temperature and for imparting

first order character to the change at T_c. Since the continuity of

the elastic strain will certainly favor larger polar domains developing

at temperatures immediately below any local T_c, it may well be that the

lower value of the electrostriction constant is a necessary feature

of the relaxor. Additional measurements on different relaxor crystals

would be of interest to confirm this hypothesis.

In this connection, it is perhaps significant that the decrease

of the "relaxation range" in the PT-containing solid solutions is

correlated with a marked increase in the values of the Q constants,

and that in the systems containing more than 13% PT which exhibit

true remanent polarization, the Q constants are up to values comparable to those in typical ferroelectric perovskites.

B. The peculiar inverse hysteresis in the bias behavior of the weak field dielectric permittivity would appear to be a phenomenon unique to relaxor ferroelectrics. Since the DC field in these measurements is applied in increments with more than 20 minutes wait between data points it appears unlikely that the origin is kinetic, but it must also be remembered that the grain resistivity of PMN is very large ($\sim 10^{16}$ ohm cm) at room temperature so that space charges can take very long times to accumulate and dissipate.

It is difficult to speculate on the origin of the phenomenon because of the plethora of mechanisms which could contribute in the ceramic samples, and clearly similar measurements should be carried through on single crystal PMN for a range of fields, frequencies, and timings.

The thermal expansion behavior in PMN is, we believe, a fortuitous consequence of the diffuse phase transition. If like most other ferroelectric perovskites, there is a small positive volume increase on passing into the ferroelectric phase, the diffuse transition will distribute this increase over a range of temperatures, helping to counteract the normal thermal contraction. It is then to be expected that expansion coefficients be anomalously small in the Curie region, and that manipulations of the Curie temperatures and Curie ranges by limited solid solution should permit some manipulation of the expansion properties.

In this context, it would be interesting to have measurements of the hydrostatic pressure dependence of the Curie range, or measurements of the single crystal electrostriction constants from which the pressure and volume dependence could be calculated.

The major motivation for the present study of the PMN family materials was for the possible practical use in slow-speed micropositioner-type applications where the absence of a stable domain structure would eliminate the remanent dimension changes after field application and the drift of dimensions which is associated with the domain switching processes which accompany aging in the normal piezoceramics. The higher field levels which are required for equivalent displacements are, we believe, not of significant disadvantage since the terminal voltages required can be kept low by using integrated noble metal electrodes[19].

An unexpected feature of the electrostriction measurements was the absence of dimensional drift due to space charge effects. Normally it is to be expected that the initial linear potential gradient across any homogeneous dielectric will be degraded by space charge accumulation and the non-ohmic nature of the electrode contact to most semi-insulators. Possible reasons for the rather unexpected but most useful DC stability are the very high insulation resistance of the PMN, which in single crystal form gives the material very stable quadratic electro-optic properties, and in our ceramic materials the grain:grain boundary structure which no doubt provides a limited heterogeneity in the transport and probably serves to reduce space charge accumulation.

ACKNOWLEDGMENT

REFERENCES

1. G.A. Smolenskii, V.A. Isupov, A.I. Agtanovskaya, N.N. Krainik. Soviet Phys. Solid State 2, 2584 (1961).

2. W.A. Bonner, E.F. Dearborn, J.E. Geusic, H.M. Marcos, L.G. VanUitert. Appl. Phys. Lett. 10, 163 (1967).

3. V.A. Bokov, I.E. Mylnikova. Soviet Phys. Solid State 3, 613 (1961).

4. W.A. Bonner, L.G. VanUitert. Mat. Res. Bull. 2, 131 (1967).

5. B. Krause, D.L. Gibbon. Z. Krist. 134, 44 (1971).

6. A.A. Berezhnoi. Opt. Spect. 31, 432 (1971).

7. G.A. Smolenskii, N.N. Krainik, A.A. Berezhnoi, I.E. Mylnikova. Fiz. Tverd. Tela. 10, 467 (1960).

8. G.A. Smolenskii, A.A. Berezhnoi, N.N. Krainik, I.E. Mylnikova. Izv. Akad. Nauk SSSR Ser Fiz 33, 282 (1969).

9. G.A. Smolenskii, Ferroelectrics 7, 99 (1974).

10. G.A. Smolenskii, J. Phys. Soc. Japan 28, 26 (1970).

11. V.A. Bokov, I.E. Mylnikova. Fiz Tverd. Tela 2, 2906 (1968).

12. A.A. Berezhnoi, V.N. Buchman, L.T. Kudinova, I.E. Mylnikova. Fiz. Tverd. Tela 10, 255 (1968).

13. G.A. Smolenskii, V.A. Isupov, A.I. Agranovskaya, S.N. Popov. Fiz. Tverd. Teda. 6, 790 (1964).

14. V.A. Isupov. Fiz. Tverd. Tela 6, 790 (1964).

15. V.J. Fritzberg, R.N. Rolov. Izv. Akad, Nauk SSSR Ser Fiz 28, 649 (1964).

16. B.N. Rolov. Izv. Akad. Nauk SSSR Ser. Fiz. Techn. 6, 14 (1966).

17. S. Nomura, J. Kuwata, S.J. Jang, L.E. Cross and R.E. Newnham. Mat. Res. Bull. 14(6) 769-774 (1979).

18. A.F. Devonshire. Phil. Mag. 40, 1040 (1949).

19. L.E. Cross, N. Coda. Final Report on DARPA-ONR Contract N00014-77-C-0045.

FIGURE CAPTIONS

Figure 1.   Lattice constant as a function of composition in PMN:PT
           solid solutions.

Figure 2.   Microstructure observed by SEM of $(1-x)$PMN:(x)PT solid
           solutions. (a) PMN; (b) 0.95PMN:0.05PT; (c) 0.90PMN:0.10PT
           (d) 0.87PMN:0.13PT; (e) 0.85PMN:0.15PT; (f) 0.80PMN:0.20PT.

Figure 3.   Dielectric dispersion in a 0.87PMN:0.13PT solid solution.

Figure 4.   Dielectric permittivity as a function of temperature in
           $(1-x)$PMN:(x)PT solid solutions at a fixed frequency of 100 kHz.

Figure 5.   Dielectric saturation as a function of DC biasing field in
           0.9PMN:0.1PT solid solution.

Figure 6.   Range of the inverse hysteresis of dielectric saturation
           and dispersion of the temperature of maximum permittivity
           in PMN:PT solid solutions.

Figure 7.   (a,b) Inverse dielectric susceptibility (dielectric stiffness)
           as a function of temperature in $(1-x)$ PMN:(x)PT solid
           solutions. (c) Curie constant C as a function of composi-
           tion in PMN:PT solid solutions.

Figure 8.   Dielectric hysteresis loops measured using Sawyer-Tower
           method of $(1-x)$PMN:(x)PT solid solutions.

Figure 9.   Maximum remanent polarization P_R as a function of temperature
           in $(1-x)$PMN:(x)PT solid solutions.

Figure 10.   Thermal strain of $(1-x)$PMN:(x)PT solid solutions.

Figure 11.   Block diagram of strain gauge equipment.

Figure 12.   Transverse strain as a function of electric field in
            $(1-x)$PMN:(x)PT solid solutions.

Figure 13.   Longitudinal strain as a function of electric field of 0.9 PMN:0.1PT.

Figure 14.   Transverse strain as a function of electric field and frequency in 0.9 PMN: 0.1PT.

Figure 15.   Transverse strain as a function of (polarization)^2 in (1-x)PMN:(x)PT solid solutions.

Figure 16.   Electrostriction constant $\bar{Q}_{12}$ as a function of temperature in (1-x)PMN:(x)PT solid solutions.

Figure 17.   Average electrostriction constants $\bar{Q}_{12}$ and $\bar{Q}_{11}$ as a function of composition.

Fig. 1

(d)

(a)

(e)

(b)

(f)

(c)

Fig. 2

Fig. 3

DIELECTRIC PERMITTIVITY (ϵ')

9.000

6.000

3.000

X=0

X = 0.05

X=0.1

-100   0   200   300

TEMPERATURE (°C)

(a)

DIELECTRIC PERMITTIVITY

9.000

6.000

3.000

X=0.13

X=0.12

X=0.2

TEMPERATURE (°C)

(b)
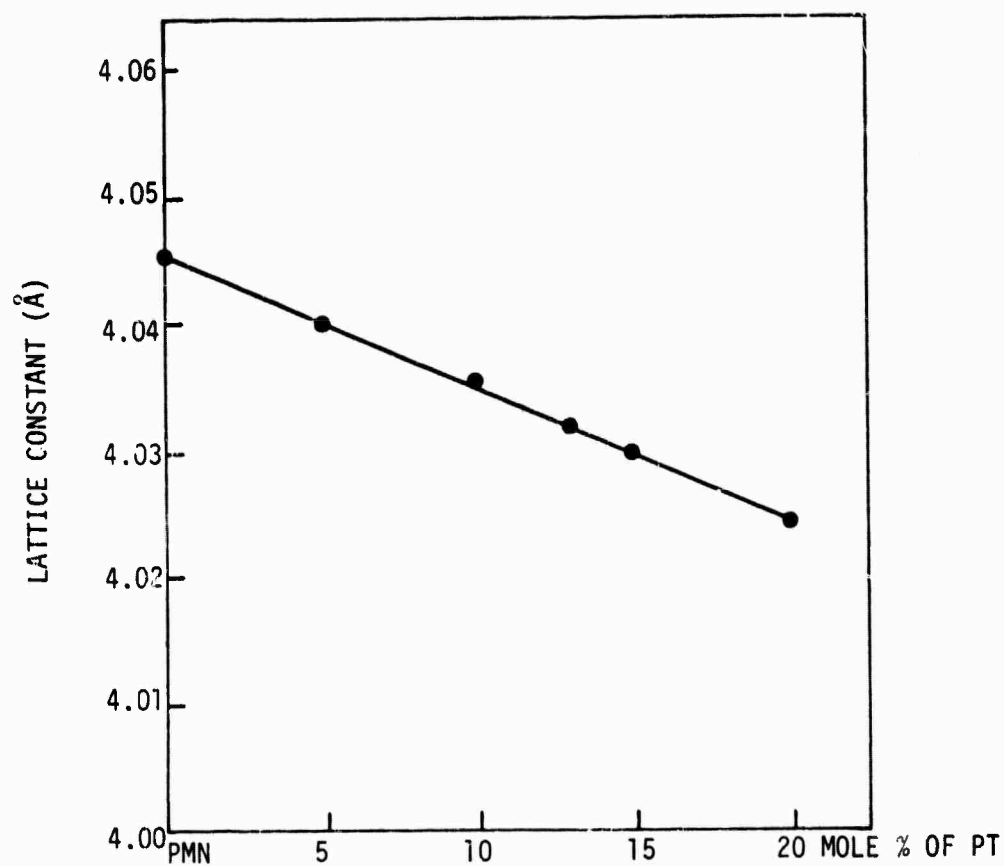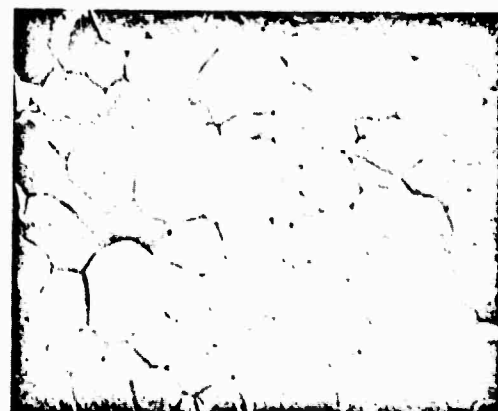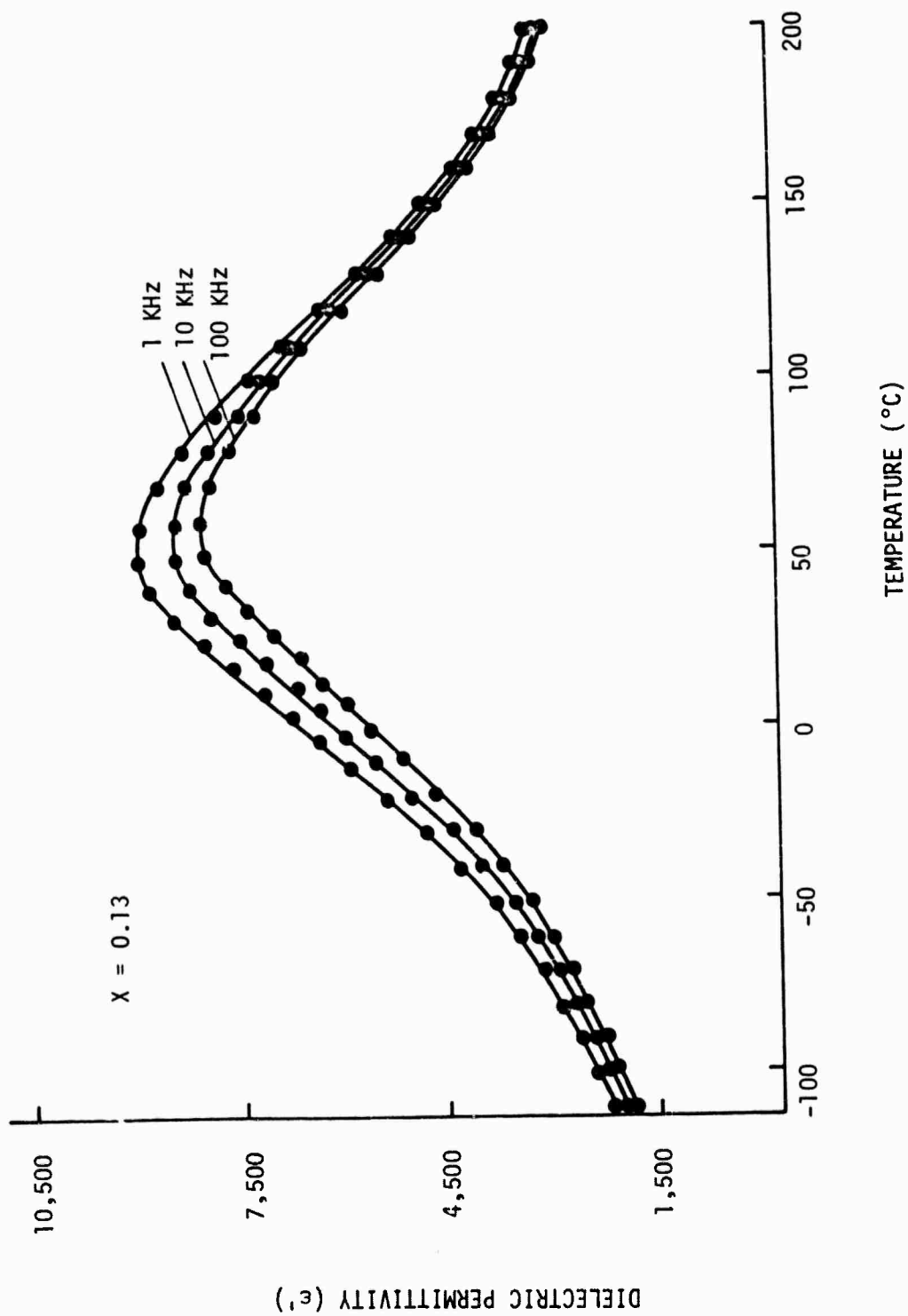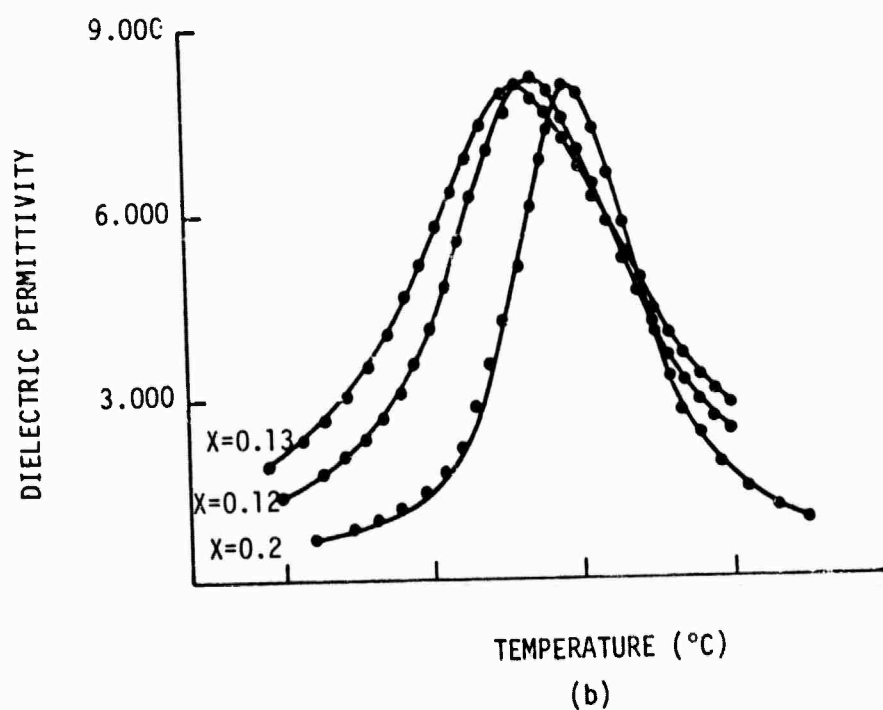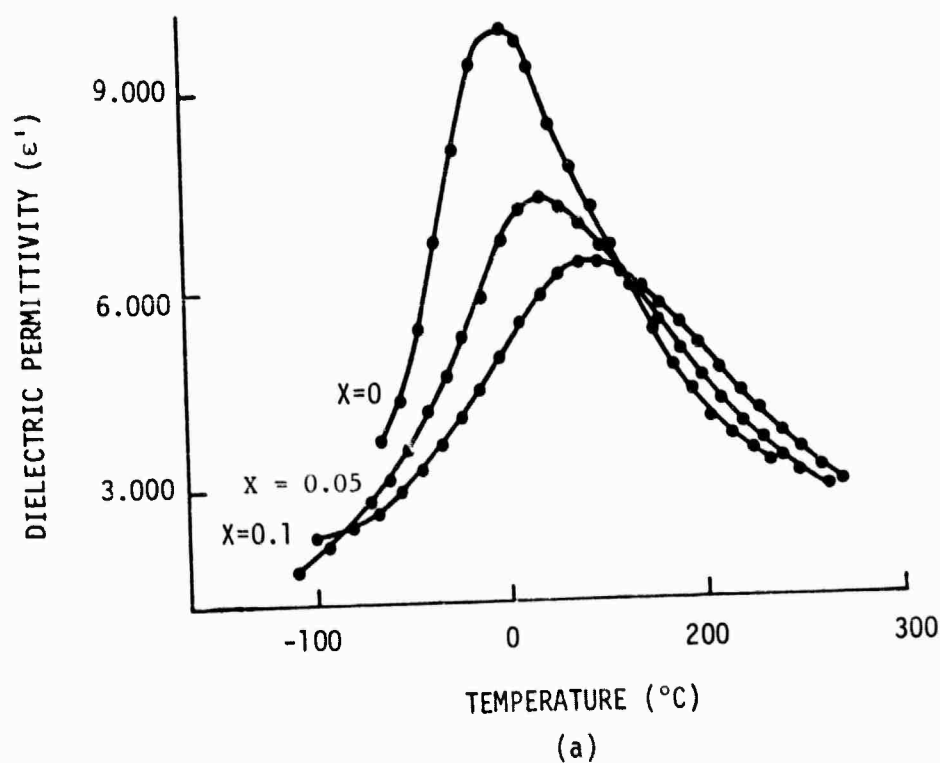
Fig. 4
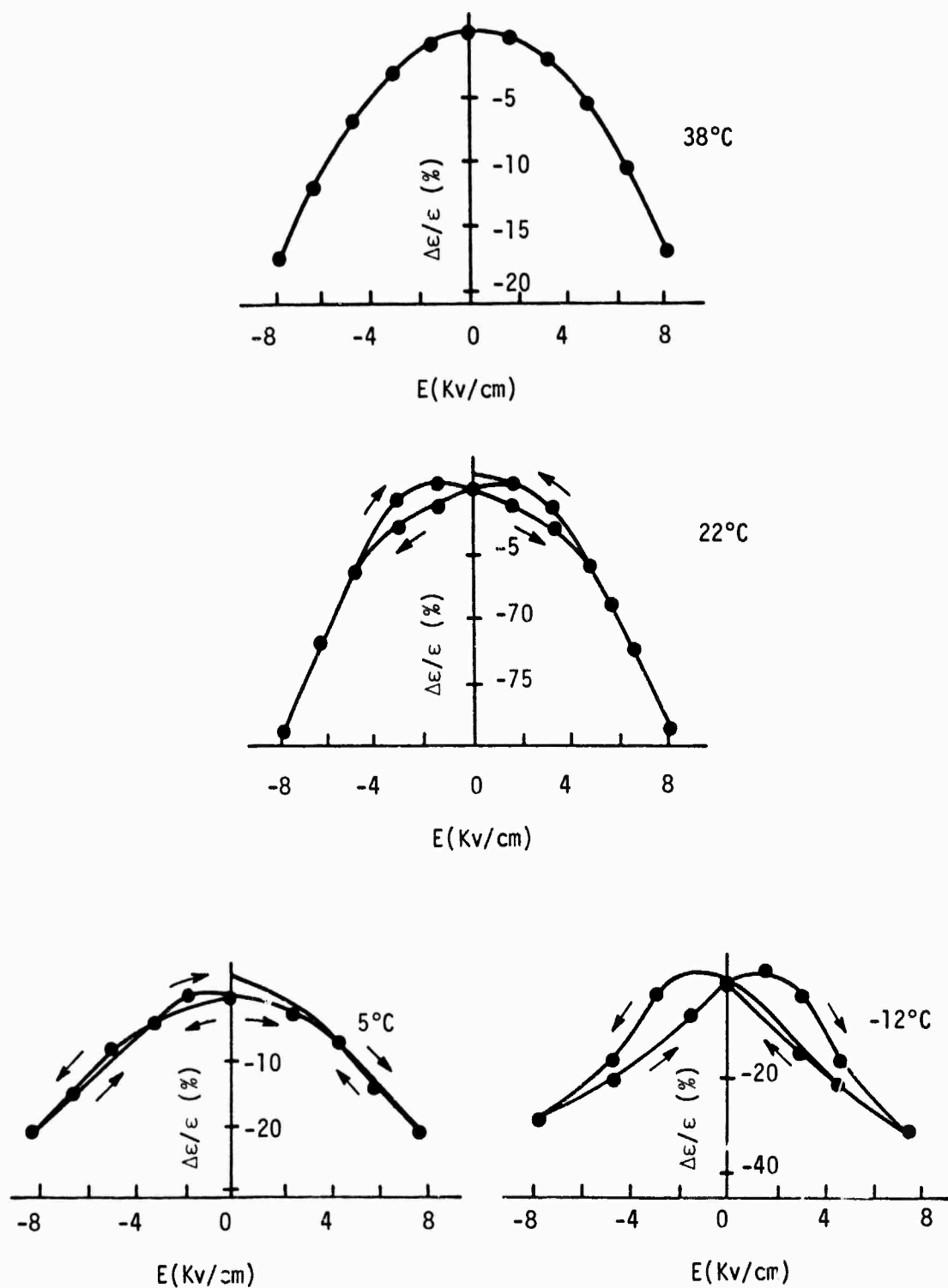
Fig. 5
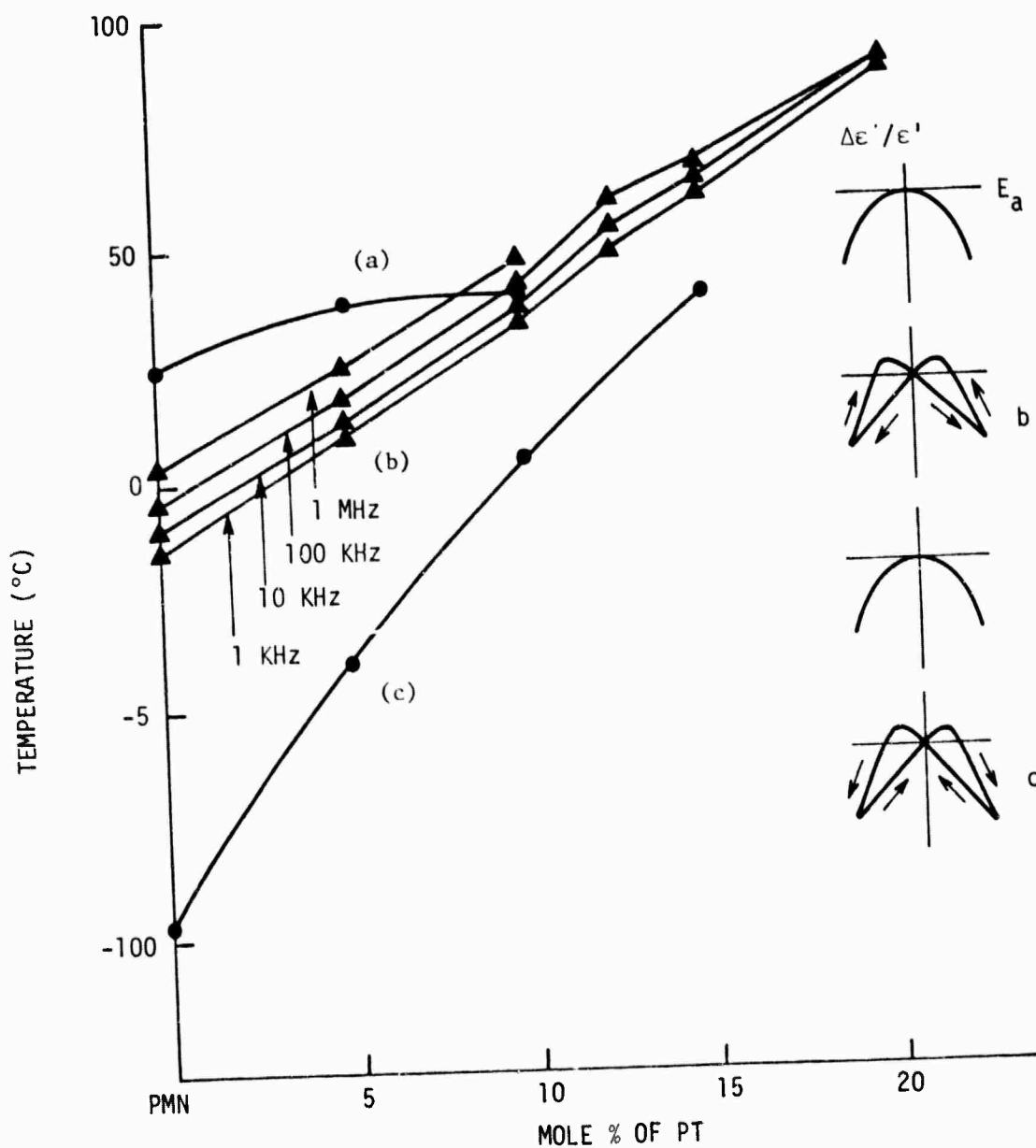
Fig. 6
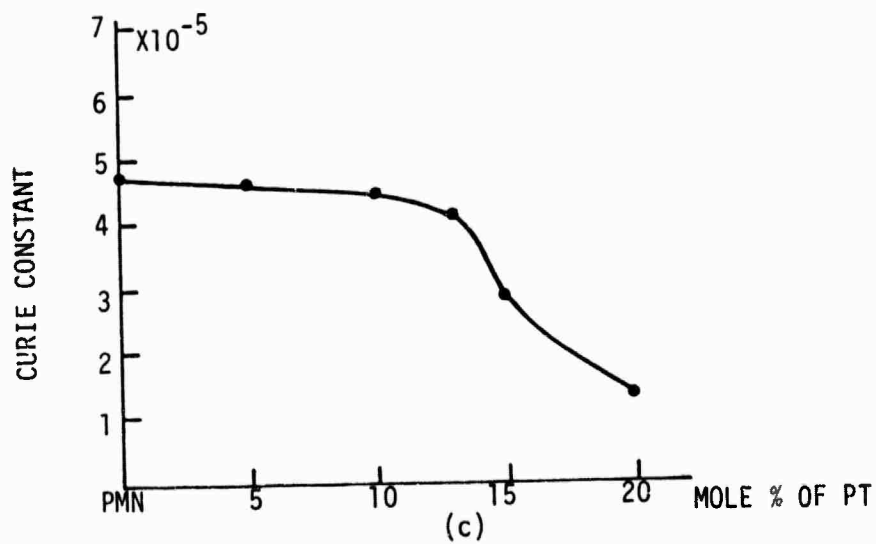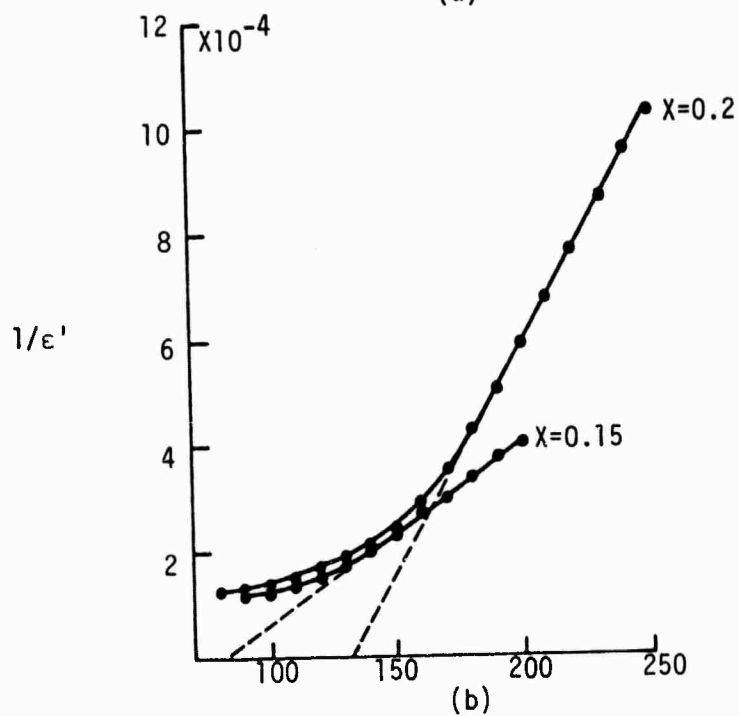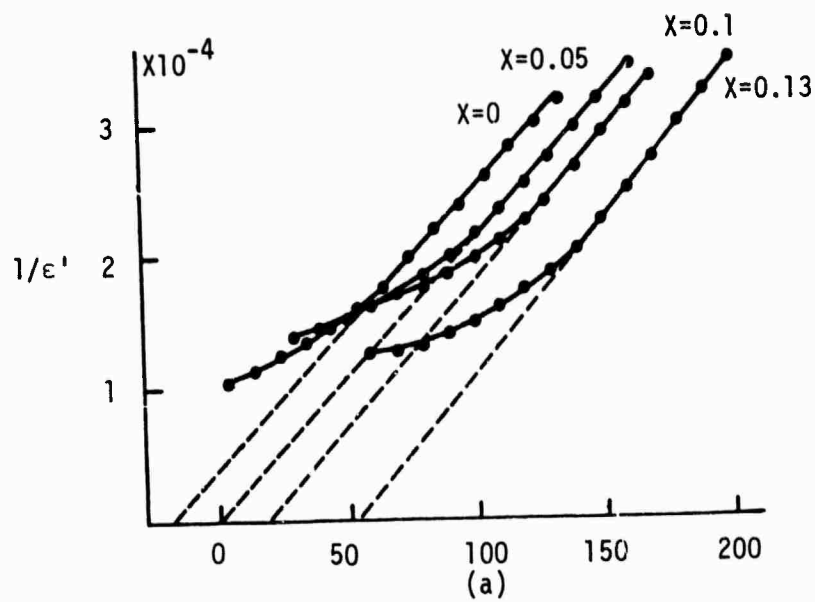
Fig. 7
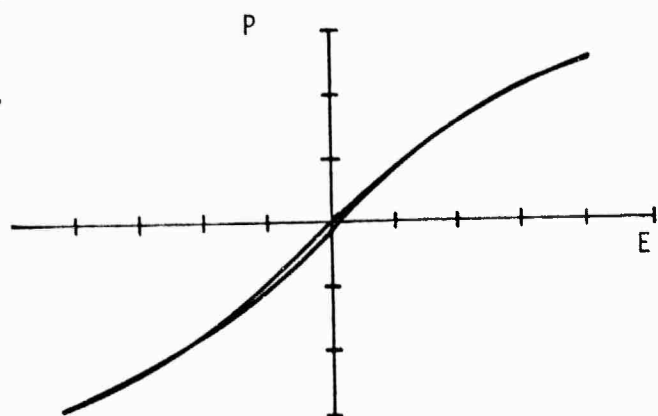
X = 0　　　　　　　T = 23°C
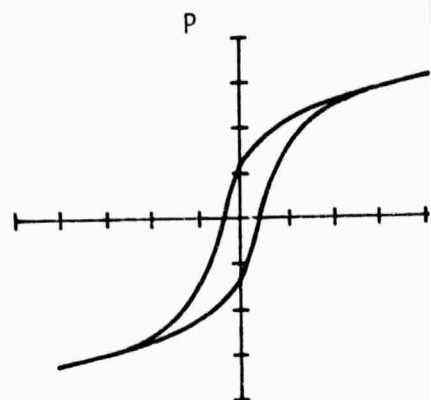
X = 0.13　　　　　T = 23
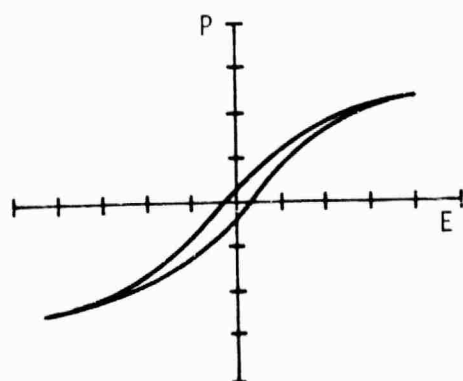
X = 0.15　　　　　T = 97°C

X = 0.2　　　　　T = 100

Fig. 8

Fig. 9

REMANENT POLARIZATION (C/M²)

TEMPERATURE (°C)

X = 0
X = 0.05
X = 0.1
X = 0.13
X = 0.15
X = 0.2

Fig. 10

Fig. 11

Fig. 12

LONGITUDINAL STRAIN

X = 0.1

E(Kv/cm)
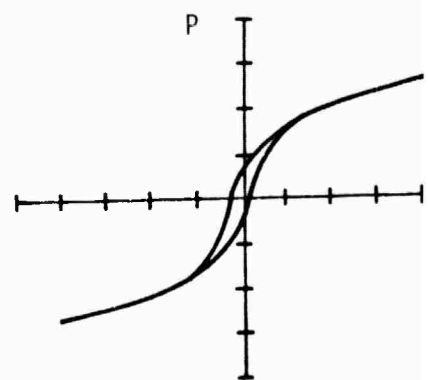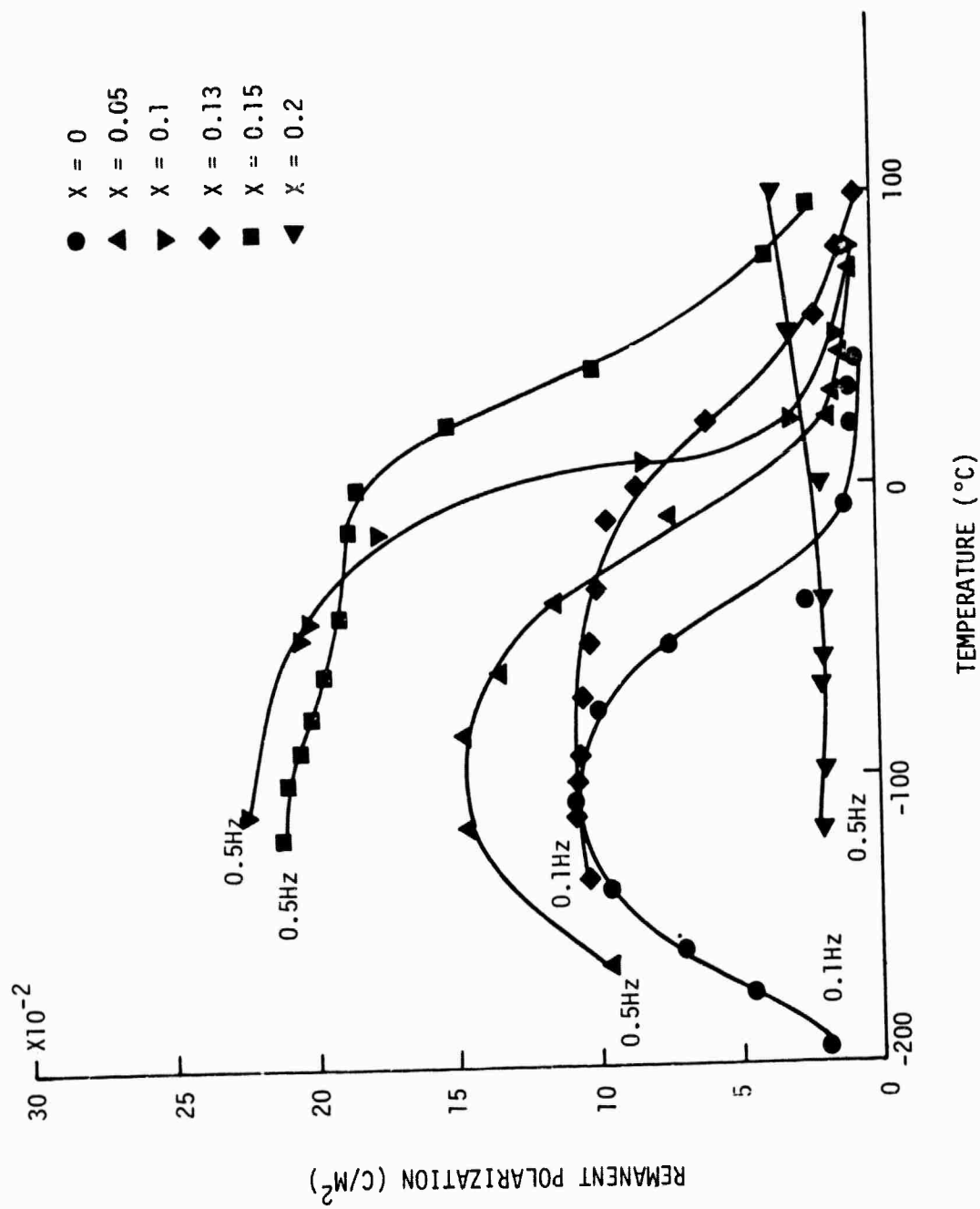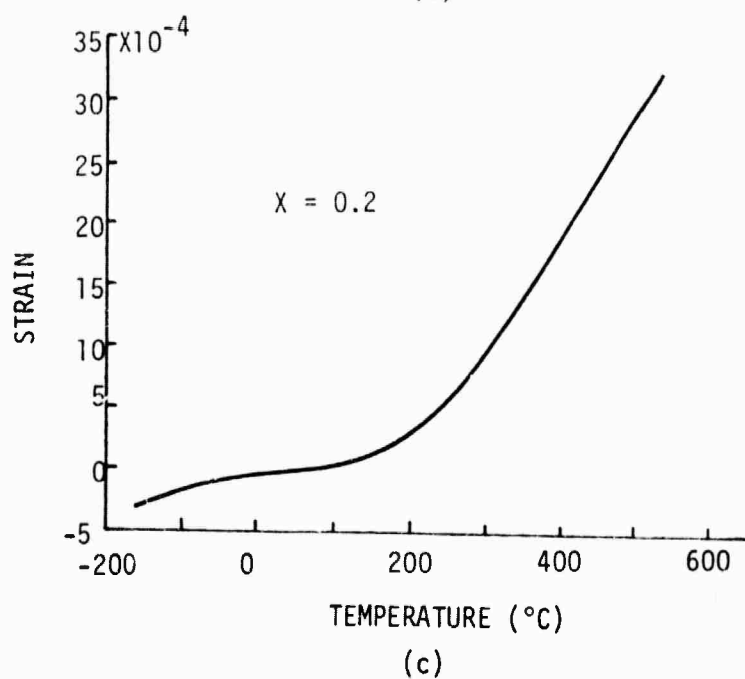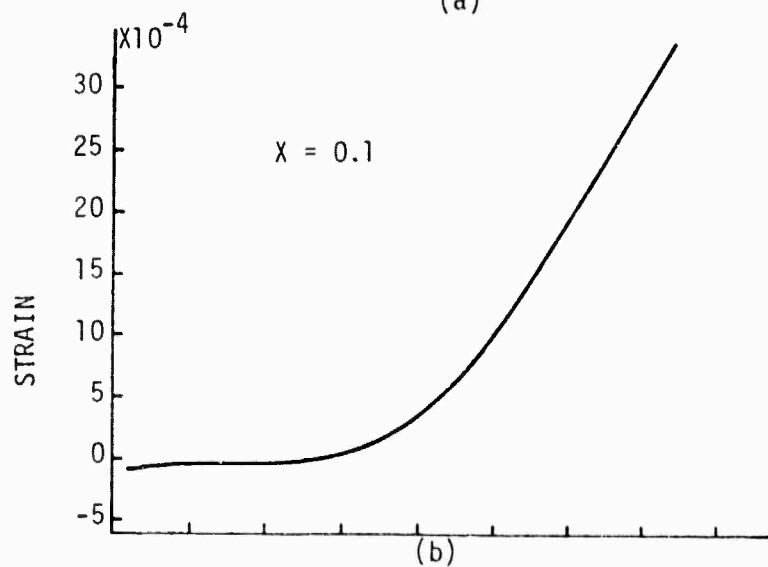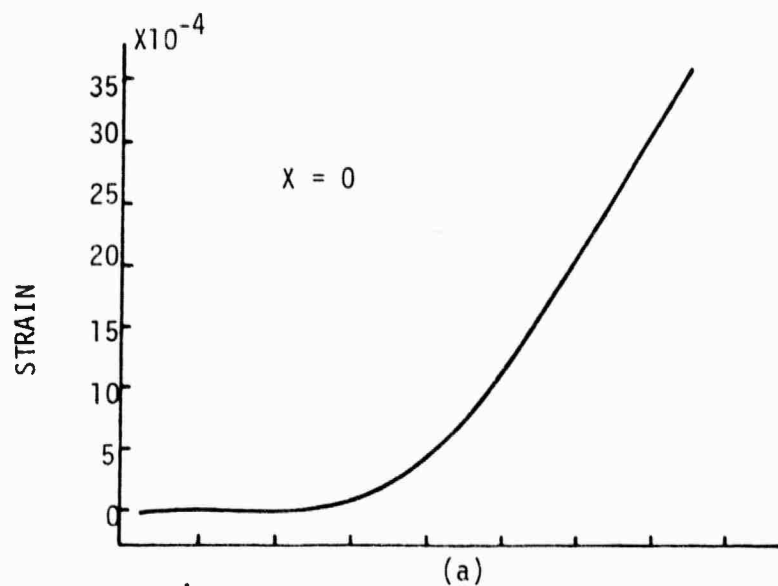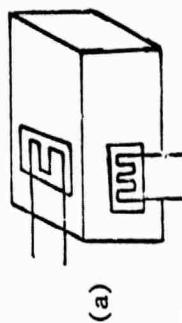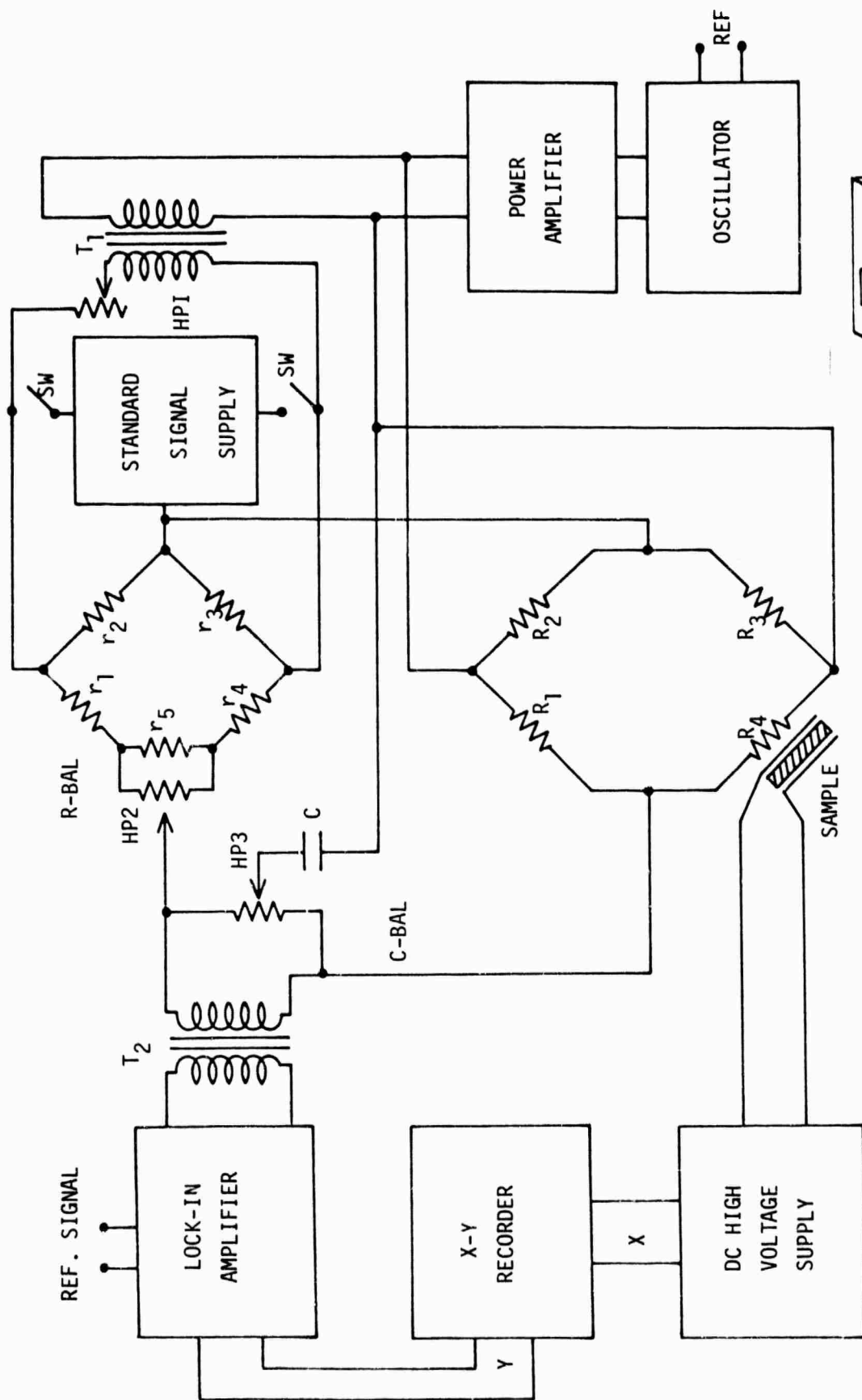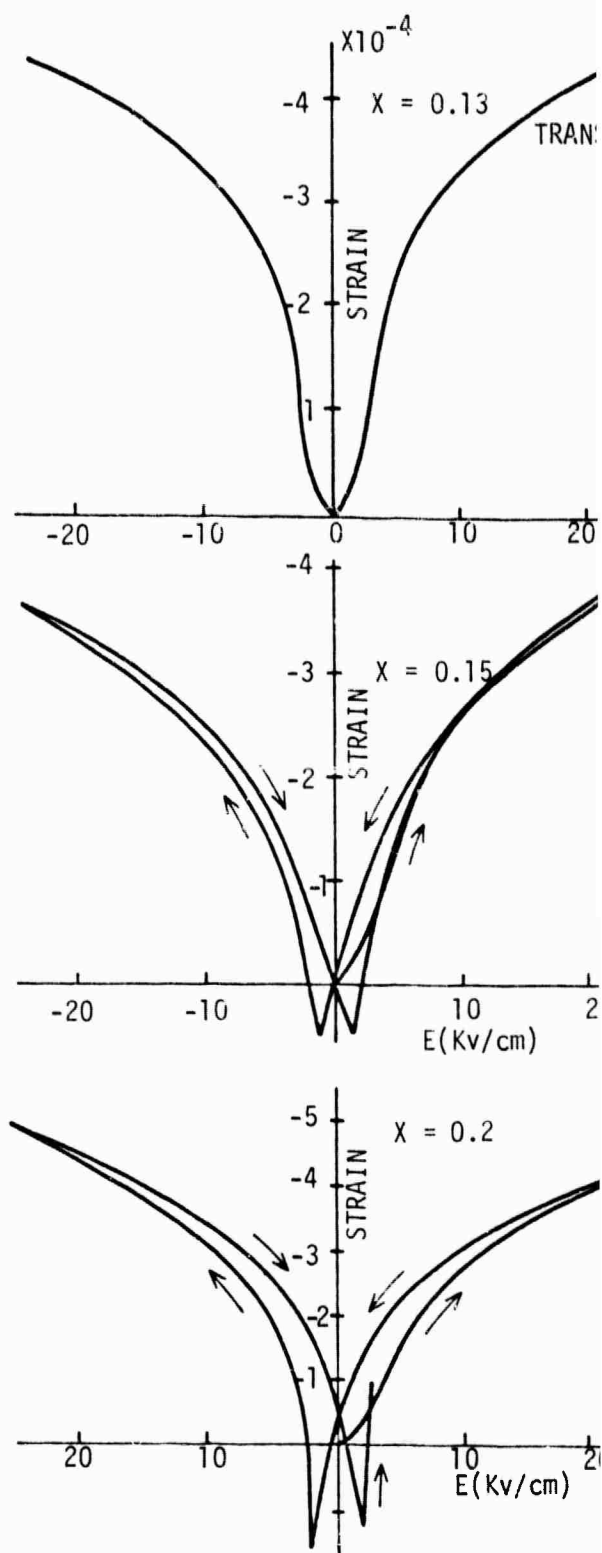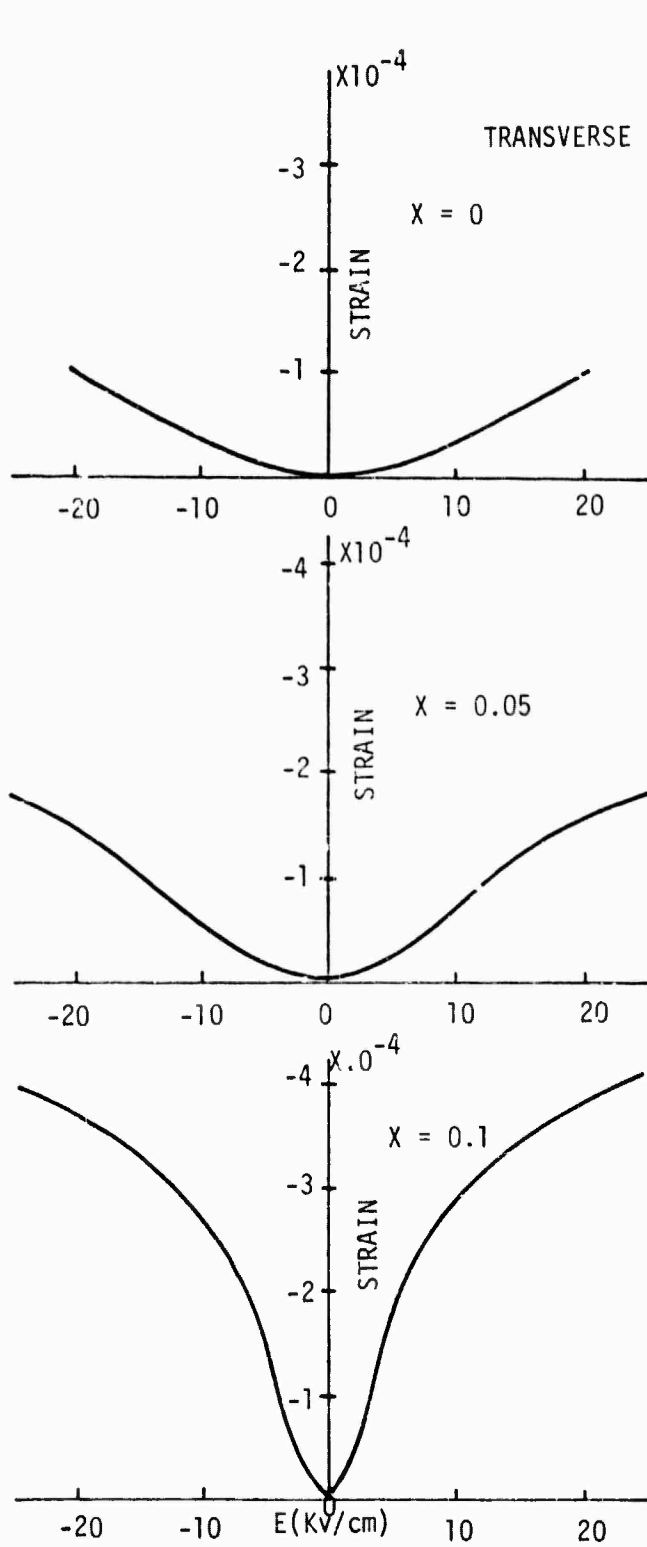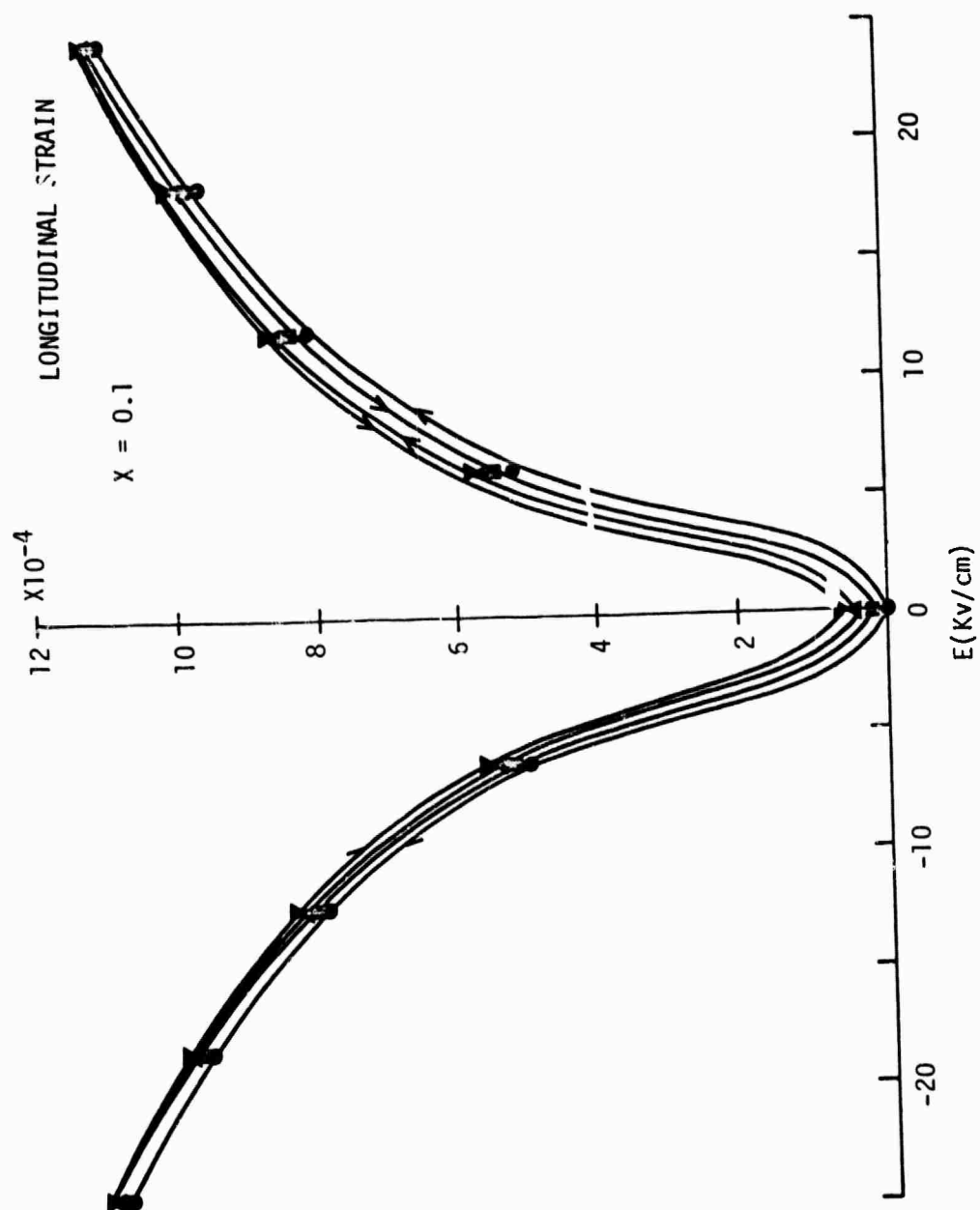
Fig. 13
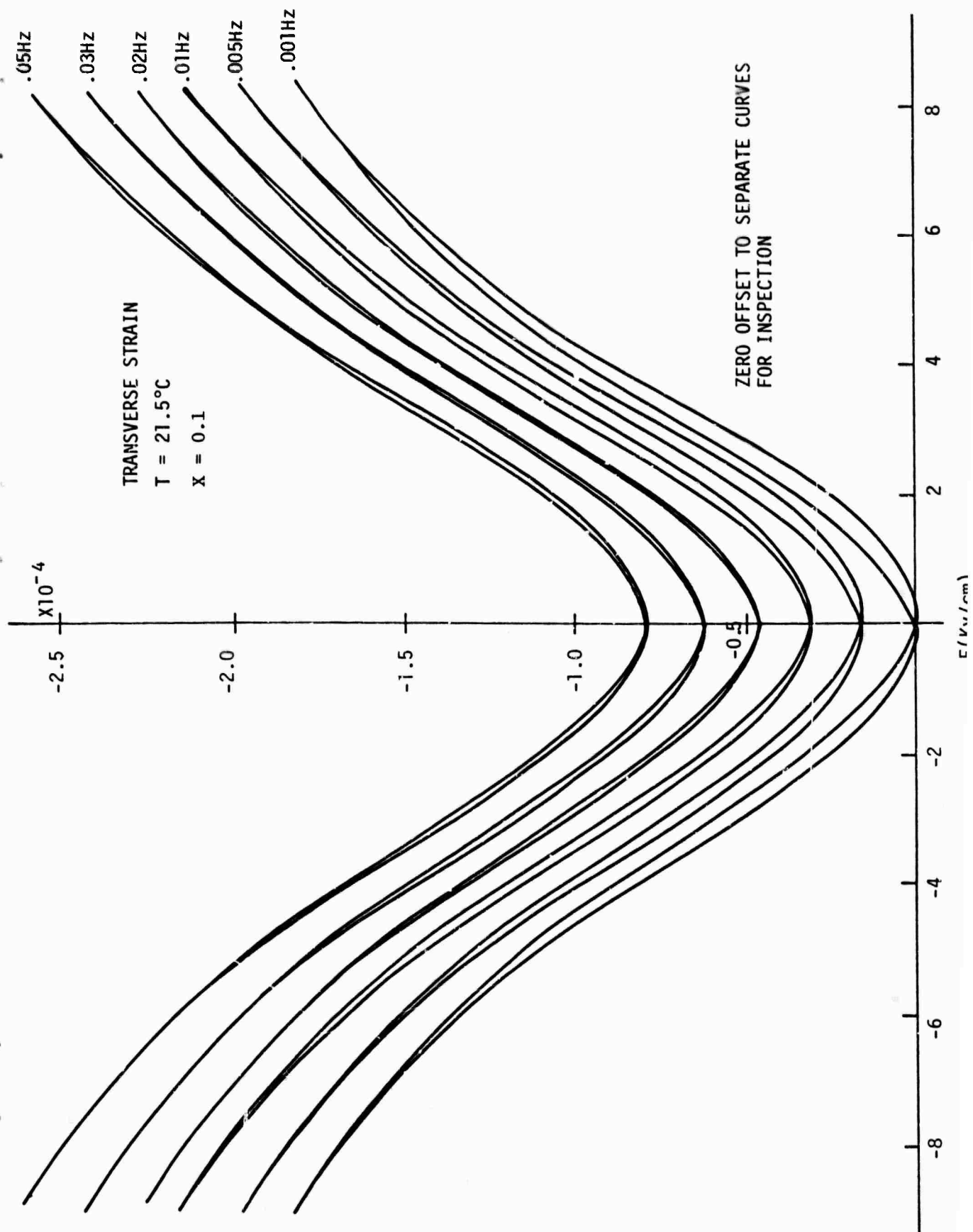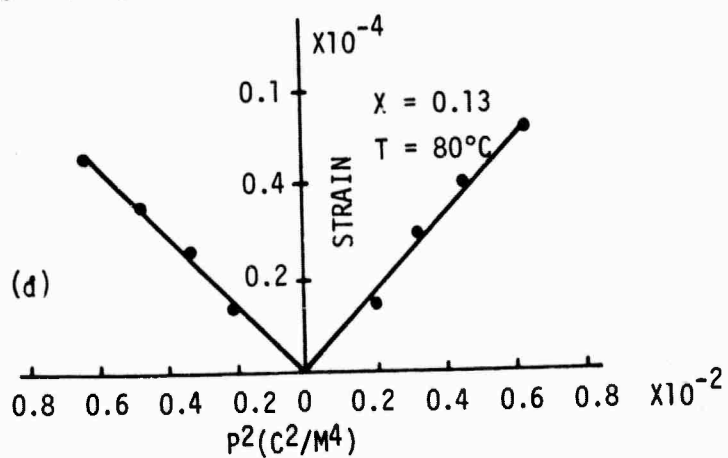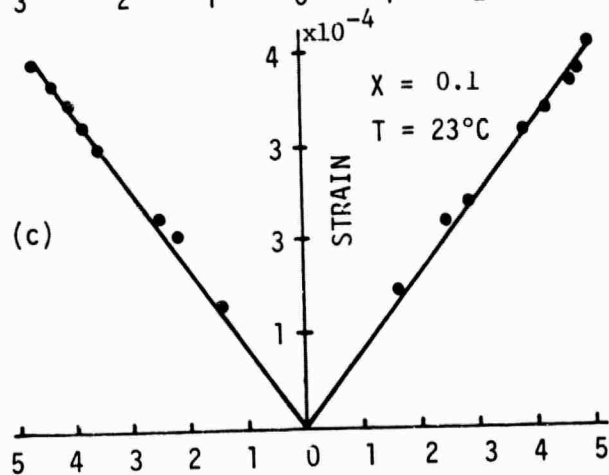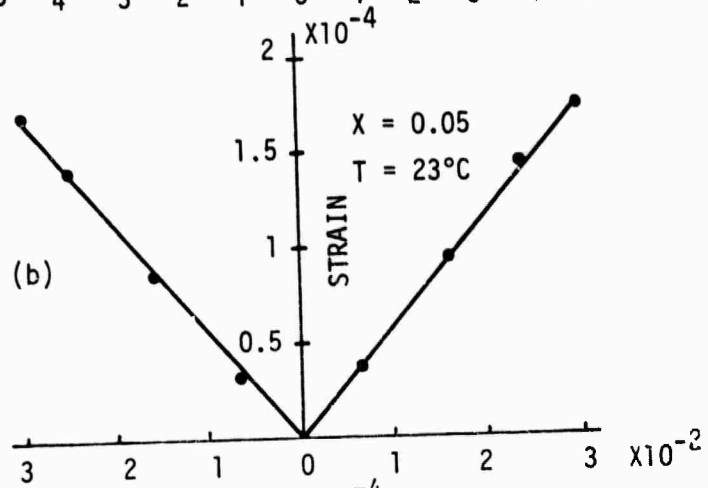
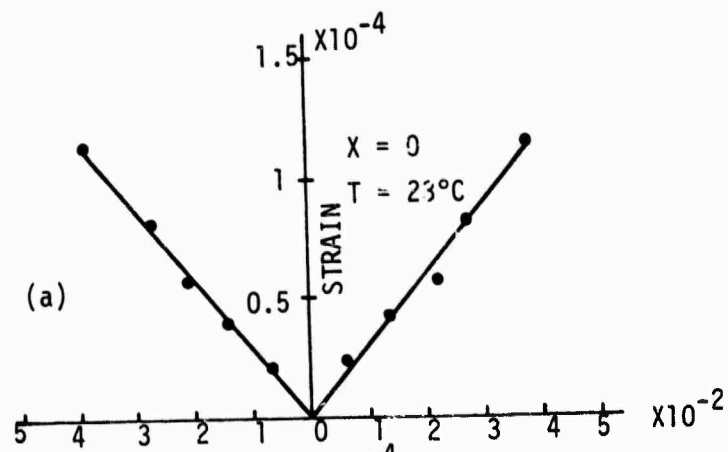Fig. 15
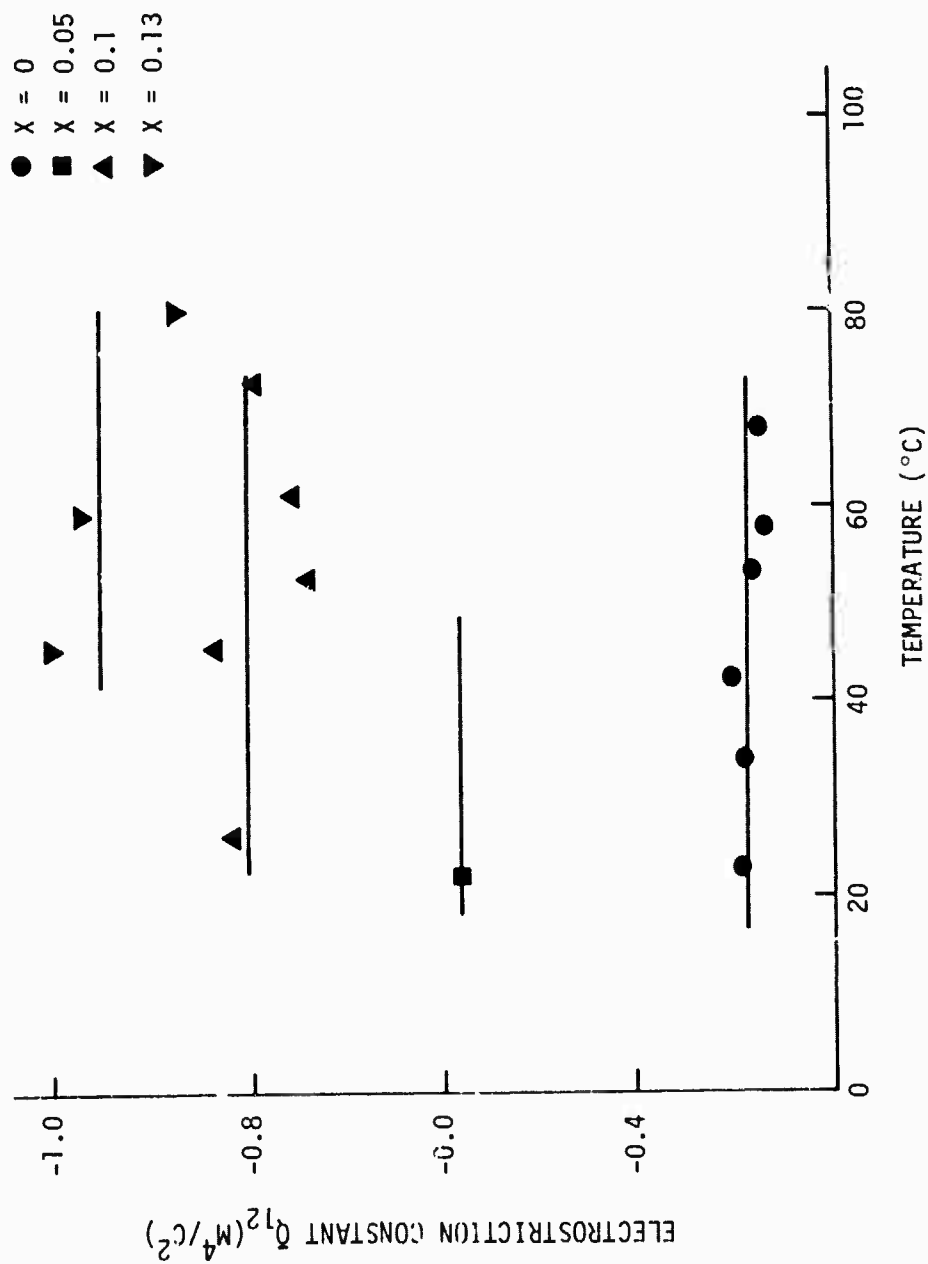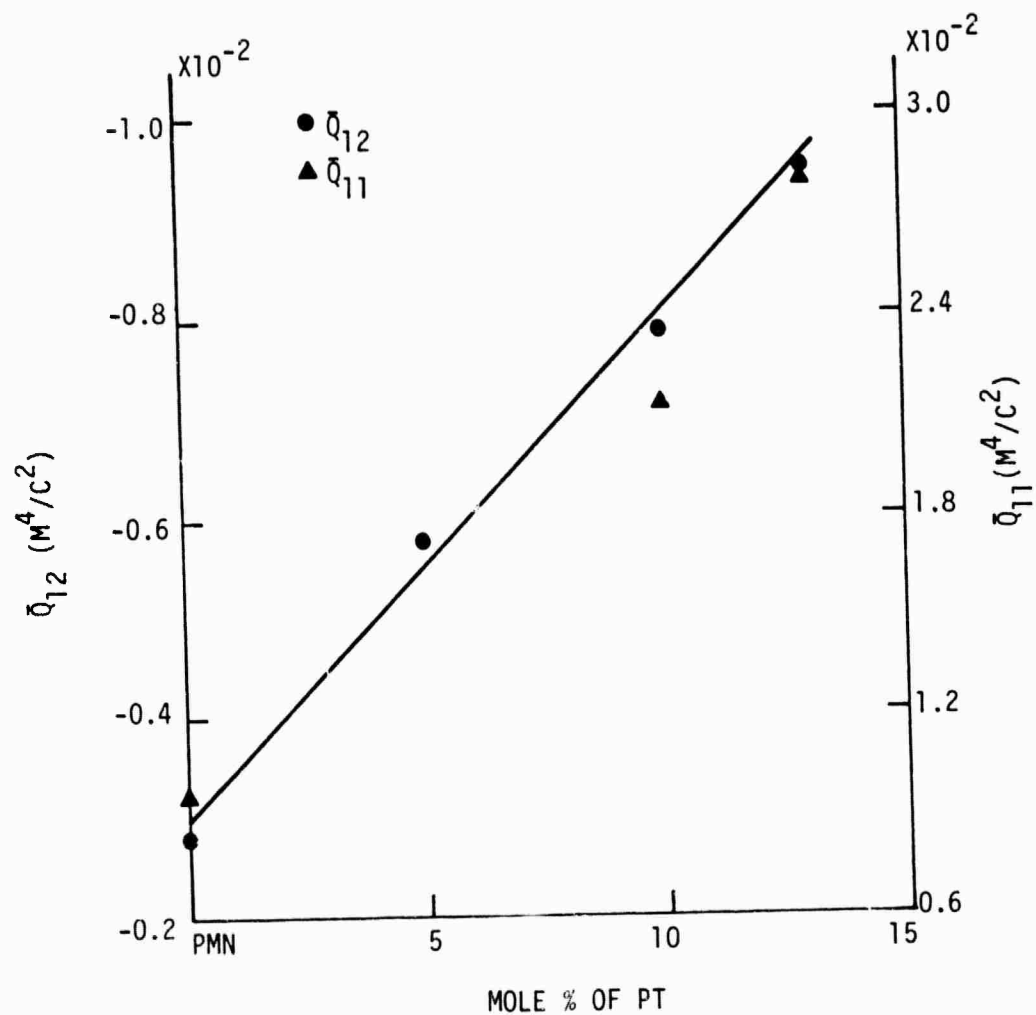
Fig. 16

Fig. 17

APPENDIX 4

Al_2O_3-PZT Tape-Cast Composite Materials

K.A. Klicker, J.V. Biggers and R.E. Newnham

Al_2O_3-PZT Tape-cast Composite Materials

K. A. Klicker
J. V. Biggers
R. E. Newnham

Materials Research Laboratory
The Pennsylvania State University
University Park, PA 16802

Abstract

Techniques have been developed to produce composites of PZT and Al_2O_3 fibers using tape casting. The success of these techniques in establishing intimate contact between the PZT and Al_2O_3 is studied. Problems encountered in sintered composites due to chemical interaction of the PZT and Al_2O_3 and the physical interference of the Al_2O_3 fiber with the densification of the PZT phase are investigated.

Introduction

Al_2O_3 fiber (20 μm diameter) and whiskers (.5 μm diameter) have been incorporated into a lead zirconate titanate (PZT) matrix using tape casting techniques. The fibers were intended to serve two purposes. Since Al_2O_3 fiber and whisker are mechanically stronger than PZT parts, a properly designed composite of PZT and Al_2O_3 ought to mechanically stronger than PZT alone. The use of tape casting allows the orientation of the fibers and whiskers within two dimensional planes of the composite. The two dimensionally aligned fibers and whiskers could in effect clamp the PZT. A PZT grain undergoes a large strain in the direction of the spontaneous polarization of the grain[1]. In an unclamped PZT ceramic the spontaneous polarization of the ceramic is somewhat randomized by the effect of the strain in one grain on strain and therefore the direction of spontaneous polarization in neighboring grains. A ceramic which is clamped in two dimensions is prevented from undergoing strain in those two dimensions. Such a ceramic ought to have a higher spontaneous polarization in a direction perpendicular to the clamping, since the strain which accompanies the spontaneous polarization could only be accommodated in that direction.

In this study we have developed a technique for the two dimensional alignment of Al_2O_3 fibers and whiskers through the use of tape casting. The multilayer parts were fired at various temperatures so that the fired density would be maximized. Micrographs of the sintered parts were examined on an SEM to find if reaction occurs between the Al_2O_3 fibers and the PZT matrix and if so the effect of firing temperatures.

Procedure

Two different PZT's were used to make composites. PZT 501A[I] is a commercial PZT. A PZT of composition $PbZr_{0.6}Ti_{0.4}O_3$ was produced by mixing

I Ultrasonic Powders, Inc., South Plainfield, NJ.

PbO^{II}, $ZrO_2{}^{III}$ and $TiO_2{}^{IV}$ by ball milling for 3 hours in a plastic jar in alcohol, pan-drying and then calcining for one hour at 950°C. The calcined bulk was crushed with a mortar and pestle and passed through a 200-mesh screen.

A slip for tape casting PZT was made by adding 70 wt% PZT and 30 wt% of a commercial organic binder[V] to a 250 ml plastic jar. Several 5 mm diameter zirconia milling cylinders were put into the plastic jar to aid in mixing. The jar was placed on a slowly turning (about 40 rpm) ball mill for two days.

The alumina fibers[VI] were received in bundles 12 inches in length. Each bundle contained approximately 40 alumina fibers. The fiber had an approximate diameter of 20 microns. Due to the difficulty in separating and handling fibers of this size they were used in bundles. The alumina whisker[VII] which was loosely agglomerated was added directly to the PZT-binder slip during the initial mixing because of the small size (.5 micron diameter) of the whiskers.

The tape casting procedure consisted of passing a glass plate beneath a hopper filled with slip at a constant speed. A doctor blade attached to the hopper determines the thickness of the layer of slip which is cast on the glass plate[2]. For making $PZT-Al_2O_3$ fiber composites, the fiber bundles were placed on the glass plate so that the several fiber bundles were parallel to the directi

---

II N.L. Industries, Inc., Highstown, NJ.

III Harshaw Chemical Corp., Cleveland, Ohio, Lot I-75.

IV Whittaker, Clark and Daniels, Inc., S. Plainfield, NJ, Lot 77G-27-8.

V Cladan, Inc., San Diego, CA, Binder B-62.

VI E.I. DuPont de Nemours & Co., Experimental Station, Wilmington, DE.

VII Busar, Inc., Springfield, VA., Type T#K-4B.

of the tape casting. The upstrear ends of the bundles were fixed to the glass plate with scotch tape. The remaining length of the fiber bundle was not held in place. However, as the tape casting was begun at the fixed end of the fiber bundles, the casting of the slip caused the fiber bundles to remain parallel and oriented in the direction of the tape casting operation. For making tapes of PZT or PZT plus Al_2O_3 whisker the tape casting procedures as described above were followed.

The following procedure was used to produce all of the composite parts. The tapes, air-dried on the glass plate, were cut into one-inch squares and pressed into four-layer multilayers by stacking and pressing at 50°C and 5000 psi. A binder burnout phase up to a temperature of 650°C over a period of 24 hours was done. Multilayers of 501 A, 501A + Al_2O_3 fiber, 501 A + Al_2O_3 whisker, $PbZr_{.6}Ti_{.4}O_3$ + Al_2O_3 fiber and $PbZr_{.6}Ti_{.4}O_3$ were fired in an electric resistance furnace. The firing rate was about 240°C/hour up to a temperature of either 1120°C, 1220°C, 1260°C, 1290°C, or 1310°C. There was no soak period at the maximum temperature. The furnace was turned off and the multilayer cooled in the furnace. The multilayers to be fired were placed on platinum foil and sealed in an alumina crucible along with 40 grams of a PbO source material. The PbO source material of composition 501 A + 1 mole% PbO or $PbZr_{.6}Ti_{.4}O_3$ + 2 mole% PbO maintained a P_{PbO} which resulted in negligible weight change.

One of each type of multilayer which had been fired at each temperature was polished and examined with a JEOL 50 A scanning microscope[VIII] equipped with a KEVEX μX system 700[IX]. The KEVEX unit was used for quantitative

---

VIII   JEOL, Inc., Japan.

 IX   KEVEX, Foster City, CA.

chemical analysis of the samples. Windows were set for Al, Zr, Ti, and Pb. Several samples of each type of multilayer which had been fired at each temperature were tested for density with a mercury porousimeter[X].

Results and Discussion

1. Effectiveness of the Tape Casting Technique

Figure 1 is a cross-section of an Al_2O_3 fiber-PZT 501 A composite. The cluster of dark circles is the cross-section of a bundle of fibers. It is noteworthy that due to the flow of the slip during tape casting, the PZT phase is present between all of the fibers even though some of the fibers are quite close to each other and possibly were initially in contact in the bundle. Although there is considerable porosity throughout the composite, the porosity is not associated just with the fibers, but is uniformly distributed throughout the body. Figure 2 also shows the advantage of tape casting which can produce composites of fiber and PZT in which the PZT matrix is continuously distributed about the fibers. It is doubtful that cold pressing of fibers and powders would produce such a distribution of the powder around the fibers without breaking the fibers.

Figure 3 is a micrograph of an Al_2O_3 whisker in a matrix of PZT 501 A. Because the whiskers are so small (about .5 micron), it is difficult to find the whisker using an SEM even in the porous samples such as shown in Fig. 3. No whiskers could be found in the composites which were sintered at higher temperatures. This failure to find the whiskers could be attributed to several factors: the small size of the fibers, the lack of an open structure which makes the cylindrical shape of the whisker more obvious in porous bodies, and reaction with the PZT. To demonstrate the effectiveness of tape casting

---

X American Instrument Co., Silver Spring, MD, J5-7146.

a slip into which whiskers or short fibers have been mixed for producing composites in the whiskers or short fibers were aligned, a few composites of $PbZr_{.6}Ti_{.4}O_3 + ZrO_2$ fiber[XI] were fabricated. The ZrO_2 fiber (diameter 8 μm) are larger than the Al_2O_2 whisker and are more easily seen on micrographs. Figure 4 is a micrograph of a composite of 20 vol% ZrO_2 and 80 vol% $PbZr_{.6}Ti_{.4}O_3$. The fibers are generally aligned in the plane of the micrograph and the porosity is not associated with the fibers.

2. Reaction of Al_2O_3 with PZT Compounds

The sintering temperature necessary to achieve sufficient density to make poling of a 501 A or $PbZr_{.6}Ti_{.4}O_3$ part possible is in the range of 1260°C to 1310°C. However, it is quite likely at such temperatures that the Al_2O_3 may react with the PZT. The phase diagrams $PbO-Al_2O_3$ and $PbO-TiO_2$[3] both show compounds containing Al_2O_3 at the above mentioned temperature range. Previous work[4,5] with composites of PZT matrix and Al_2O_3 whisker have not mentioned any such reactions. To avoid reactions of the Al_2O_3 and PZT, firings were done at temperatures 1120°, 1220°, 1260°, 1290°, and 1310°C, in order to minimize the firing temperature and still maximize the density. Figure 5 is a micrograph of the as-received Al_2O_3 fiber. Figure 6 shows a fracture surface of a $PbZr_{.6}Ti_{.4}O_{.3}$ composite. It is obvious from comparison of Figs. 5 and 6 that the Al_2O_3 fibers have been affected by the matrix.

Since the reaction of the bulk of the fiber, not just the fiber surface, is of interest, fibers examined with the KEVEX system were such as those in the lower portion of Fig. 2. By polishing the composites, it was possible to examine the interior of the fiber. The KEVEX analysis revealed both Ti and Pb within the Al_2O_3 fibers in composites from each firing temperature except the composite fired at 1120°C which could not be polished because of the large amount of porosity. The analysis also revealed that the relative

---

XI   Zircar Products, Inc., Florida, New York, Type ZYBF-2.

amounts of Ti and Pb varied for different areas within the fiber with some areas being rich in Ti and others rich in Pb. Figure 7 reveals areas similar in appearance to the PZT bulk material, within the fiber. In the composite of Al_2O_3 fiber-$PbZr_{.6}Ti_{.4}O_3$ fired at 1310°C none of the fibers were present but only channels where the fibers used to be. A few firings of the fiber alone in the same PbO atmosphere were done to find out if the PbO vapor reacted with the fiber. No reaction was detectable, either visually with the SEM or with powder x-ray diffraction.

Density of the PZT-Fiber Composites

After calculating the theoretical density of the PZT-fiber and PZT-whisker composites, the percent theoretical density of the composites was calculated. Figure 9 compares the densities of these composites as a function of sintering temperature. As shown by the graph, the multilayers containing Al_2O_2 fiber and whisker do not attain a density of greater than 85% of theoretical density. The multilayer of 501 A alone has a density of greater than 95% at the same firing temperature. While the density of a PZT multilayer is 95% of theoretical when fired at 1290°C, as shown in Fig. 7, the PZT phase of a composite fired at 1290°C is quite porous. This inability of the PZT phase to densify is shown on a large scale in Fig. 8. The fiber bundles in these composites are seen as white lines in the composite. The fiber bundles were not uniformly distributed throughout the composite but are spaced a few millimeters apart. Before sintering the sides on the green composites were all straight. The sintered composites have a contorted edge since the PZT phase near the fiber bundles has not sintered (or drawn in) as have the PZT phase further from the bundles. There are several possible explanations for the shrinkage of the part as a function of proximity of fiber bundles. Two of these explanations deal with the effect of the reaction of the PZT phase with the Al_2O_3 fiber. The KEVEX

indicates the presence of Pb and Ti within the fiber. As the stoichiometry of the PZT grains near the fiber is probably charged, by loss of Pb, Ti, and Zr to reaction with the Al_2O_3, the sintering kinetics of the PZT phase may be affected in a way that retards sintering. Secondly, Al ions from the fibers may be diffusing into the PZT phase and also affecting the sintering. The only way that the PZT phase could achieve high density would require the PZT phase not sinter to the fibers but to slip along the fibers as sintering of the PZT occurs. If PZT grains are sintering to the fiber, as some PZT grains certainly must be doing since reaction of the PZT with the Al_2O_3 is occurring, then the slipping of the PZT grains along the fiber will become more difficult. PZT grains will sinter to the grains which have sintered to the fibers and in this way layers of PZT grains may exist which are to some degree prevented from making the rearrangements necessary to achieve a high density. Figure 8 shows that the shrinkage of the PZT phase becomes greater with distance from a fiber bundle.

The only data taken for composites of PZT 501 A ÷ Al_2O_3 whisker was the density as a function of firing temperature. As shown by Fig. 9, the highest density obtained was about 84% of theoretical density. Since the whiskers are much shorter than the fibers which run the whole length of the composite, the effect of whisker in restraining the shrinkage of the PZT should not be as great. Also, since the whisker is so much smaller than the fibers the whisker may be more consumed by the reaction with the PZT and less likely to mechanically restrain the PZT from sintering. Even had the whiskers been visible with the SEM, the use of the KEVEX system to analyze the chemical components of the whisker would not have been possible since the electron beam is several hundred angstroms in diameter. The reaction of the whisker and PZT should be more pronounced because the Al_2O_3 whisker has a much greater surface area per unit volume than the fibers.

Conclusion

The original task of developing a composite of Al_2O_3 fiber or whisker and PZT with enhanced alignment polarization due to clamping of the composite in a two-dimensional plane was not achieved. Presence of the fibers and whiskers prevented the sintering of the PZT phase to suitable densities. Reaction of the PZT matrix with the fiber and whiskers makes the mechanical strength and therefore the ability to clamp the PZT grains doubtful. Tape casting techniques were developed which allow for alignment of fibers and whisker within a two-dimensional plane. Tape casting produces a green composite of fibers and PZT with a homogeneous pore distribution despite the proximity of the fibers in bundles.

Possibilities exist to overcome some of the problems found with Al_2O_3-PZT composites. The amount of PbO available for reaction with the Al_2O_3 could be reduced by beginning with a PbO deficient powder or by firing without a PbO source to maintain the P_{PbO}. However, a deficiency of PbO results in the appearance of ZrO_2 as a second phase. The amount of ZrO_2 in the composite could be reduced by using a PZT with a greater Ti/Zr ratio. This has limited value since most PZT compositions of interest are located within the area of the morphotropic boundary.

Use of co-precipitated PZT powders will allow for a lowering of the firing temperature, since these powders are more reactive than mixed oxide powders. Being more reactive, the co-precipitated powder should also react more readily with the Al_2O_3. Even if the Al_2O_3 remains as a separate phase, the inability of the composites to sinter to suitable densities to allow successful poling remains a problem. The presence of a liquid phase might facilitate rearrangement of the PZT grains and could make slippage of the grains along the fibers during sintering easier. There must be good bonding between the fiber and or whisker and the PZT matrix if the fiber and whisker are to clamp and constrain

the PZT grains. Solving either the problem of density or reaction fibers would be difficult and solving both seems doubtful.

References

1. B. Jaffe, W.R. Cook, Jr. and H. Jaffe. Piezoelectric Ceramics, Academic Press, London and New York (1971).

2. J.V. Biggers, T.R. Shrout and W.A. Schulze. Densification . Tape Cast PZT, Am. Ceram. Soc. Bull. (in press, 1979).

3. E.M. Levin, C.R. Robbins and H.F. McMurdie. Phase Diagrams for Ceramists, Edited by M.K. Reser, The American Ceramic Society, Inc., Columbus, Ohio (1964).

4. R.C. Pohanka, R.W. Rice, J. Pasternak, P.L. Smith and B.E. Walker. Strength and Fracture of Navy Type 1 Sonar Ceramics. Proc. Workshop on Sonar Transducer Materials, Naval Research Laboratory, Washington, DC, 205-235 (1976).

5. W. Lester. A New Composite Ceramic Piezoelectric Transducer Material, Internal Technical Memorandum IW69-20-TM-1U (1970).
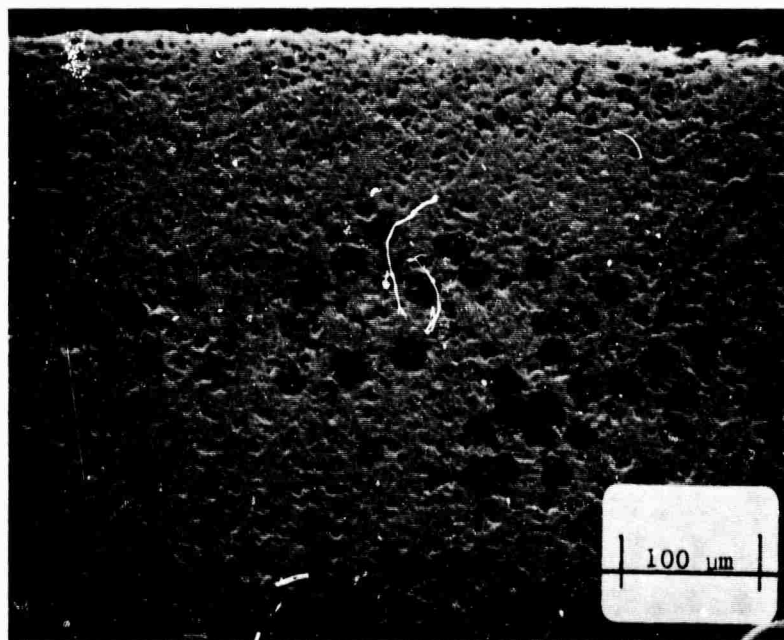
Fig. 1.   Cross-section of an Al_2O_3 fiber: PZT 501A
composite. Dark circles show cross-section
of Al_2O_3 fibers.

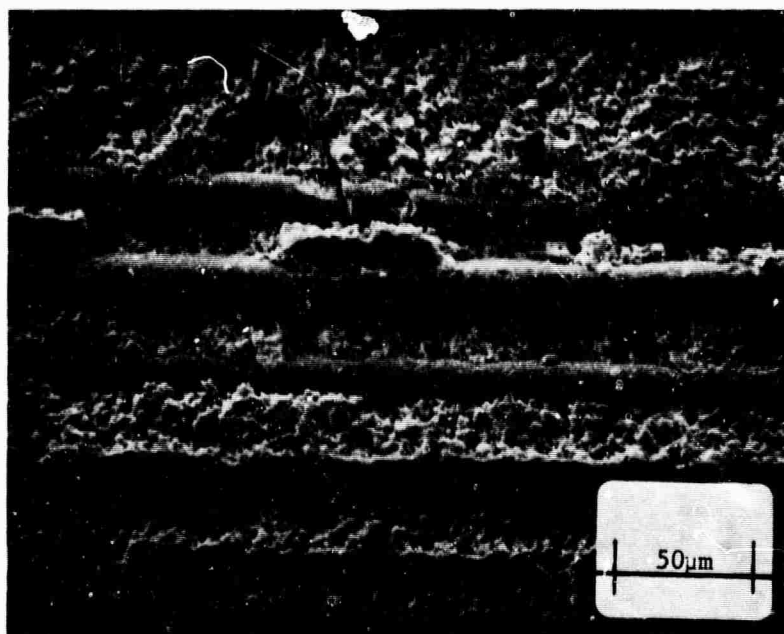

Fig. 2.   Longitudinal section through the Al_2O_3:PZT
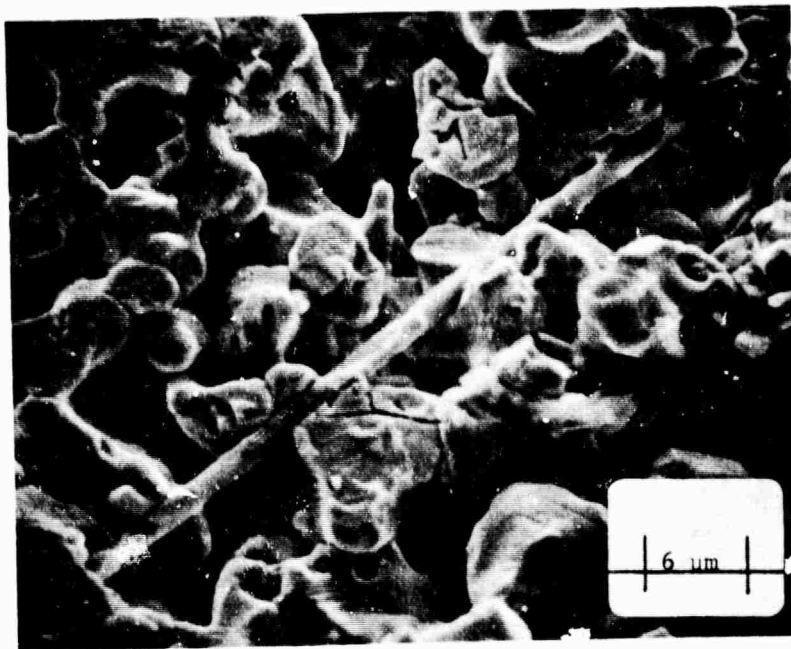composite showing good filling between fibers.

Fig. 3. SEM micrograph of a single Al$_2$O$_3$ whisker in a low density PZT 501A matrix.
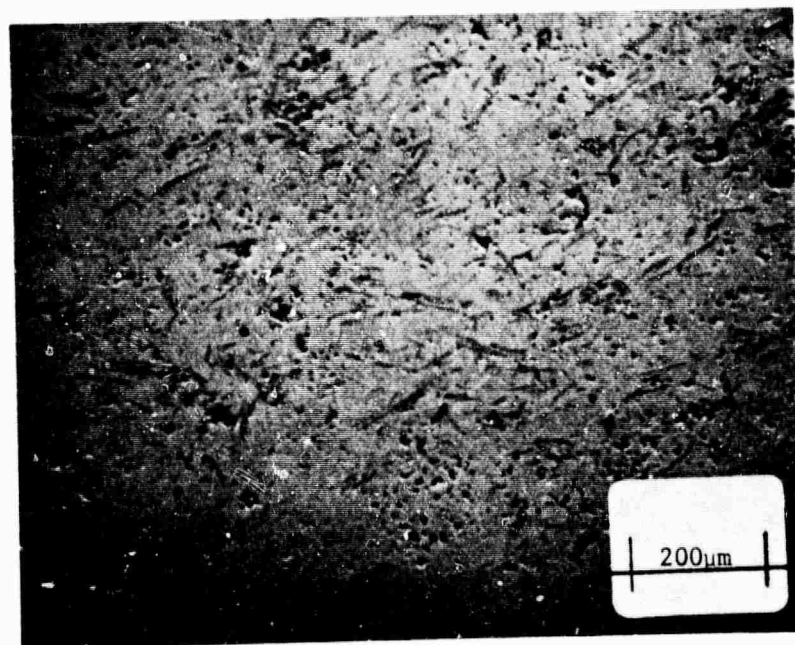
Fig. 4. Section through a composite containing 20 volume % Al$_2$O$_3$ fibers.
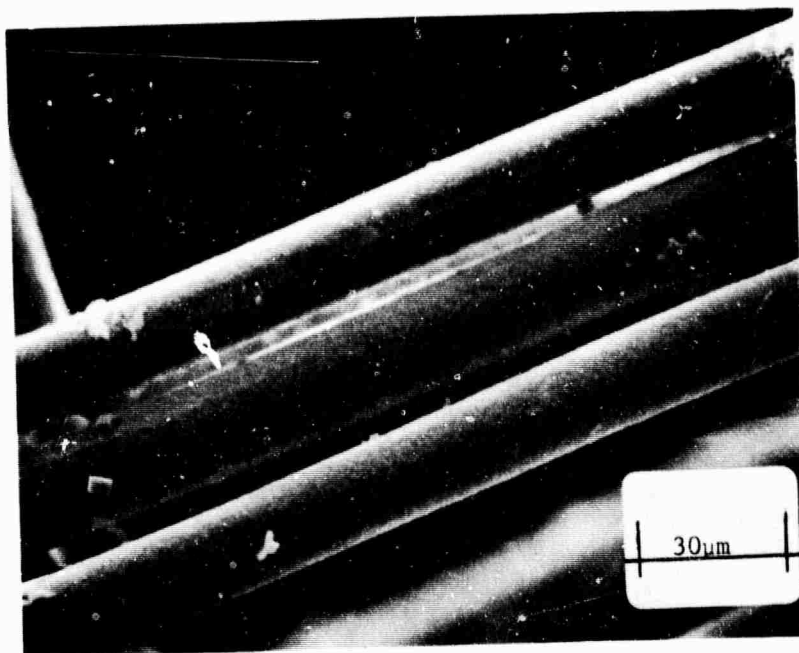
Fig. 5. Al_2O_3 fiber showing surfaces before any treatment.

Fig. 6. Fracture surface of Al_2O_3:PZT composite showing degradation of fiber surface in contact with the matrix phase.
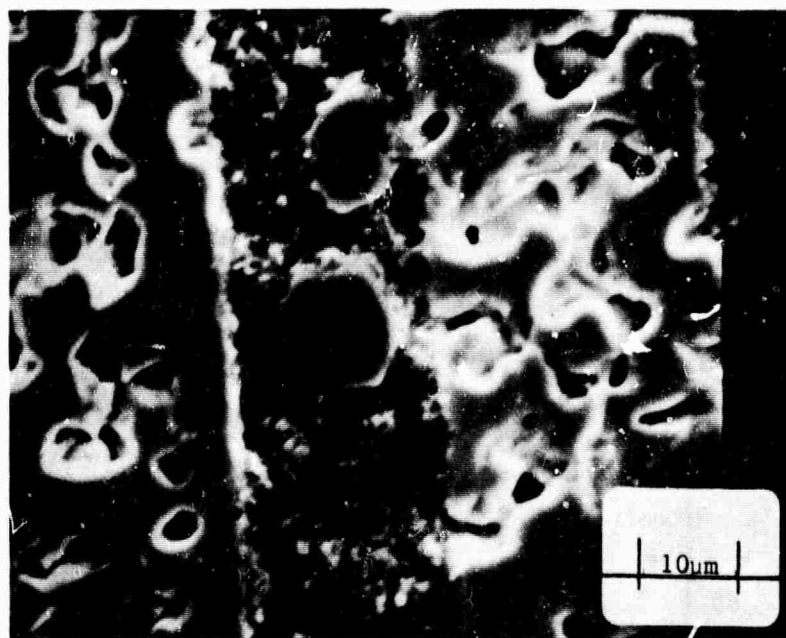
Fig. 7. SEM image of a cross-section through an
Al$_2$O$_3$ fiber of the composite showing internal
structure due to reaction with the PZT.
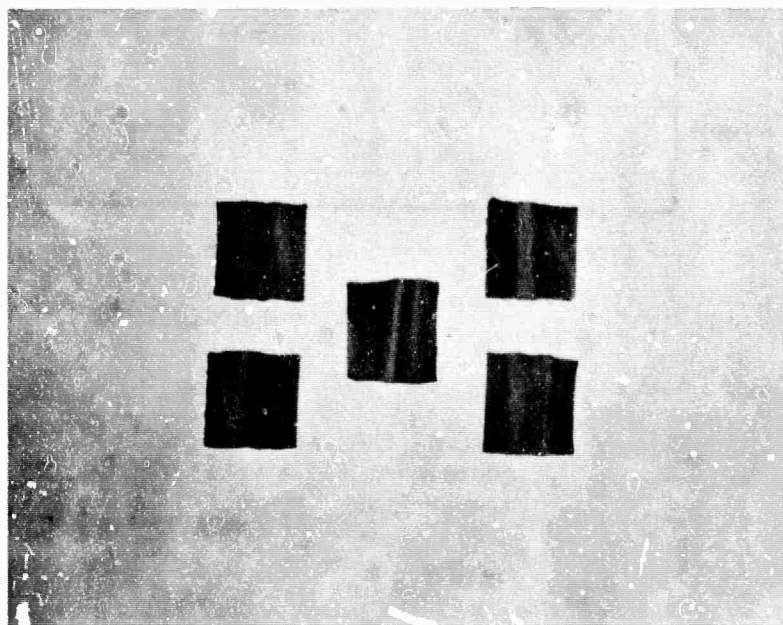
Fig. 8. Macrophotograph of Al$_2$O$_3$:PZT 501A tapes after
densification showing limitation of shrinkage
by the incorporated fibers.
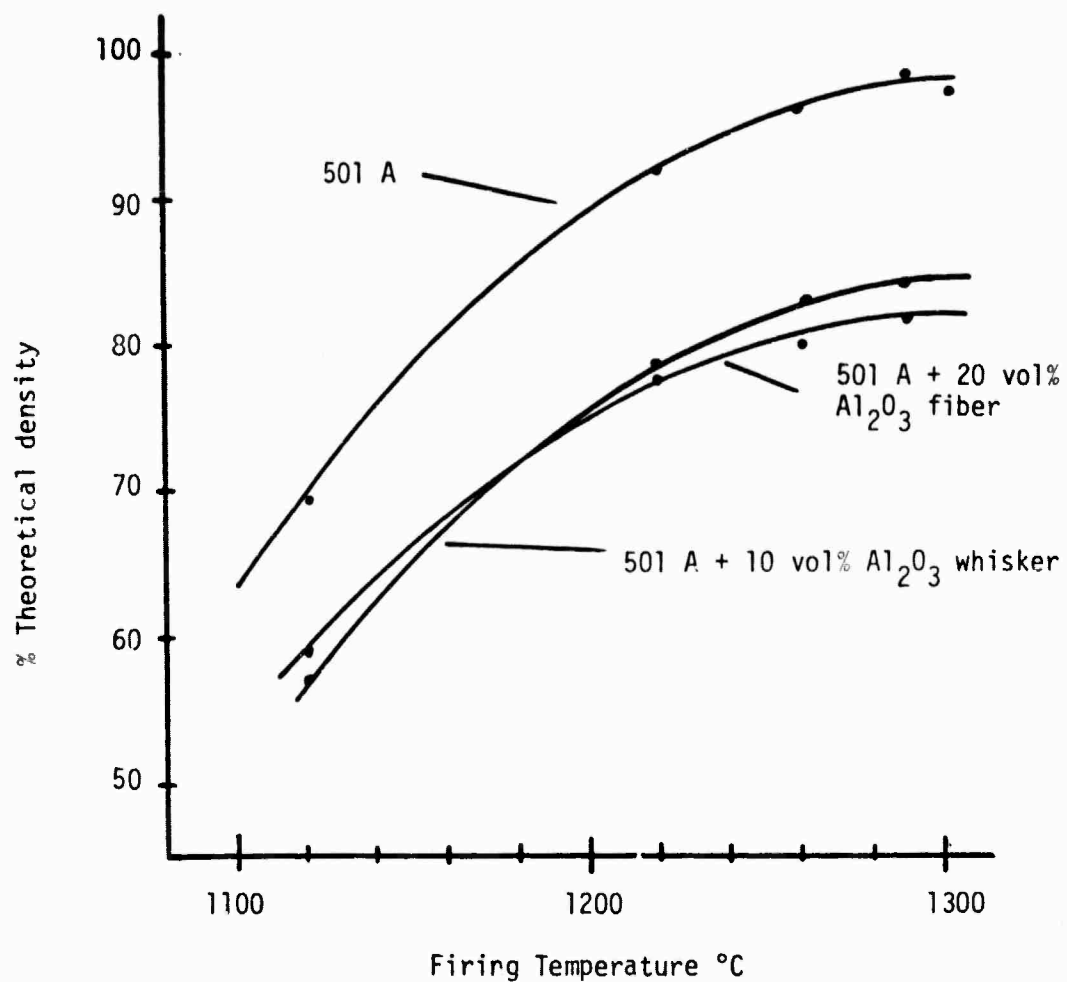
Figure 9. Percent theoretical density of multilayers containing PZT 501A as a function of firing temperature.

APPENDIX 5

Piezoelectric Properties of $Pb_5Ge_3O_{11}$ Bonded PZT Composites

W.A. Schulze and J.V. Biggers

PIEZOELECTRIC PROPERTIES OF $Pb_5Ge_3O_{11}$ BONDED PZT COMPOSITES

W.A. Schulze and J.V. Biggers
Materials Research Laboratory
The Pennsylvania State University
University Park, Pennsylvania 16802

ABSTRACT

$Pb_5Ge_3O_{11}$ was used to form dense piezoelectric composites with PZT at temperatures below 1000°C. The composite material demonstrated that the ferroelectric component may be stabilized against depoling by an insulating grain boundary phase. Composites prepared using 30% $Pb_5Ge_3O_{11}$ almost fully stabilized the polarization against reverse field of 40 kv/cm, with $d_{33} = 65 \times 10^{-12}$ m/v and $k = 470$.

Introduction

In this paper we are reporting on a study which explores the possible use of an insulating weakly polar grain boundary phase to help stabilize poled PZT grains against depoling under high drive conditions.

The PZT formulations presently used for high drive field applications utilize a charge migration to develop what appears experimentally as an internal bias field. This internal field shifts the center of the normal polarization field hysteresis loop by producing an electric and possibly elastic restoring force which attempts to return the polarization state to its original level.

The mechanisms responsible for the creation of an internal bias field in ferroelectric materials are all based on the stabilization of the domain configuration. The following is a summary of the mechanisms as described by Carl and Hardtl (1):
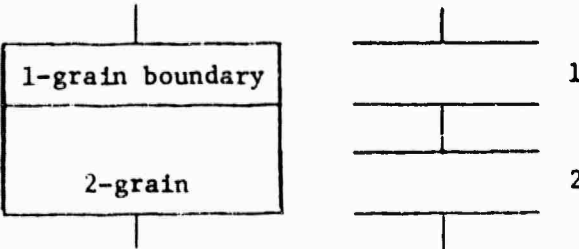
Volume Effect: Impurity atoms or vacancies may occupy energetically preferred sites in the lattice that favor a certain direction of the spontaneous polarization. This effect will exist throughout the bulk of the domain.

Domain Wall Effect: In this case, defects diffuse into the domain wall regions and fix their position. The driving force may be elastic or electric and the result is a lowering of the wall energy. This gives the crystal a "memory" for wall location even if the domain is moved or removed temporarily.

Grain Boundary Effect: A second phase in the grain boundary leads to surface charge which compensates the bound charge at the termination of a domain in the boundary region. The polarization is given a preferred direction but the domain wall remains mobile.

Externally all three models should appear as internal bias fields and be indistinguishable. The fixing procedures require thermally activated migration and therefore take time to establish their full effect. Since the grain boundary effect does not stabilize the domain wall, there should be little decrease in tan δ as compared with the other two effects which should reduce the domain wall contribution. It is the grain boundary effect that we felt could be modeled using the ferroelectric $Pb_5Ge_3O_{11}$ as a liquid phase sintering aid for a PZT based piezoelectric.

The model structure assumes an even distribution of grain boundary phase of volume ^1V and permittivity $^1\epsilon_{33}$ around uniform grains which are denoted here by superscript 2. The average piezoelectric coefficient $\bar{d}_{33}$ should follow a simple series equation (2):

$$\bar{d}_{33} = \frac{^1v\,^1d_{33}\,^2\epsilon_{33} + ^2v\,^2d_{33}\,^1\epsilon_{33}}{^1v\,^2\epsilon_{33} + ^2v\,^1\epsilon_{33}}$$

If the grain boundary phase is a good insulator and has little or no reversible polarization, the composite cannot be poled unless compensation charge can be transported to the ferroelectric grains. For this reason the experiment utilizes high temperatures and fields for long times to allow charge transport to the PZT grain surfaces. Conversely, it can be predicted that the poled composite cannot be depoled under high field for times that are short compared to the charge transport time constants.

Preparation and Characterization of Specimens

Powder

The $Pb_5Ge_3O_{11}$ (PGO) and the $Pb(Zr_{.45}Ti_{.55})O_3$ were prepared from reagent grade oxides by calcining and regrinding to the desired particle size. A second PZT was used in some of the formulations. It was a commercial powder (501A)* and was used as received or calcined to a larger particle size.

The PGO was formed by calcining twice at 650°C for 24 hours with an intermediate regrinding in an agate mortar. The PZT 45/55 was first calcined for 24 hours at 750°C, ground for 24 hours in a plastic mill using alumina cylinders, then calcined at 1100, 1200, or 1300°C for 1 hour. The material was then crushed in a mortar and reground in a mill for 24 hours.

---

*Ultrasonic Powder 501A, Ultrasonic Powders, Inc., South Plainsfield, NJ.

The PGO-PZT composites were prepared by mixing in a small plastic mill. About 1 wt% of PVA binder was added and the powder was pressed at 40 Kpsi into disks 1.27 cm in diameter and 0.2 cm thick. The binder was removed at 500°C during a 30 minute burnout. The firings were done by placing the sample (resting on a Pt foil) in a preheated furnace and removing at the indicated time to cool at room temperature. The only exceptions were the O_2 firings which were inserted and removed from the hot zone by sliding a long silica tube through the furnace. In this case the heat-up and cool-down times were judged to be longer.

Calcined powders were characterized by an automated SEM procedure (3), which through x-ray emission was able to separately analyze the size and shape distribution of the $Pb_5Ge_3O_{11}$ and PZT after all mechanical procedures except compacting were completed.

In all the samples analyzed, the PGO ranged between 1 and 6 microns with a mean about 2.4 µm. There were inconsistencies with the PZT size due to grinding: The 1300°C calcine required the greatest effort to reduce the hard sintered compact, and consequently ended with the finest particle distribution and a mean diameter of 2.0 µm; the 1100°C calcine had a mean of 2.7 µm, and the 1200°C material had a mean of 4.0 µm. Comparing these numbers to the microstructures it could be seen that the 1100°C material was reduced to high surface area aggregates composed of a few grains. The 1300°C material was reduced to particles that are comparable to the original grain sizes. PGO attacks the PZT grain boundary material at a much higher rate than the grains. This effect was also observed in wetting and etching studies of dense PZT surfaces, where PGO totally wet the surface and eventually dissolved the grain boundary, allowing individual grains to be removed (4).

DTA

A DuPont Model 900 DTA* was utilized to study melting and recrystallization of the various liquids during the sintering process. Measurements were made at a rate of 20°C/minute. Instead of the normal Al_2O_3 standard, PZT powder was used to minimize baseline drift.

DTA analysis of PGO bonded $BaTiO_3$ was used by Park (5) to prove that although the starting compound was the ferroelectric $Pb_5Ge_3O_{11}$(5:3), a rapid reaction converted it to the ferroelastic (centric) $PbGeO_3$ (1:1) form (6). During long sintering times the PGO continued to react, resulting in a $BaGeO_3$ phase.

In PGO bonded PZT the host structure is already saturated with PbO and little reaction between phases should occur. The results of DTA cycles to the sintering temperatures are summarized in Fig. 1. The low temperature (800°C) cycle indicated that instead of giving up PbO as in the $BaTiO_3$ case, the PGO dissolved PbO from the PZT and formed the high lead phase Pb_3GeO_5 (3:1) in co-existence with $Pb_5Ge_3O_{11}$. The formation of the 3:1 composition (710°C melting point) is necessary because of the very limited range of compositional stability of the 3:5 (755°C melting point) material (7). Heat treatments to 900°C and 1050°C indicate that the PGO probably remains in the 3:1 and 5:3 phases.

The higher heat treatments and longer sintering times reduce the ability of the PGO phases to crystallize on cooling. At 900°C the recrystallization is broadened and reduced from 630°C for the 800°C firing to 490°C. In the 1050°C runs, crystallization does not occur on cooling but occurs at 510°C on reheating. Longer soaks raise the temperature to 550°C and even higher.

*E.I. DuPont DeNemours & Co., Inc., Wilmington, DE.

X-Ray

Powder x-ray diffraction was conducted to confirm the existence of the 5:3 and 3:1 PGO compounds in the recrystallized composites. Peaks of non-PZT phases were observed and appeared to confirm the existence of the 5:3 compound, but because of the low intensities and overlapping patterns of these lead compounds it is impossible to make a positive identification. X-ray diffraction did, however, indicate that there was no measurable modification to the PZT structure.

Sintering

Densities reported were determined by weighing and were judged to be better than ±3%. The theoretical density is for an unreacted mixture of the PGO and PZT.

The firing runs started from pellets pressed to approximately 55% of the theoretical density. All conditions produced initial densification that was probably due to rearrangement of particles from capillary action when the PGO melts (5). The density after 10 minutes of firing is shown in Fig. 2 as a function of concentration and temperature. At low PGO concentrations, there is insufficient densification even at 1000°C. With increased liquid content, temperature becomes a strong factor in initial densification. This may reflect the expected decrease in viscosity and increase in solubility of the PZT phase with temperature.

Figures 3a and 3b are typical of the densification relations observed. Five percent PGO did not yield high densities under any conditions. It appears there was insufficient liquid to fill the pore structure and promote the intermediate densification which was probably a solution-precipitation process allowing for better particle arrangement. With increasing liquid content, the time scale was compressed and near maximum densification was
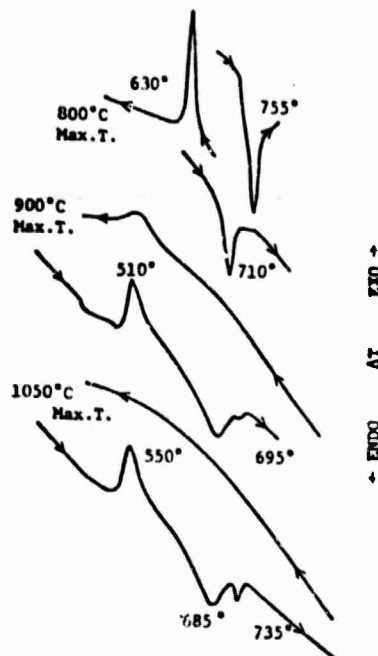

FIG. 1
Significant sections of DTA curves for PZT 45/55 (1100°C)-20% $Pb_5Ge_3O_{11}$ composite material.

FIG. 2
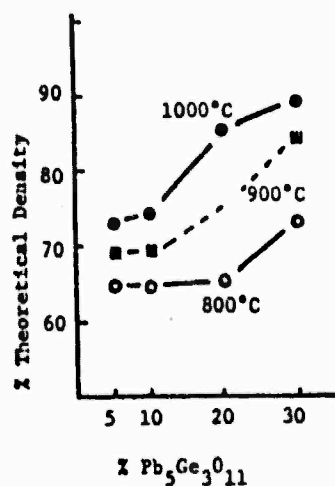Density at 10 minutes for PZT 501A (1100°C) $Pb_5Ge_3O_{11}$ composites.
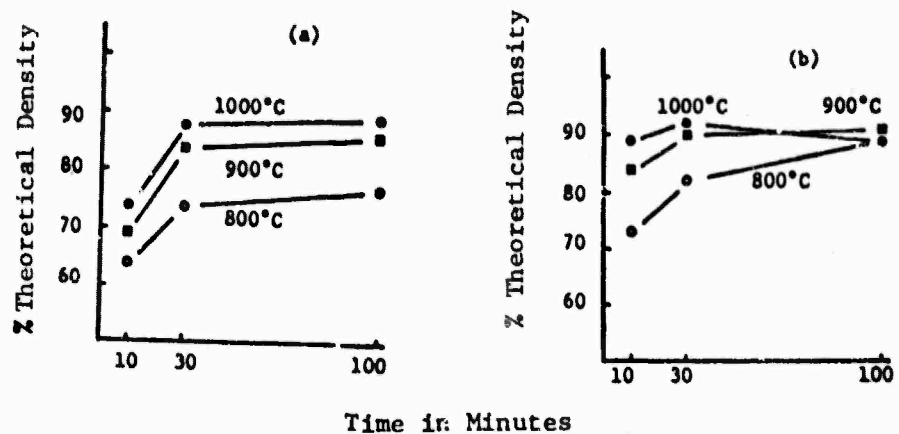
FIG. 3
Densification of PZT 501A (1100°C)–$Pb_5Ge_3O_{11}$ composites.

(a)   (b)
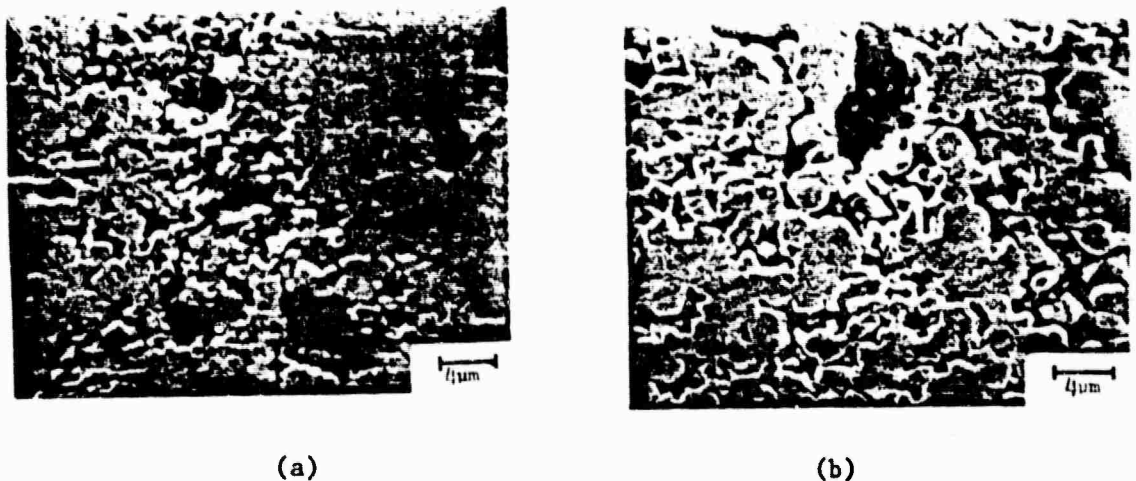
FIG. 4
Etched micrographs of 20% $Pb_5Ge_3O_{11}$ composites fired at 1000°C for 100
minutes using (a) PZT 45/55 (1100°C) or (b) PZT 45/55 (1300°C). (See
additional micrographs at end of this paper).

reached in 30 minutes. Micrographs indicate there was little grain growth for
short times and low temperatures, but a doubling of the grain size was observed
for longer times at high temperatures.

A second sintering mechanism is also evident in the polished and etched
microstructures of both the 1100° and 1300°C materials (Fig. 4a and 4b) fired
at 1000°C for 100 minutes. The grains are not totally surrounded by the PGO,
but have formed into a network of sintered ceramic suggesting a breakdown of
the simple series model used to analyze the electrical data.

The densification in air maximized at about 92%. Near this density poro-
sity normally closes and gases become trapped. It is possible at 1000°C that
nitrogen is relatively insoluble and would block further densification. Firing

in oxygen under near identical conditions increased the maximum densities to above 95%, and processing in a gas-isostatic-hot press showed a further in-increase to 99%.

During this sintering study, there was little weight loss recorded. The two exceptions were: firing in a vacuum and 1000°C firing with 30% PGO. The 30% PGO samples lost between 2 and 3% of their weight after 100 minutes at 1000°C and were the only samples to show a decrease in density with firing time.

Dielectric

Dielectric measurements and poling were conducted utilizing sputtered gold electrodes. All dielectric measurements were made on unpoled samples at a temperature rate of 4°C/minute. Poling conditions were 180°C at 40 KV/cm for 0.5 hours. Polarization field hysteresis loops were generated on a standard Sawyer-Tower type circuit at 1 Hz.

Relative permittivity, dielectric loss, remanent polarization and piezo-electric coefficient were measured to determine to what degree the various fabrication parameters influenced the series connectivity. The data in Table 1 for two different processing conditions are compared to the values calculated for the composite from a simple series and a compound model.

Figure 5 shows the permittivity-temperature curves for several composites and are typical of all composites with greater than 85% theoretical density. Dielectrically, there is no evidence of a permittivity anomaly in the series PGO phases. Heat treating procedures that were successful in producing a heat of recrystallization in DTA runs and very weak x-ray lines did not significantly
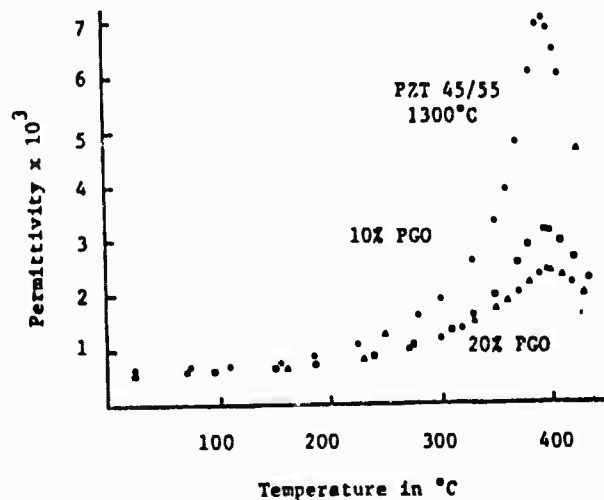
FIG. 5
Temperature dependence of permittivity for PZT 45/55 and PZT
45/55-$Pb_5Ge_3O_{11}$ composites fired at 1000°C for 30 minutes.

Table 1
Dielectric Properties

XPGO	K,tan δ 25°C	1 KHz	K_max-Tc 100 KHz	tan δ 1 KHz-Tc	P_R 1Hz uC/cm²	E_c 1Hz KV/cm		$ε_{33}$ x10^{-12} m/v Fixed	Reversible	% PZT Connected P_r	d_{33}
PZT 501 fired 1330°C											
0	1540	0.017	21000	0.038	36.4	11.8		0	450		
PZT 501-1100°C fired 1000°C for 100 min Unpoled											
10	930	0.021	5520	0.074	12.4	14.3		—	—		
20	670	0.019	3340	0.170	5.9	13.0		—	—		
30	410	0.016	1410	0.400	1.7	16.5		—	—		
Poled 180°C - 30 min - 30 KV/cm											
10	1030	0.018	—	—	11.5	14.1	16.1	55	129	32	29
20	680	0.017	—	—	5.7	11.7	14.6	65	50	16	11
30	430	0.016	—	—	1.5	8.2	11.9	54	10	4	2
PZT 501-1300°C fired 900°C for 100 min Unpoled											
10	700	0.018	3280	0.120	8.4	15.1		—	—		
20	612	0.019	2770	0.?	5.5	13.3		—	—		
30	434	0.016	1350	0.?70	1.7	9.8		—	—		
Poled 180°C - 30 min - 30 KV/cm											
10	710	0.017	—	—	6.2	11.6	16.0	114	82	17	18
20	630	0.019	—	—	4.8	11.6	15.0	72	43	13	10
30	467	0.016	—	—	1.2	8.0	11.6	62	8	2	2
Series Model											
10	525	760			0			144	0	0	0
20	300	360			0			78	0	0	0
30	200	22?			0			49	0	0	0
Series model plus Z parallel connectivity											
10	830	6830			10.9			101	135	30	30
20	486	3460			?3			66	68	15	15
30	226	640			0.7			48	9	2	2

alter the permittivity curves. This suggests that the recrystallization is occurring primarily at triple points and filled void areas or that the degree of recrystallization is too small to affect the dielectric constant. The insensitivity of the PZT transition temperatures (±5°C) supports the conclusion drawn for x-ray diffraction—that there is little solubility of the Ge in the PZT structure. At the transition, the loss at 1 KHz is large and conduction dominated (100 KHz, tan δ < 0.005) with increases in tan δ proportional to the PGO content. If the 1 KHz loss is used to calculate a resistivity for the series PGO that appears to "short" the insulating PZT grains, the resistivity of the PGO phases is 10^7 Ωcm at 300°C and 6 x 10^5 Ωcm at 400°C. These levels, when compared to values for PZT of 10^{10} Ωcm and 10^8 Ωcm (?) respectively, indicate that the high temperature poling conditions should allow compensation charge to flow to the PZT grains.

High-field Sawyer-Tower measurements (40 KV/cm peak) were used to determine the switchable polarization. In all cases the remanent polarization and the peak induced polarization dropped rapidly with increased liquid phase. This was accompanied with a decrease in the field of zero polarization (E_c). If it is necessary to have a continuous PZT path to switch polarization at 1 Hz, then a percentage of connected PZT can be calculated. These values range from above 30% for 10% PGO to about 2% for 30% PGO.

Poling the composites generally decreases the switchable and induced polarization. Poling also causes small asymmetries in the hysteresis loops with an internal bias field or offset field of less than 2.5 KV/cm for all samples.

The d_{33} values produced during high temperature and long time poling were found to be composed of two parts. One component was easily reversible at room temperature and the other was stable even after hundreds of 1 Hz cycles with 40 KV/cm maximum field levels. If a hysteresis loop was stopped in the poling direction, the measured d_{33} was the sum of polarization fixed by high temperature poling and the reversible polarization. If the loop was stopped after a field opposing the poling field, then the d_{33} results from the difference of the two polarizations. From these two values the fixed or field stable and reversible components were calculated. The reversible component decreased with increasing PGO content, as did P_R, indicating that the amount of connected PZT phase is decreasing and the composite is approaching the series model.

If the simple series model is permitted to include a continuously connected PZT shunt, then the calculated values would tend toward the experimental data. To estimate the percentage of connected PZT phase, it was assumed that all the P_R or reversible d_{33} was a measure of the shunt material. These calculated percentages are listed in Table 1. The values of calculated permittivity still fall short of actual levels and support the microstructural observation that much of the grain boundary material is found in regions that parallel the host phase rather than a continuous film in series with the PZT grains.

Conclusions

Sintering

Liquid phase sintering is quite complicated. Most of the theoretical and experimental analyses of the process have been for the commercially important tungsten carbide-cobalt systems. Lenel (9) has postulated three stages of densification:

1. Particle rearrangement after liquid phase formation.

2. Solution of the solid phase in the liquid followed by precipitation.

3. Normal "solid state" diffusional processes.

It is likely that the dominant process in densification will vary depending on the composition, amounts, and physical characteristics of the phases. In his study of liquid phase sintering, Kingery (10) concludes that solution-precipitation is the most important. Eremenko (5) concludes that the nature and amount of the solid and liquid forming phase will determine which process predominates.

Park (5) has conducted a very thorough study of liquid phase densification in the $BaTiO_3$-PGO system. He concludes that the important feature of the sintering processes in his materials is the initial pore size distribution. In his work, it appeared that the PGO phase was only able to fill pores of a certain size and smaller. The lack of grain growth also suggests that solution-precipitation was not important.

The sintering results obtained with the PGO-PZT mixtures show that both particle rearrangement and solution-precipitation are occurring in the system. Figure 3 clearly shows the importance of both temperature and the amount of liquid phase on the rearrangement process. As expected, the 30% PGO composite shows the most rapid initial rate at low temperatures. The solution-precipitation occurring at higher temperatures is also indicated from the grain growth observed at increased time.

Dielectric

The liquid phase processing was investigated to produce a piezoelectric stabilized from depoling by an insulating grain boundary phase. The models proposed by Carl (1) indicate that a grain boundary insulator unlike the other stabilization mechanisms should not decrease domain wall motion and consequently decrease tan δ. This is supported by the very limited change in tan δ recorded for all specimens.

The insulating grain boundary material differs markedly from the other stabilization methods in the degree of reversible polarization. Normal "hard" PZT exhibits a switchable polarization of the same magnitude as the unmodified PZT. The PZT-PGO (30%) composites, however, have remanent polarizations of only 1/20 the host PZT. It appears that for overall fields up to to 40 KV/cm the grain boundary phase effectively blocks switching of the PZT grains by inhibiting the transport of compensation charge and isolating the grains from compensation by the bound charge of domains in adjacent grains.

In this study, it was necessary to use 30 wt% (32 vol%) PGO to achieve a near ideal composite. The best compositions ($d_{33} = 65 \times 10^{-12}$ m/v) used a PZT reground after sintering to near theoretical density, with firing conditions chosen to limit particle to particle sintering. If processing condition could be optimized to achieve a series composite at the 15% PGO level, the PZT-PGO material would approach the d_{33} values of the "very hard" PZT compositions with superior polarization stability.

Acknowledgment

References

1. K. Carl and K.H. Härdtl, Ferroelectrics 17, 473 (1978).

2. R.E. Newnham, D.P. Skinner and L.E. Cross, Mat. Res. Bull. 13, 525 (1978).

3. G.G. Johnson, Jr., E.W. White and D. Strickler, "Image Analysis Techniques," Symposium on Electron Microscopy of Microfibers, HEW Publ. No.(FDA)77(1977).

4. M. Rusinko, Dielectric Mixing in the PLZT-$Pb_5Ge_3O_1$ System, B.S. Thesis, The Pennsylvania State University (1975).

5. S.M. Park, Liquid Phase Sintering of Heterophasic Dielectric in the System Barium-Titanate-Lead (5) Germanium (3) Oxygen (11), Ph.D. Thesis, University of Illinois at Urbana-Champaign (1977).

6. V.D. Sal'nikov, S.Y. Stefanovich, I.D. Datt, Y.Y. Tomashpol'skii and Y.N. Venevtsev, Sov. Phys. Crystallogr. 21(1) 113 (1976).

7. W.K. Zarcker, M. Delfino, J.P. Dougherty, O. Sicignano, J. Ladell and J.A. Nicolosi, J. Elect. Mat. 6(2) 125 (1977).

8. B. Jaffe, W.K. Cook, Jr. H. Jaffe, "Piezoelectric Ceramics," Academic Press, New York (1971).

9. F.V. Lenel, Trans. AIME 175, 878 (1948).

10. W.D. Kingery, J. Appl. Phys. 30, 301 (1959).
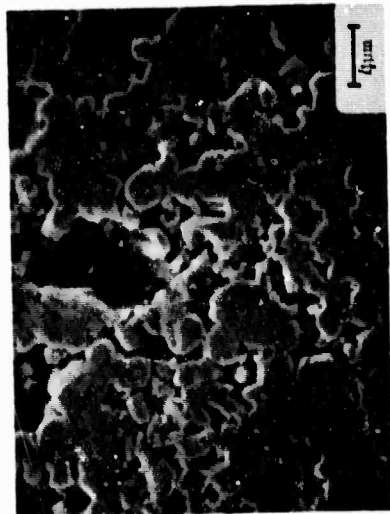
PZT 1300°C + 20% PGO   FINE GRIND
1000°C - 100 MIN

PZT 1300°C + 20% PGO   COARSE GRIND
800°C - 30 MIN

PZT 45/55   1300°C - 1 HR

PZT 1100°C + 20% PGO
1000°C - 100 MIN
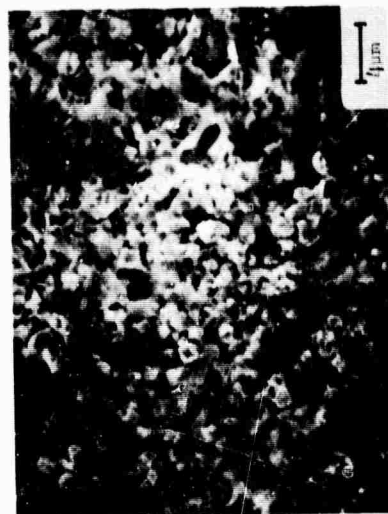
PZT 1100°C + 20% PGO
800°C - 30 MIN
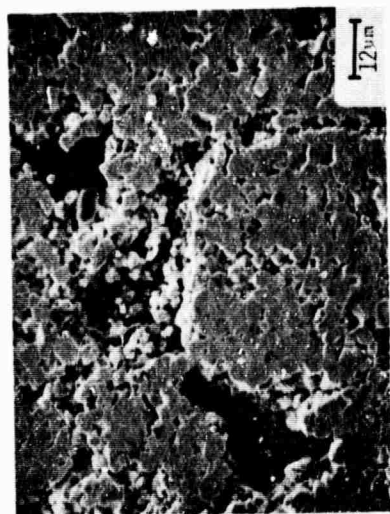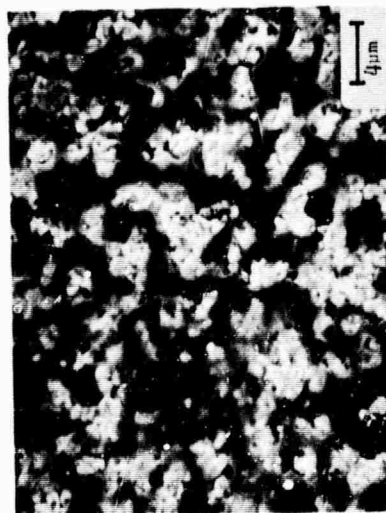
PZT 45/55   1100°C - 1 HR

APPENDIX 6

Piezoelectric Properties of Internally Electroded
PZT Multilayer

L.J. Bowen, T.A. Shrout, W.A. Schulze and J.V. Biggers

Piezoelectric Properties of Internally Electroded PZT Multilayers

L. Bowen, T. Shrout, W. Schulze and J. Biggers

Materials Research Laboratory
The Pennsylvania State University
University Park, Pennsylvania 16802

Abstract

For transducer applications, materials in the lead zirconate-lead titanate solid solution series are preferred because of their high piezoelectric coefficients and favorable chemical and mechanical properties. Unfortunately, PZT transducers generally require high driving voltages and impedance matching can be difficult. The present work describes an attempt to overcome these problems by applying to piezoelectric materials an internal electroding technique commonly employed in the multilayer capacitor industry.

The internally electroded devices are prepared by screen-printing platinum electrodes onto tape-cast PZT, stacking the electroded tape pieces in the appropriate configuration, warm pressing and then air sintering. After grinding to expose the internal electrodes, the devices are externally electroded as required and poled. These devices have been prepared from "hard" and "soft" commercial grades of PZT and are intended for resonant and strain applications respectively.

The relative permittivity, dissipation factor and piezoelectric coefficients are largely unaffected by the presence of internal electrodes, and these devices show greatly improved strain:voltage ratios compared to conventional materials. The use of internal electrodes has also been demonstrated to have little effect on the frequency constant, even in the transverse mode, since the volume fraction of electrode is quite small (approximately 5%) and the density and elastic compliance terms almost cancel out when platinum electrodes are employed.

Internally electroded components have a higher dielectric breakdown strength than conventional devices and are extremely versatile. As an example of the type of device for which internal electroding is particularly suitable, a piezoelectric transformer has been designed and tested. This device exhibits improved voltage step-up characteristics compared to present designs.

Introduction

For electromechanical transducer applications, materials in the lead zirconate-lead titanate solid solution series are widely used because of their high piezoelectric coefficient and favorable chemical and mechanical properties. Although electrical driving conditions for PZT transducers vary depending on their composition and dimensions, for most applications a high driving voltage is required and consequently impedance matching can be difficult. Attempts have been made (1) to overcome this problem by bonding together electroded piezoelectric discs with organic adhesive to form internally electroded macrocomposites. Although success has been obtained in some applications using this approach, it should be possible using exisitng multilayer capacitor technology to produce a similar composite more simply and with improved electromechanical properties.

Internally electroded multilayer capacitors are produced (2) by applying metal electrodes onto thin tape cast sheets of high dielectric constant material, such as barium titanate, assembling the electroded tape into the required device configuration and firing to form a dense body. The resulting composite has greatly enhanced capacitance-to-volume ratio for a given operating voltage and has the additional advantage of high dielectric breakdown strength arising from the thinness of the insulating ceramic layers (3).

In the present work this technique has been employed to produce low voltage transducers from commercial PZT formulations. It will be demonstrated that internal electroding can also be beneficial in other types of devices, e.g. in piezoelectric transformers.

Experimental

Device Configurations

To investigate the utility of internal electroding in electromechanical applications, three types of devices have been studied. The device configuration which offers the greatest potential in transducer applications is shown in Figure 1(a). It consists of overlapping internal electrodes separated by insulating PZT layers, with alternate electrodes exposed on opposite ends of the device and connected together by an external electrode applied after firing. The poling and driving fields are applied to the external electrodes so that adjacent PZT layers are poled in opposite directions but driven in phase. Although most of the present work has been restricted to devices have only four internal electrodes, it is possible to use a far greater number. Devices with up to one hundred electrodes have been prepared in the course of the

present work and this is typical of the number commonly used in the multilayer capacitor industry (2).

Figures 1(b) and 1(c) show two other device configurations which have been fabricated to test the effects of internal electrodes on electrical and mechanical properties. Figure 1(b) illustrates a "plain" device made by pressing together five layers of PZT tape without internal electrodes, while Figure 1(c) shows a "sandwich" structure consisting of alternate layers of PZT and equally spaced platinum internal electrodes. In both of these devices the poling voltage is applied through the whole thickness of the sample.

Device Preparation

In preparing the devices two commercial* grades of PZT have been used: a "soft" PZT (manufacturer's designation 501A) for high strain applications and a "hard" composition (401-888) for resonance work. Property data for these materials have been published elsewhere (4).

The device fabrication route is shown in Figure 2. PZT powder mixed with liquid organic binder is tape cast (5) 0.25 mm thick, dried, cut into 25 mm squares and electroded with platinum paste** by screen-printing. The tape pieces are then stacked in the appropriate configuration, warm-pressed at 30MN m^{-2} and 50°C to form a coherent device structure, and the binder burned out in flowing air at 700°C over a 30 hour period. Firing at 1300°C for 90 minutes in the presence of a lead oxide source gave specimens over 95% dense. In some cases a one-hour hot-isostatic pressing (4) operation at 1300°C under 20MN m^{-2} argon pressure has been used to remove the remaining porosity. After grinding the fired specimens to expose the internal electrodes as required, external electrodes are applied as fired on silver paste*** and electrical connections made to these by soldering on 0.2 mm diameter silver wire.

Figure 3 is a scanning electron micrograph of a sectioned 501A multilayer specimen. This sample has been etched in a dilute aqueous mixture of hydrofluoric and hydrochloric acids to expose the grain boundaries. The platinum electrode is incompletely sintered but fully coherent and appears from the etched features to be bonded to the surrounding ceramic by an intermediate second phase. In all the specimens examined the internal electrodes appeared to be continuous.

---

*Ultrasonic Powders Inc., South Plainfield, NJ 07080

**Engelhard Industries, East Newark, NJ 07029, Type E-305-A.

***Dupont Electronic Products, Wilmington, DE 19898, Type 7095.

The devices are characterized to determine the effect of internal electrodes on relative permittivity, dissipation factor, and piezoelectric coefficient. The strain/field characteristics of the 501A material were evaluated by dilatometry, driving the device through the d_{31} piezoelectric coefficient. Resonance spectra for bar-shaped specimens prepared from both 501A and 401-888 PZT were obtained and compared using a network analyzer*.

Results and Discussion

Electrical Properties

Some electrical properties of the various device configurations prepared from 501A and 401-888 PZT compositions are compared in Table 1. Relative permittivity values for the internally electroded 501A are reduced by approximately 15% compared to plain specimens of the same composition, although for the multilayer devices this difference may be due to inaccuracies in estimating the active electrode area rather than an inherent material property. The dissipation factor and d_{33} piezoelectric coefficient are unaffected by the presence of internal electrodes in the sandwich configuration, but in the multilayer configuration the dissipation factor is increased and a reduction in d_{33} of 20% is seen. Furthermore, values of d_{31} for the 501A multilayer devices are similarly reduced compared to measured values for the other device structures. The effects of this reduction in piezoelectric coefficient on the use of these devices in strain applications is discussed in the following section.

Strain Properties

The devices were evaluated for static displacement applications using the d_{31} piezoelectric coefficient by applying an electric field through the thickness or between internal electrodes, and measuring the displacement with a DCDT** across the width. 501A was chosen as the test material because of its high piezoelectric coefficient.

Strain/field characteristics for the three types of device are shown in Figure 4. These specimens have been cycled in the electric field approximately ten times to attain equilibrium hysteresis. Although hysteresis is severe for all three specimen configurations, it must be remembered that 501A is a soft PZT composition and that the field levels employed in the strain experiments are considerably higher, at 1000 KV m^{-1}, than would be employed in most

---

*Hewlett-Packard Model 8407A.

**Model 24DCDT-050, Hewlett-Packard, Medical Engineering Division.

practical applications. For field levels up to 700 KV m^{-1} the strain behavior of the plain and sandwich structures are very similar, but both differ from the characteristics displayed by the multilayer configuration, which requires a higher electric field to obtain displacement. However, the actual voltage required to obtain a given strain in the multilayer device is considerably less than the voltage needed to obtain the same strain in the other devices, e.g. considering four internal electrode devices of the same thickness, the voltage needed to obtain 0.01% strain in the multilayer configuration is only one-third that required for the sandwich structure. Still lower voltages can be used if more internal electrodes are incorporated into the multilayer device.

The inferior strain/field characteristics of the multilayer configuration explain the low piezoelectric coefficient values reported in Table 1 for this device. The explanation for these inferior characteristics lies in mechanical clamping caused by the presence of electromechanically "dead" regions located at the internal electrode lead-ins. At the edges of the device an unpoled region exists between the emerging, but not yet overlapping, internal electrodes. Since the applied field is zero at these edges the strain must also be zero, and the edges then clamp the deforming interior of the device. The clamping phenomenon is further illustrated in Figure 5 which shows the measured strain in the center of the multilayer deivce to be greater than at its edges for a given field. Clamping must be taken into account when using this device. It may be possible to reduce its magnitude by removing as much of the edges of the device as the dielectric breakdown strength will allow, or by using highly compliant lead-ins on a sandwich type structure.

To demonstrate the feasibility of the multilayer device configuration in large displacement applications a 100 active layer device has been built, using 401-888 PZT to minimize hysteresis, and driven through the d_{33} piezoelectric coefficient. The results, shown in Figure 6, indicate a linear strain/field relationship up to field levels of 1000 KV m^{-1} which correspond to an effective d_{33} of 223 x 10^{-12} CN^{-1}.

Resonant Properties

Reference to Table 1 shows that the mechanical quality factor, Q_M, of the plain and sandwich materials is lower than the manufacturer's value for both 501A and 401-888 compositions. This discrepancy may have arisen from differences in the ceramic processing conditions or, alternatively, from differences in measuring technique since the commercial data are for radial mode resonance,

whereas the present values are derived from the fundamental longitudinal mode resonance of long, thin bars. Q_M is approximately 30% lower for the plain 401-888 material compared to the internally electroded specimens. However, this disparity might merely be due to differences in porosity level since similar specimens, when hot-isostatically pressed to near theoretical density, exhibited Q_M values of 601 and 592 for the plain and sandwich materials respectively.

Resonance spectra over the frequency range 0.1 - 10 MHz are shown in Figures 7(a) and 7(b) for 501A and Figure 8 for 401-888 PZT bars (approximate dimensions 12 x 1.5 x 10.mm). The internally electroded specimens each contained four internal electrodes and five active layers. Care was taken to ensure that the plain and internally electroded bars of each material were of identical dimensions.

The fundamental longitudinal mode resonance is on the extreme left in both figures. For each material the resonance spectra are almost identical, regardless of the presence of internal electrodes. This is especially true for the hard 401-888 material (Figure 8) in which no peak shift or damping is detectable even in the thickness resonance mode, indicative of insignificant damping by the internal electrodes. In the 501A materials the thickness mode resonance frequencies are reduced by approximately 10% in the internally electroded device compared to the plain specimen. This is accompanied by a reduction in peak amplitude for the thickness mode peaks. The data in Figures 7 and 8 suggest that, while the presence of platinum internal electrodes may interfere with the fundamental thickness mode resonance of soft piezoelectrics, they have little effect on the resonant properties of high Q_M materials.

The data in Figure 8 suggest that, while the presence of platinum internal electrodes may interfere with the fundamental thickness mode resonance of soft piezoelectric ceramics, they have little effect on the resonant properties of high Q_M materials.

The influence of internal electrodes on the frequency constant, N, of a piezoelectric resonator can be better understood from a consideration of the classical resonance equation:

$$N = f_r L = \frac{1}{2\sqrt{\rho \cdot S}} \tag{1}$$

where f_r is the fundamental resonant frequency, L the governing dimension, ρ the density and S the elastic compliance. In the thickness mode the alternate

ceramic and metal layers in an internally electroded device approximate closely
to a series-linked composite, the mean elastic compliance ($\bar{S}$) of which can be
estimated using the equation:

$$S = \frac{Pt_L \cdot Pt_S + PZT_L PZT_S}{Pt_L + PZT_L} \quad (2)$$

In the present devices, $PZT_L/Pt_L \approx 20$, $PZT_{S_{33}^E} = 13.9 \times 10^{-12} \, m^2 N^{-1}$ (6).
The average density for a composite containing four internal electrodes is 8.260
kg m^{-3} assuming densities of 7600 and 21500 kgm^{-3} for PZT and platinum respect-
ively. Hence the calculated frequency constant values are 1538 Hzm for the
plain 401-888 and 1497 Hzm for the internally electroded material, a difference
of only 2.7%. This difference is kept small because changes in the mean density
and mean elastic compliance values in equation (1) are of opposite sign, and
therefore compensate to some extent, and the thickness of the platinum layers
relative to the PZT layers is small. Hence it should be possible to employ a
wide range of internal electrode materials without affecting the fundamental
thickness mode resonance, by tailoring the densities, elastic compliances and
relative thicknesses of the ceramic and metal phases.

Piezoelectric Transformer

One resonant application in which internal electroding can be beneficial
is the piezoelectric transformer. Conventional piezoelectric transformers (7)
comprise a long thin piezoelectric ceramic bar, the primary end of which is
thickness poled, while the secondary end is longitudinally poled as shown in
Figure 9(a). When operated at the longitudinal mode fundamental resonance
frequency the secondary d_{33} piezoelectric coefficient is driven efficiently
by the primary d_{31} piezoelectric coefficient. The voltage step-up capability
is determined by the relative lengths of the poled regions and by the driving
and loading conditions (8).

In the present work an internally electroded primary has been employed to
obtain a significant improvement in step-up ratio over the conventional design.
The actual device configuration used is shown in Figure 9(b). The primary is
a nine internal electrode multilayer linked to a 401-888 PZT secondary by a
separate internally electroded region which acts as one of the secondary elec-
trodes. This arrangement is intended to provide increased secondary electrode
area, thus permitting more uniform poling and greater charge collection capacity
than is possible with the conventional secondary configuration. The overall

dimensions of the device are 15 x 6 x 1.5 mm and the operating frequency is approximately 100 kHz.

Figure 10 compares the voltage step-up ratio, and its variation with load resistance, for four types of transformer: (A) conventional, (B) conventional with high output secondary electrodes, (C) multilayer input/low output secondary electrodes, and (D) multilayer input/high output secondary electrodes. Data presented are for transformers of similar size driven at their fundamental resonant frequency, with the voltages measured peak-to-peak and the input peak voltage constant. In all the transformers an increase in voltage step-up ratio with increasing load resistance is seen. However, the transformers equipped with a multilayer primary have a greatly improved step-up ratio compared to those having a conventional input.

Conclusions

Platinum internal electrodes have been introduced in a multilayer configuration into commercial PZT formulations to form transducers capable of operation at greatly reduced voltages compared to conventional electromechanical devices. The presence of internal electrodes has been shown to have little effect on the electrical and resonant properties of the PZT materials. The internally electroded structures are produced by a tape casting technique which readily lends itself to the production of complex device configurations. As an example of the type of device for which internal electroding is particularly suitable, a multilayer input piezoelectric transformer has been built which shows improved voltage step-up characteristics compared to conventional designs.

The main advantages of internally electroded multilayer transducers over present devices can be summarized as follows:

1. The thin insulating layers in the multilayer device have high dielectric breakdown strength permitting the use of higher poling fields.

2. The multilayer devices can be driven at considerably lower voltages than conventional materials. Depending on the numbers of internal electrodes used, the operating voltage can be reduced by up to two orders of magnitude, thus greatly facilitating impedance matching.

3. The tape casting fabrication approach is highly versatile and allows the economical construction of complex devices.

References

1. R. Holland and E.P. Eernisse. Design of Resonant Piezoelectric Devices. Research Monograph No. 50, MIT Press, 1969, p. 89.

2. G. N. Howalt, R.A. Breckenridge and J.M. Brownlow. J. Amer. Ceram. Soc. 30:237-242 (1947).

3. W.D. Kingery. Introduction to Ceramics. 2nd Ed., John Wiley and Sons, 1976, p. 963.

4. Appendix

5. Appendix

6. A. Simmons and H. Wang. Single Crystal Elastic Constants and Calculated Aggregate Properties. 2nd Ed., MIT Press, 1971.

7. H.W. Katz. Solid State Magnetic and Dielectric Devices. John Wiley and Sons, 1959, Ch. 5.

8. W.B. Harrison and U. Beane. Relationship of Piezoelectric Properties to High Voltage Transformer Performance. Paper presented at American Ceramic Society Annual Meeting (Electronics Division), Dallas, 1973.

Table I

Specimen Configuration	Poling Conditions	K (1 kHz, low-field)	tan δ	d_{33} $CN^{-1} \times 10^{-12}$	$-d_{31}$ $CN^{-1} \times 10^{-12}$ (low field)	Q_M (Longitudinal mode)
501A plain	3000 KV m^{-1}	1800	0.015	470	240	21
501A sandwich	2 minutes	1550	0.015	450	240	31
501A multilayer*	100°C	1500	0.036	360	210	--
501A commercial data		2000	0.014	400	175	80
401-888 plain	2500 KV m^{-1}	936	0.002	295	--	397
401-888 sandwich	10 minutes	911	0.002	270	--	562
401-888 multi-layer*	125°C	794	0.003	210	--	--
401-888 commercial data		1000	0.003	215	95	1000

*Active area approximated
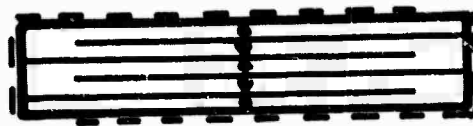
(a)

(b)

(c)

- - - - - EXTERNAL ELECTRODES

───── INTERNAL ELECTRODES

→ POLING DIRECTION
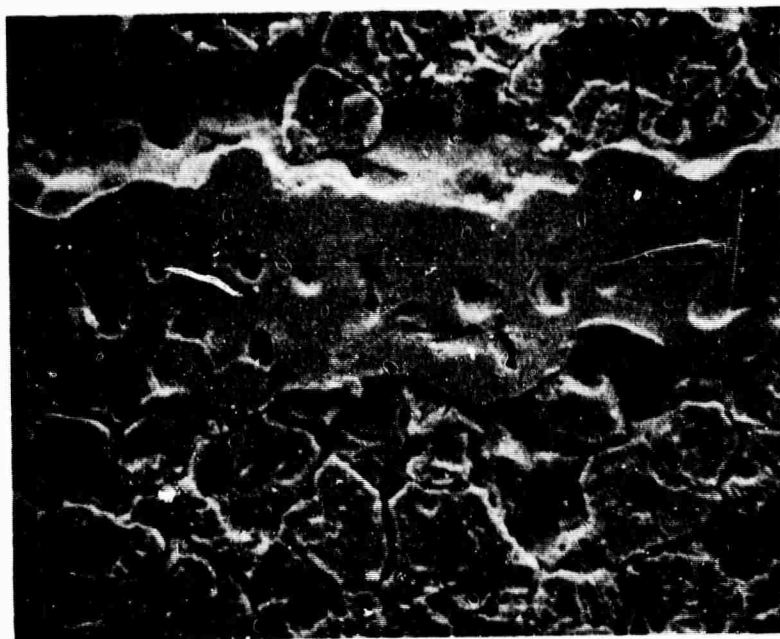
Fig. 1. Device configurations under investigation.
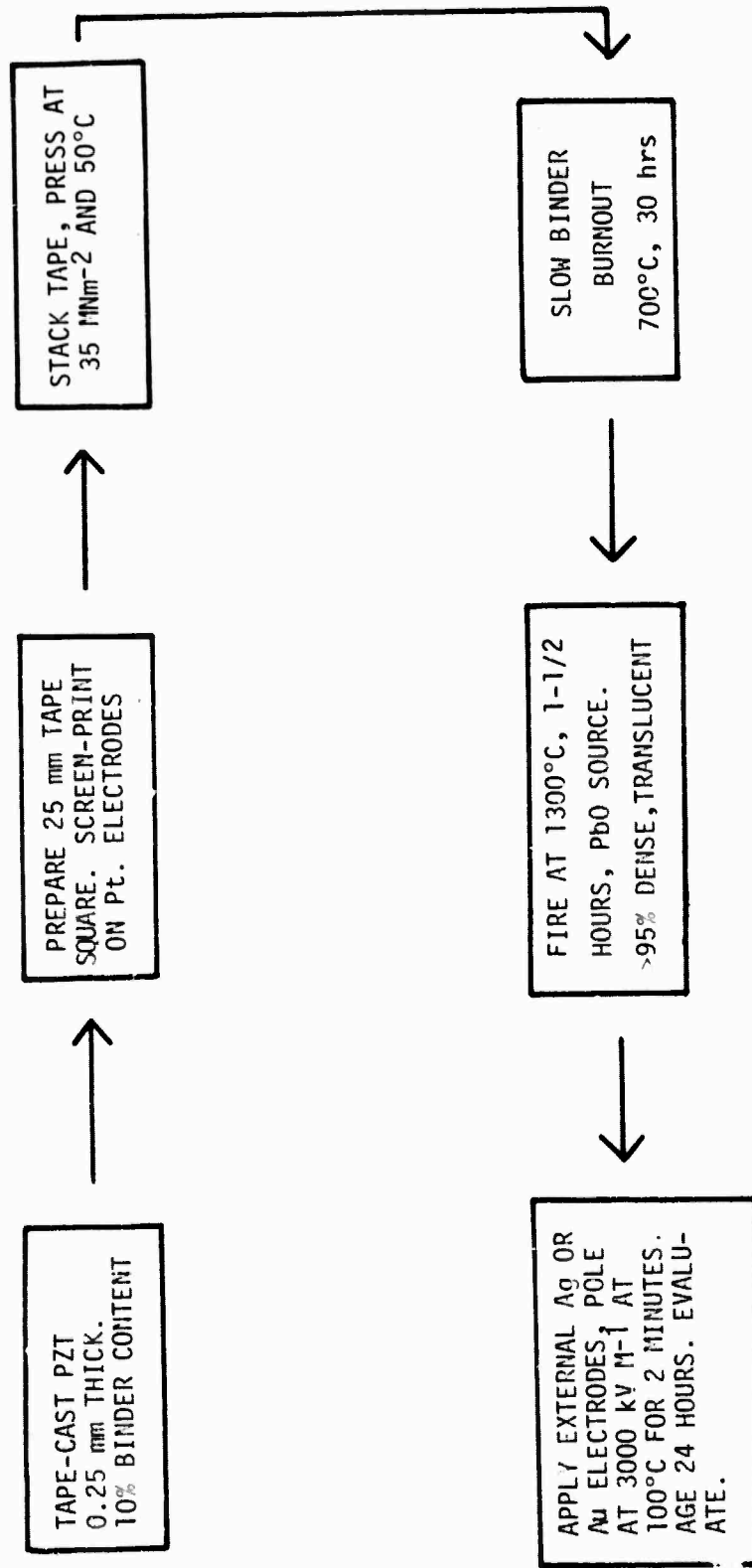
Fig. 2. Device fabrication route.

├─ 10 μm ─┤

Fig. 3. Micrograph showing a platinum electrode
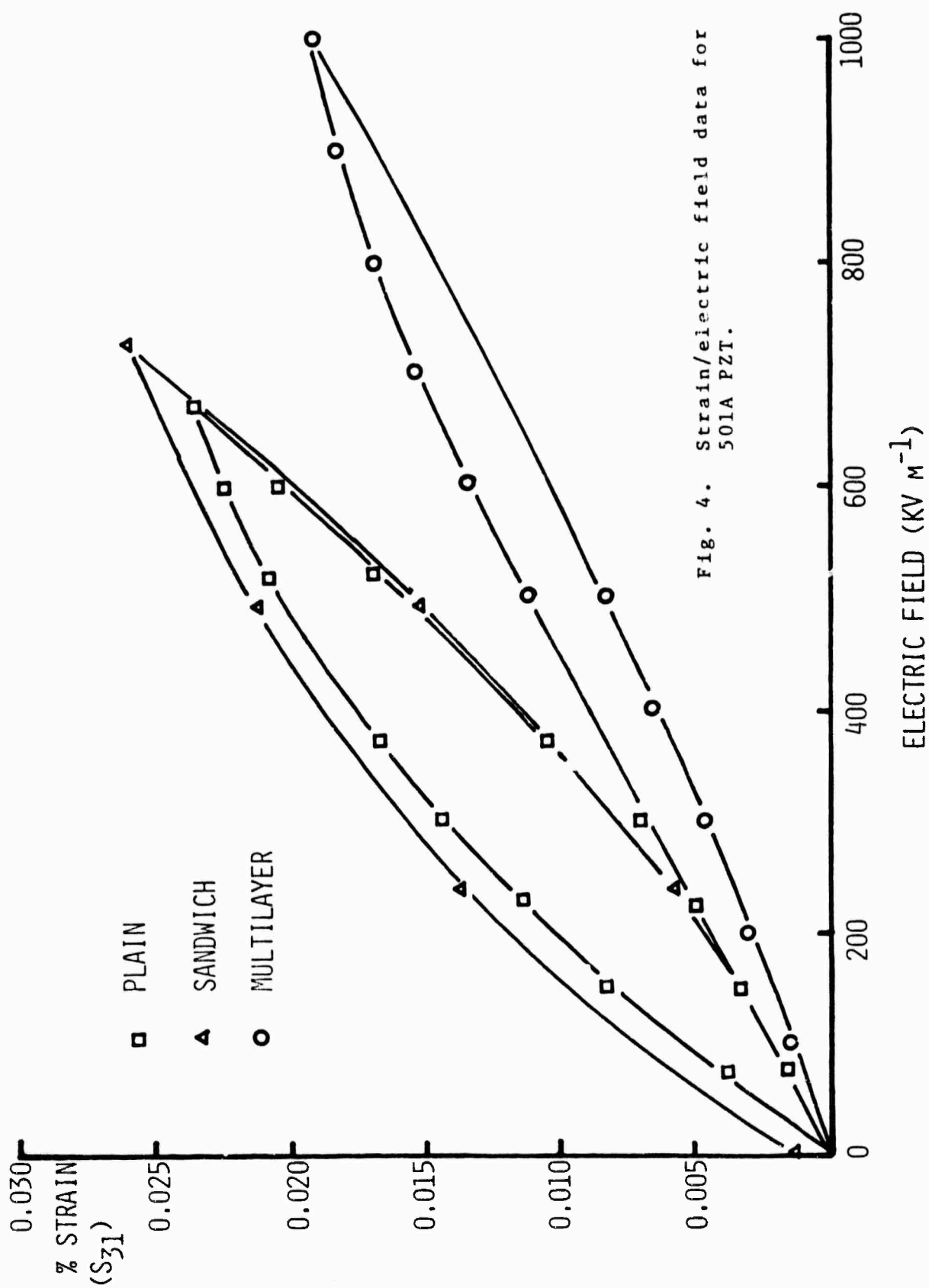in an internally electroded specimen.
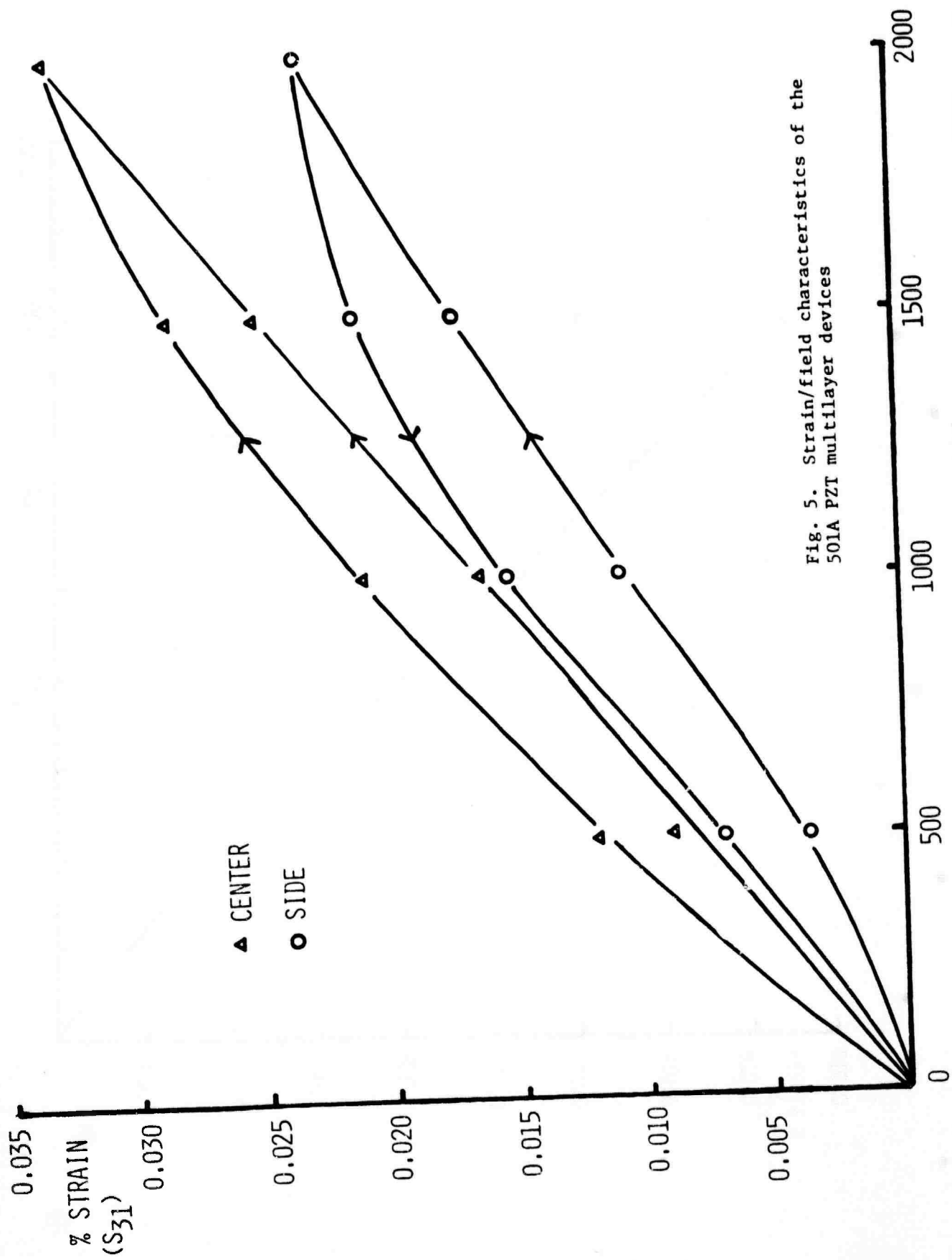
Fig. 4. Strain/electric field data for 501A PZT.

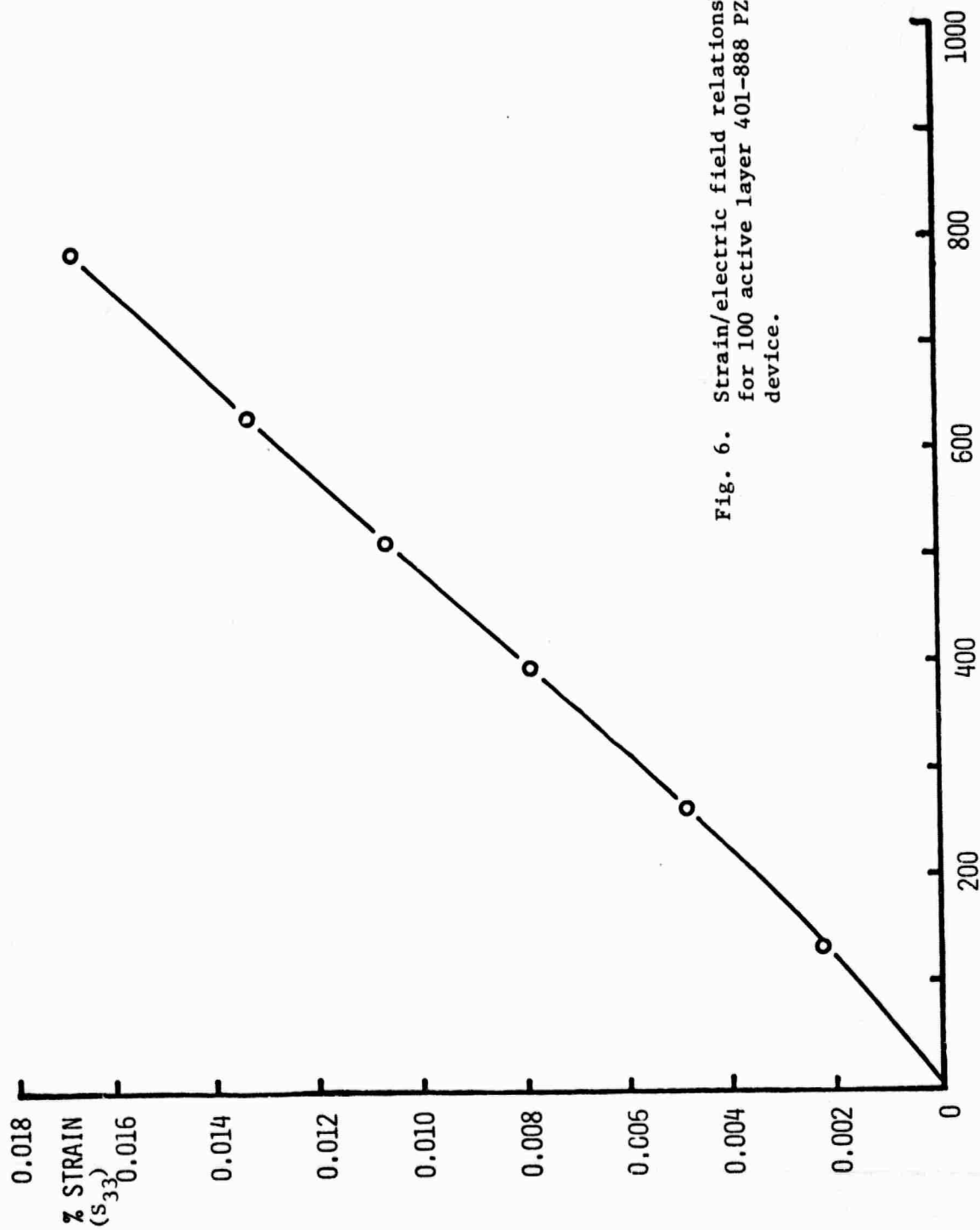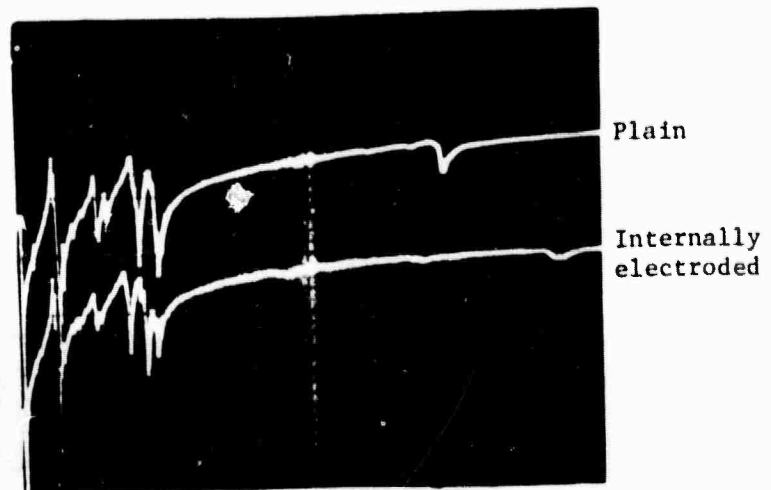Fig. 5. Strain/field characteristics of the 501A PZT multilayer devices
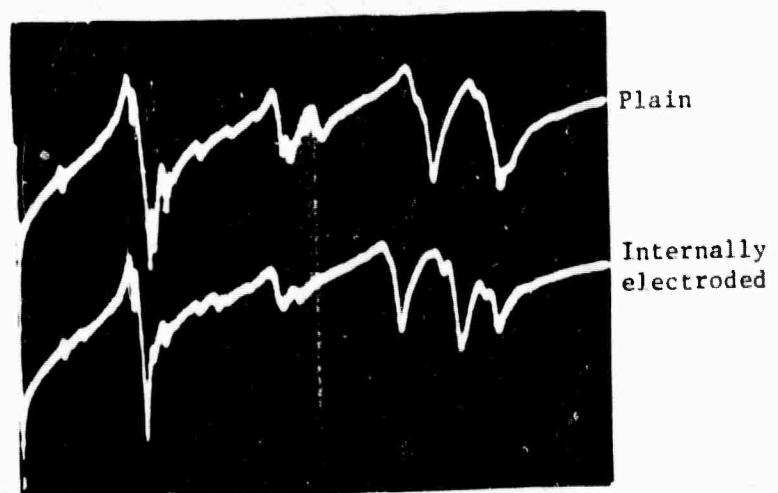
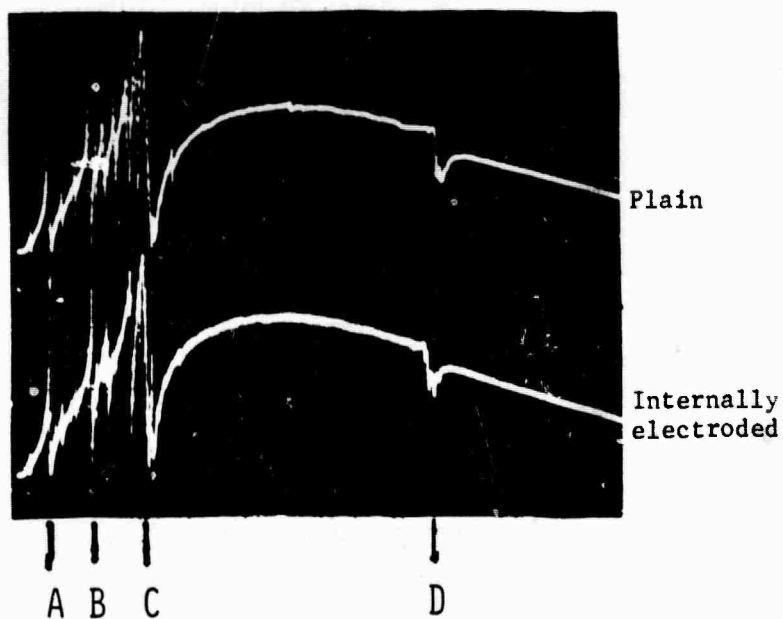Fig. 6. Strain/electric field relationship for 100 active layer 401-888 PZT device.

% STRAIN (s_{33})

0.018
0.016
0.014
0.012
0.010
0.008
0.006
0.004
0.002
0

0   200   400   600   800   1000

(a) Horizontal scale 1 MHz/div

(b) Horizontal scale 300 kHz/div

Fig. 7.   Resonance spectra for 501A PZT bars.

Plain

Internally electroded

A - Fundamental length mode

B - Fundamental width mode

C - Fundamental thickness mode

D - 3rd harmonic, thickness mode

Fig. 8.   Resonance spectra for 401-888 PZT bars.
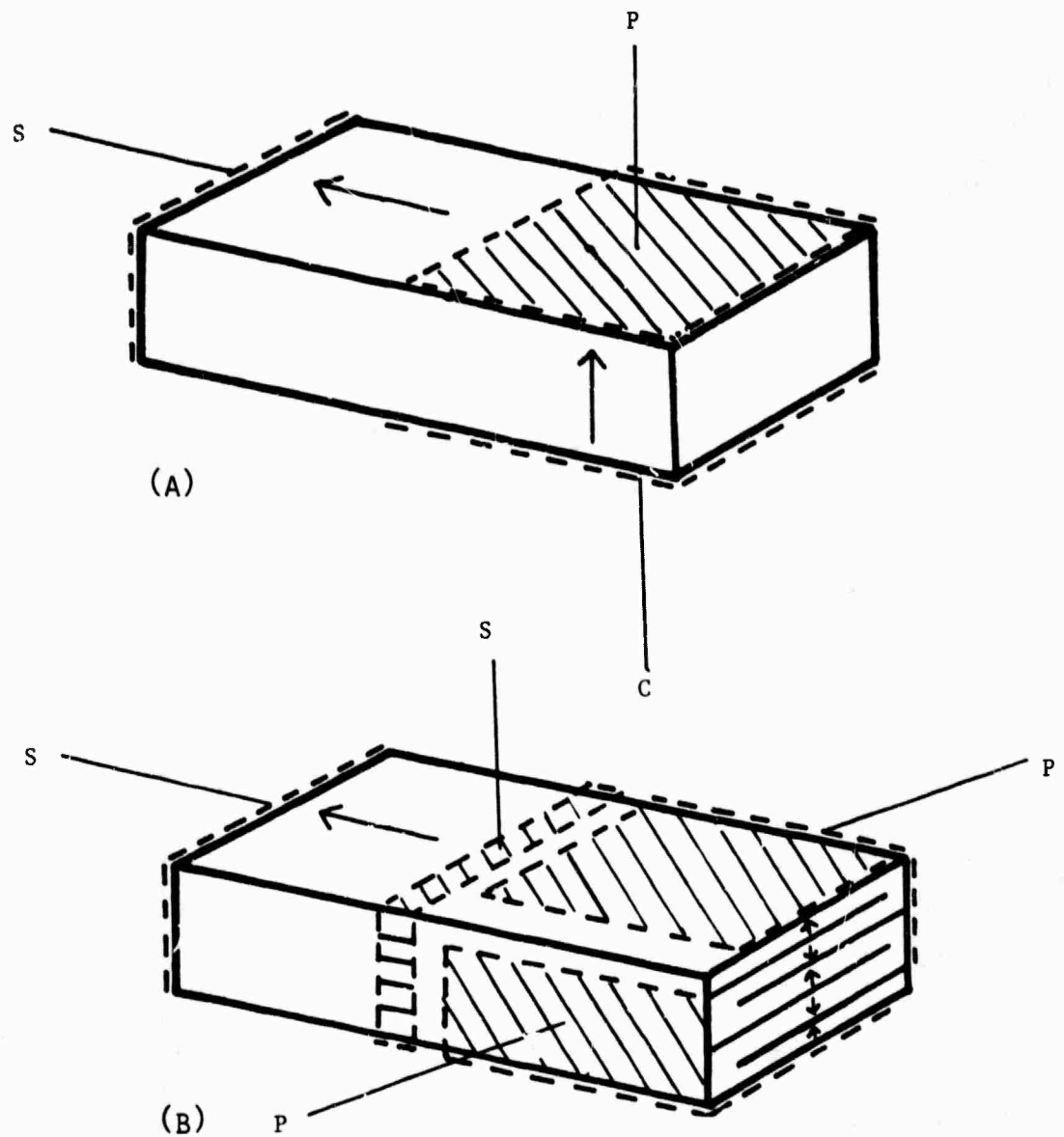Horizontal scale 1 MHz per div.

Figure 9. (a) conventional, (b) multilayer input/high output
transformer configurations.

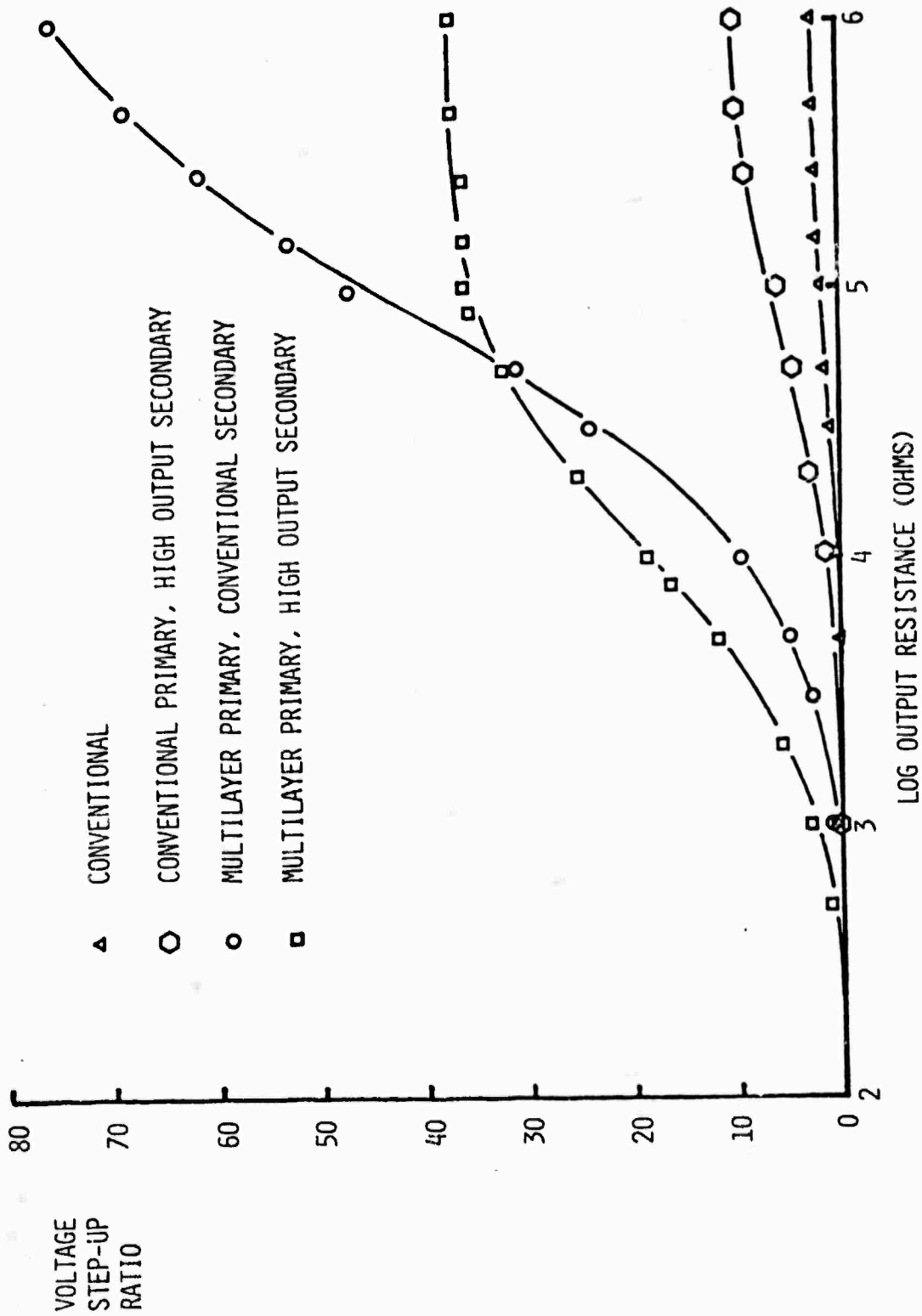P - Primary electrodes

S - Secondary electrodes

C - Common

Fig. 10. Transformer ratio as a function of load resistance for the various transformer configurations.

APPENDIX 7

Electromechanical Behavior of Antiferroelectric-Ferroelectric
Multilayer PZT Based Composites

T. Shrout, W.A. Schulze and J.V. Biggers

"Electromechanical Behavior of Antiferroelectric-Ferroelectric

Multilayer PZT Based Composites"

T. Shrout, W. A. Schulze and J. V. Biggers
Materials Research Laboratory
The Pennsylvania State University
University Park, Pennsylvania 16802

Abstract

Using a tape casting process, lamellar heterogeneous devices comprised of layers of a commercial soft ferroelectric (modified PZT) and an antiferroelectric (modified PZSnT) were produced. Such devices were found to behave in a similar way to that of a transpolarizer and to effectively stabilize the polarization in the soft material under high field cycling conditions.

Introduction

Extensive research has shown that when $Pb(Zr,Ti)O_3$ (PZT) ceramics are doped with various cations, specific electromechanical properties can be optimized, resulting in piezoceramics useful for device applications[1,2]. For example, the modification of $Pb(Ti,Zr)O_3$ ceramics by adding small amounts of Nb_2O_3 or La_2O_3 decreases the mechanical quality factor (Q) and the coercive field (E_c) and increases the electromechanical coupling factor and the volume resistivity. This type of ceramic is qualitatively referred to as "soft material" and is commercially used in microphones and phonograph pickups.

Conversely, $Pb(Ti,Zr)O_3$ ceramics modified with transition metal oxides, such as Fe_2O_3 and MnO_2, have a high mechanical quality factor and a high coercive field and are called "hard materials." Such ceramics are suitable for high-power ultrasonic transducers (e.g. sonic and ultrasonic cleaners) because of their stable polarization and low mechanical and dielectric losses under high field cycling[3].

The tremendous effort over the past two decades, optimizing piezoelectric properties, has led us to believe that further significant improvements cannot be made by compositional modifications alone.

Earlier references[4,5] have shown that specific electromechanical properties can be further improved upon by fabricating inhomogeneous ceramic devices.

In the work described here we have utilized the tape casting process[6] to fabricate devices with a structure that could lead to stability under high field drive conditions.

Heterogeneous Model Concept

Stabilizing the polarization may be achieved by using the electrical control concept of the transpolarizer[7]. In Fig. 1-b the transpolarizer is shown as two oppositely poled ferroelectric crystals in a series configuration. This combination behaves as a linear capacitor up to very high field levels and has been used to control the impedance level in electroluminescent ferroelectric display systems[8].

In Fig. 1-a, if both ferroelectric 'a' and 'b' are initially poled in the same direction as soon as the total voltage exceeds $2V_c$, where V_c is the coercive field for each crystal, then dipole switching can occur as each crystal will approximately drop V_c and experience a field sufficient for switching. If, however, 'a' is poled up, 'b' down as in a transpolarizer (Fig. 1-b), then when the applied voltage exceeds $2V_c$, 'b' will begin to switch. The current will try to flow through 'b' but 'a', being already fully switched in the + direction, cannot pass this current by switching and thus potential will build up across 'a' keeping 'b' always at V_c. Unless some alternative current path is provided, for example, by an alternative resistive path, 'b' cannot switch even for voltages $V_A \gg 2V_c$.

Using the aforementioned electrical concept, we propose to fabricate by tape casting a lamellar heterogeneous device composed of a "soft" ferroelectric (modified PZT) in series with an antiferroelectric (modified PbSnZT) of high critical field (antiferroelectric to ferroelectric switching field) (Fig. 1-c). During the poling operation 'a' layers (ferroelectric) will try to switch. However 'b' layers which are antiferroelectric cannot switch and field must build up across the 'b' layers until the point where the antiferroelectric to ferroelectric (AF-F) phase change can be forced. Only at this point can the soft ferroelectric pole. Once poled, displacement continuity

will hold the 'b' layers in the ferroelectric phase initially, but slowly over time the bound charge at the a-b interface will be replaced by true charges through conduction and phase 'b' will slowly relax back to the stable antiferroelectric condition.

For weak reversible fields such as those generated by the piezoelectric effect in 'a' layers the 'b' layers are chosen to have similar dielectric permittivity to 'a' and thus will not seriously attenuate the piezoelectric signal. For large cycling fields, or pulse depoling fields up to the transition field in 'b' layers no depolarization (depoling) will be possible due to the transpolarizing effect. Thus by suitably selecting an antiferroelectric with a very high critical field, it should be possible to fabricate piezoelectric devices with stability superior to that of present homogeneous "hard" materials.

Experimental

Sample Preparation

A commercial organic liquid suspension system* (binder) and PZT** powder were used to produce the tapes needed in fabricating the lamellar devices.

The composition $Pb_{.95}La_{.018}Ba_{.02}(Zr_{.60}Ti_{.10}Sn_{.30})O_3$, selected from Ref. (9) was reported to be ferroelectric below $\approx 10°C$ and antiferroelectric above. The room temperature dielectric permittivity (k) was given as ≈ 1100 an the critical field level was found to increase with temperature. Reacted powder was produced using mixed oxides calcined for three hours at 870°C. The calcined slug was then ground sufficiently to pass a 325 mesh sieve. Tapes approximately 10 mils thick were produced using a procedure as described in Ref. (10). A post casting pressing operation, also referred in Ref. (10) was used to increase the green density of the antiferroelectric tapes (≈ 3.1 g/cc) to that of the ferroelectric tapes (≈ 3.7 g/cc).

*Claydon Binder B-62, Lot 117, Cladon Inc. 11404 Sorrento Valley, San Diego, CA 92121.

**Ultrasonic Powder PZT-501A, Ultrasonic Powders, Inc. 2383 S. Clinton Ave. South Plainsfield. NJ 07080.

One-inch squares of each composition were stacked and laminated in homogeneous "monolithic" and heterogeneous model configurations. Monolithic configurations consisted of layers of similar compositions and they were used as comparative standards. The heterogeneous model consisted of layers of anti-ferroelectric tape in series with layers of ferroelectric tape (50/50 v/o). To prevent possible interaction and diffusion between the two compositions an internal Pt barrier electrode was used. This was achieved by silk screening PT ink on the green PZT tape prior to lamination. The devices consisted of between 4 and 8 layers. The multilayers were heated slowly to 700°C over a 30-hour period to remove any organic binder materials. Sintering was done in closed high purity alumina crucibles. The multilayer tapes were placed on Pt foil and a small amount of lead zirconate was added as a source of PbO. A silicon carbide resistance furnace with a programmable controller was used, the heating rate being 200°C/hr with a soak temperature of 1310°C for a period of one hour. The samples were allowed to cool in the furnace with power off.

The fired samples were found to be at least $\simeq$ 95% theoretically dense as determined by water displacement.

Measurements

Electromechanical properties were measured on the fired monolithic and antiferroelectric/ferroelectric multilayers (designated AF/F multilayer). A control model was formulated to best describe mathematically the proposed heterogeneous model (Fig. 1-c) for use as a comparative standard. It consisted of individual fired antiferroelectric and ferroelectric multilayers, mechanically and electrically jointed in series by silver electrode paste.

Electromechanical properties were also measured on monolithic multi-layers fabricated from a typical "hard" PZT powder (Ultrasonic PZT-401).

Electrodes of sputtered on gold and air-dry silver were placed parallel to the layers. Dielectric permittivity and loss (tan δ) as a function of temperature were measured using an automatic capacitance bridge* at 1 kHz.

Displacement-field (DE) hysteresis loops were observed over a temperature range of -35 to 90°C, with a Sawyer Tower circuit, using various field levels at 60 Hz. A wide temperature range was used to observe the charge stability in the antiferroelectric and ferroelectric states.

Samples were poled in a stirred silicon oil bath at 90°C by applying a dc field at 30 KV/cm for at least two minutes. Such a field was also adequate to force the antiferroelectric/ferroelectric phase change allowing the "soft" PZT to pole in the AF/F multilayer samples. The completeness of poling was checked by measuring the piezoelectric d_{33} using a** Berlincourt d_{33} meter.

After aging for 24 hours the samples were cycled in a 90°C oil bath at various field levels for 1 minute. Piezoelectric d_{33} was found after each field application and was used as a measure of polarization stability.

Results and Discussion

Microstructure

A typical SEM micrograph of an antiferroelectric/ferroelectric multilayer can be seen in Fig. 2. The sharp contrast of the two different grain sizes at the Pt interface suggest that little interaction took place. A further check using an x-ray fluorescence unit (SEM Joel-50A†) indicated no diffusion of La, Sn, Ti, Pb or Pt species, within the detection limits of the unit. Further, no diffusion or interaction was found in regions without a Pt layer, indicating that a diffusion barrier was not required.

---

*Hewlett Packard (Model 4270A) Automatic Capacitance Bridge, Hewlett Packard 1-59-1 Yoyogi, Tokyo. Japan 151.
**Berlincourt (Model 3300) d_{33} meter, Channel Products Inc. 16722 Park Circle Dr Chagrin Falls, Ohio 44020.
†Kevex-ray (Model 3203-50), Kevex-ray. 898 Mattler Rd., Burlingame, Ca. 94010. JEOL-50A SEM, JEOL Ltd, Tokyo, Japan.

Electromechanical Data

DC hysteresis loops indicated that the modified PZSnT composition was ferroelectric below room temperature, with the loop pinching off at around 25°C. No sharp ferroelectric to antiferroelectric transition was observed.

Typical DE loops for the "soft" ferroelectric, antiferro-electric and AF/F multilayer samples, and control model, at 90°C, are shown in Figs. 3a-d. D. E. loop data for samples at -35°C, 35°C, and 90°C are found in Table 1. The phases present at the various temperatures are also reported. The critical field level (E_f) for the antiferroelectric was found to increase with temperature as expected. The highest reported value was at 90°C, thus the reason 90°C was chosen for the polarization stability (depoling) investi-gation.

In Table 1 it can be seen that the AF/F multilayer model and control model configurations had lower ferroelectric polarizations (P_f) than either monolithic antiferroelectric or "soft" PZT ferroelectric samples. One would expect the value of P_f for an antiferroelectric/ferroelectric multilayer to be at least that of the lower of the two individual compositions. It is believed that the low reported values could be the result of improper elect-rode adhesion inducing error in the area term used in calculating the polar-ization (P_f).

Dielectric permittivity and piezoelectric d_{33} data are reported in Table 2. It was found that the k and d_{33} values, along with the D.E. loop data, for the AF/F multilayers were found to be quite similar to that of the control model and that both were in good agreement with the predicted values (k and d_{33}) calculated from series connection equations[4].

Figure 4 shows the effect of piezoelectric d_{33}, that of poled samples with field cycling. Rapid depolarization in the "soft" ferroelectric was found to occur at relatively low fields, with the "hard" (PZT-401) ferro-electric being able to withstand appreciable field levels before significant depoling occurred.

Clearly shown was the ability of both the AF/F multilayers model and control model samples to withstand extremely high depoling (driving) fields, up to 24 Kv/cm, significantly higher than for the "hard" ferroelectric.

Note, however, samples used in the depoling study were aged only 24 hours and that well aged samples, especially "hard" materials, may be considerably more stable[3].

Summary and Conclusions

In this work, it was shown that a lamellar heterogeneous device, comprised of a "soft" PZT ferroelectric and an antiferroelectric (modified PZSnT) could be fabricated by the use of a tape casting process.

Further, such a device utilized the electrical control concept of a transpolarizer to effectively stabilize the polarization in the soft ferroelectric material.

By selecting a temperature (90°C) at which the antiferroelectric had a high critical field level (E_f) it was shown that proposed model devices (AF/F multilayer and control model) were dielectrically more stable (harder) under high field cycling, than a typical commercially used hard PZT (under low aging conditions).

References

1. B. Jaffe, W.R. Cook, Jr. and H. Jaffe, Piezoelectric Ceramics (Academic Press, London and New York (1971).

2. J. Randeraut and R.E. Setterington (Ed.) Piezoelectric Ceramics (N.V. Philips Giocilampentabricken, Eindhoven, The Netherlands, 1974)

3. K. Carl and K.H. Härdtl, "Electrical After-Effects in Pb(Ti,Zr)O_3 Ceramics," Ferroelectrics 17, 473-486 (1978).

4. D.P. Skinner, R.E. Newnham and L.E. Cross, "Flexible Composite Transducers," Mat. Res. Bull. 13, 599-607 (1978).

5. R. Lapek, "Multilayer Ceramic Capacitors," U.S. 3,549,415, Dec. 1970.

6. J.C. Williams, Treatise on Materials Science and Technology. Edited by F.Y. Wang, Vol. 9, Ceramic Fabrication Process, pp 173-198, Academic Press (1976).

7. C.F. Pulvari, "An Improved Field-Controlled Polarization-Transfer Device and the Operating Features of the Exploratory Content Addressable Memory System," IEEE Trans. Electron Dev. ED-16, 6, 580-587 (1969).

8. G.W. Taylor, "The Design and Characteristics of a 1200-Element Ferroelectric-Electroluminescent Display," IEEE Trans. Electron Dev. ED-16, 6, 565-575 (1969).

9. B. Jaffe, "Research on Antiferroelectric Materials," Clevite Co. Tech. Rpt. No. 302490 (1962).

10. J.V. Biggers, T.R. Shrout and W.A. Schulze, "Densification of Tape Cast PZT," Am. Ceram. Soc. Bull. (in print, 1979).
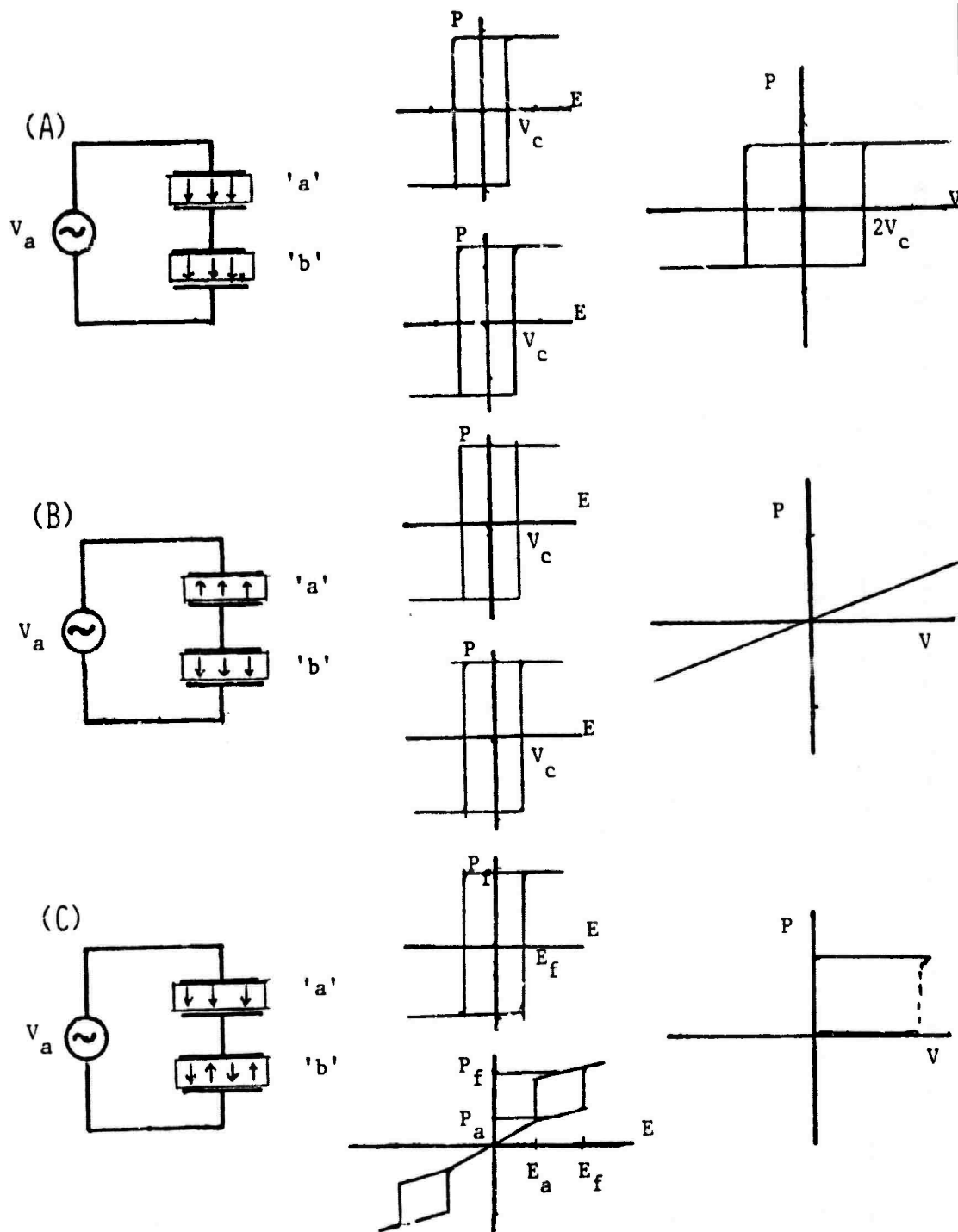
Fig 1. Two identically poled ferroelectric crystals 'a' & 'b' in
a series configura ion. (A) Ferroelectric crystals poled in
the same direction showing individual hysteresis loops and the
summation. ($2V_c$ = the sum of the individual coercive voltages
(B) Transpolarizer configuration using two oppositely poled
crystals in series resulting in a linear P.V. relationship up
to high field levels. (C) Antiferroelectric ('b') ferroelectr
('a') series configuration resulting in a stable polarization
field relationship. (P_f=polarization of ferroelectric state,
P_a = polarization of antiferroelectric before critical switchin
field (E_f), E_a= field for reversion to antiferroelectric state

Table 1. D. E. Hysteresis Loop Data for the Various Multilayer Configurations.

Sample	Temperature °C	Phase Present	E_f KV/cm	E_a KV/cm	P_f μC/cm²	P_a μC/cm²
'soft' ferroelectric (PZT-501)	-35 °C	ferroelectric	12.0		39.2	
antiferroelectric (PZSnT)		ferroelectric	11.5		32.9	
AF/F multilayer			11.4		28.5	
Control Model			12.6		29.4	
'soft' ferroelectric	35 °C	ferroelectric	8.0		45.0	
antiferroelectric (PZSnT)		antiferroelectric	16.5	-	39.5	-
AF/F multilayer			7.9	-	28.5	-
Control Model			13.0	-	32.9	-
'soft' ferroelectric	90 °C	ferroelectric	8.0		30.4	
antiferroelectric (PZSnT)		antiferroelectric	21.2	3.0	30.1	3.8
AF/F multilayer			13.7	2.6	23.4	3.9
Control Model			19.1	6.1	26.3	3.5

Table 2. Electromechanical Data for the Various Multilayer
Configurations.

Sample	Dielectric Constant $K_{25°C}$	Piezoelectric d_{33} (10^{-12}C/N)
'soft' ferroelectric	1700	350
'hard' ferroelectric	1000	225
antiferroelectric (PZSnT)	1160	0
AF/F multilayer	1300	135
Control Model	1420	145
Calculated *	1380[†]	142[††]

* K & d_{33} values calculated from series model equations[4].

[†] $1/K_{calc} = V_1/K_1 + V_2/K_2$, V_1 and V_2 are volume fractions and K_1 and K_2 dielectric constants for the ferroelectric and antiferroelec respectively.

[††]
$$d_{33} = \frac{V_1{}^1 d_{33} K_1 + V_2{}^2 d_{33} K_2}{V_1 K_2 + V_2 K_1}$$
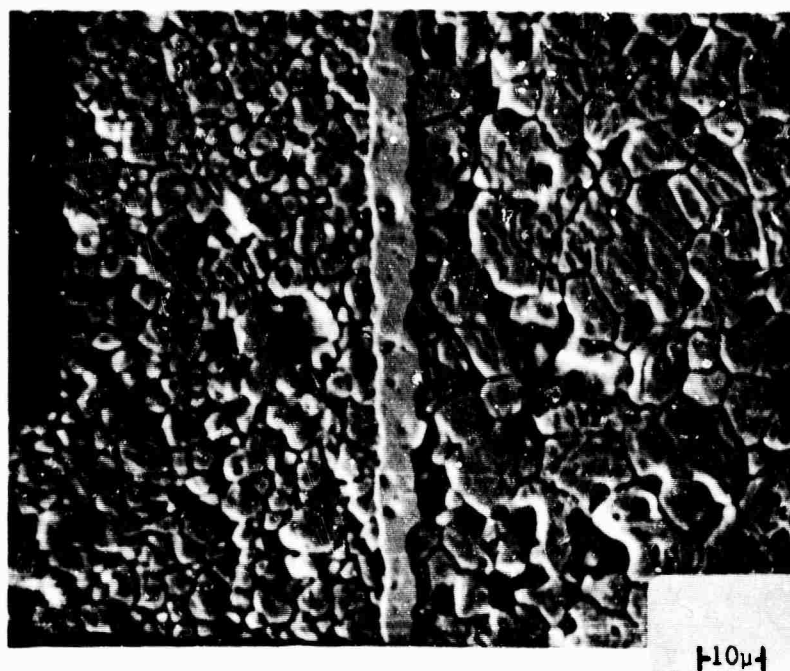
Fig. 2. Photomigrograph of an antiferroelectric (right)/ferroelectric (left) multilayer with platinum barrier electrode.
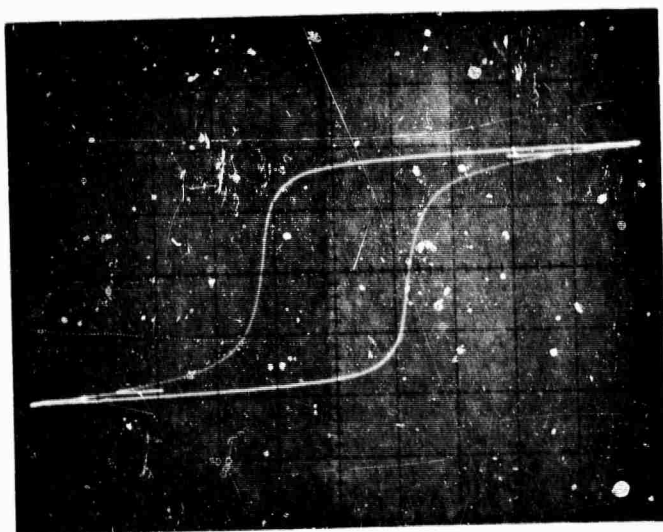
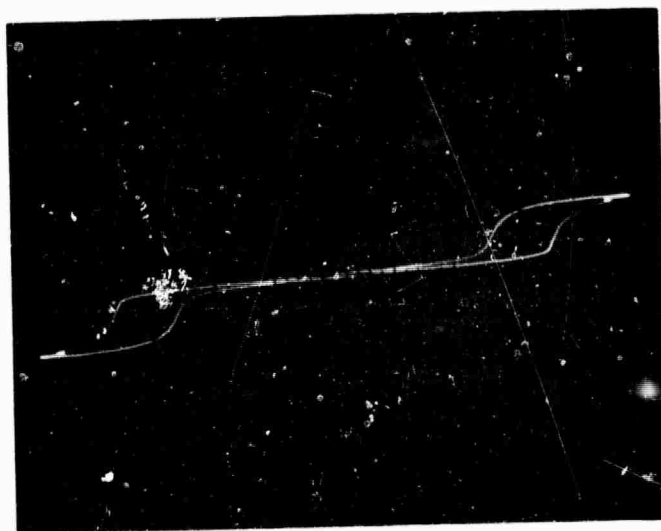Fig. 3a. DE hysteresis loop for "soft" ferroelectric at 90°C.

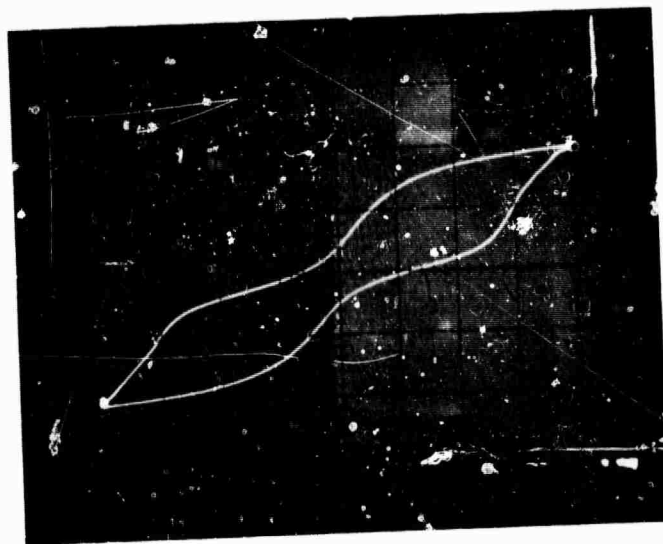Fig. 3b. DE hysteresis loop for antiferro-electric at 90°C.

Fig. 3c. DE hysteresis loop for antiferro-
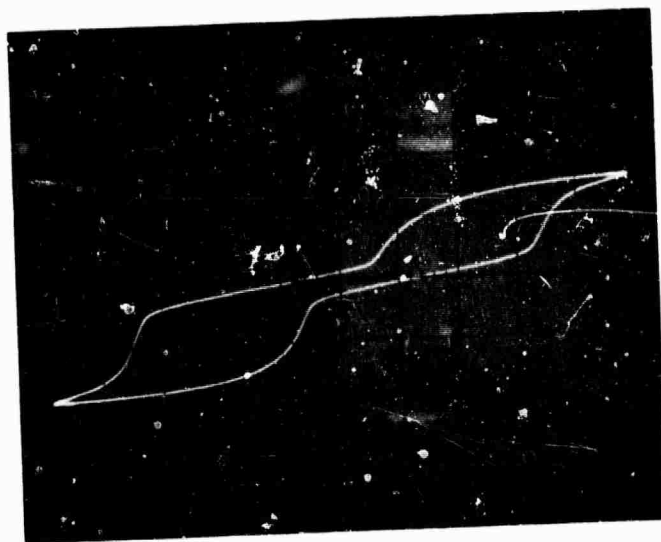electric/ferroelectric multilayer
at 90°C.

Fig. 3d. DE hysteresis loop for antiferro-
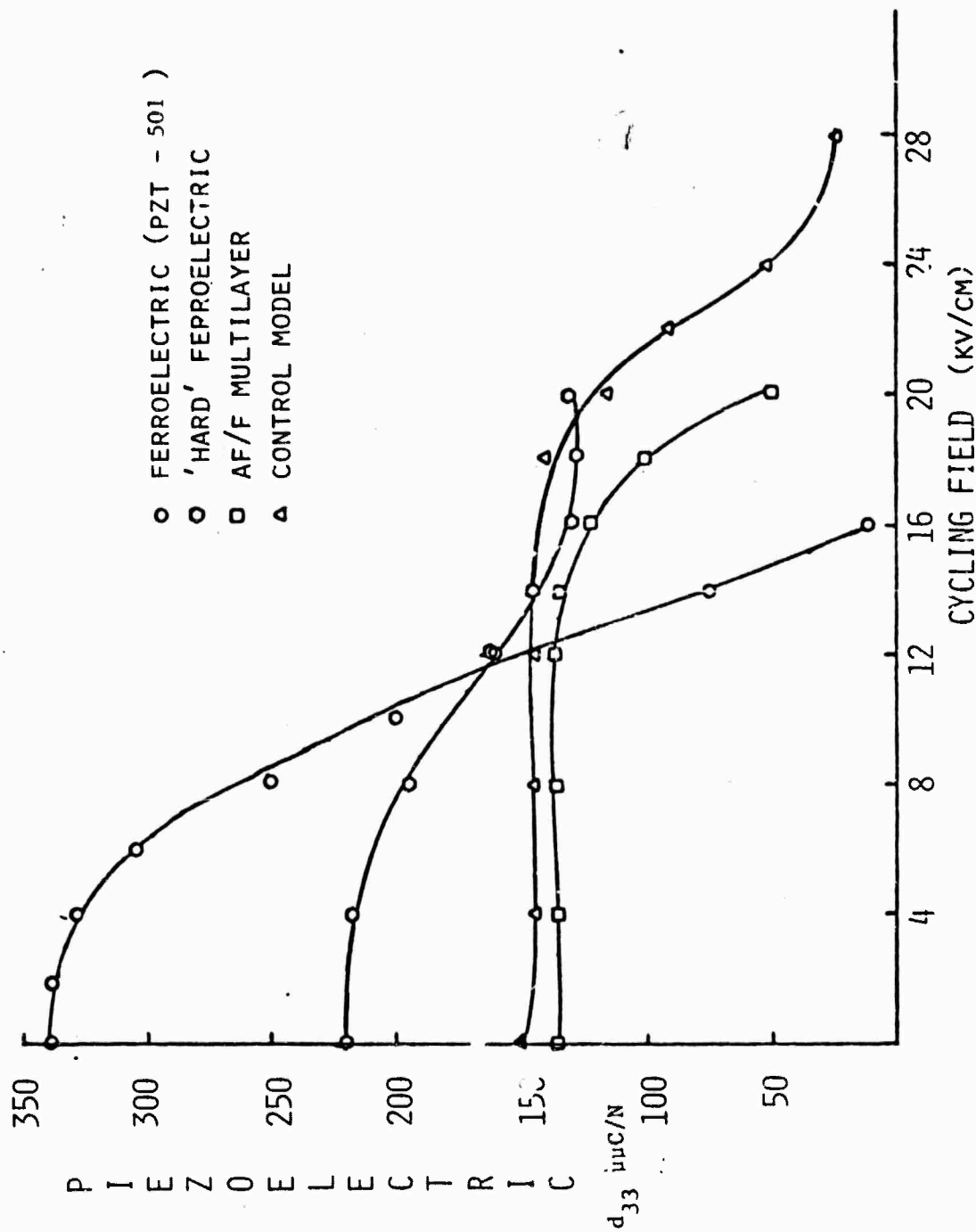electric/ferroelectric control
model at 90°C.

FIG 4. Piezoelectric d_{33} as a function of applied cycling field. (60 hz –1 min)

APPENDIX 8

A Phenomenolgical Gibbs Function for the $PbZrO_3:PbTiO_3$
Solid Solution System

A. Amin, B.A. Badger, Jr., H. McKinstry and L.E. Cross

A Phenomenological Gibbs Function for the $PbZrO_3$:$PbTiO_3$
Solid Solution System

A. Amin, B.A. Badger, Jr., H. McKinstry and L.E. Cross

Abstract

The ADAGE computer graphics system has been used to develop a
modified Devonshire form for the elastic Gibbs function to describe
the simple proper ferroelectric phases in the $PbZrO_3$:$PbTiO_3$ family
of crystalline solid solutions. The unusual morphotropic phase
boundary between tetragonal and rhombohedral forms has been used
to help delineate the coefficients in the function at that composi-
tion. For the Devonshire formulation, spontaneous strain in the
ferroelectric phases is assumed to be electrostrictive in origin
and an x-ray determination of the strains as function of composition
and temperature has been used to derive the composition and tempera-
ture dependence of the higher order stiffness coefficients. The
Gibbs function which has been derived permits the calculation of the
full family of thermal, elastic, dielectric, and piezoelectric para-
meters for the ferroelectric single domain states and an evaluation
of the manner in which these parameters change under different elastic
and electric boundary conditions.

A Phenomenological Gibbs Function for the $PbZrO_3$:$PbTiO_3$

Solid Solution System

I. INTRODUCTION

In many ferroelectric crystals it has often proven useful to correlate
the dielectric, piezoelectric, and elastic properties of paraelectric and
ferroelectric phases by phenomenological thermodynamic theory. The change
in the thermodynamic potential associated with the onset of the ferroelectric
phase is described through a Taylor series expansion in powers of the
order parameter (e.g. of the dielectric polarization in the simple proper
ferroelectric)and of the coupling parameters to other interesting thermodynamic
variables.

The permitted terms and coupling parameters are limited by the crystal
symmetry of the prototypic paraelectric structure, and the coefficients of
these terms are assumed to be continuous through any of the phase transitions
into and between ferroelectric phases.

For many crystals this Landau:Ginsburg:Devonshire formalism gives an
excellent semiquantitative description of the dielectric,elastic, piezoelectric
and electrothermal properties when only the lowest order terms are linearly
temperature dependent, higher order terms temperature independent and often
for a very truncated series expansion[1,2,3]. For a more accurate description
over a wider temperature range additional higher order terms, and/or tempera-
ture dependent higher order coefficients can be included[4,5].

In ferroelectric polycrystalline ceramics, a complete Gibbs function is
particularly valuable since often the mechanical and electrical boundary con-
ditions upon the individual crystallites are uncertain, and it is frequently
not clear whether "abnormal" properties are intrinsic and to be associated

with these boundary conditions, or are extrinsic and associated with such phenomena as domain and phase boundary motion. The situation can become particularly interesting when the ferroelectric is at a composition or temperature close to a ferroelectric:ferroelectric phase boundary where quite minor changes in the boundary stresses can give rise to major changes in the property tensors[6,7].

For materials where good single domain single crystals are available, the individual components of the property tensors can be measured over a wide temperature range, and the development of a suitable energy function is quite straightforward. In systems where only ceramic samples are available and good single crystals are unobtainable, the procedure is more complicated and must necessarily be indirect.

The lead zirconate:lead titanate (PZT) crystalline solution system is an excellent example where good single domain single crystal data are unavailable even for the ferroelectric end member ($PbTiO_3$). It is a system where the technological materials of most interest are grouped about a ferroelectric:ferroelectric transition (the so-called morphotropic phase boundary) and for which a representative Gibbs function could be of considerable use.

In the approach described in this paper, an ADAGE graphics computer and an IBM 370 computer have been programmed to solve the polynomial equations of the LGD treatment. The coefficients of the energy function, and their linear temperature derivatives are under dial control in the analogue section of ADAGE and the output is presented graphically as a ΔG:T diagram. The highly unusual feature of morphotropy (degeneracy between tetragonal and rhombohedral solutions of the function) has been used to distinguish the very limited set of coefficients which will reproduce this phenomenon.

Experimental data least likely to be strongly influenced by the ceramic character of the PZTs have been used to characterize the composition dependence

of the ΔG function and to permit a machine plotting of the full phase diagram for the single cell PZT compositions and of the dielectric, piezoelectric, and electrothermal characteristics of compositions in this phase region.

2. PHENOMENOLOGICAL ENERGY FUNCTION

The elastic Gibbs free energy for a simple proper ferroelectric derived from a prototypic phase of m3m symmetry may be expressed in the form[3].

$$
\begin{aligned}
\Delta G = {} & A(P_1^2 + P_2^2 + P_3^2) + B(P_1^4 + P_2^4 + P_3^4) + C(P_1^2 P_2^2 + P_2^2 P_3^2 + P_3^2 P_1^2) \\
& + D(P_1^6 + P_2^6 + P_3^6) + E(P_1^4(P_2^2 + P_3^2) + P_2^4(P_1^2 + P_3^2) + P_3^4(P_1^2 + P_2^2) \\
& + F P_1^2 P_2^2 P_3^2 + 1/2\, S_{11}(X_1^2 + X_2^2 + X_3^2) - S_{12}(X_1 X_2 + X_2 X_3 + X_3 X_1) \\
& - 1/2\, S_{44}(X_4^2 + X_5^2 + X_6^2) - Q_{11}(X_1 P_1^2 + X_2 P_2^2 + X_3 P_3^2) \\
& - Q_{12}(X_1(P_2^2 P_3^2) + X_2(P_3^2 + P_1^2) + X_3(P_1^2 + P_2^2)) \\
& - Q_{44}(X_4 P_2 P_3 + X_5 P_1 P_3 + X_6 P_1 P_2)
\end{aligned} \tag{1}
$$

where ABCDEF are simply related to the dielectric stiffness and higher order stiffness coefficients, S_{11}^P, S_{12}^P, S_{44}^P the elastic compliances, measured at constant polarization, Q_{11}, Q_{12}, Q_{44} the cubic electrostriction constants in polarization notation. The expression is complete up to all sixth power terms in polarization, but contains only fourth order terms in electrostrictive and elastic behavior.

The first partial derivatives of the energy with respect to the components of P, X, and T give the electric field E_i, the negative of the strain $-x_{ij}$, and the entropy change $- S$ respectively.

$$
\frac{\partial \Delta G}{\partial P_1} = E_i \text{ (a)}, \quad \frac{\partial \Delta G}{\partial X_i} = -x_i \text{ (b)}, \quad \frac{\partial \Delta G}{\partial T} = -S \text{ (c)} \tag{2}
$$

Appropriate second partial derivatives give the dielectric stiffness, elastic compliances and piezoelectric constants

$$\frac{\partial^2 \Delta G}{\partial P_i \partial P_j} = \chi_{ij} \text{ (a)} \quad \frac{\partial^2 \Delta G}{\partial X_i \partial X_j} = -S_{ij} \text{ (b)} \quad \frac{\partial^2 \Delta G}{\partial P_i \partial X_j} = -b_{ij} \text{ (c)} \tag{3}$$

The equations (2)a with $E_i \equiv 0$, taken together with the condition that (3) must have positive values give the conditions for stability of the spontaneously polarized states. The four solutions of (1) which are of interest for the PZT family dielectrics are

Cubic

$$P_S = 0 \text{ (a)} \qquad \Delta G = 0 \text{ (b)} \tag{4}$$

Tetragonal

$$P_S = \frac{-2B \pm (2B)^2 - 4(3D)A)^{1/2}}{6D} \quad \text{(a)} \quad \Delta G = AP_S^2 + BP_S^4 + DP_S^6 \quad \text{(b)} \tag{5}$$

Orthorhombic

$$P_S = \frac{-(2B+C) \pm ((2B+C)^2 - 4(3D+3E) A)^{1/2}}{2(3D+3E)} \quad \text{(a)}$$

$$\Delta G = 2AP_S^2 + 2(B+C)P_S^4 + 2(D+E)P_S^6 \quad \text{(b)} \tag{6}$$

Rhombohedral

$$P_S = \frac{-(2B+2C) \pm ((2B+2C)^2 - 4(3D+6E+F)A)^{1/2}}{2(3D+6E+F)} \quad \text{(a)}$$

$$\Delta G = 3AP_S^2 + 3(B+C)P_S^4 + (3D+6E+F)P_S^6 \quad \text{(b)} \tag{7}$$

where the coefficients A through F are continuous functions of composition and A, B and F are temperature dependent.

Spontaneous elastic strains in the ferroelectric single domain states under the conditions $X_i \equiv 0$ may be deduced from the equations 2(b) under the conditions $P_i = P_{Si}$ which lead to the relations

Cubic

$$x_1 = x_2 = x_3 = x_4 = x_5 = x_6 = 0 \tag{8}$$

Tetragonal

$$x_1 = Q_{11}P_1^2, \quad x_2 = x_3 = Q_{12}P_1^2, \quad x_4 = x_5 = x_6 = 0 \tag{9}$$

Orthorhombic

$$x_1 = x_2 = (Q_{11}+Q_{12})P_1^2$$
$$x_3 = 2Q_{12}P_1^2, \quad x_4 = x_5 = 0, \quad x_6 = Q_{44}P_1^2 \tag{10}$$

Rhombohedral

$$x_1 = x_2 = x_3 = (Q_{11}+2Q_{12})P_1^2 \tag{11}$$
$$x_4 = x_5 = x_6 = Q_{44} P_1^2$$

It may be noted that in (10) the strain system appears monoclinic as it is expressed with respect to the original cube axes (1,2,3), and that the strain tensor may be diagonalized by a 45° rotation in the 1,2 plane corresponding to the proper choice of orthorhombic axes.

Dielectric stiffnesses take the forms:

Cubic

$$\frac{1}{\chi_{11}} = \frac{1}{\chi_{22}} = \frac{1}{\chi_{33}} = 2A, \quad \frac{1}{\chi_{12}} = \frac{1}{\chi_{23}} = \frac{1}{\chi_{31}} = 0 \tag{12}$$

Tetragonal

$$\frac{1}{\chi_{11}} = 2A + 12BP_S^2 + 30DP_S^4$$
$$\frac{1}{\chi_{22}} = \frac{1}{\chi_{33}} = 2A + 2CP_S^2 + 2EP_S^4, \quad \frac{1}{\chi_{12}} = \frac{1}{\chi_{23}} = \frac{1}{\chi_{31}} = 0 \tag{13}$$

Orthorhombic

$$\frac{1}{\chi_{11}} = \frac{1}{\chi_{22}} = 2A + (12B+2C)P_S^2 + (30D+14E)P_S^4$$
$$\frac{1}{\chi_{33}} = 2A + 4CP_S^2 + 4EP_S^4, \quad \frac{1}{\chi_{12}} = 4CP_S^2 + 16EP_S^4, \quad \frac{1}{\chi_{23}} = \frac{1}{\chi_{31}} = 0 \tag{14}$$

<u>Rhombohedral</u>

$$\frac{1}{\chi_{11}} = \frac{1}{\chi_{22}} = \frac{1}{\chi_{23}} = 2A + (12B+4C)P_S^2 + (30D+28E+2F)P_S^4$$

$$\frac{1}{\chi_{12}} = \frac{1}{\chi_{23}} = \frac{1}{\chi_{31}} = 4CP_S^2 + 16EP_S^4 + 4FP_S^4 \tag{15}$$

and the piezoelectric polarization related b coefficient

<u>Cubic</u>

$$b_{ij} \equiv 0 \tag{16}$$

<u>Tetragonal</u>

$$b_{11} = 2Q_{11}P_1$$

$$b_{12} = b_{13} = 2Q_{12}P_1 \tag{17}$$

$$b_{26} = b_{35} = Q_{44}P_1$$

<u>Orthorhombic</u>

$$b_{11} = b_{22} = 2Q_{11}P_1$$

$$b_{12} = b_{13} = b_{21} = b_{23} = Q_{12}P_1 \tag{18}$$

$$b_{16} = b_{26} = b_{34} = b_{35} = Q_{44}P_1$$

<u>Rhombohedral</u>

$$b_{11} = b_{22} = b_{33} = 2Q_{11}P_1$$

$$b_{12} = b_{13} = b_{23} = b_{21} = b_{31} = b_{32} = 2Q_{12}P_1 \tag{19}$$

$$b_{15} = b_{16} = b_{26} = b_{24} = b_{35} = b_{34} = Q_{44}P_1$$

Thus if the temperature and composition dependence of the stiffness parameters are known, the full family of polarizations, dielectric, and piezoelectric properties of the single domain states can be determined.

3. COMPUTATION PROCEDURE

To give the observed Curie Weiss behavior of dielectric permittivity in the paraelectric phase, it is evident from equation (12) that the coefficient A must be a linearly increasing function of temperature passing through zero at the Curie Weiss temperature θ where A changes from negative to positive values. The temperature θ must be below the ferroelectric transition temperature (T_c). The A,B,C,... coefficients may be functions of both temperature and composition, but in any crystalline solution system, it is expected that the variation be smooth and continuous across the whole phase diagram.

Initial studies have suggested that even if the parameters A,B,C,D are given linear temperature dependence, a proper tetragonal:rhombohedral morphotropy cannot be developed from the simple Devonshire function (E=F=0). However, by adding a positive E parameter to destabilize the orthorhombic phase and a negative F parameter to restabilize the rhombohedral phase, tetragonal and rhombohedral phases can be made coincident over a wide temperature range without any interleaving orthorhombic region.

To permit ready visualization of the influence of the A $\rightarrow$ F parameters on the resulting phase stabilities, the ADAGE was programmed to operate in a split screen mode. The right-hand half of the screen plots ΔG_1 vs T for all possible stable phases. ΔG_1 is derived from a computer solution of the equations (5) and (7) which yield the appropriate values of P_1 at each temperature. On the ADAGE the A $\rightarrow$ F are under dial control and linear temperature coefficients can be added to either the parameters B or F. Markers are inserted at each of the intersections of the different phase stabilities, marking the equilibrium transition temperatures. This information on phase stabilities is then transferred to the left portion of the screen, the parameters A $\rightarrow$ F are incremented to new values under machine control and the process is repeated.

In this manner, a hypothetical phase diagram can be rapidly built up for any given initial choice of parameters and any chosen scheme of parameter increments. Since the starting values and progression increments are under analog control on the ADAGE system, new combinations can be "dialed" in at the start of each run and a wide range of parameter combinations can be tested in quite a short period.

Experience using this plotting program has confirmed our earlier expectations in that:

1. We cannot reproduce morphotropy with the simple Devonshire function.

2. In the Devonshire formalism, as expected, the parameter $\phi = C/2B$ controls the relative stability of tetragonal to orthorhombic and rhombohedral phases. However, the orthorhombic phase always interleaves or is degenerate with the rhombohedral.

3. To generate a near vertical tetragonal-rhombohedral boundary requires a positive value of E and a negative value of F.

4. For all parameter combinations which generate a near vertical (morphotropic phase boundary at Zr:Ti ratio $\sim$1:1) the orthorhombic phase is always very close to (but metastable with respect to) the overlapping tetragonal and rhombohedral stability curves.

Morphotropy has been obtained with the following parameters:

$$A = A_o(T-\theta), \quad A_o = 1/C\varepsilon_o$$

$$\phi = C/2B = -1.20 \text{ in PbZrO}_3 \text{ changing linearly with composition to}$$
$$+0.80 \text{ in PbTiO}_3$$

$$E = 80 \times \frac{8000}{\varepsilon_o}$$

$$F = 450 \times \frac{-45000}{\varepsilon_o} \quad \text{in PbZrO}_3 \text{ changing linearly with composition}$$

$$\text{to } 200 \times \frac{-20000}{\varepsilon_o} \quad \text{in PbTiO}_3$$

4. SCALING AND FINAL FITTING OF THE ENERGY PARAMETERS

Having developed a small family of dimensionless parameters which generate a sharp morphotropic change between rhombohedral and tetragonal phases, the task is to scale and refine the fitting so that it describes quantitatively the properties of real PZT compositions. For this purpose, it is clearly necessary to draw upon additional experimental data. It is desirable that in choosing the appropriate results care be taken in selecting those parameters and measurements which are least likely to be perturbed by the ceramic boundary conditions.

In this fitting we chose:

1. The composition dependence of the ferroelectric phase transition temperature (T_c).

2. The temperature dependence of P_S for a series of carefully characterized compositions across the tetragonal and the single cell rhombohedral compositions in the phase diagram.

There appears to be rather general agreement as to the nature of (1) with good accord between several sets of measurements by independent observers. For (2) it is not possible to measure P_S directly in these ceramic solid solutions. However, making use of equations (9) and (11) we may relate the spontaneous strains x_{11}, x_{22}, and x_{44} to the appropriate calculated values of P_S^2.

The strains x_{11}, x_{22}, x_{44} were determined by high temperature x-ray powder diffraction. Using the relations (9) and (11), P_S^2 was derived from the experimenta data and calculated and measured P values were fitted using θ, Q_{11}, Q_{12}, Q_{44}, and $P_S(T_c)$ as fitting parameters. It was very interesting to note that even

given complete lack of constraint, the required Q values do not change markedly with composition and that a good fitting of observed and calculated values can be obtained with composition independent Q parameters.

After adjusting the P_S, T_c, Q_{11}, Q_{22}, Q_{44} and θ parameters, recalculation of the phase diagram for the new T_c and θ values confirmed that minor changes had not significantly degraded the initial fitting of morphotropy, and a final trimming of the equations leads to the following parameter scheme.

To quantify the Gibbs function, it is necessary to select the scaling parameter χ_o. In materials with lower T_c values, this is readily accomplished by a direct measurement of the dielectric permittivity as a function of T above T_c in the paraelectric phase and a fitting to the Curie Weiss law.

For the PZTs, the high Curie temperatures lead to considerable difficulty and values of Curie constant have been reported ranging from 1.5 to 15 x 10^5. As in most ceramic systems where the Maxwell-Wagner phenomenon augments the "true" permittivity values, the highest frequency values are most representative of the crystallite permittivity and this suggests that the lower end of the range measured should be more representative. An alternative fitting method which becomes possible when the full energy function is delineated. Calorimetric data can then be used to scale the dielectric parameter.

5. COMPARISON OF EXPERIMENTAL AND CALCULATED PARAMETERS FOR PZT

5.1 Phase Diagram

The experimental phase diagram, made up from a wide sequence of experimental measurements by many different authors[3] is shown in Fig. 1. The region of interest which is accessible to the simple phenomenology involves the single cell compositions in the regions marked P_c, F_T, and $F_{R(HT)}$. Antiferroelectric orthorhombic and multicell rhombohedral $F_{R(LT)}$ phases cannot be discussed.

A first trial at the phenomenological fitting using a linear T_c vs composition to explore the possibilities of morphotropy is shown in Fig. 2. The final fitting using the parameters listed in the previous section is shown in Fig. 3, plotted over the experimental data for comparison.

For the region between 0.3 and 1.0 mole fraction $PbTiO_3$, the free energy as a function of composition is shown in Fig. 4 for temperatures of 25°C, 125°C, and 300°C. The crossover corresponding to the morphotropic phase boundary (MPB) is shown dotted on Fig. 4.

5.2 Spontaneous Polarization

Data are not available in the literature for P_S in any of the PZT compositions of interest. There are some single crystal values for pure lead titanate and one set of measurements of P_S vs T[9] summarized in Fig. 5. To give the trend of polarization in a wider range of compositions spontaneous strain was measured as a function of temperature for a number of well characterized powder samples. Compositions with tetragonal room temperature symmetry are summarized in Fig. 6 and rhombohedral compositions in Fig. 7. Fitting the equations (9) and (11) to these data, the values of the Q_{ij} required are shown in Fig. 8, and the θ and $(T_c-\theta)$ values in Fig. 9.

For this choice of parameters and with the constants chosen to generate morphotropy, the calculated polarization curves are given in Fig. 10 together with the "experimental" values derived assuming the pure electrostrictive origin of the phenomenon. From these curves the trend of P_S at 25°C as a function of composition across the phase diagram is depicted in Fig. 11.

5.3 Dielectric and Piezoelectric Single Domain Properties

Calculated single domain dielectric parameters for pure $PbTiO_3$ (Fig. 12), PZT 50:50 (Fig. 13), and PZT (60:40) (Fig. 14) have been derived. It should be noted that in these figures the susceptibility χ is almost identical to the

normal dielectric permittivity and that scales for values above and below T_c are different. The change in the room temperature components of χ calculated as a function of composition are shown in Fig. 15.

Piezoelectric constants d_{33}, d_{31}, and d_{15} are calculated as a function of temperature for pure $PbTiO_3$, and for PZT (50:50) in Figs. 16 and 17 respectively, and the corresponding temperature dependent g values g_{33}, g_{31}, and g_{15} are given in Figs. 18 and 19. Modifications of the room temperature d values as a function of composition at room temperature are depicted in Fig. 20 with the related g values in Fig. 21.

5.4 Hydrostatic Stress Dependence of the PZT Properties

One major reason for seeking a more complete phenomenological description of the PZT family of crystalline solutions is the possibility that it would offer to calculate the change in crystallite properties under changes of external boundary conditions such as must occur in the piezoceramics.

To give a concrete example, the influence of hydrostatic stress on the phase stability and properties has been derived for compositions close to morphotropy. The results will be given only in very brief outline here as more detailed work on both electrical and elastic boundary conditions is nearly completed and will be presented as a whole elsewhere.

In the calculations of phase stability and properties under 5.1 to 5.3 we have assumed that in equation (1) all $X_{ij} \equiv 0$. However, to derive new phase stabilities and new properties under any static stress system it is necessary only to substitute the appropriate X_{ij} values into equation (1) and to repeat the previous method of solution.

For a hydrostatic stress (hydrostatic tension or compression)

$$X_{11} = X_{22} = X_{33} = \sigma$$
$$X_{12} = X_{23} = X_{31} = 0$$

Choosing an appropriate value for σ, the first derivative equations

$$\frac{\partial \Delta G}{\partial P_1} = 0$$

are solved to give new values of the polarizations $P_{1(s)}$ under stress, which can be reinserted in the equation (1) to delineate the ΔG as a function of composition and temperature.

For compositions near morphotropy, the resulting energies at 0, 7, and 11 kbar pressure are shown in Fig. 22, and for 0, 7, 11, 15 kbar tension in Fig. 23. From data similar to these at many intermediate pressures, the variation of the composition at which morphotropy occurs, as a function of stress is given in Fig. 24.

Calculations have also been made of the shift of phase boundary at temperatures both above and below room temperature, and of the polarization, permittivity, and piezoelectric response under static compressions and tensions.

6. DISCUSSION

The agreement between experimental and phenomenological descriptions of morphotropy exhibited in Fig. 3 is obviously very good and has been achieved without any abrupt changes in the energy parameters. In fact the continuous linear variations chosen extend from $PbZrO_3$ to $PbTiO_3$. The Gibbs free energy difference between stable and metastable phases at the $PbTiO_3$ composition agrees well with that proposed by Henning and Hardtl[ ] on empirical grounds, though from our calculations the free energies themselves are not linear functions of the composition.

For the parameters chosen, the calculated polarizations agree quite well with those derived from spontaneous strain measurements though there is some evidence from the more rapid rise near T_c in the calculated data that the

series expansion is too rapidly truncated, or correspondingly that the tem-
perature coefficients on the highest order terms are too small. The electro-
striction constants derived in this analysis are comparable with the measured
constants for $PbTiO_3$ and as expected do not change significantly with compo-
sition across the whole phase diagram.

With the constant χ_o chosen to provide a good fitting with the available
thermal data, the calculated permittivity temperature curves are not unreason-
able, with values of the Curie Weiss slope being as expected towards the lowest
values measured in PZTs. At the lead titanate end of the composition system,
the high stability of the tetragonal phase is exhibited in the lower values of
transverse susceptibility (X_{11}). However, on approaching the morphotropic
phase boundary X_{11} begins to increase markedly. Calculated values for χ are,
however, still not much more than half the values usually measured even in
hard PZTs.

The behavior of the piezoelectric d and g coefficients again appears to
reflect the significantly lower dielectric polarizability of the single domain
state — the calculated g coefficients being on the whole slightly larger than
the measured values and the calculated d coefficients being small even for
very hard PZTs. Two explanations appear at present to be possible:

1. The higher dielectric polarizability in the ceramic is extrinsic,
with significant contributions from either domain or phase boundary motion,
even in the hard PZTs.

2. Present thermal data are inaccurate, and a smaller value of X_o is
required. Alternatively, higher frequency dielectric measurements on very
carefully characterized single phase PZT ceramics could be used to measure
directly the Curie Weiss slope in the paraelectric phase.

It seems very probable that both explanations may be partly responsible for the differences, but without more reliable experimental evidence it is difficult to adduce the level of correction required. Certainly with more modern calorimetry it should be possible to improve upon existing thermal data, and newer bridge and microwave methods should permit a clear evaluation of the dielectric response.

We hope that the ability which the present phenomenology affords to tie together all aspects of the thermo-elasto-dielectric behavior may provide the necessary incentive to accomplish these remaining tasks.

Comment on the influence of the elastic and dielectric boundary conditions on the phase diagram and the property responses will be reserved for a later paper.

References

1. Mueller, H. Phys. Rev. 47, 175 (1935); 57, 829 (1940); 58, 563 (1940); 58, 805 (1940).

2. Ginsburg, V. J. Exp. Theor. Phys. SSSR 15, 739 (1945).

3. Devonshire, A.F. Phil. Mag. 40, 1040 (1949).

4. Buessem, W.R., Cross, L.E., Goswami, A.K. J. Am. Ceram. Soc. 49, 33 (1966).

5. Goswami, A.K., Cross, L.E. Phys. Rev. 171, 549 (1968).

6. Cross, L.E. Phil. Mag. 7, 44 (1953).

7. Buessem, W.R., Cross, L.E., Goswami, A.K. J. Am. Ceram. Soc. 49, 36 (1966).

8. Jaffe, B., Cook, W.J., Jaffe, H. Piezoelectric Ceramics, Academic Press, London, p. 136 (1971).

9. Gavrilyachenko, V.G., Spinko, R.I., Martynenko, Fesenko. Soviet Phys. Solid State 12, 1203 (1970).

10. Henning, D., Härdtl, K.H. Proc. Int. Conf. Science of Ceramics, Baden Baden, W. Germany (1971).

LEGENDS FOR FIGURES

Fig. 1   Phase diagram for the crystalline solutions in the $PbZrO_3$:$PbTiO_3$
          System.

Fig. 2   Initial fitting to generate a morphotropic rhombohedral (R), tetra-
          gonal (T) phase boundary using a linear T_c vs composition.

Fig. 3   Superposition of experimental and phenomenological PZT phase diagrams.

Fig. 4   (a) Elastic Gibbs free energy as a function of composition across the
              the single cell region of the PZT phase diagram for three tempera-
              tures above room temperature.

          (b) Elastic Gibbs free energy as a function of composition across the
              single cell region of the PZT phase diagram for three temperatures
              below room temperature.

Fig. 5 P_S as a function of temperature for single crystal PbTiO3. Experimental
          points and phenomenological calculation.

Fig. 6   Spontaneous strain in PZT powder samples measured by high temperature
          x-ray powder diffraction for samples in the tetragonal phase field.

Fig. 7   Spontaneous strain as a function of temperature in powder samples of PZT
          measured by high temperature x-ray powder diffraction for samples in
          the single cell rhombohedral phase field.

Fig. 8   Values of the polarization related electrostriction constants Q_{11}, Q_{12},
          Q_{44} required to fit calculated and experimental polarization data
          across the PZT phase diagram.

Fig. 9   Values of the Curie Weiss temperature θ and the difference between Curie
          Weiss temperature and phase transition temperature T_c required to fit
          experimental and phenomenological P_S data across the PZT phase diagram.

Fig. 10 Calculated values of P_S at 25°C as a function of composition across the
          single cell compositions in the PZT phase diagram.

Fig. 11 (a) Comparison of calculated and "observed" polarization P_S as a
              function of temperature for several PZT compositions.

          (b) Calculated P_S vs T for several PZT compositions in the region
              below room temperature.

Fig. 12 Calculated dielectric susceptibility for pure $PbTiO_3$.

Fig. 13 Calculated dielectric susceptibility as a function of temperature in
          a 50:50 PZT.

Fig. 14 Calculated dielectric susceptibility as a function of temperature in
          a rhombohedral 60:40 PZT.

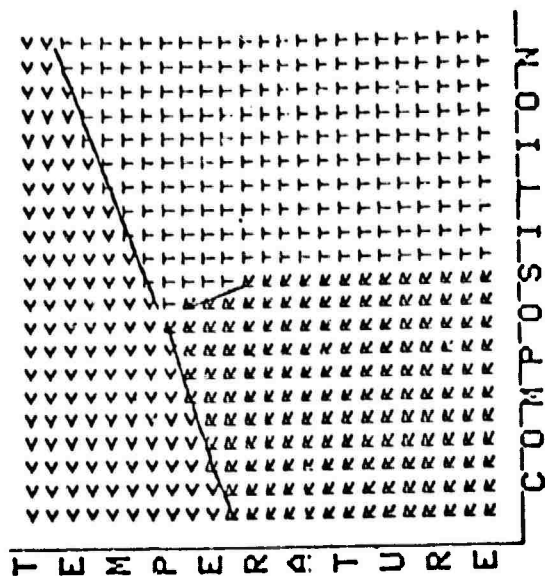Fig. 1. Phase diagram for the crystalline solutions in the PbZrO₃:PbTiO₃ (PZT) system.

Fig. 2. Initial fitting to generate a rhombohedral (R) tetragonal (T) phase boundary using a linear T_C vs composition.

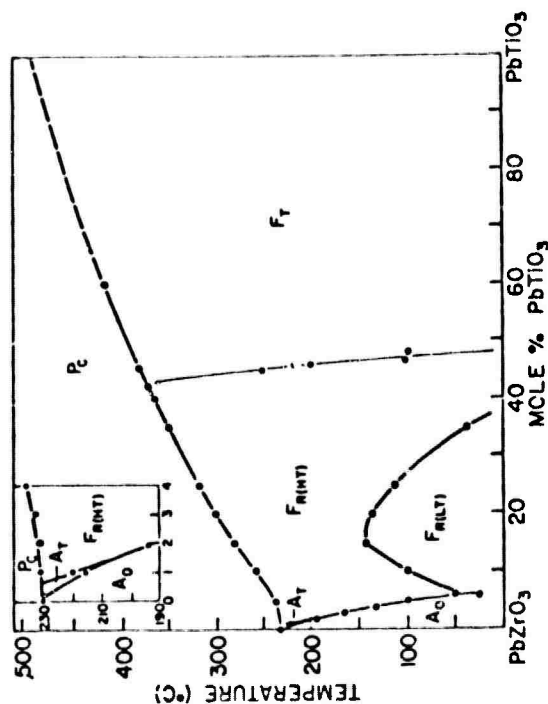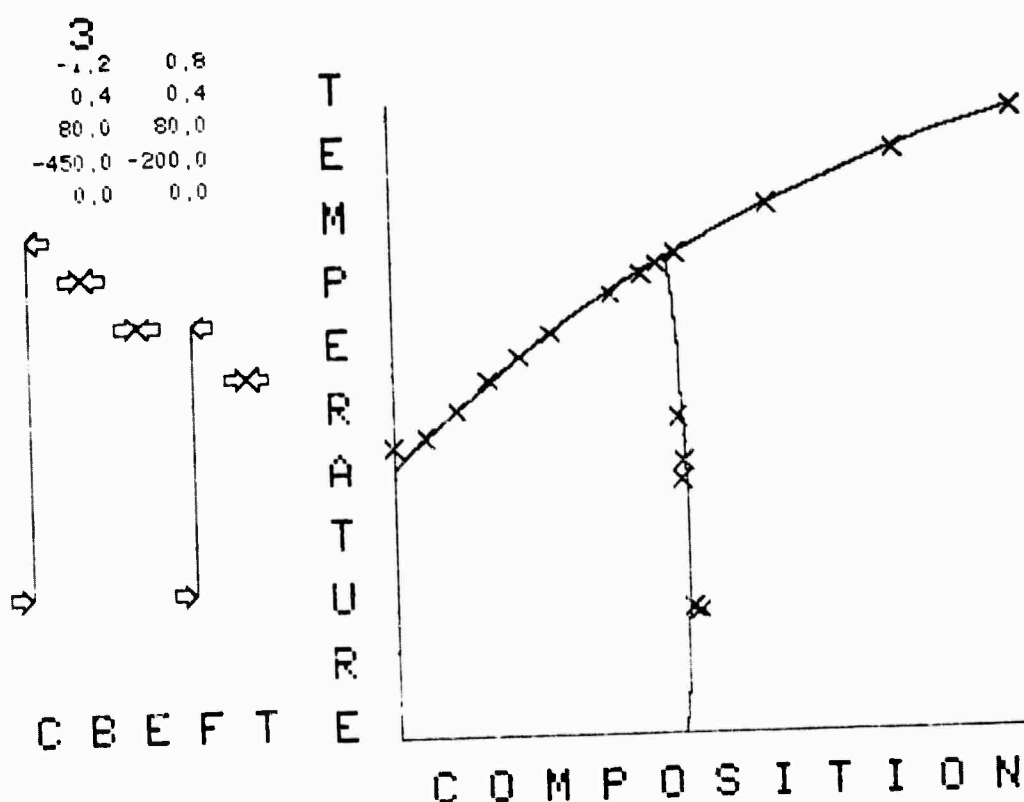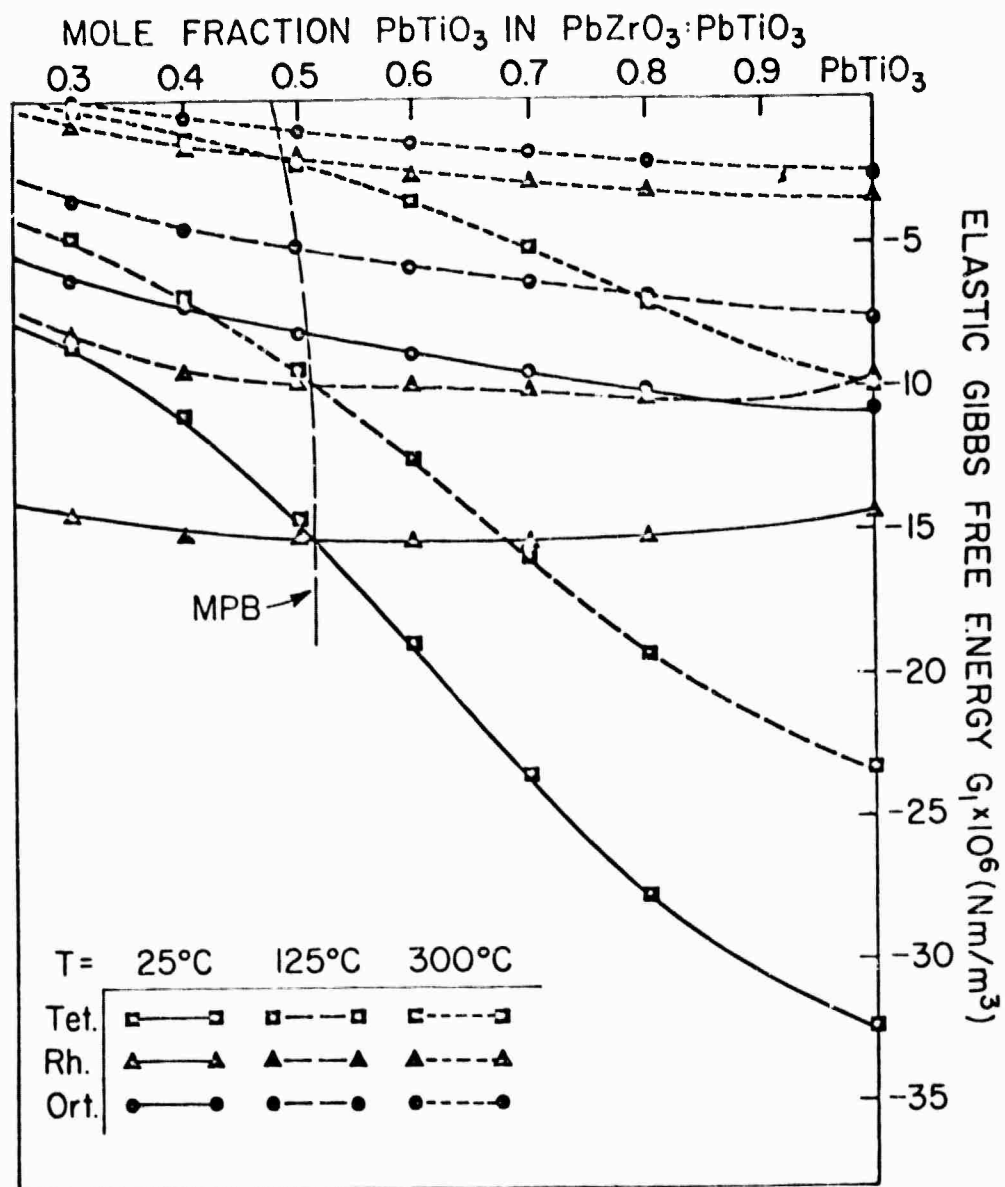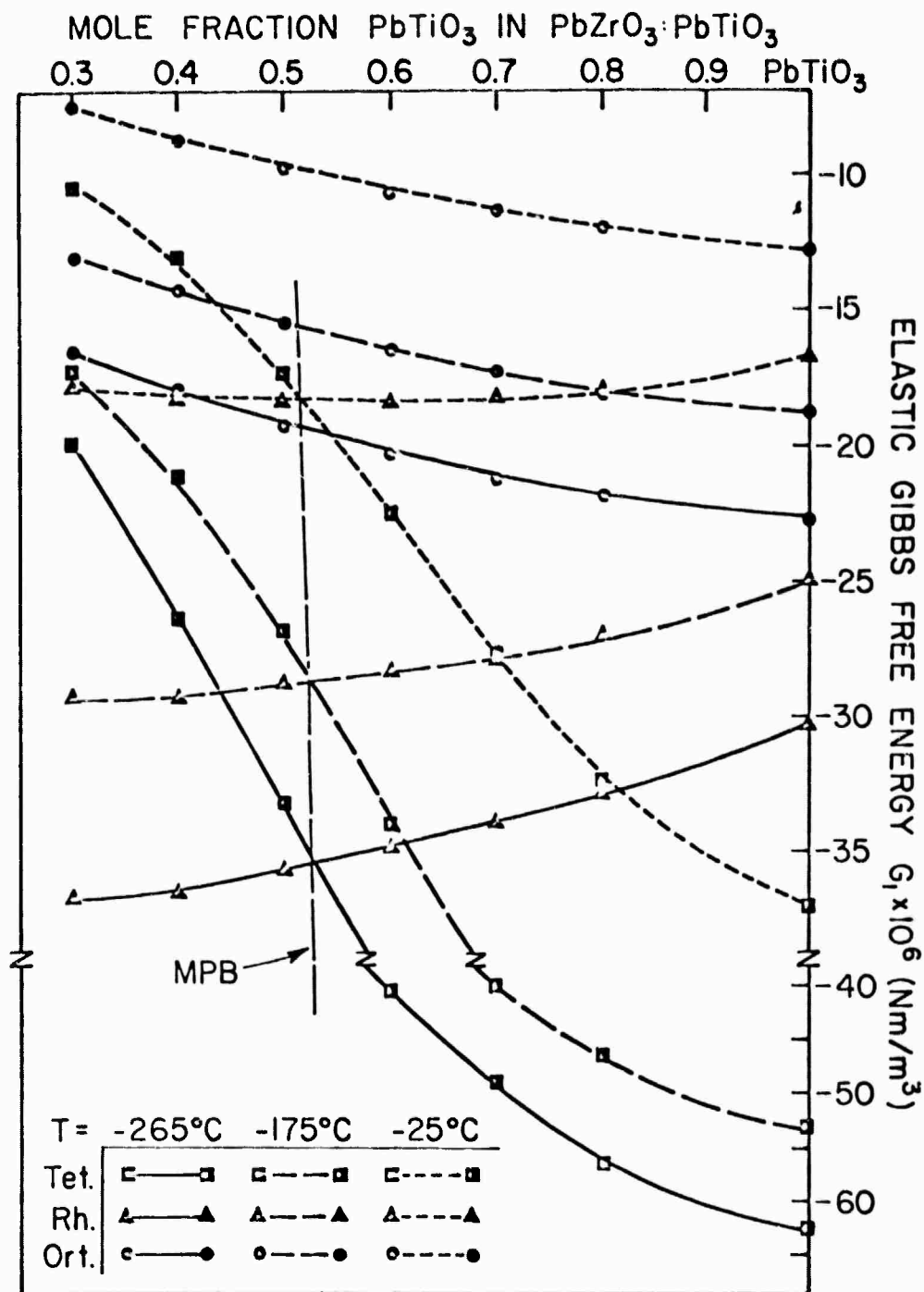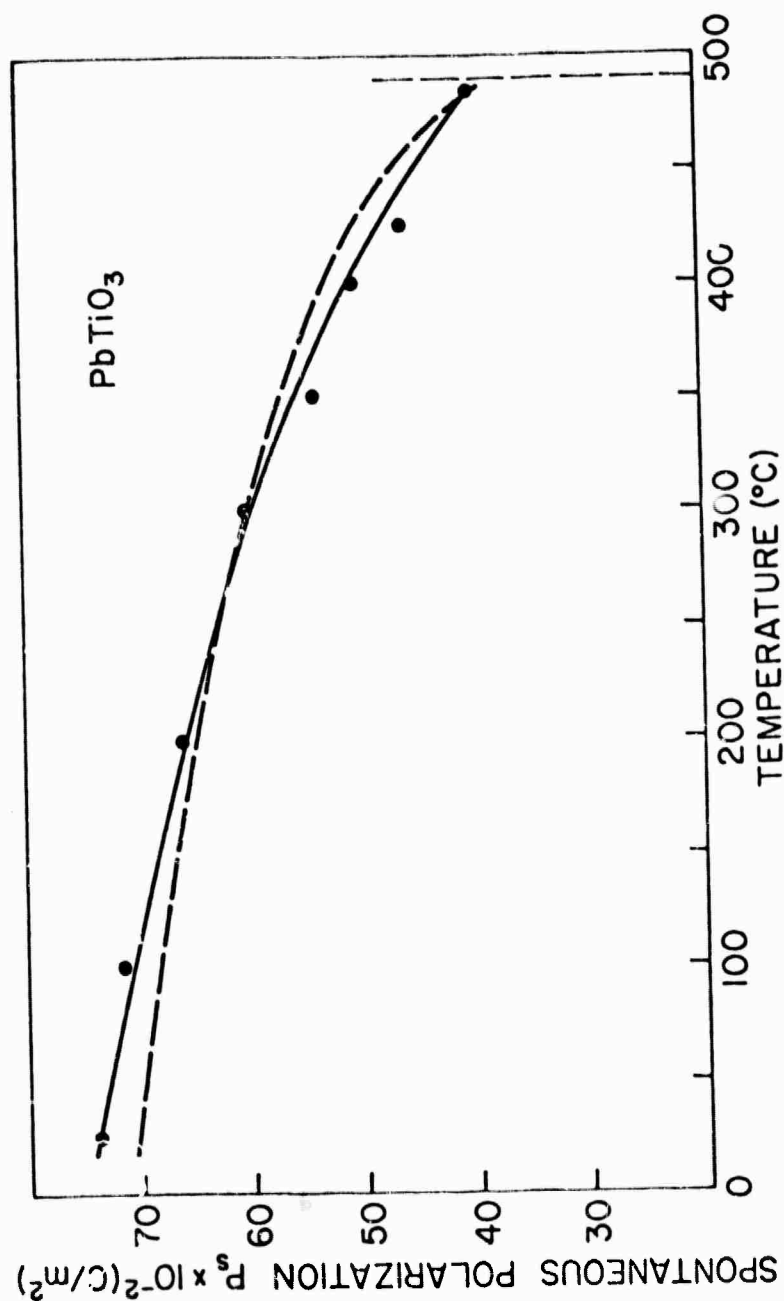Fig. 3. Superposition of experimental and phenomenological PZT phase diagrams.

Fig. 4a. Elastic Gibbs free energy as a function of composition across the single cell region of the PZT phase diagram for three temperatures above room temperature.

Fig. 4b. Elastic Gibbs free energy as a function of composition across the single cell region of the PZT phase diagram for three temperatures below room temperature.

Fig. 5. P_s as a function of temperature for single crystal $PbTiO_3$. Experimental points and phenomenological calcuations.

Fig. 6.   Spontaneous strain in PZT powder samples measured by
high temperature x-ray powder diffraction for samples
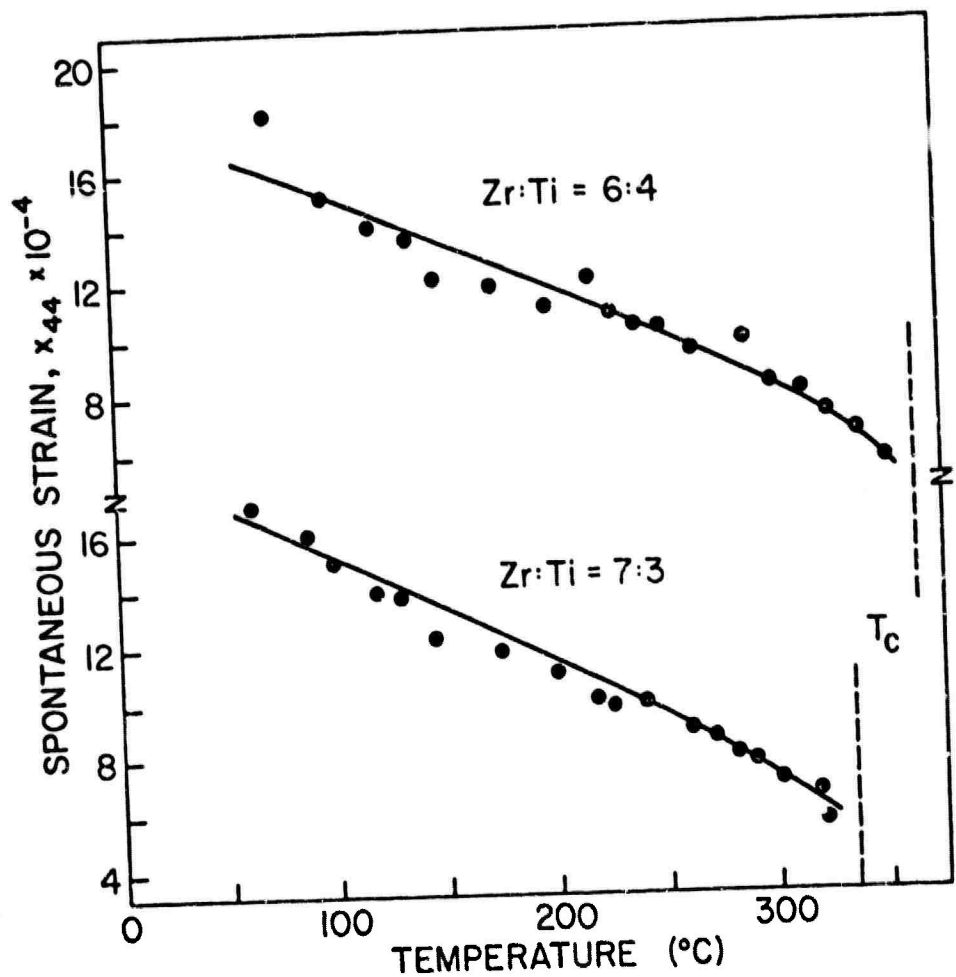in the tetragonal phase field.

Fig. 7.   Spontaneous strain as a function of temperature in powder samples of PZT measured by high temperature x-ray powder diffraction for samples in the single cell rhombohedral phase field.
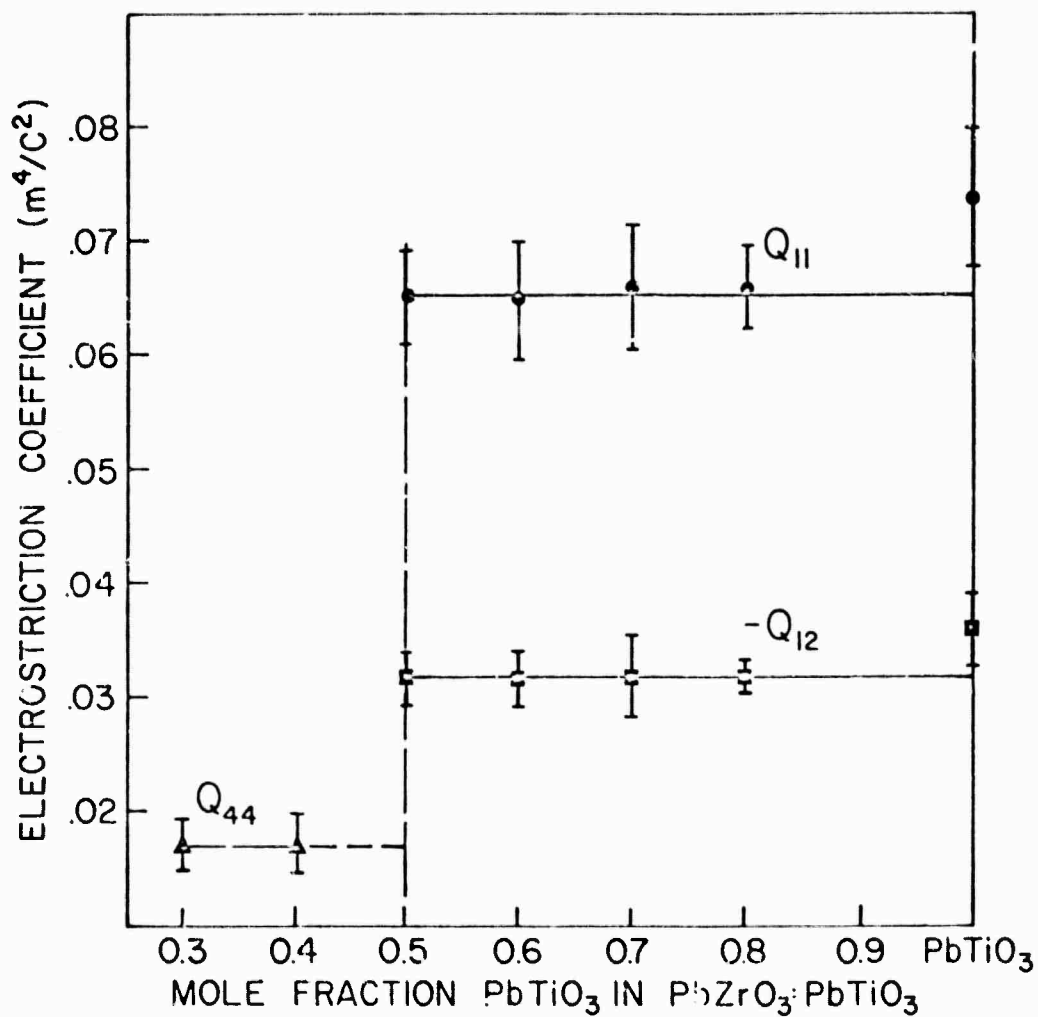
Fig. 8. Values of the polarization related electrostriction constants Q_{11}, Q_{12}, Q_{44} required to fit the calculated and experimental polarization data across the PZT phase diagram.
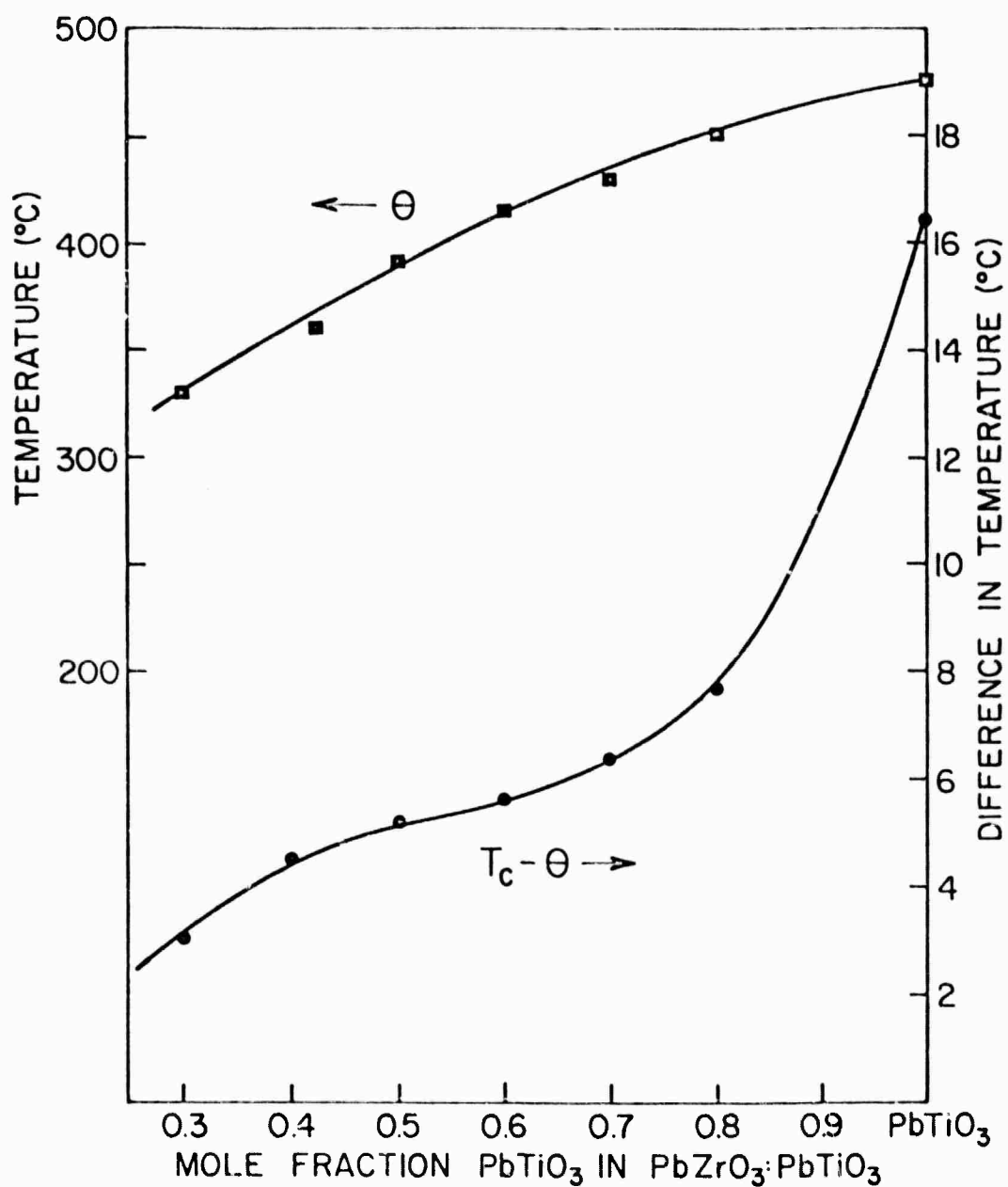
Fig. 9. Values of the Curie Weiss temperature θ and the difference between Curie Weiss temperature and phase transition temperature T_c required to fit experimental and ...enomenological P_S data across the PZT phase diagram.
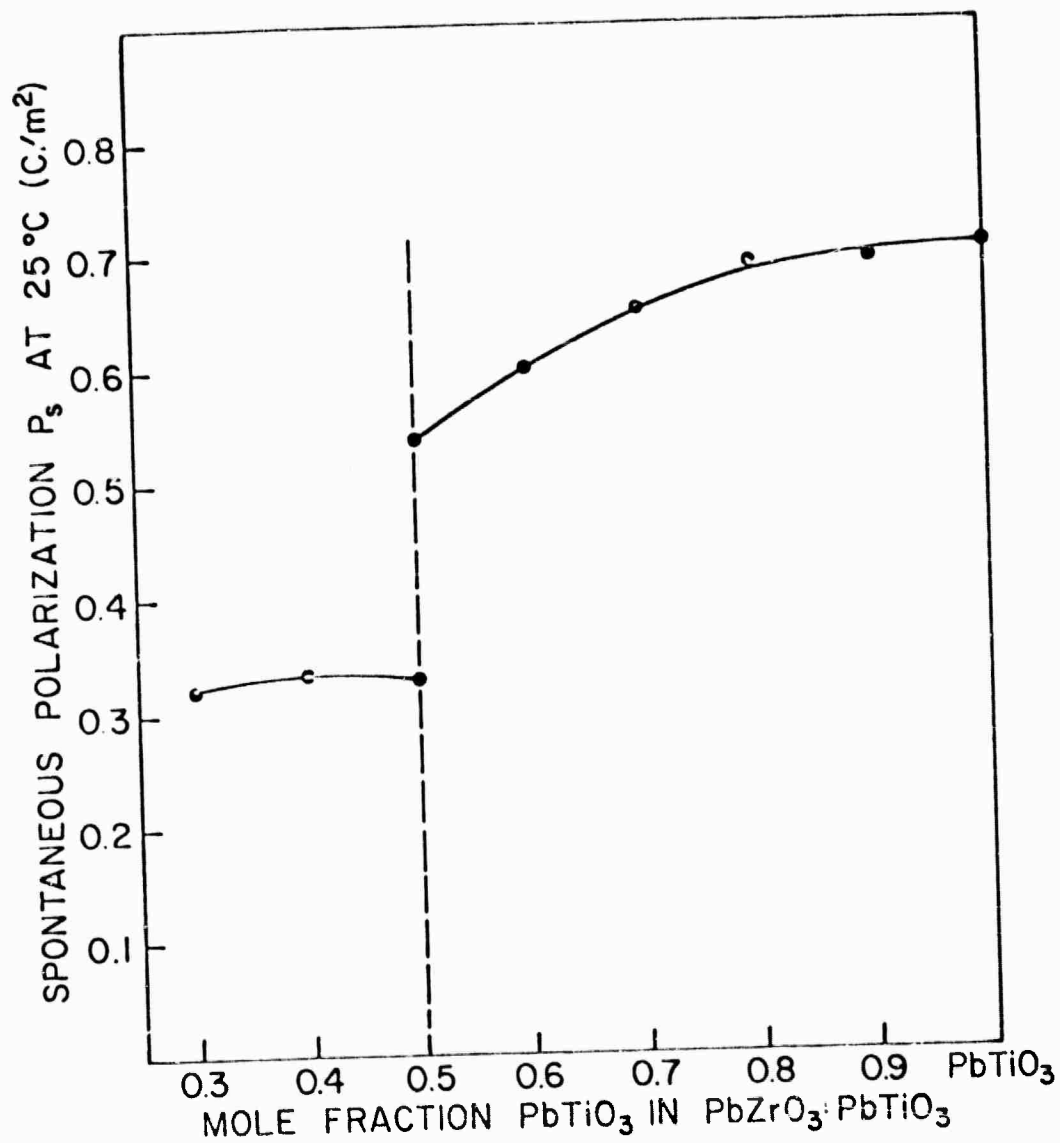
Fig. 10.   Calculated values of P_S at 25°C as a function of composition across the single cell compositions in the PZT phase diagram.
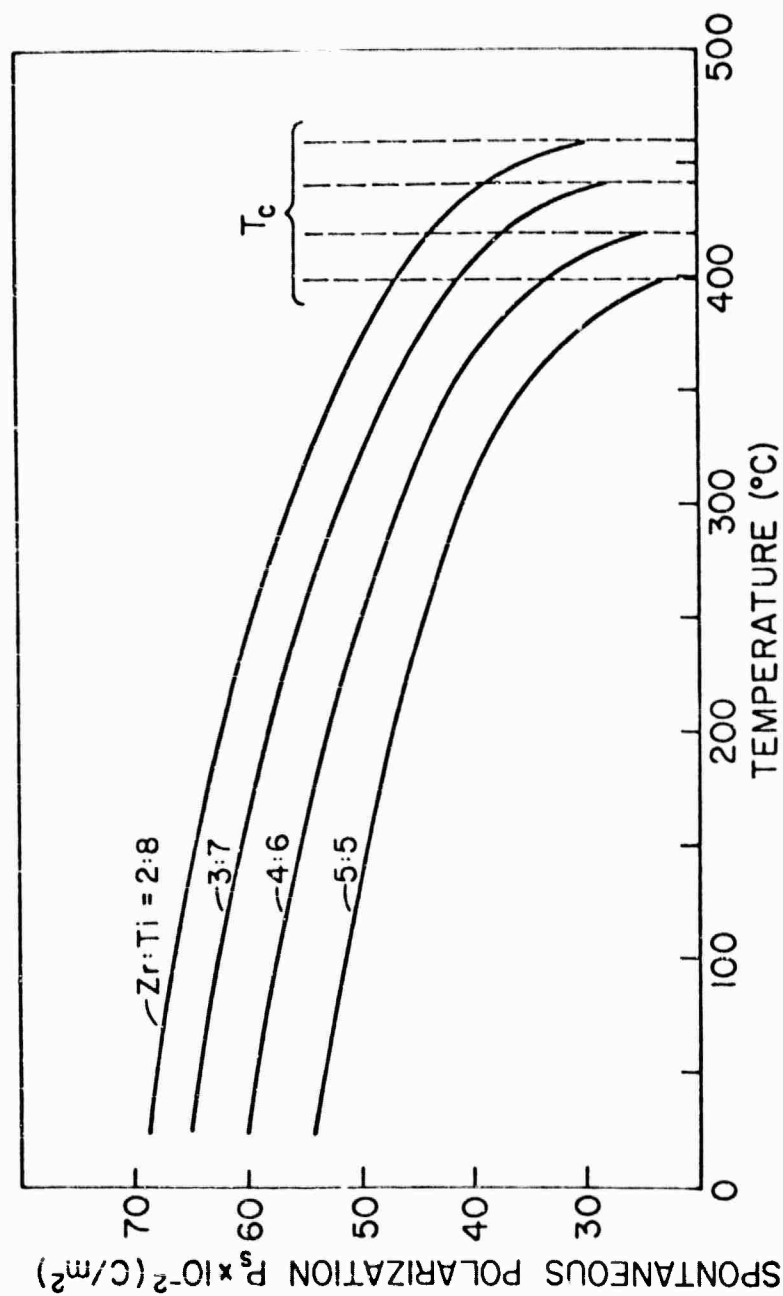
Fig. 11a. Comparison of calculated and observed polarization P_s as a function of temperature for several PZT compositions.
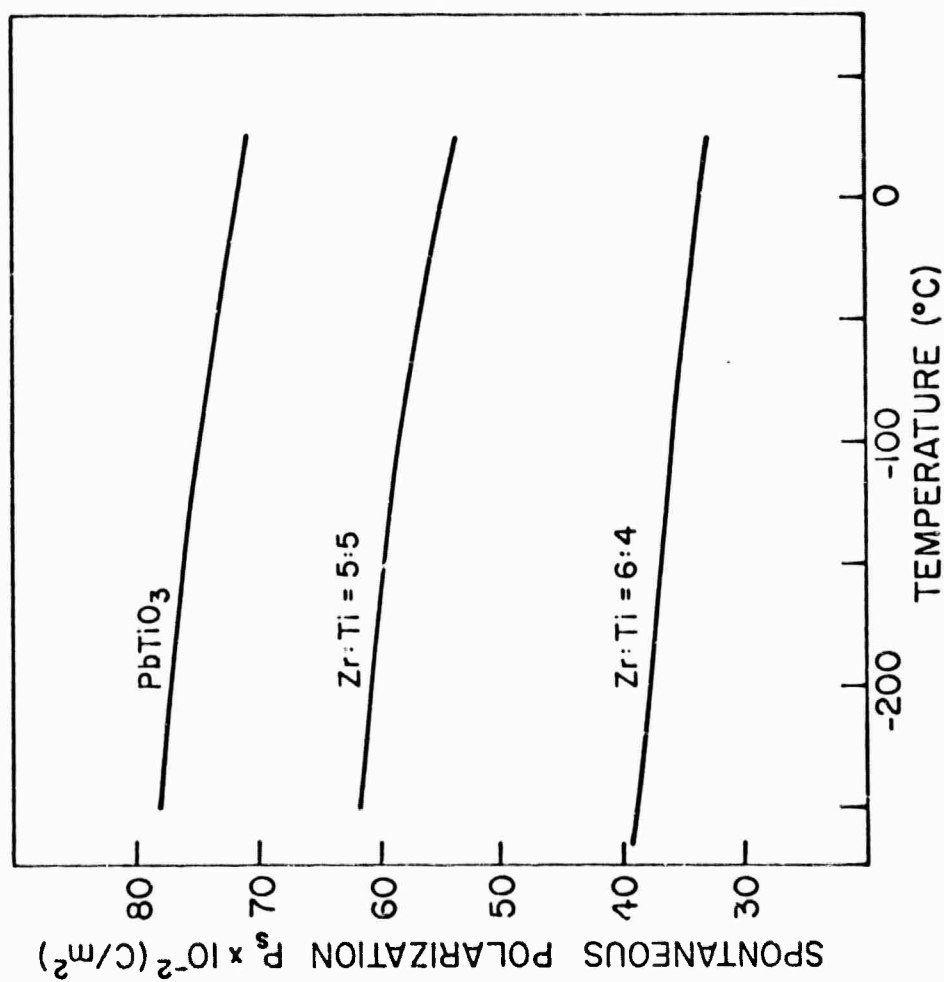
Fig. 11b. Calculated P_s vs T for several PZT compositions in the region below room temperature.
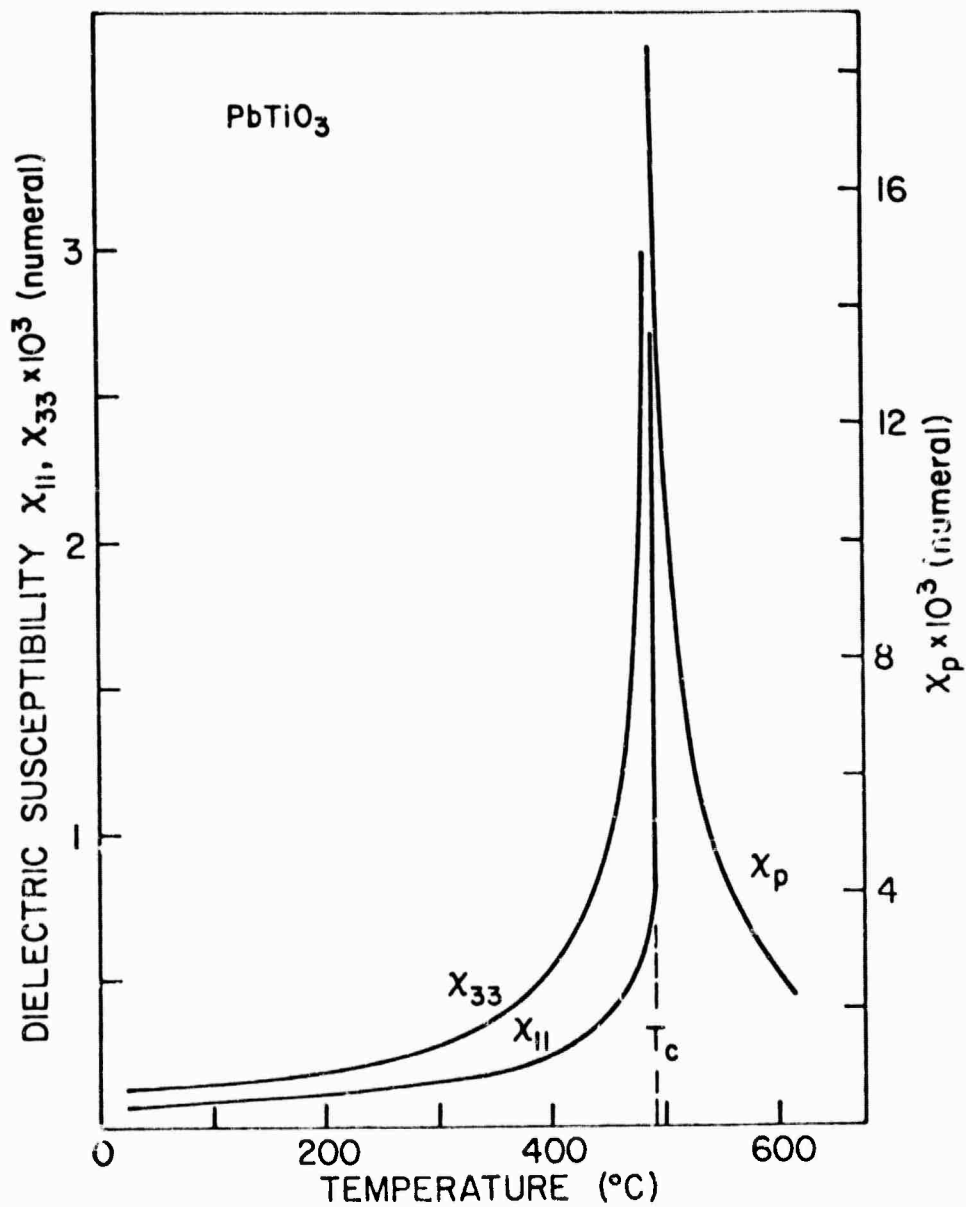
Fig. 12. Calculated dielectric susceptibility for pure PbTiO₃.
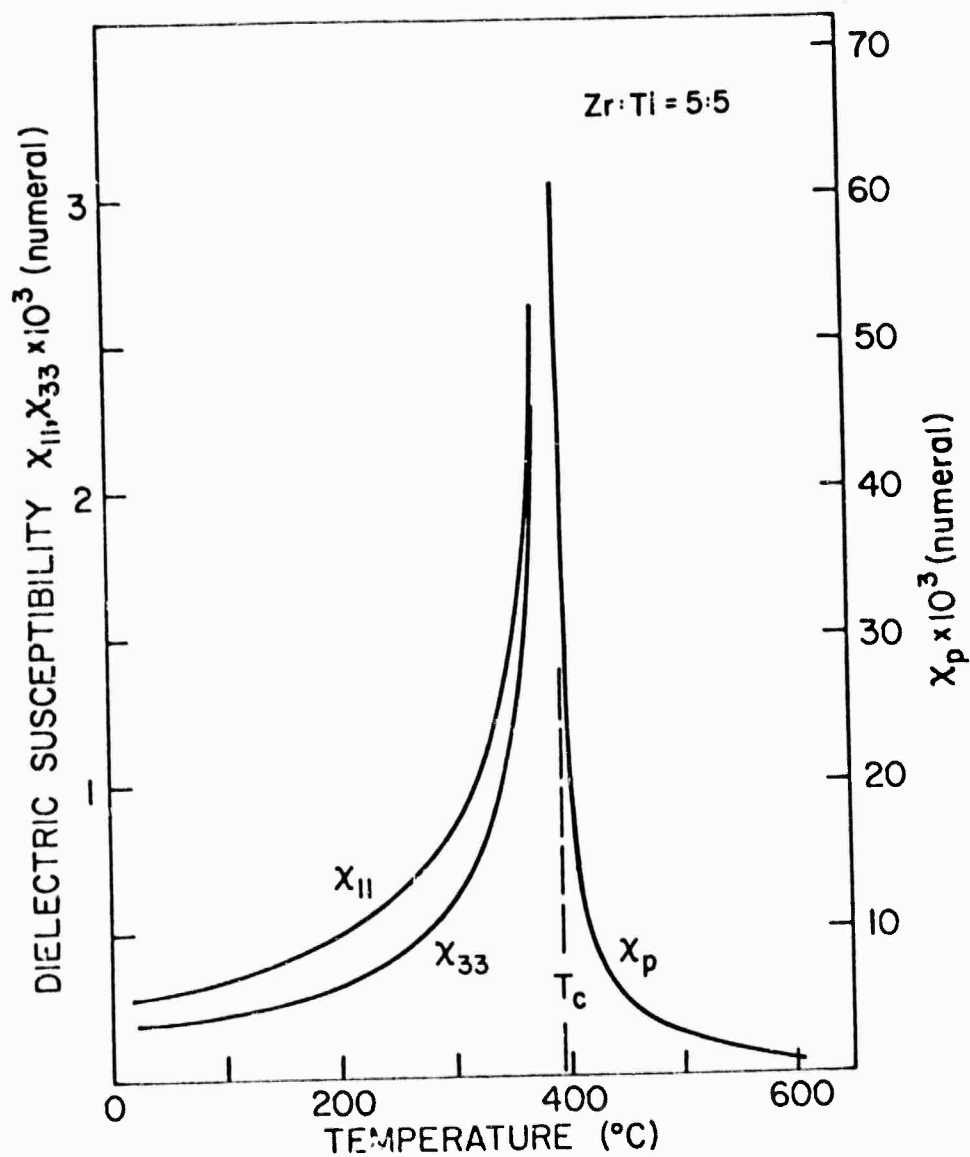
Fig. 13. Calculated dielectric susceptibility as a function of temperature in 50:50 PZT.
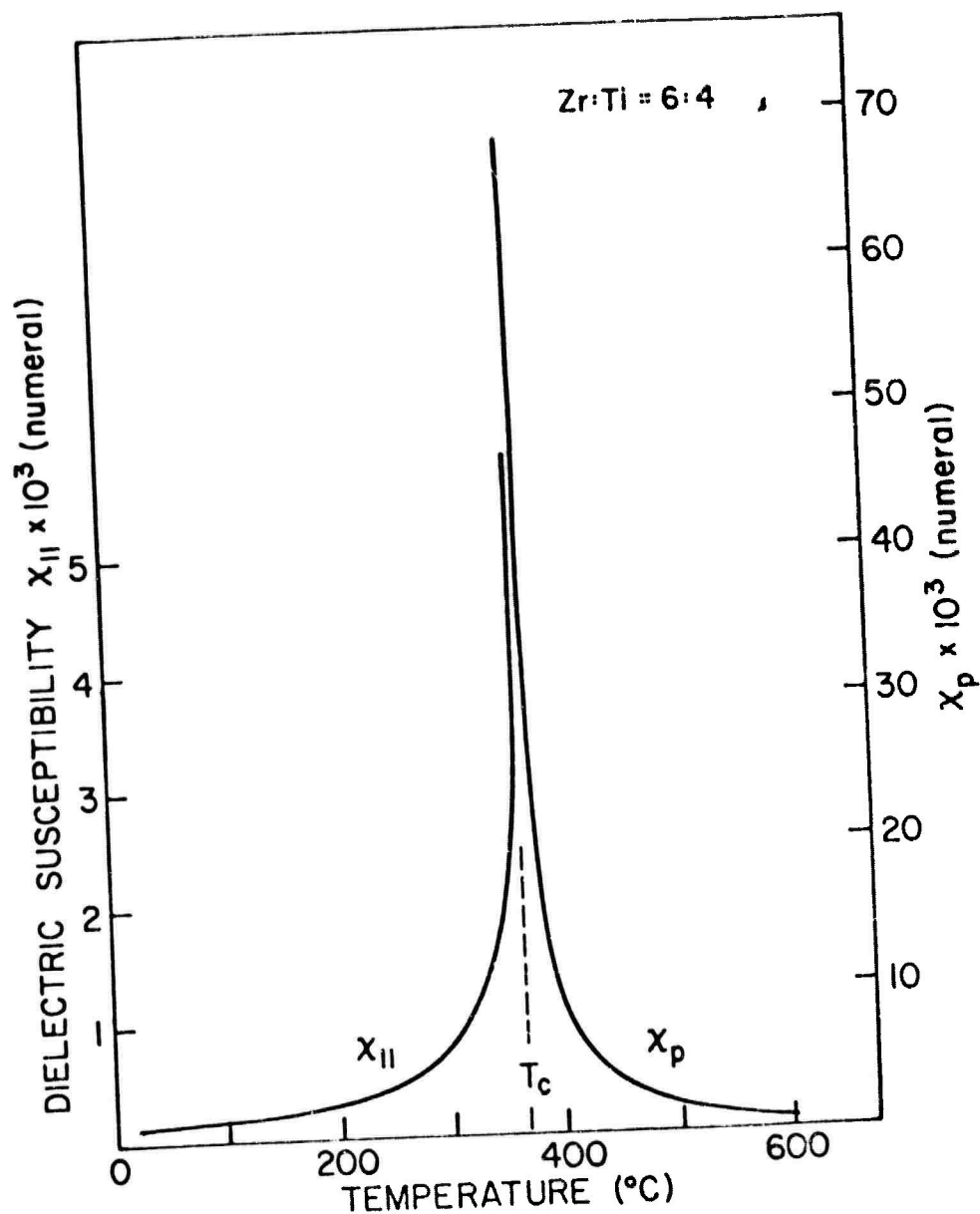
Fig. 14. Calculated dielectric susceptibility as a function of temperature in rhombohedral 60:40 PZT.
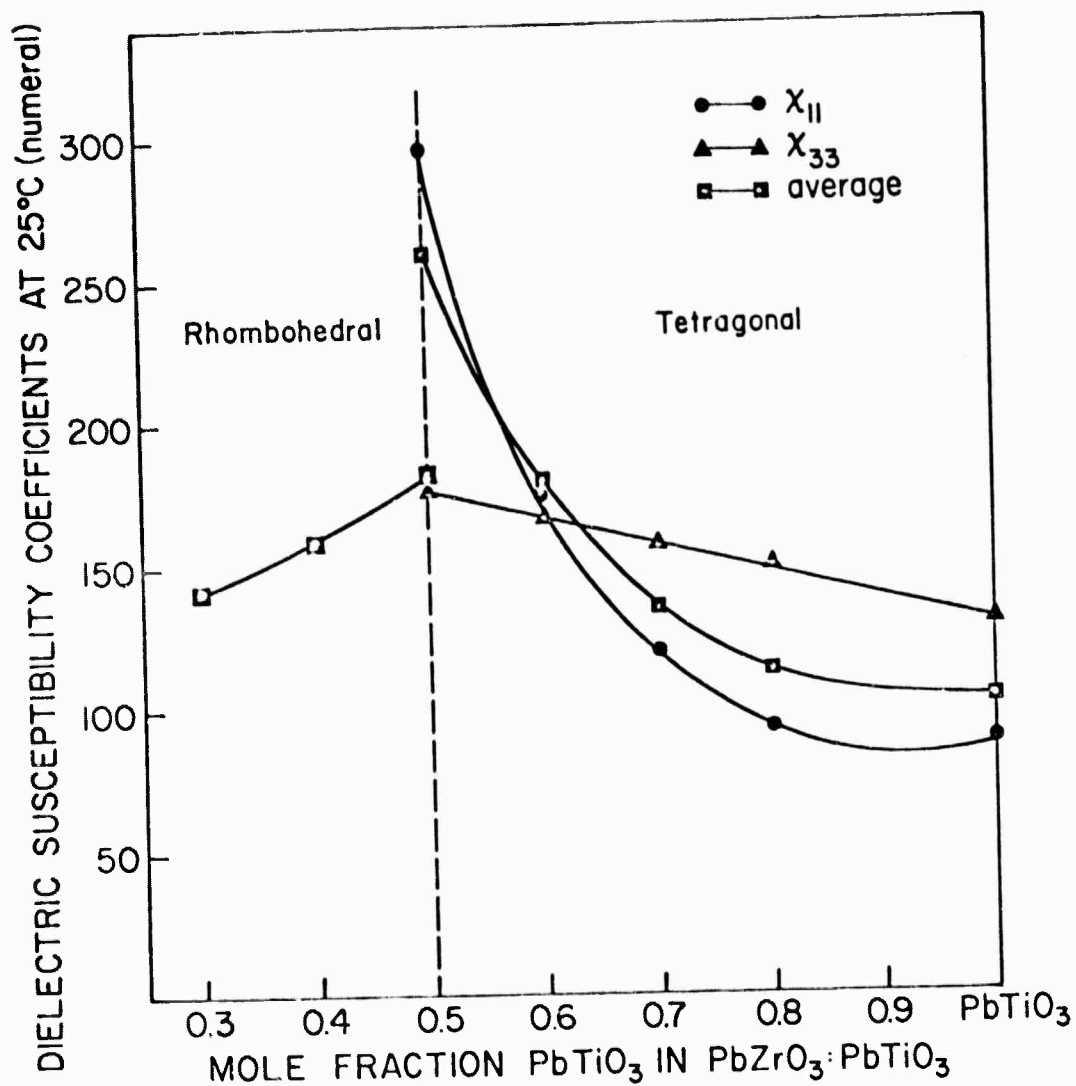
Fig. 15. Dielectric susceptibility in PZT at 25°C as a function of composition across the single cell PZT compositions.
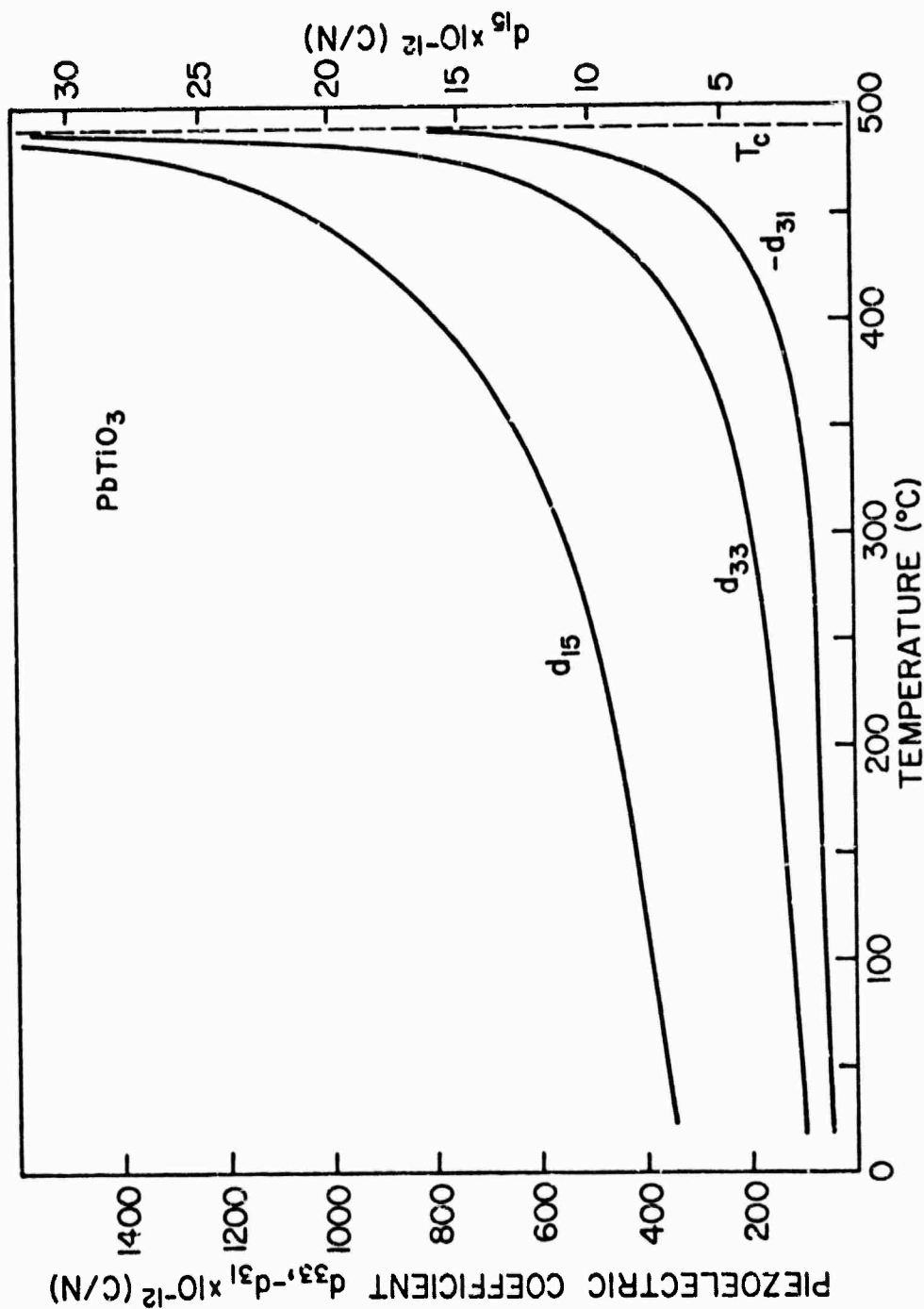
Fig. 16. Calculated d coefficients for single domain PbTiO$_3$ single crystal.
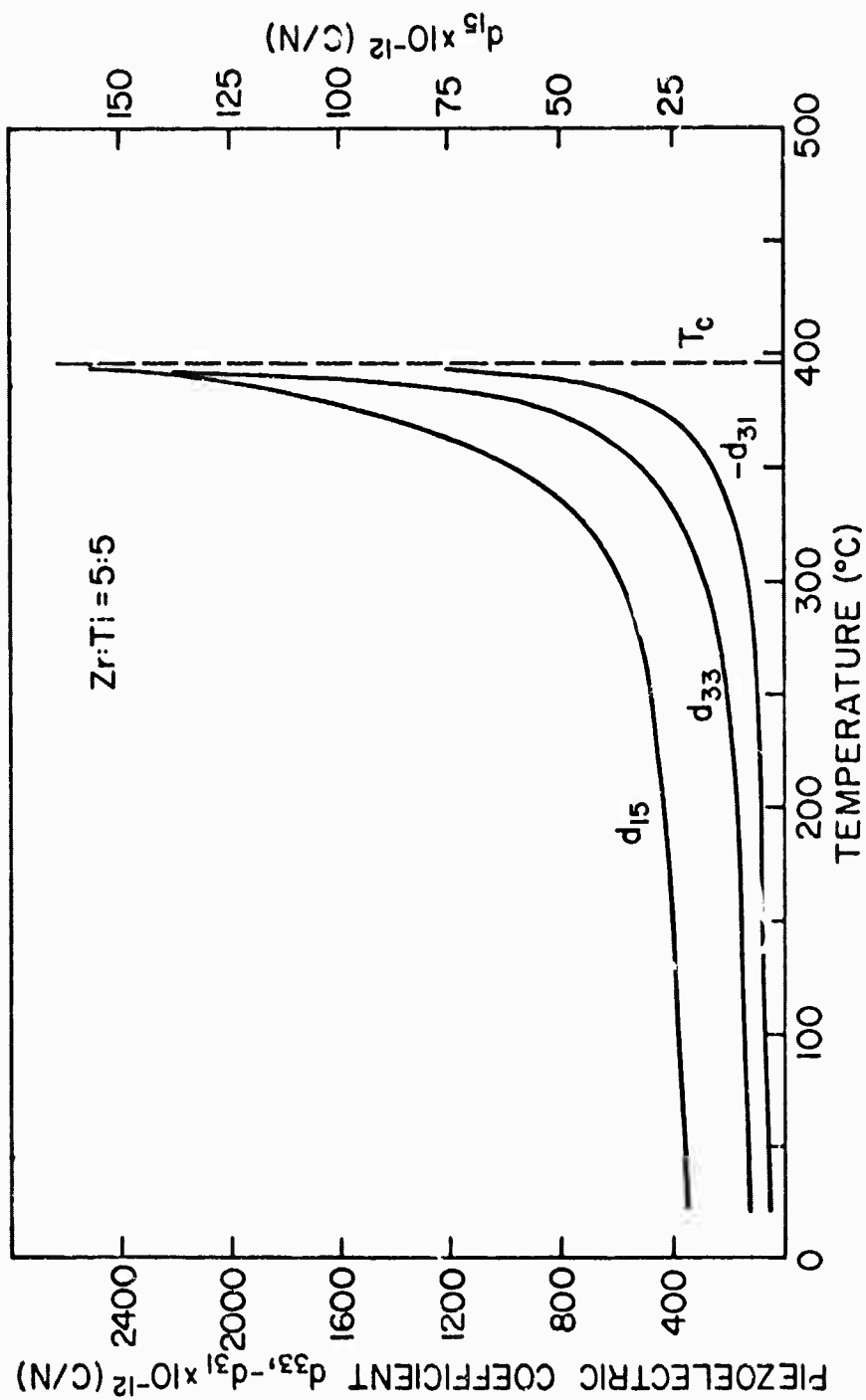
Fig. 17. Calculated d coefficients for a single domain single crystal of 50:50 PZT composition.
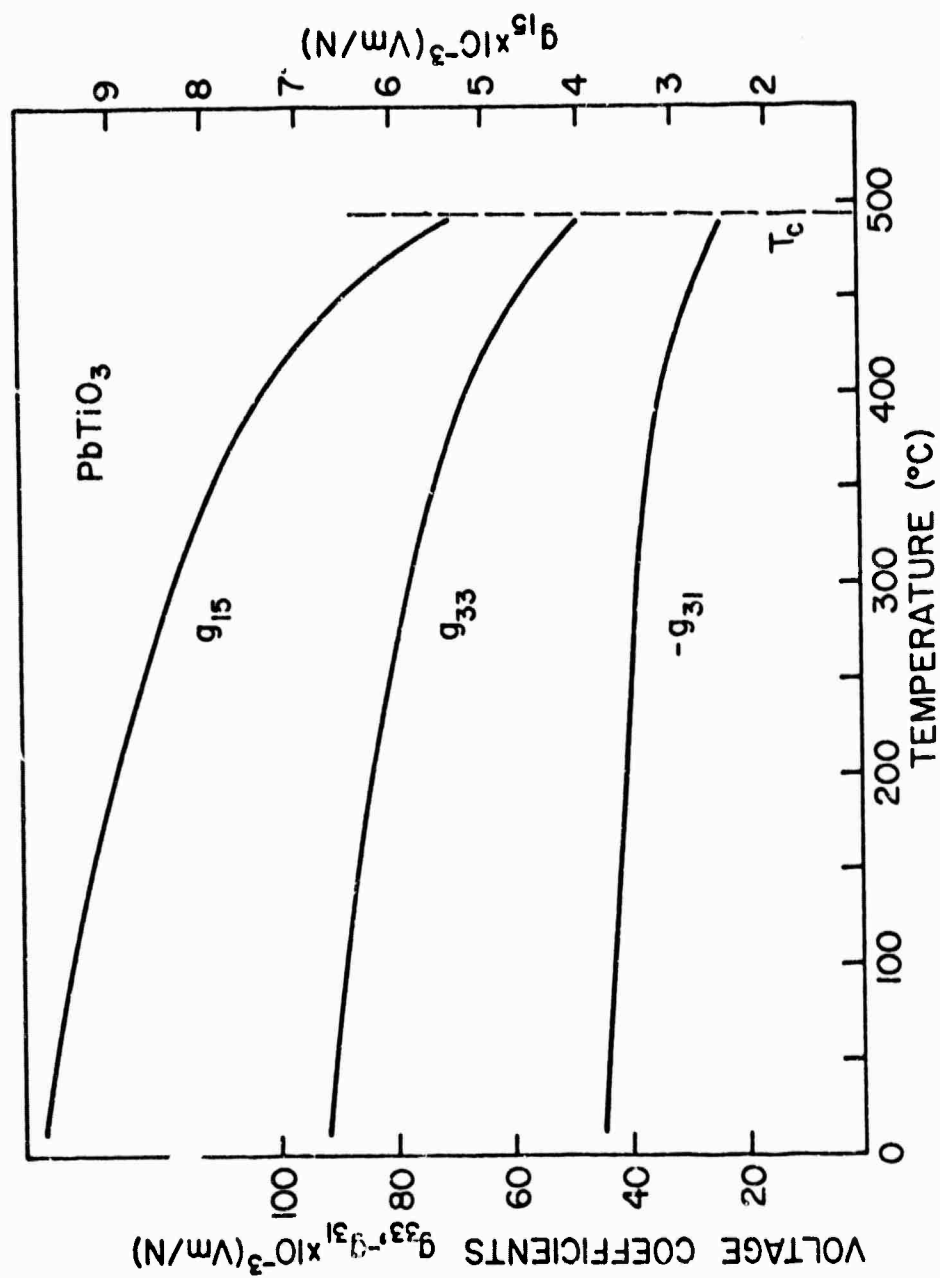
Fig. 18. Calculated g coefficients for a single domain PbTiO$_3$ single crystal.
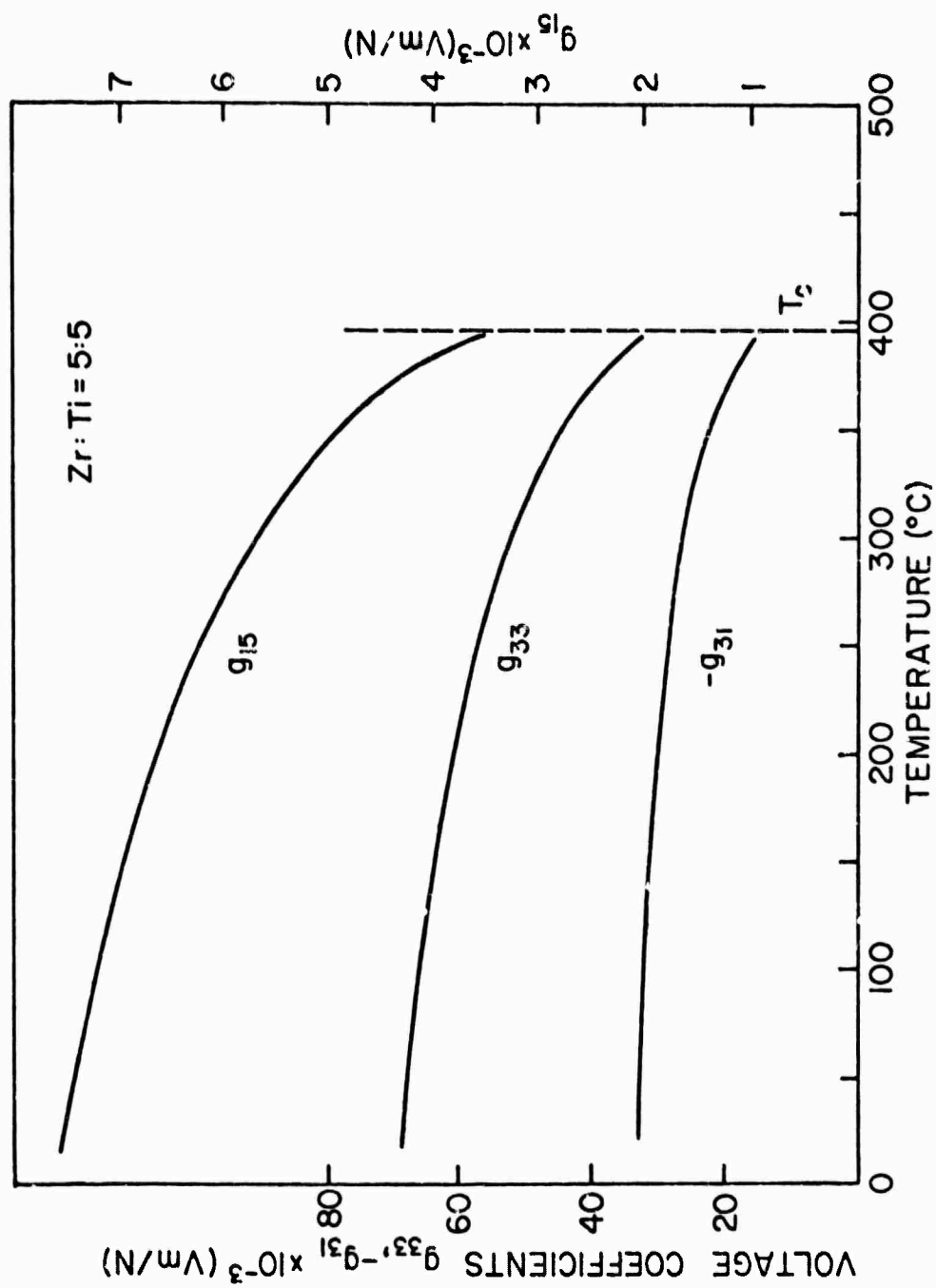
Fig. 19. Piezoelectric g coefficients for a single domain PZT of 50:50 Zr:Ti composition.
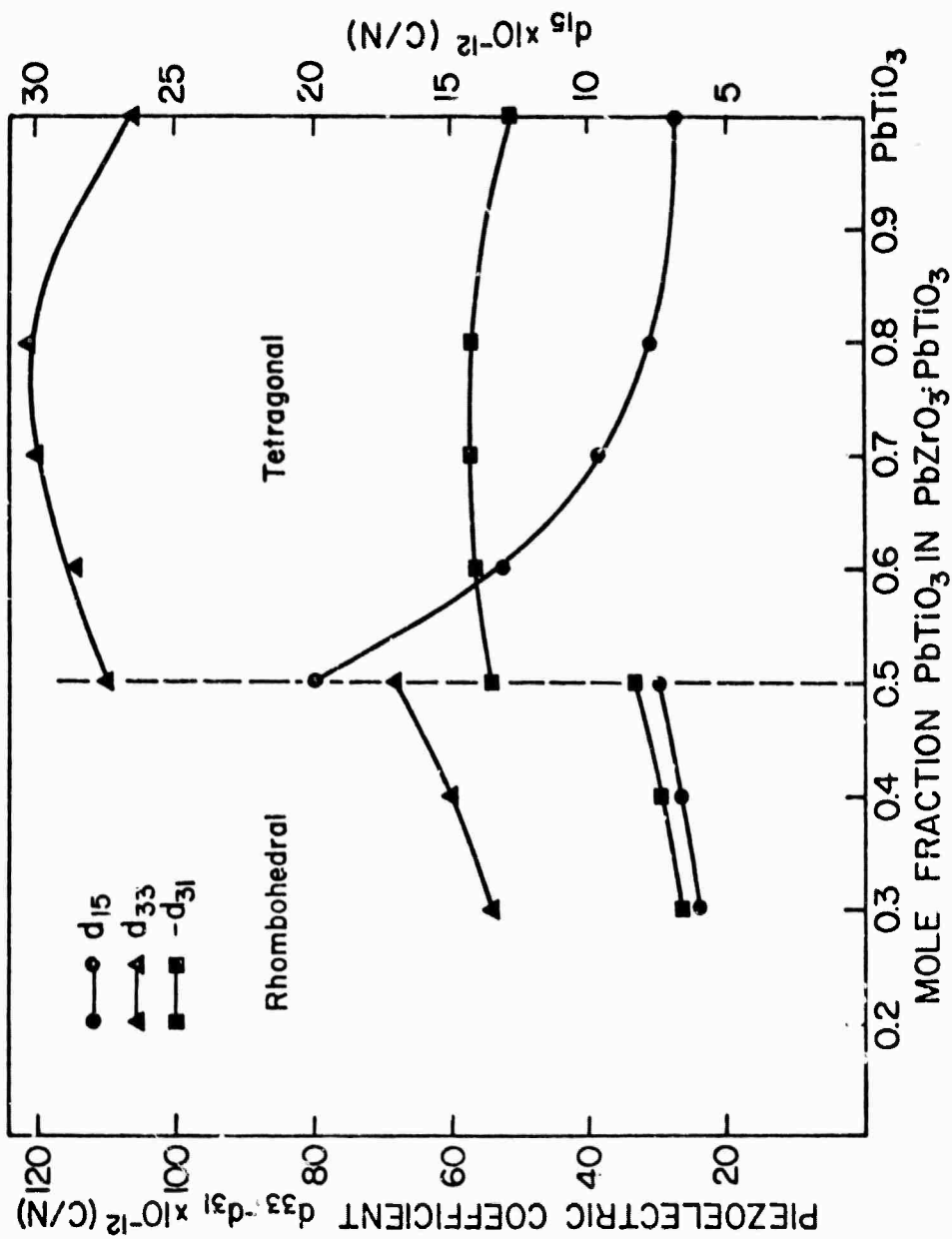
Fig. 20. Piezoelectric d coefficients at 25°C as a function of composition across the single cell PZT phase diagram for single domain single crystals.
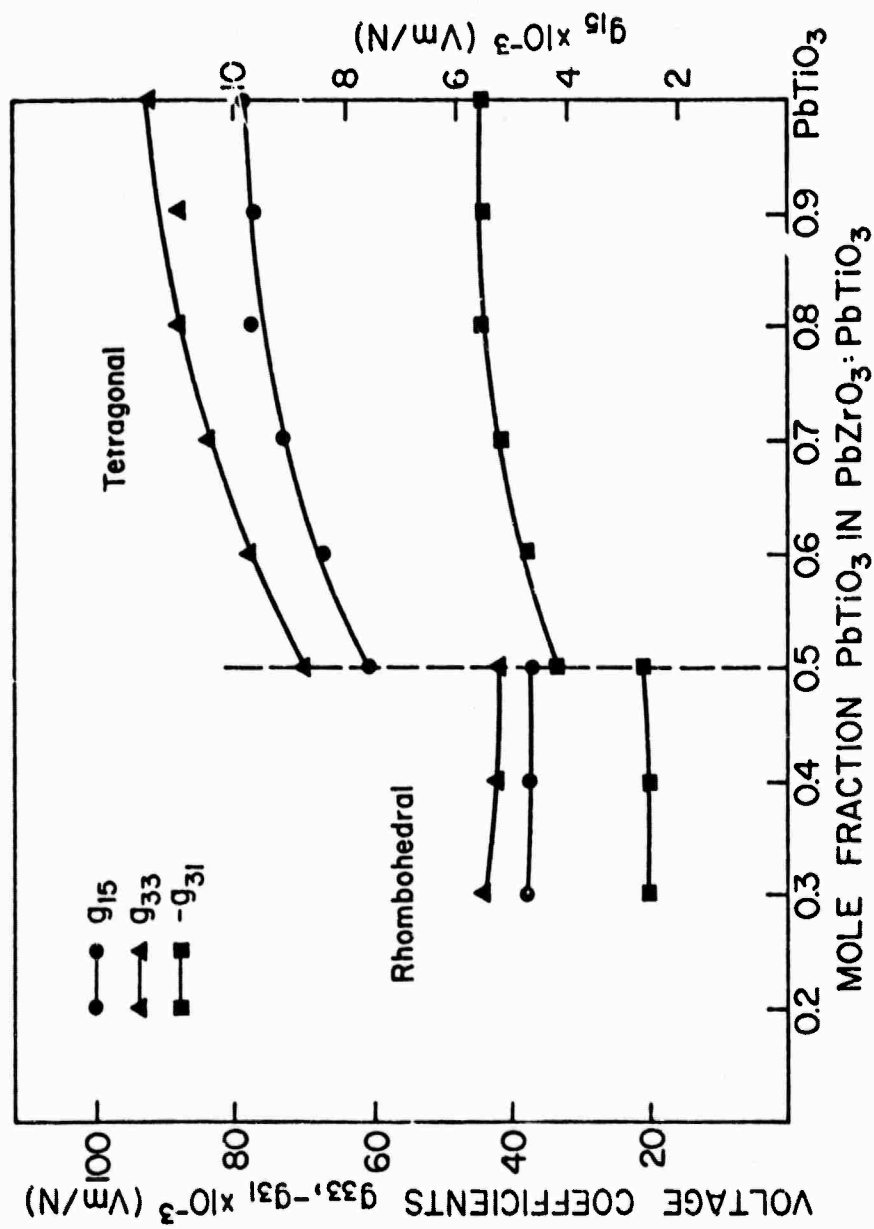
Fig. 21. Piezoelectric g coefficients calculated for single domain single crystals of PZT at 25°C.
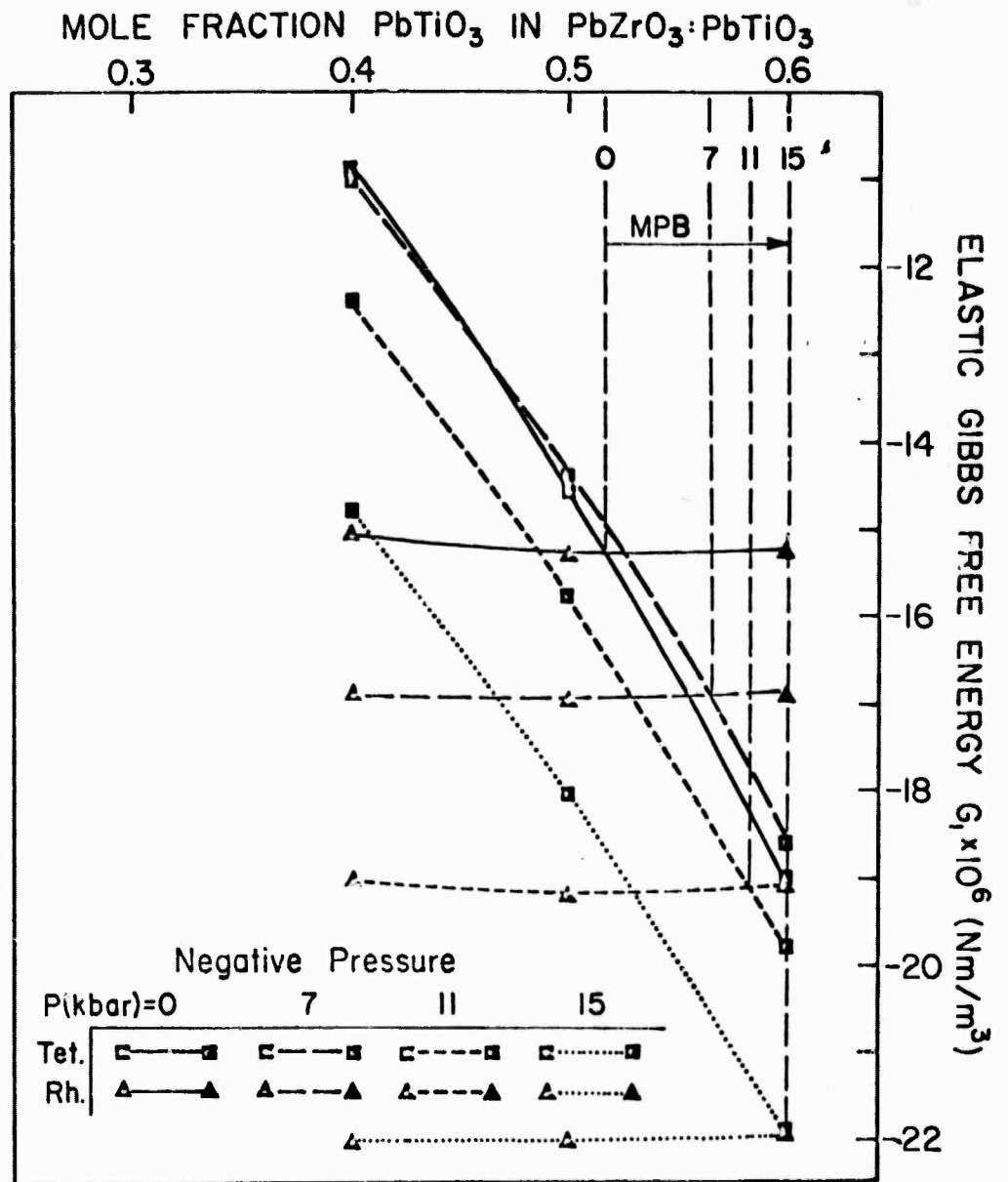
Fig. 22. Elastic Gibbs free energy under high hydrostatic pressure at 25°C for compositions close to morphotropy in the PZT in the PZT phase diagram.
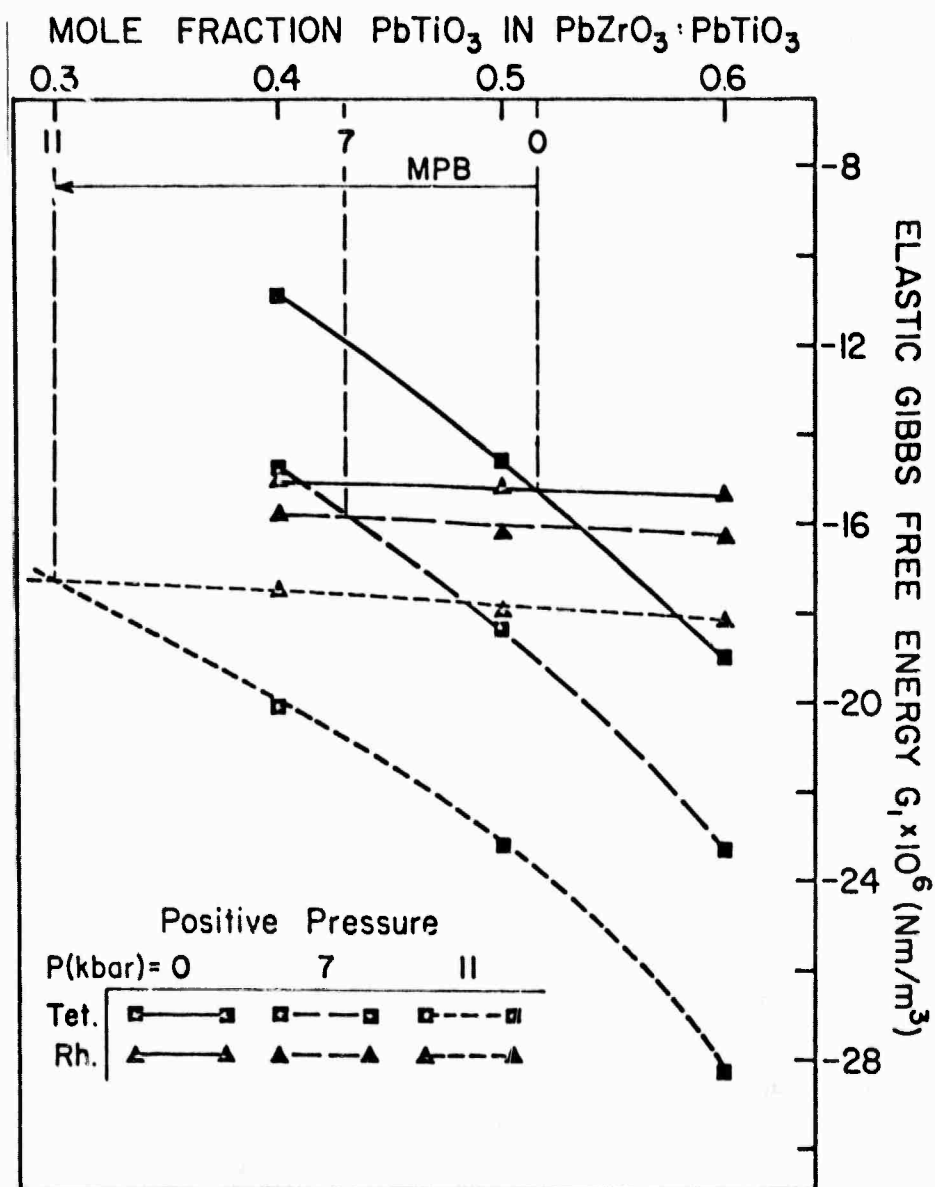
Fig. 23. Elastic Gibbs free energy as a function of hydrostatic
pressure at 25°C for compositions of PZT close to
morphotropy.
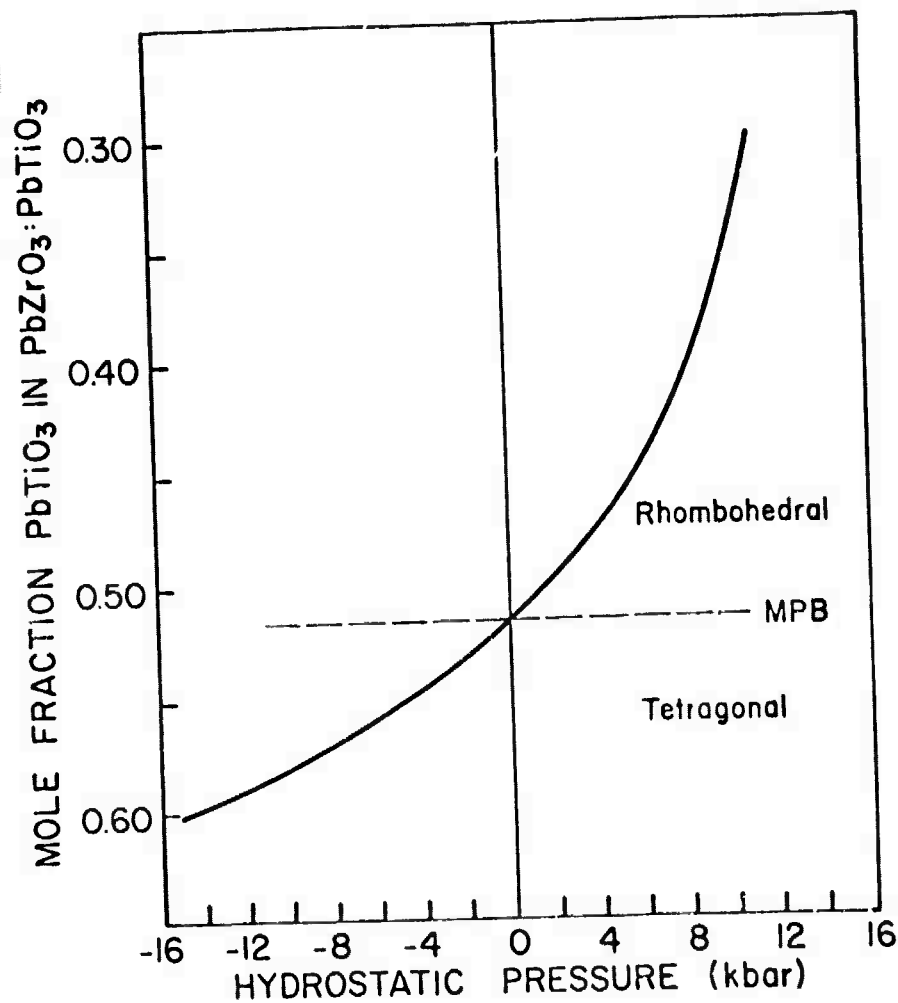
Fig. 24. Shift of the composition at which the morpho-
tropic boundary occurs as a function of
hydrostatic compression and tension applied
at 25°C to a PZT on the zero stress morphotropic
composition.

APPENDIX 9

Solid State Reactions in the System $PbO-TiO_2-ZrO_2$

D.L. Hankey and J.V. Biggers

Solid State Reactions in the System $PbO-TiO_2-ZrO_2$

D. L. Hankey and J. V. Biggers
Materials Research Laboratory
The Pennsylvania State University
University Park, PA 16802

Abstract

The reaction sequence for the formation of PZT solid solutions
was investigated. The formation reaction was studied by utilizing
differential thermal analysis (DTA), wet chemical titrimetric
techniques for determination of uncombined PbO, and x-ray diffrac-
tion analysis for phase determinations as a function of calcining
temperatures and times. Calcining reaction diagrams are presented
for PZT compositions and a reaction sequence is proposed.

Introduction

The processing of electrical ceramics such as lead zirconate-lead titanate solid solutions used in the manufacture of piezoelectric devices is a very sensitive procedure with respect to reproducibility of the electromechanical properties of the fired product. Variations in the major processing variables (powder characteristics, calcining conditions, etc.) affect this reproducibility. Numerous papers have been presented which discuss the effects of processing parameters on the grain size, density, and electrical properties of fired PZT ceramics[1-5]. Similarly, studies of the reactions occurring during the calcining procedure have been reported since it is an extremely important step in the preparation of ceramics. As shown by Buckner and Wilcox[1], calcining temperatures have a strong influence on the properties of the fired ceramics. Presumably, the dependence of fired properties on calcining conditions is primarily related to the phases and their respective concentrations which result from the solid state reactions of the mixed oxides.

Major differences in the solid-phase reactions which occur during the calcination step of PZT ceramics have been reported. Mori et al.[6] conducted the initial investigations using high-temperature x-rays and differential thermal analysis. Studying the entire range of lead zirconate-lead titanate solid solutions, he concluded that the formation reaction followed two steps are presented in Table 1. The mixed oxides formed a solid solution of $PbTiO_3$ and ZrO_2 which eventually transformed into the PZT solid solution.

Matsuo and Sasaki[7] obtained contrasting results by utilizing x-ray diffractometry and wet chemical analyses for the determination of the phases and the relative amounts of uncombined oxides as a function of calcining temperature and times. Figure 1 is a reproduction of the reaction diagram prepared by Matsuo and Sasaki for the system $2PbO-TiO_2-ZrO_2$. From Table 1 it can be seen

that their reaction sequence for PZT formation is different from that of Mori. They report the formation of $PbTiO_3$ as the first product, followed by the formation of intermediate PZT solid solutions. Subsequently, the intermediate products react to form the stoichiometric PZT solid solution.

More recently, Speri[8] employed x-ray diffraction techniques in conjunction with simultaneous differential thermal analysis and thermogravimetry to determine the reaction sequence. In Table 1, Speri's reaction mechanism is presented The two intermediate products, $PbTiO_3$ and $(PbO)_{ss}$, react to produce the stoichio metric PZT. The $(PbO)_{ss}$ is indexed, according to x-ray diffractometry, as a tetragonal solid solution of PbO containing $PbTiO_3$ and ZrO_2.

The following work was conducted with PZT compositions prepared from mixed oxides. It is an attempt to obtain more detailed information concerning the reaction sequence in PZT formation and kinetic data on the calcination reactions.

Experimental Procedure:

PZT compositions ($PbZr_xTi_{1-x}O_3$) were prepared from mixed oxides for x = 0.5 0.52, 0.55 and 0.60. Figure 2 illustrates the processing and characterization flow chart. The raw material oxides used were: 99.6% pure orthorhombic PbO* (yellow), 99.9% pure tetragonal TiO_2** (anatase) and 99.9% pure monoclinic ZrO_2†. Loss on ignition of each of the oxides was determined. This data was incorporated into the calculation for preparation of the compositions in order to ensure exact stoichiometry. The weighed oxides were homogenized by wet ball milling the powders in a 500 ml polyethylene ball mill with deionized water

*Dry litharge from National Lead Industries, Hightstown, NJ.
**Lot 77G-27-8 from Whittaker, Clark and Daniels, Inc., South Plainfield, NJ
†Harshaw ZrO_2, Lot 1-75 supplied by Honeywell, Inc., Minneapolis, Minnesota.

for a period of 24 hours. The mill charge consisted of 1 gram molecular weight of powder ($\sim$325 g), 500 g of 3/8" ZrO_2 radius-end cylinders, and 100 ml of deionized H_2O. After wet milling, the powders were pan-dried for 12 hours at 1200°C. Finally, the powders were dry ball milled for four hours with an equivalent volume of ZrO_2 cylinders. This prevented any powder segregation which can accompany the drying procedure.

Surface area was determined by a BET method* and particle geometry was measured using a beam-controlled SEM image analysis[9].

The calcining studies were performed in closed 99.9 wt% Al_2O_3 crucibles (50 ml) in a SiC resistance furnace. The temperature gradient was less than 5° in the hot zone. Calcining temperatures ranged from 500°-900°C, while the calcining times varied from 2-24 hours in two-hour intervals. The furnace was preheated to the appropriate temperatures, and the crucibles containing the uncalcined powders were placed in the furnace and allowed to equilibrate for 15 minutes. The crucibles were removed at the end of the respective time intervals and air-quenched.

The phases in the calcined powders were determined by x-ray diffractometr using CuK_α radiation through a Ni filter. The powders were granulated through a 325-mesh screen prior to preparing the slides. In addition, the amount of uncombined PbO in each calcined powder was determined using wet chemical tech- niques described by Robinson and Joyce[10].

Differential thermal analysis (DTA) curves were obtained for the various PZT compositions in the temperature range from 25-850°C using the DT-716 analyzer**. The standard cell (Pt) contained 25 mg pure Al_2O_3. Twenty to 30 mg samples were employed for the DTA experiments in the test cell (Pt). The sensitivity was 5 uv/inch and the heating rate was 10°C/minute.

Thermogravimetric analysis (TGA) of the PZT compositions was carried out in an air atmosphere using the TG-716 Analyzer**. Sixty to 90 mg samples were heated at 5°C/minute, and the sensitivity was 200 uv/inch.

*Monosorb Surface Area Analyzer by Quanta Chrome Corp., Greenvale, NY.
**Produced by Harrop Laboratories in Columbus, OH; used with Harrop Lab. Mode
TA-700 Control Console (DT-716, TG-716) Analyzer.

Results and Discussion

Figure 3 is a plot of % PbO reacted vs calcining time for various calcining temperatures of $PbZr_{0.5}Ti_{0.5}O_3$. As expected, the % PbO reacted isothermally increases as a function of time. Also, the reactivity of PbO is greatly increased at higher calcining temperatures. For example, the % PbO reacted approaches 100% for very short calcining times above 800°C.

Figures 4 and 5 are calcining reaction diagrams for the compositions $PbZr_{0.50}Ti_{0.50}O_3$ and $PbZr_{0.55}Ti_{0.45}O_3$, respectively. The region boundaries are approximate, but nevertheless, illustrate the fact that there are different phase assemblages present during the calcination step. Other phases with concentrations of a few percent may also be present in the various regions, since they may not have been detected with x-ray diffractometry. However, much information can be obtained on the reaction process from Figs. 4 and 5. For example, in Figure 4, x-ray analyses show no products resulting from calcining in Region 1. However, increasing the calcining temperature for a fixed time of four hours, Region 1 becomes Region 2 at ∿490°C as $PbTiO_3$ and $(PbO)_{ss}$ are discerned in the x-ray diffraction patterns. Similarly, Region V becomes Region VI at ∿750°C as the $PbTiO_3$ and $(PbO)_{ss}$ react to form PZT of the correct stoichiometry.

The phase $(PbO)_{ss}$ has been reported to exist in previous studies. Matsuo and Sasaki[11] investigated the PbO-rich side of the system $PbO-TiO_2$ by calcining mixtures up to 50-50 molar % of PbO and TiO_2 at 800°C. Using chemical and x-ray analyses, only the phases $PbTiO_3$, orthorhombic PbO (starting material) and tetragonal PbO were found in the calcined mixtures. They concluded that the orthorhombic PbO had dissolved some TiO_2 and converted to the tetragonal form. Furthermore, they reported that additional calcinings of the 3-phase mixtures resulted in a disappearance of $PbTiO_3$. Thus, they concluded that the orthorhombic PbO converted to tetragonal PbO by dissolving $PbTiO_3$. A tetragonal

solid solution was formed and they presented a plot of the decreasing lattice

parameters of the solid solution as the PbTiO$_3$ content was increased to 12 mol

Similarly, Speri[8] experimented with mixtures of PbO and TiO$_2$. For PZT

compositions near the morphotropic boundary, there are approximately 2 moles

of PbO and 1 mole of TiO$_2$. Calcining these mixtures of PbO and TiO$_2$ between

690 and 810°C, Speri analyzed the x-ray diffraction patterns to identify the

resulting phase(s). The reaction product could not be identified with known

patterns, but the d-spacings were all slightly smaller than the corresponding

tetragonal PbO line. From Matsuo and Sasaki's report[11] it would appear that

the solid solution of PbTiO$_3$ into PbO would account for the smaller

d-spacings. Therefore, Speri also concluded that the reaction product was a

tetragonal solid solution of PbTiO$_3$ with orthorhombic PbO (thus converting PbC

tetragonal phase). Speri also studied reactions in the PbO-ZrO$_2$-TiO$_2$ systems

He concluded that the product of the first reaction is PbTiO$_3$, while the secor

reaction product is a tetragonal PbO solid solution formed from PbTiO$_3$, ZrO$_2$

the orthorhombic PbO. In our present work, we have duplicated some of Speri'

work on the calcined mixtures and our preliminary identification of this (PbO

phase is in agreement with Speri.

The important point is that the calcining reaction diagrams appear to b

more complicated than those initially presented by Matsuo and Sasaki. Also,

phases different from those reported by Mori[6] and Sasaki and Matsuo[7] were

present in our powders during the calcining process. The phases in the pre

study were, however, in agreement with those by Speri[8].

Figure 6 is a compilation of the DTA curves for the four compositions

investigated. It appears that the reaction sequence can be described by th

endothermic reactions. In Fig. 6 the endotherms are represented in each cu

by the numbers 1, 2, and 3. Each corresponding endotherm occurs at approxi

mately the same temperature for each composition. Combining these data with those obtained from the calcining reaction diagrams and Fig. 3, a reaction scheme is proposed for the three endotherms:

(1) $PbO + TiO_2 \rightarrow PbTiO_3$

(2) $PbTiO_3 + PbO + ZrO_2 \rightarrow (PbO)_{ss}$

(3) $(PbO)_{ss} + PbTiO_3 \rightarrow PbZr_xTi_{1-x}O_3$
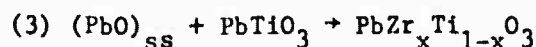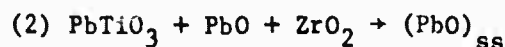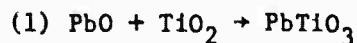
This reaction sequence is listed in Table 1 and corresponds to that proposed by Speri.

Russel and Spink[12], on the contrary, reported a different type of DTA behavior of PZT materials. They reported exothermic formation of $PbTiO_3$ near 600°C and a "complex" undetermined endothermic reaction between 700 and 800°C. However, they did not have any supporting calcination data from x-ray diffraction or wet chemical analyses. Finally, thermogravimetric analyses (TGA) showed that the only significant weight loss in the powders below 850°C corresponded to that expected from the loss on ignition.

Conclusion

Several different analytical techniques including wet chemical, x-ray diffraction, thermogravimetric, and differential thermal analyses have been used to follow the course of the solid state reactions occurring during the calcining of PZT compositions near the morphotropic boundary.

We have presented a tentative calcining diagram d proposed a three-step reaction sequence involving initial formation of $PbTiO_3$ followed by its reaction with PbO and ZrO_2 to form a PbO solid solution phase. The final PZT is formed by reaction of the PbO_{ss} phase with unreacted ZrO_2 and $PbTiO_3$.

To better understand the calcining reactions, the kinetics of the formation and the composition of the PbO_{ss} phase must be determined as a function of calcining conditions.

References

1. D.A. Buckner and P.D. Wilcox, Effects of Calcining on Sintering of Lead Zirconate-Titanate Ceramics, Am. Ceram. Soc. Bull. 51[3] 218-222 (1977).

2. T. Yamaguchi, S.H. Cho, M. Hakomori and H. Kuno, Effects of Raw Material and Mixing Methods on the Solid State Reactions Involved in Fabrication of Electronic Ceramics, Ceramurgia International 2[2] 76-80 (19

3. T.B. Weston, Studies in the Preparation and Properties of Lead Zirconate-Lead Titanate Ceramics, J. Can. Cer. Soc. 32[100] 100-115 (1963).

4. A.H. Webster, T.B. Weston and V.M. McNamara, The Effects of Some Variation in Fabrication Procedure on the Properties of Lead Zirconate-Titanate Ceramics Made from Spray-Dried Co-Precipitated Powders, J. Can. Cer. Soc. 35[1] 61-68 (1966).

5. J.V. Biggers, D.L. Hankey and L. Tarhay. The Role of ZrO_2 Powder in Microstructural Development of PZT Ceramics. Materials Science Research II: Processing of Crystalline Ceramics. Edited by Hayne Palmour II R.F. Davis, T.M. Hare. pp 335-342, Plenum Press, NY (1978).

6. S. Mori et al., National Technical Report, 10[1] 32-40 (1964).

7. Y. Matsuo and H. Sasaki, Formation of Lead Zirconate-Lead Titanate Solid Solutions, J. Am. Ceram. Soc. 48[6] 289-291 (1965).

8. W.M. Speri, Thermal Analysis of Processes Which Occur During the Calcin of Adulterated and Unadulterated Lead Zirconate-Lead Titanate, Ph. Thesis, Rutgers University, NJ (1969).

9. J. Lebiedzk, R.G. Burke, S. Troutman, G.G. Johnson, Jr. and E.W. White Scanning Electron Microscopy, Part 1, 26-33 (1973).

10. A.E. Robinson and T.A. Joyce, Preparation of Lead Zirconate-Titanate Compositions, Trans. Brit. Cer. Soc. 61[2] 85-93 (1962).

11. Y. Matsuo and H. Sasaki, PbO-Rich Side of the System PbO-TiO$_2$, J. Am. Ceram. Soc. 46[3] 409-410 (1963).

12. V.A. Russel and C.H. Spink, The Differential Thermal Analysis Behavior of Lead Zirconate-Titanate Materials, Thermochim. Acta 19[1] 45-54 (1977).

Table 1. Comparative table of reaction sequence in PZT formation

Mori	Matsuo and Sasaki	Speri	Present Stud Mixed Oxide P
P + Z + T	P + Z + T	P + Z + T	P + Z + T
$\sim$550°C	500-600°C	610-710°C	$\sim$550°C
$(PT + Z)_{ss}$	PT + P + T + X	PT + P + Z + T	PT + P + Z + T
650-1000°C	600-700°C	710-790°C	$\sim$680°C
PZT	$PT + (PZ_xT_{(1-x)})$	$PT + (PbO)_{ss}$	$PT + (PbO)_{ss}$
	750-850°C	790-850°C	700-800
	PZT	PZT	PZT

P = Orthorhombic PbO   PT = Tetragonal $PbTiO_3$

Z = Monoclinic ZrO_2 $PZT = PbZr_xTi_{1-x}O_3$

T = Tetragonal TiO_2 $(PbO)_{ss}$ = Solid solution of $PbO, PbTiO_3, ZrO($

$(PT+Z)_{ss}$ = Solid solution of $PbTiO_3$ & ZrO_2
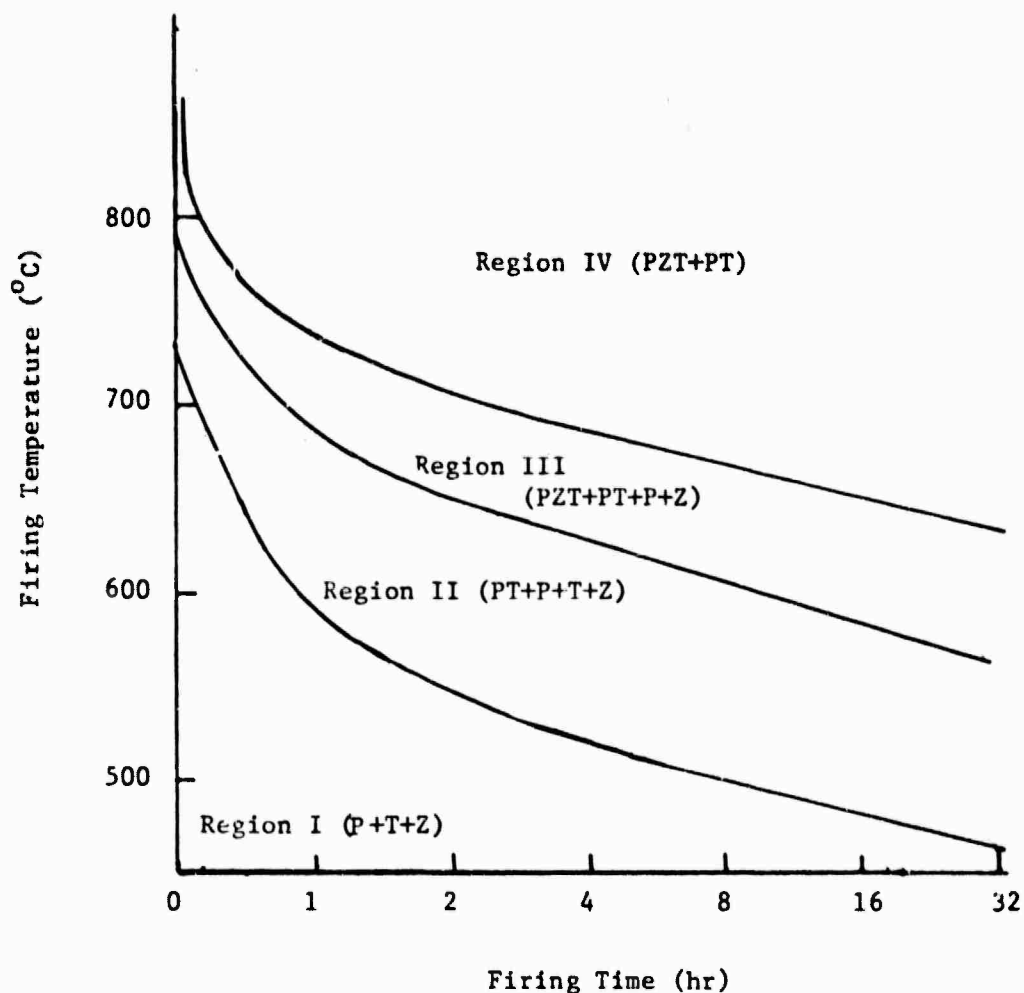
Fig. 1 Reaction diagram for $Pb(Zr,Ti)O_3$ formation in the system $2PbO-TiO_2-ZrO_2$. (●)Points were determined by x-ray and chemical analysis, and (O) points were determined by chemical analysis. P = orthorhombic PbO, Z = monoclinic ZrO_2, T = tetragonal TiO_2, PT= tetragonal $PbTiO_3$. and PZT = $Pb(Zr_{1-\lambda}Ti_\lambda)O_3$. Zero firing time is the time at which the temperature of each pellet has just reached the temperature of the furnace. (From Matsuo and Sasaki, Ref. 7).
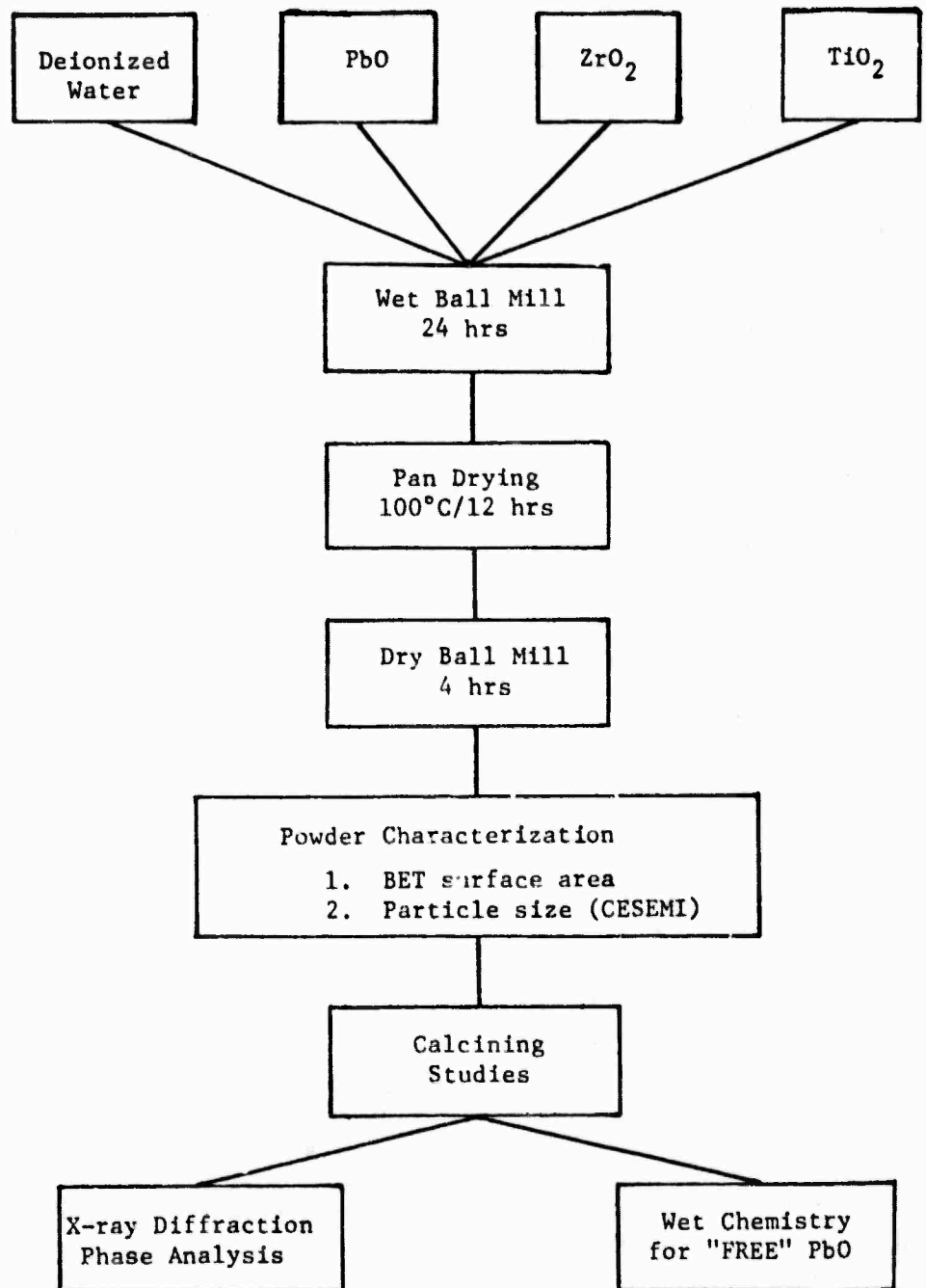
Fig. 2 Processing and characterization flow chart.

TEMPS: 500, 600, 700, 800, 900°C
TIME: 2-24 hrs in 2-hr steps
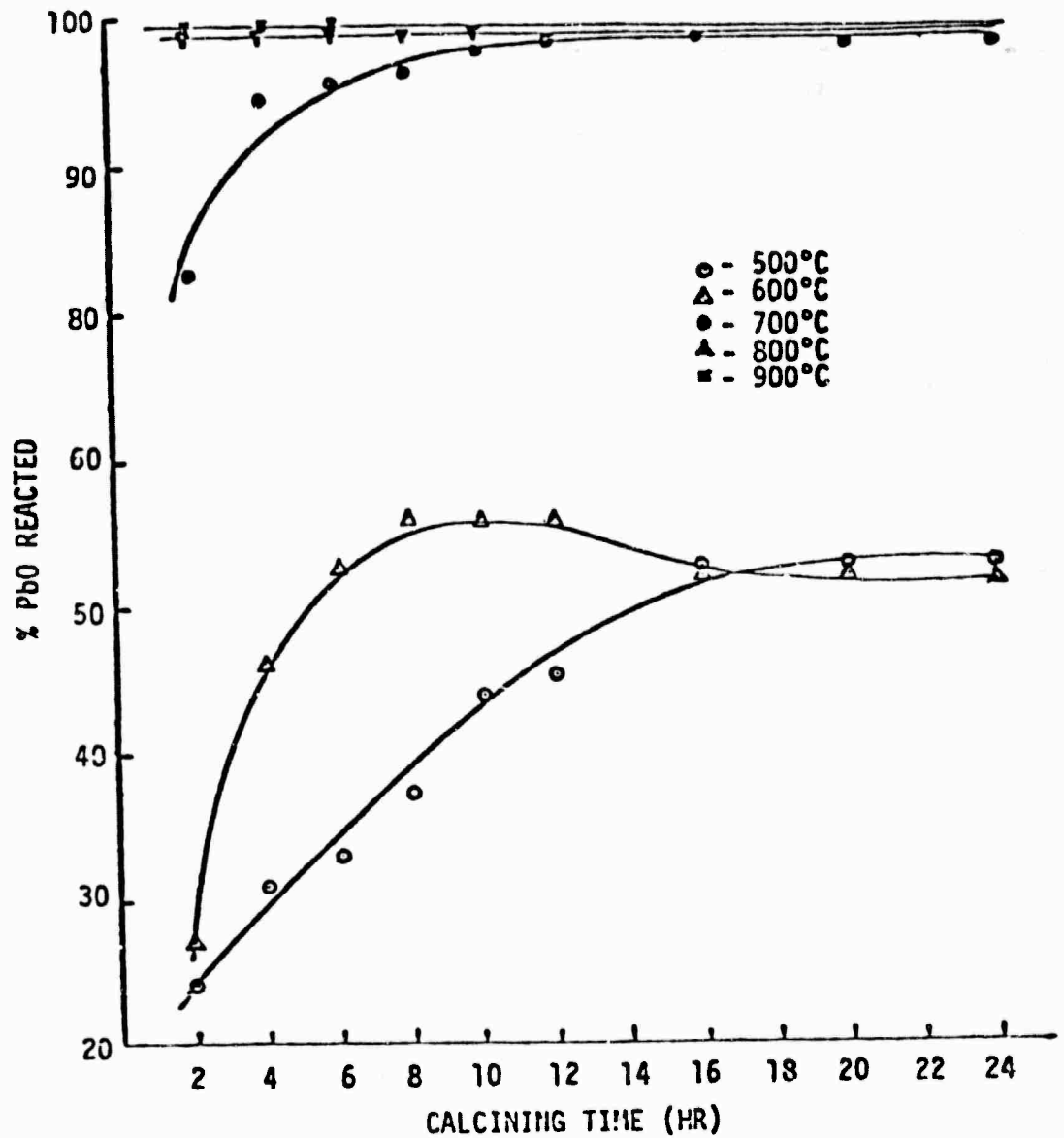
Fig. 3 % PbO reacted vs calcining time for various temperatures of $PbZr_{0.50}Ti_{0.50}O_3$.
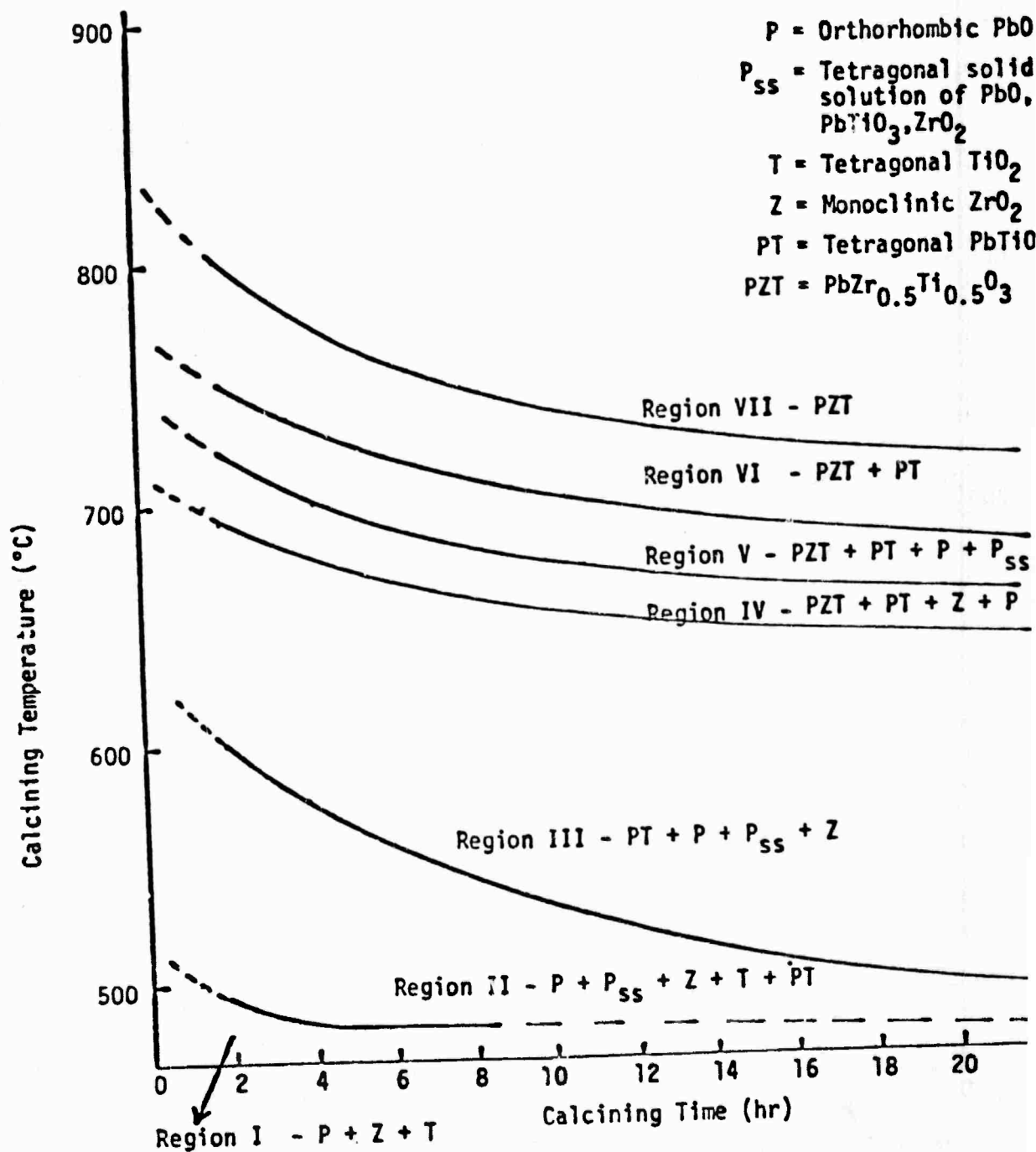
Fig. 4 Calcining reaction diagram for $PbZr_{0.50}Ti_{0.50}O_3$.

14
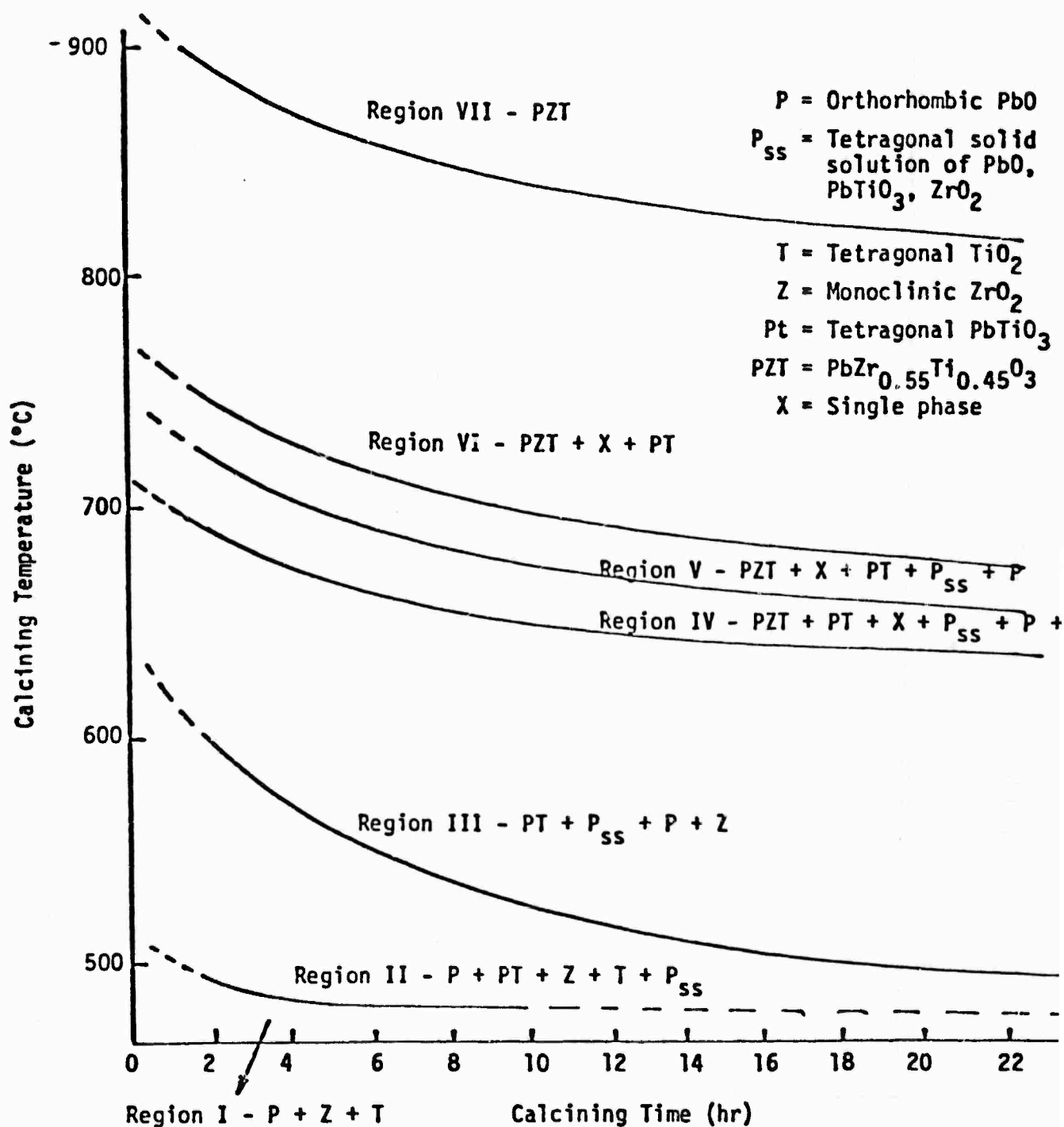
Fig. 5 Calcining reaction diagram for $PbZr_{0.55}Ti_{0.45}O_3$
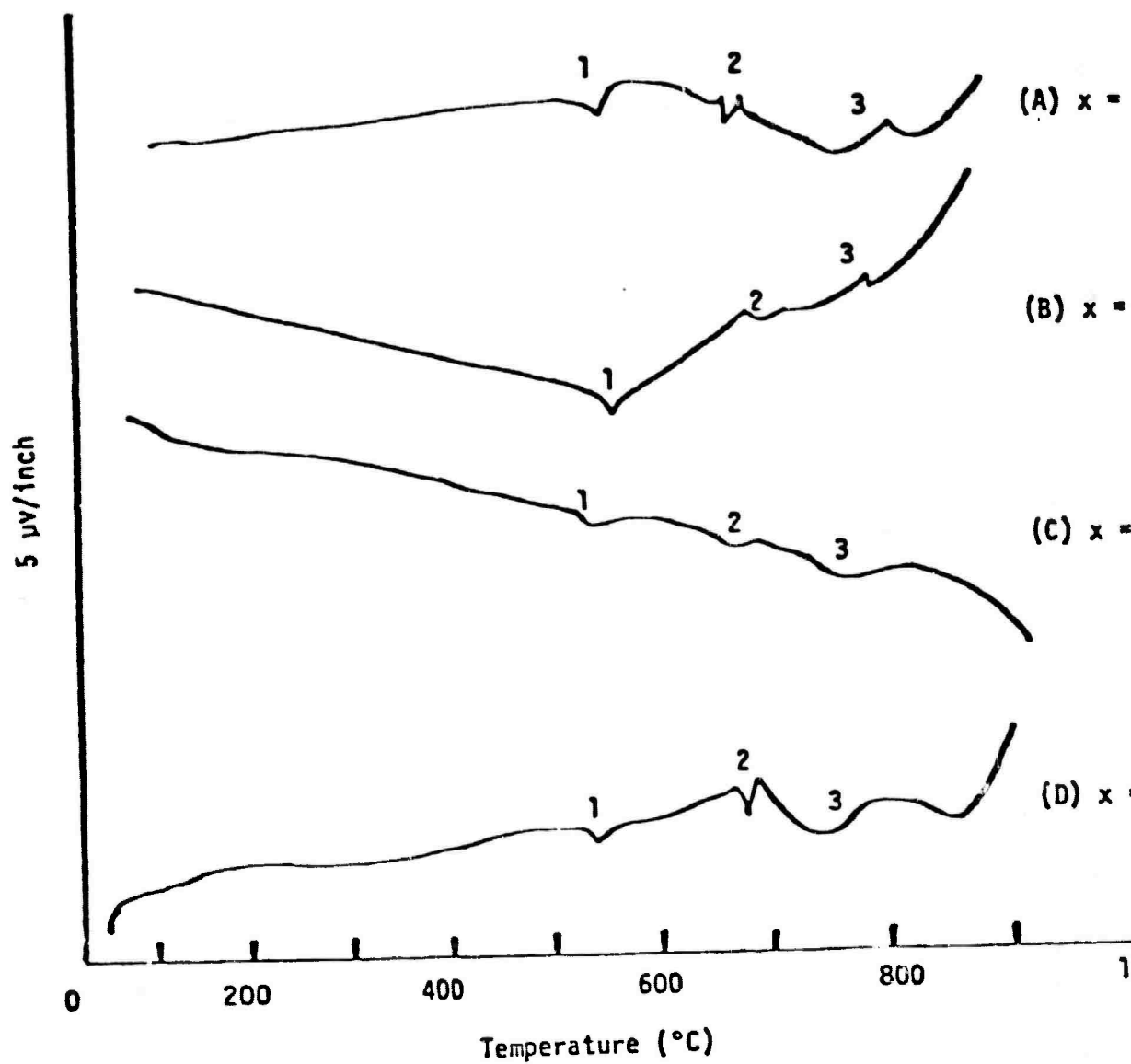
Fig. 6 DTA curves for compositions of $PbZr_xTi_{1-x}O_3$.

APPENDIX 10

Reactivity of Chemically Prepared Lead Zirconate-Lead Titanate
Solid Solutions

S. Venkataramani and J.V. Biggers

Reactivity of Chemically Prepared Lead Zirconate-Lead Titanate

Solid Solutions

S. Venkataramani and J. V. Biggers
Materials Research Laboratory
The Pennsylvania State University
University Park, Pennsylvania 16802

Abstract

The reaction sequences in chemically prepared lead zirconium titanates were studied as a function of temperature and periods of calcining. The reactivity of the ultrafine oxyhydroxide complex of the lead zirconium titanate is so high and the reaction is so different in that (1) the formation of lead zirconium titanate is complete even at as low temperatures as 600°C and (2) the formation is spontaneous and is not sequential to the formation of a lead titanate and the lead oxide solid solution phases. The DTA, TGA, x-ray diffraction, and wet chemical analysis were used to characterize the reaction products.

Reactivity Studies of Chemically Prepared PZTs

INTRODUCTION

The reaction sequences and the formation of the intermediate products, as well as the final PZT from a mixture of the constituent oxides (PbO, ZrO_2, and TiO_2), have been extensively studied[1,2,3,4]. Various reaction sequences have been proposed which include (i) the formation of $PbTiO_3$ and an intermediate PZT before combining to form the required PZT; (ii) the formation of $PbTiO_3$ and an intermediate PbO_{ss} before forming the PZT, and (iii) formation of $PbTiO_3$ and further reaction with ZrO_2 to form the required PZT.

Although it is well established[5,6,7] that in the calcination of a PZT mixture made from precursor chemical compounds of the respective oxides, e.g. alkoxides, nitrates, oxalates, citrates, etc., the completion of PZT formation occurs at much lower temperatures than in the case of conventional mixed oxide compositions, the sequence of reaction has not been looked into in any detail. It is generally proposed that the formation of PZT from chemical precursors on calcining is a one-step process whereby the intermediate hydroxy on nitrate complex decomposes to form PZT without forming any other intermediate products like $PbTiO_3$.

Reaction sequences on calcining chemically prepared PZT compositions were investigated using x-ray diffraction phase analysis DTA/TGA and analytical chemical methods. The results were compared with the ones obtained for PZT compositions from mixed oxides.

EXPERIMENTAL

Preparation of PZT Compositions

Four compositions of PZT, $PbZr_xTi_{1-x}O_3$ with x = 0.5, 0.52, 0.55, and 0.(were prepared both by mixing the respective oxides and by precipitating from alkoxides of zirconium and titanium and PbO. Figure 1 explains the processes involved.

The precipitated and dried PZT compositions were characterized for purity (spec. analysis) and surface area and particle size. The spec. analysis indicated Fe, Si, and Al as the only trace impurities <.001. The BET surface area measurements revealed a specific surface of 70-100 M^2/gm. The CESEMI technique for the particle size distribution analysis proved futile due to extreme agglomeration. Extreme dilution of the dispersion resulted in too few particles to have any conclusive result. However, the SEM pictures tend to reveal the particle size range of about 0.1 µM.

DTA AND TGA STUDIES

All the compositions were studied for the loss by TGA and the reaction sequences by DTA.

The loss of hydroxyl and other occluded species was complete by 400°C, and the PbO loss started to occur around 850°C.

Figure 2 is the DTA data of the chemically prepared PZT compositions.

The endotherms around 400°C and 300-600°C are very diffused and correspond to the decomposition of the hydroxide and the completion of PZT formation respectively.

X-Ray Diffraction and Chemical Analysis Studies

10 gm batches of PZT were calcined at temperatures 300°, 600°, 700°, 800°, and 900°C for periods ranging from 0 to 24 hours in covered sintered alumina crucibles. The calcined samples were tested for weight loss. Phase analysis was studied by x-ray diffraction and complemented by unreacted PbO estimation by chemical analysis. The PbO was estimated by dissolving it in acetic acid and titrating against Std. EDTA using xylenol orange indicator.

RESULTS AND DISCUSSION

Figures 3, 4, and 5 represent the result of the above mentioned studies. From the XRD analysis and the chemical analysis the reaction sequence of the

PZT hydroxide complex on heating is as follows (Fig. 3).

$$PZT \xrightarrow{\;300-700\;} PZ_yT_{1-y} + (P+Z+T)^*$$

$$\Big| \sim 700$$

$$PZT$$
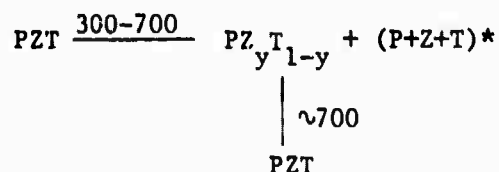
*amorphous to x-ray.

From Figs. 3, 4, and 5 it is seen that the reactivity of PbO to complete PZT formation is a function of time and temperature, the completion being rapid above 700°C.

In contrast to the mixed oxide PZT compositions there is no distinguishabl intermediate product as PT or PbO_{ss}. The results agree with the other studies on the calcination of chemically prepared PZTs. The evidence of unreacted PbO is due to the fact that the hydroxylation of PbO during the precipitation process is not complete and there exists a fraction of unreacted PbO depending on the process parameters. The above is attributed to the fact that on sublimation of cryochemically prepared PZT-nitrate granules[8] no intermediate products or free PbO were seen. After 2 hours at 500°C more than 90% of PbO was bound to the PZT solid solution. Similar results have been obtained by spray-drying nitrate mixtures of PZT and hydroxides of coprecipitated $PbTiO_3$.

CONCLUSION

Thus the completion of PZT formation on calcining is more rapid and less complex in the case of coprecipitated compositions due (i) extremely high chemical homogeneity and (ii) almost complete reaction to form PZT. The precipitate complex is a PZT hydroxide which directly decomposes to PZT. The primary advantage of this is that there will be minimum deviations of stoichiometry and the absence of any intermediate trace products which would have a derogatory effect on the final sintered ceramic in terms of the electrical properties.

REFERENCES

1. S. Mori et al., National Tech. Report 10[1] 32-40 (1964).

2. Y. Matsuo and H. Sasaki, J. Amer. Ceram. Soc. 48[6] 289-291 (1965).

3. M.M. Speri, Ph.D. Thesis, Rutgers University (1969).

4. N.S. Ibraimov, N.C. Troshin, I.A. Silant'eva, Zh. A. Doigaya and V.A. Golovnin, Translated from Izv. Ake. Nauk. SSSR, Neorg. Mat. Vol. 14, 276-279.

5. J. Thompson, Jr., Ceram. Bull. 53@52 421-424, 435 (1974).

6. M. Marata, et al., Mat. Res. Bull. 11, 323 (1976).

7. A.H. Webster, T.B. Weston and R.R. Craig, J. Can. Ceram. Soc. 34, 121-129 (1965).

8. Yu. d. Tret'yakov, et al., Translated from Izv. Aka. Nauk. SSSR, Nerog. Mat. 13[10] 1825-1829 (1977).

9. V.V. Prisedskii, Dissertation, Donetsk (1972).
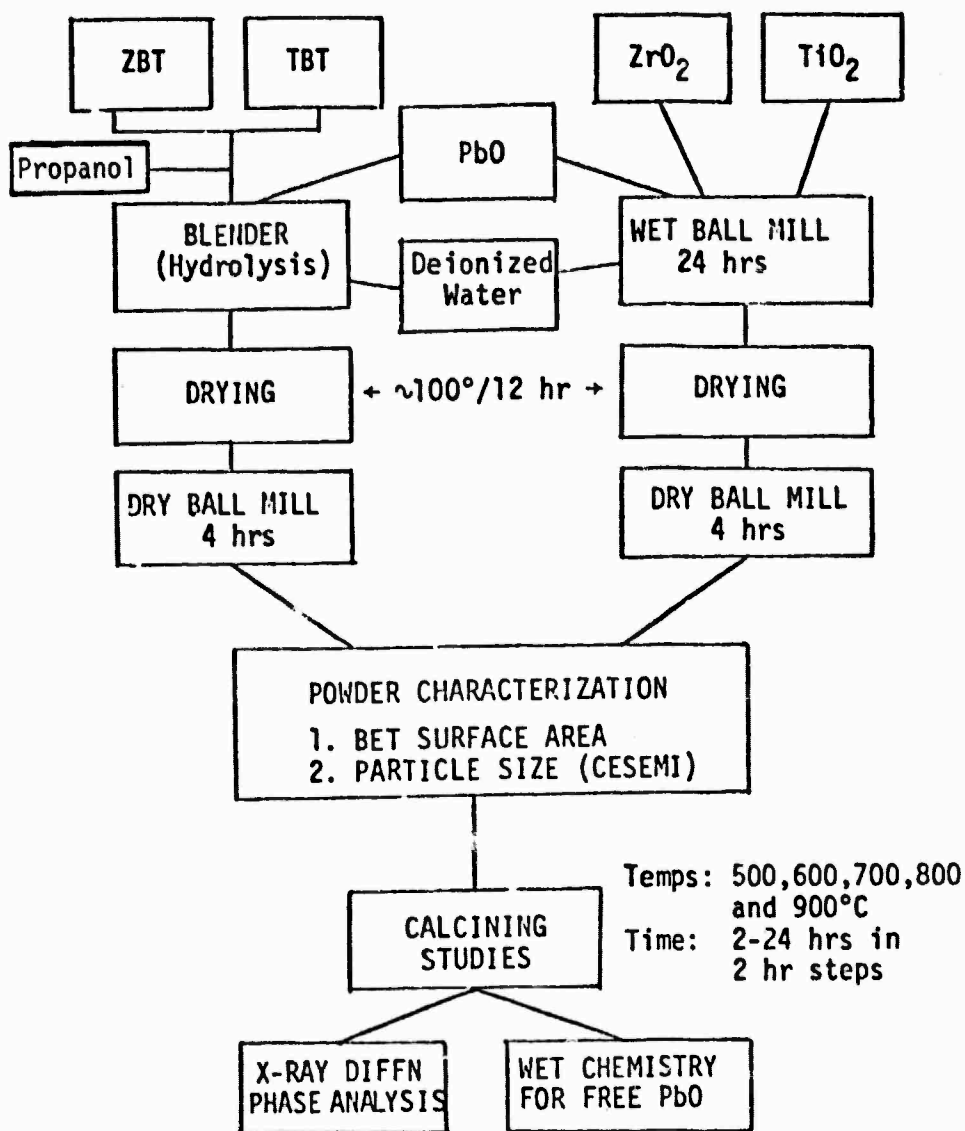
Fig. 1. Processing and Characterization Flow Chart
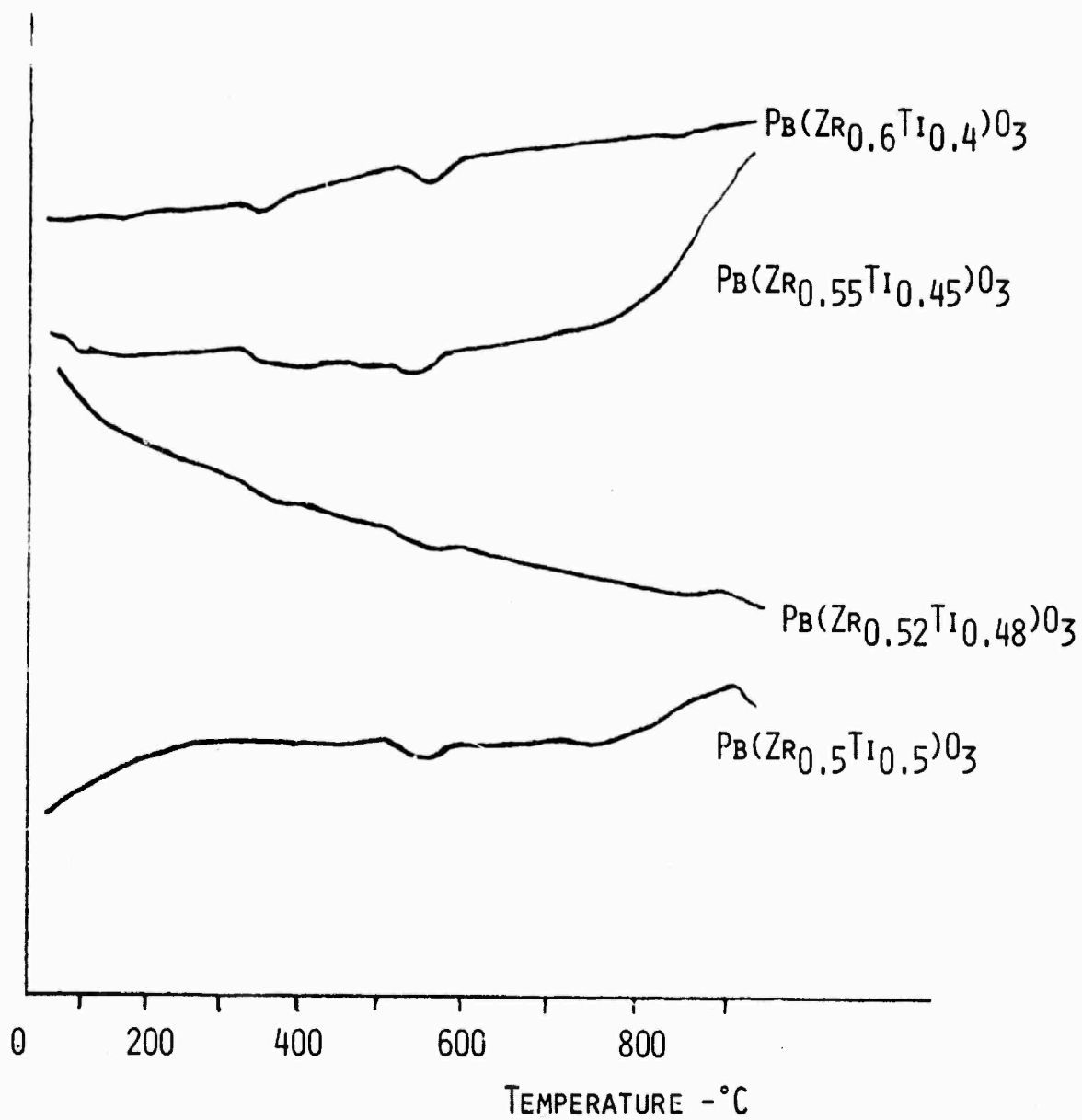
FIG. 2. DTA PATTERNS OF THE PRECIPITATED PZTS.
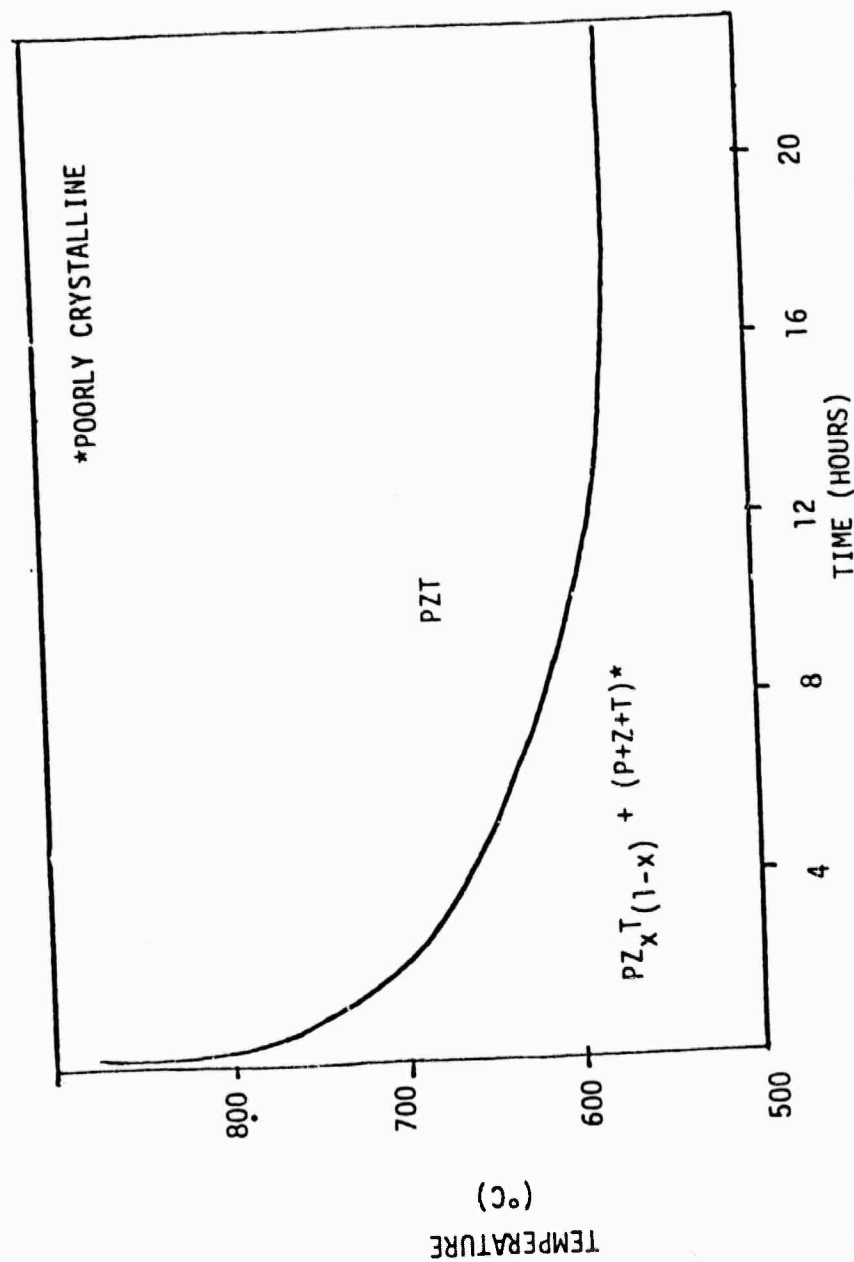
FIG.3 REACTIVITY MAP OF THE PRECIPITATED PZTs

8
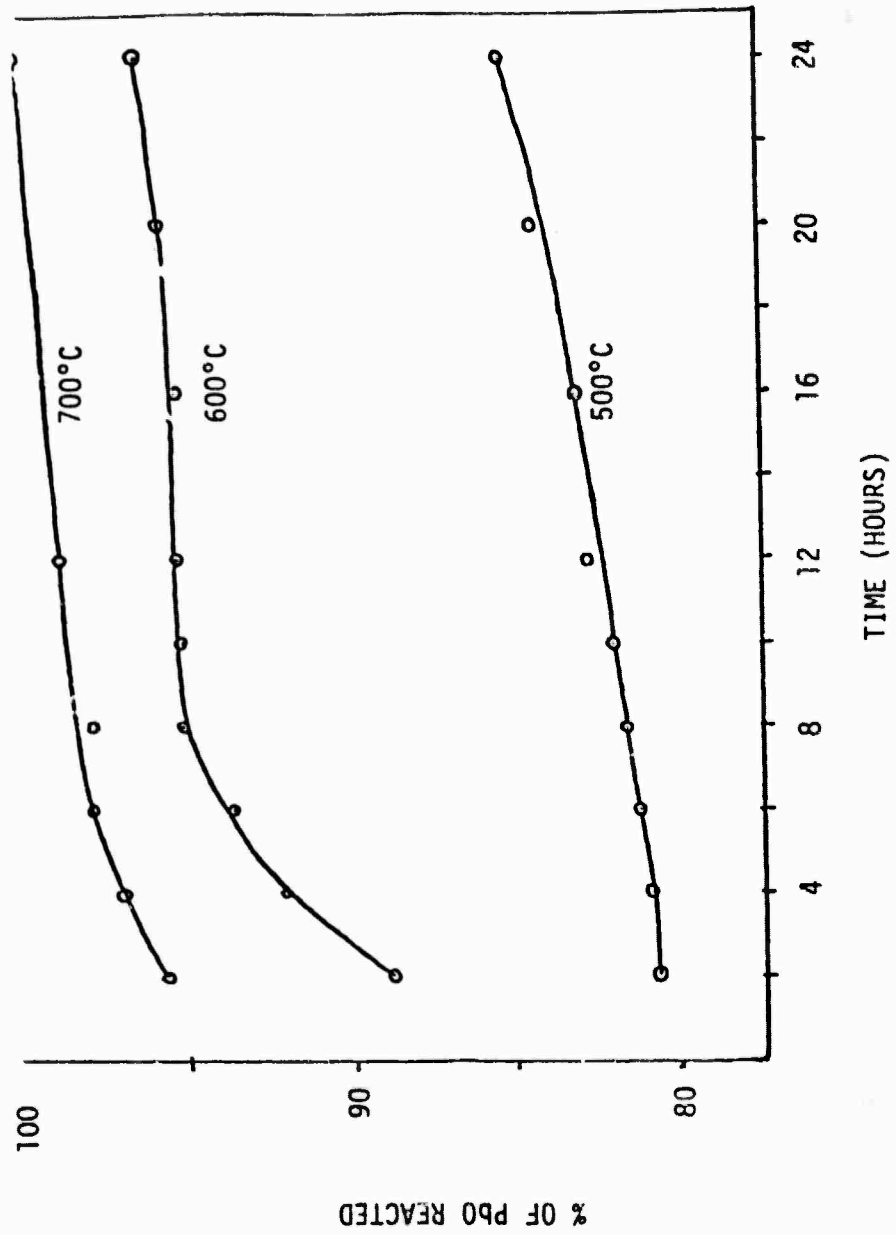
Fig. 4. PERCENT OF LEAD OXIDE REACTED AS A FUNCTION OF CALCINING
TEMPERATURE AND TIME IN THE $Pb(Zr_{0.5}Ti_{0.5})O_3$ COMPOSITION
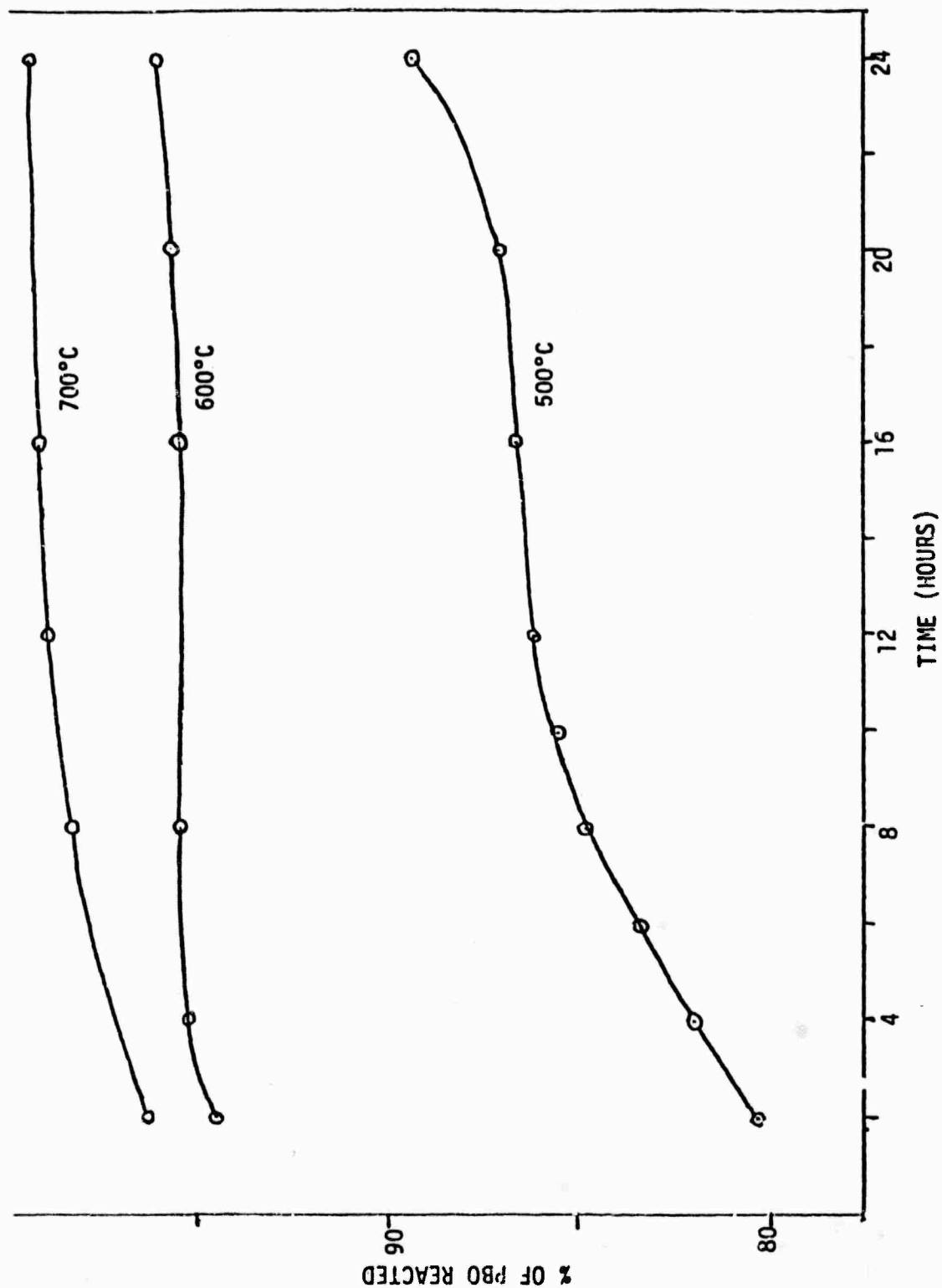
Fig. 5. PERCENT OF LEAD OXIDE REACTED AS A FUNCTION OF CALCINING TEMPERATURE AND TIME IN THE $Pb(Zr_{0.6}Ti_{0.4})O_3$ COMPOSITION.

APPENDIX 11

Hot-Isostatic Pressing of PZT Materials

L.J. Bowen, W.A. Schulze and J.V. Biggers

Hot-Isostatic Pressing of PZT Materials

L.J. Bowen, W.A. Schulze and J.V. Biggers

Abstract

A one-step hot-isostatic pressing (HIP) process is described
in which the time required to produce high quality piezoelectric
devices is considerably less than the conventional sintering
route. The small porosity reductions obtainable by HIP are shown
to have little effect on the relative permittivity, piezoelectric
coefficient and elastic compliance of PZT, but a significant
improvement in dielectric breakdown strength has been obtained.
Densification of PZT during HIP is believed to take place by
a mechanism involving particle deformation, even in materials
containing a liquid second phase at the HIP temperature.

Introduction

Lead zirconate-titanate ceramics, when sintered conventionally in air, usually contain some residual porosity, typically at the 5% level. Porosity is known (1,2) to be detrimental to both mechanical and electric properties, especially to the dielectric breakdown strength. Efforts to eliminate porosity have included the use of sintering aids (3,4), hot pressing (5,6,7), and hot-isostatic pressing (8,9). Hot pressing is capable of enhancing densification without affecting the driving force for grain growth, thus improving microstructure control. However, it is limited in shape capability to devices having simple disc configurations and requires an inert die material. Hot-isostatic pressing (HIP), on the other hand, offers the possibility of producing high density components in any shape without risk of contamination since dies are not required for the process.

Hot-isostatic pressing is the densification of a powder compact by the simultaneous application of heat and high gas pressure. To prevent gas penetration into the pores the compact must be either:

(a) Hermetically sealed in an impervious outer sheath which is capable of deformation to transmit the applied pressure to the compact (10) or

(b) Conventionally fired to the closed porosity stage (>92% of theoretical density) and then HIP without cladding in a low diffusivity pressure medium such as argon (8,9).

Aside from powder consolidation, HIP has been used commercially for healing casting defects in metal ingots and metal cladding by gas pressure bonding (10). In this context the HIP process offers the possibility of obtaining high density in composite ceramics containing materials of different composition which sinter at different rates (11).

It is the aim of the present work to report the results of an investigation on the effect of porosity removal by HIP on the dielectric properties of PZT piezoelectrics. Although the authors have HIP-densified PZT using the cladding method (platinum foil encapsulant), the majority of the results to be described have been obtained using the prefiring technique in a modified form which eliminates the need for separate prefiring and HIP stages.

Experimental

The Hot-Isostatic Press

In early attempts to build a hot-isostatic press based on conventional furnace design, problems associated with convectional heat loss at high gas pressures were encountered, leading to steep temperature gradients in the hot zone and excessive power input requirements. Experiment showed that the temperature gradients could be largely eliminated by incorporating a hearth heater into the furnace structure. However, the low thermal efficiency meant that furnace designs based on conduction and radiation controlled heat transfer had to be abandoned in favor of a system designed to eliminate convection.

Accordingly, in the present HIP design (Fig. 1) the heating element, a platinum/20% rhodium-wound alumina crucible 100 mm high x 50 mm internal diameter, is enclosed within four sealed concentric ceramic and metal cans which act as convection barriers. This arrangement, which can be readily assembled for rapid specimen turnaround, has proved to be very thermally efficient, requiring only 0.8 KVA of power to maintain the hot zone at 1300°C under 20 MNm^{-2} argon pressure. Although these HIP conditions are typical of those used for the PZT compositions under investigation, by substituting a molybdenum-wound element for the platinum/rhodium one it is possible to extend the temperature capability to 1700°C.

Hot-zone temperature was monitored using four Pt/Pt + 10% Rh thermocouples spaced 25 mm apart along the length of the hot zone. TC2 (Fig. 1) was the control thermocouple. Large specimens were found to interrupt the convection path within the hot zone and reduce its ability to even out temperature gradients Although a large temperature drop was observed in the lower part of the furnace, the temperature within the upper 25 mm of hot zone was constant to within 10°C at 20 MNm^{-2} pressure for the specimens used.

High pressure argon was provided from a 600 psi cylinder and recycled after the HIP operation using two auxiliary low pressure cylinders. About ten minutes was required for the HIP to reach a working pressure of 20 MNm^{-2} from atmospheric pressure.

Materials Processing

The lead zirconate-titanate was supplied in powder form by Ultrasonic Corporation* in "soft" and "hard" grades designated 501A and 401-888 respectively Table I shows manufacturer's data for sintered specimens made from both powders. Specimens for HIP were prepared by die pressing, tape casting (11) and extrusion and all contained an organic binder. The extruded material was made in a "honeycomb" configuration from 501 A PZT by Corning.** A hot-isostatically pressed specimen of this material is shown in Fig. 2 and represents the type of material for which HIP is the ideal densification process. No differences in HIP densification behavior between samples of the same material prepared by different forming techniques were observed.

The specimens were placed inside a platinum foil-lined alumina crucible fitted with a platinum-covered alumina lid which was previously diamond-ground to fit accurately on the crucible. The platinum covering on the lid provided a

---

*Ultrasonic Powders Inc., South Plainfield, New Jersey, 07080.

**Corning Glss Works, New York, 14830.

tight seal at the firing temperature thus minimizing contamination of the HIP
by PbO evaporation. All the specimens were sintered in the presence of powdered
lead zirconate to further obviate any change in their composition due to lead
oxide vaporization.

For comparison of their electrical properties, specimens were of three
types: conventionally fired in air, fired in oxygen, and hot-isostatically
pressed. All the specimens had the same total time at temperature. The con-
ventional firing and HIP processes are compared in Fig. 3. Conventional firing
involved a slow binder burnout in flowing air to 800°C followed by sintering
in air at 1330°C for two hours. Firings in oxygen have been undertaken because
of reports (12) in the literature that an oxygen atmosphere enhances densifica-
tion in lanthanum-doped PZT. The hot-isostatic pressings were made by a one-step
process in which binder burnout, presintering, and hot-isostatic pressing take
place in situ. One-step HIP is made possible by suitable atmosphere control
during heating. Initially the powder compact is heated at $12°C$ min^{-1} in vacuum
(<1 mm Hg) up to 500°C in order to vaporize the binder. The HIP is then back-
filled with oxygen at 760 mm Hg and the powder compact heated at 1300°C for one
hour. At this stage the specimen contains only closed pores filled with oxygen.
To complete the process the HIP is pressurized with argon to 20 MNm^{-2} pressure,
maintained under these conditions for one hour, and finally cooled under
pressure. This one-step HIP process takes only five hours including cooling
time compared to approximately forty hours total required for the conventional
air-sintering method.

Results and Discussion

1. Densification

Relative densities, measured using a vacuum mercury displacement densitometer*,

---

*The American Instrument Company, Silver Spring, Maryland, 20910.

and assuming theoretical density to be 8,000 Kg m^{-3} for all the compositions, are presented for the sintered and hot-isostatically pressed specimens in Table II. The application of argon pressure at the sintering temperature increased the density typically by 3 to 4% resulting in ceramics over 98% dense. Figure 4 shows the microstructures of extruded 501A (a) after sintering and (b) after HIP. The large pores evident in Fig. 4(a) were completely eliminated by hot-isostatic pressing, along with minor cracks introduced during extrusion.

Figures 5(a) and 5(b) respectively compare the microstructures of HIP 501A and a HIP stoichiometric PZT of composition $PbZr_{0.60}Ti_{0.40}O_3$ prepared by the present authors from high-purity mixed oxides. These specimens were prepared for SEM examination as polished sections and then etched for 25 seconds in an aqueous mixture of 5% HCl and 0.5% HF. Etching has revealed the grain boundaries and 180° domain walls in both specimens. The grain boundaries in the 501A specimen are considerably wider than those in the stoichiometrically pure PZT, indicating the presence of a second phase evenly distributed around the grains and therefore probably liquid at the HIP temperature. PbO-rich liquid second phases have previously been cited in the literature as densification aids for sintering and hot pressing PLZT (4,13) and PZT (14).

The application of pressure to a densifying powder compact is known to increase the rate of densification by increasing the effective stress between grains in contact, irrespective of whether the rate-controlling densification mechanism is particle rearrangement, diffusional creep, or plastic flow. Densification generally takes place by one or a combination of these three mechanisms. However, in hot-isostatic pressing the presence of a continuous liquid phase at the grain boundaries makes possible an alternative densification emchanism which cannot be discounted without experimental proof— that is, extrusion of liquid under pressure from between grains into the pores. This

mechanism has been shown (15) to lead to a microstructure containing compara-
tively large regions of second phase at the locations of the original pores.
No such regions were observed in the HIP 501A material by scanning electron
microscopy. In addition, densification during HIP took place over a period of
hours, consistent with a slow process involving particle deformation rather
than an extrusion process which might be expected to be rapid unless the liquid
were extremely viscous. The implication is that surface energy in the narrow
regions between grains is sufficient in this material to hold the liquid in
place against the applied pressure and permit the occurrence of conventional
densification processes.

Electrical Properties

Table II compares the values of relative permittivity and piezoelectric
coefficient for 401-888 and 501A specimens prepared by sintering and HIP. Any
differences between the values for each material are small (<10%) and are not
apparently systematically related to the processing conditions.

In order to examine the effect of HIP on the Curie temperature the change
in relative permittivity with temperature for sintered and HIP 501A specimens
was followed by heating the specimens at a constant rate of $4°C$ minute^{-1}.
The data are shown in Fig. 6 and indicate that relative permittivity and Curie
temperature are almost unaffected by the increase in density due to HIP. How-
ever, the dissipation factor, D, is somewhat reduced at all temperatures in
the HIP material compared to sintered PZT. This effect may be due to an
increase in resistivity with the reduction in porosity.

Also shown in Table II are dielectric breakdown strength values for the
various materials. In all cases an improvement in dielectric breakdown strength
is seen with increasing relative density, in agreement with results published
for hot-pressed PZT (5). For the 401-888 and extruded 501A materials the

improvement is quite marked -- about 25%. This is particularly advantageous for the extruded material in which the observed flaw distribution (Fig. 4a) peculiar to extrusion (cracks and large elongated pores) render the dielectric breakdown strength barely sufficient for poling in the sintered ceramic.

It is possible to predict the effects of porosity on the relative permittivity using linear theory. By considering the ceramic to be a two-phase material having a solid continuous phase (relative permittivity K_1) containing randomly distributed spherical pores (volume fraction V), Rushman and Strivens (16) derived on the basis of the Wiener (17) formula the following equation for the relative permittivity, $\bar{K}$, of the composite:

$$\frac{K_1 - \bar{K}}{\bar{K} + 2K_1} \approx \frac{V}{2} \qquad (K_1 \gg 1) \tag{1}$$

For small amounts of porosity (up to 20%) this formula approximates to:

$$K_1 = \bar{K}(1 + 1 \cdot 5V) \tag{2}$$

Equation (2) predicts an 8% increase in relative permittivity for a 5% reduction in porosity, comparable to the scatter in the data in Table II.

Okazaki and Nagata (1) have established empirically the general formula:

$$X = X_o e^{-AP} \tag{3}$$

A constant, P fractional porosity

which they have shown to apply to many of the electrical and elastic properties of PZT over the porosity range 0-15%. Substituting the appropriate values of X_o, A and P into equation (3) yields a 16% change in relative permittivity for 5% change in pore volume. Therefore equations (2) and (3) predict only a small improvement in relative permittivity from the reduction in porosity expected using HIP, in agreement with the experimental data of Table II.

In order to study the effect of porosity reduction on elastic properties
sintered and HIP specimens of 401-888 were prepared in the form of bars,
accurately ground to the same size, 13 x 1 x 0.5 mm, and subjected to resonance
measurements. The resonance spectra of the bars were measured over the frequency
range 0-10 MHz (no resonance peaks were observed above 10 MHz) using a Hewlett-
Packard network analyzer.*

Resonance data for air-sintered, oxygen-sintered and HIP specimens are
compared in Fig. 7. It can be seen that the reduction in porosity has had no
observable effect on peak shape or resonant frequency under the experimental
conditions used. The value of the fundamental resonant frequency (f_r) is related
to the elastic compliance, S, of a material by the equation:

$$N = f_r \ell = \frac{1}{2\sqrt{\rho \cdot S}} \qquad (4)$$

where N is the frequency constant, ℓ the controlling dimension, and ρ the
relative density. Using the data of Okazaki and Nagata (1) and equation (3) to
determine the dependence of elastic compliance on porosity, equation (4) predicts
a reduction in N of only 8% for the 4% increase in density obtained by HIP.

Conclusions

A one-step hot-isostatic pressing process has been developed which is
capable of producing high quality PZT-based materials in considerably shorter
times than conventional sintering routes. The densification mechanism during
HIP of 501 A PZT is believed to take place by particle deformation, even in
specimens which contain a liquid phase at the HIP temperature.

The predicted effects of an increase in density in piezoelectric ceramics
are generally to improve their electrical and elastic properties. However,
it has been shown, on a theoretical basis and experimentally, that the small

---

*Model 8407A, Hewlett-Packard, Palo Alto, California.

reductions in porosity obtainable by hot-isostatic pressing do not significantly affect the relative permittivity, piezoelectric coefficient and elastic compliance of PZT. The main advantages of hot-isostatic pressing lie in its ability to confer high dielectric breakdown strength on devices of complex shape and in its potential for production of high density composites.

References

1. K. Okazaki and K. Nagata. Effects of Density and Grain Size on the Elastic and Piezoelectric Properties of Pb(Zr-Ti)O$_3$ Ceramics. Mech. Behav. Mater., Proc. Int. Conf. 1st 4, 404-412, 1972.

2. W.D. Kingery. Introduction to Ceramics, 2nd ed., 930, Wiley, 1976.

3. R.B. Atkin and R.M. Fulrath. Point Defects and Sintering of Lead Zirconate-Titanate, J. Amer. Ceram. Soc. 54(5) 265-270, 1971.

4. C.S. Snow. Fabrication of Transparent Electrooptic PLZT Ceramics by Atmosphere Sintering, J. Amer. Ceram. Soc. 56(2) 91-96, 1973.

5. A.J. Mountvala. Hot-Pressing Piezoelectric and Ferroelectric Materials, Bull. Amer. Ceram. Soc. 42(3) 120-12`, 1963.

6. K. Okazaki. Sintering Process of Lead Zirconate-Lead Titanate Ceramics by Hot Pressing and Their Electrical Properties, Mem. Def. Acad. Japan, VII(2) 383-398, 1967.

7. V.L. Balkevich and C.M. Flidlider. Hot Pressing of Piezoelectric Ceramics in the PZT System, Ceram. Int. 2(2) 81-87, 1976.

8. K.H. Härdtl, Gas Isostatic Hot-Pressing Without Molds, Bull. Amer. Ceram. Soc. 54(2) 201-205, 1975.

9. K.H. Härdtl. A Simplified Method for the Isostatic Hot Pressing of Ceramics, Philips Tech. Rev. 35, 65-72, 1975.

10. H.D. Hanes, D.A. Seifert and C.R. Watts. Hot-Isostatic Processing, MCIC Report 77-34, November 1977, Metals and Ceramics Information Center, Columbus, Ohio.

11. T. Shrout, W.A. Schulze and J.V. Biggers. The Effect of Post Costing Pressing on the Density to the Cost PZT, to be publsied, Bull. Am. Ceram. Soc.

12. G. Snow. Improvements in Atmosphere Sintering of Transparent PLZT Ceramics, J. Amer. Ceram. Soc. 56(9) 479-480, 1973.

13. R.H. Dungan and A.S. Snow. Hot-Pressing Range Diameter PLZT Electrooptic Ceramics, Amer. Ceram. Soc. Bull. 56(9) 781-782, 1977.

14. V.V. Prisedskii, L.G. Gusakova and V.V. Klimov, The Kinetics of the Initial Stage of Sintering of Lead Zirconate-Titanate Ceramic, Izvestiya Akademii Nauk SSSR, Neorganischeskie Materialy 12(11) 1995-1976.

15. U. Engel and H. Hübner. Strength Improvement of Cemented Carbides by Hot-Isostatic Pressing. J. Mat. Sci. 13, 2003-2012, 1978.

16. D.F. Rushman and M.A. Strivens. The Effective Permittivity of 2-Phase Systems, Proc. Phys. Soc. 59, 1011-1016, 1947.

17. Wiener, Leipzig Ber. 62, 256, 1910.

Table I. Commercial Data for Ultrasonics 501A and 401-488 Ceramics

Material	Relative permittivity	Dissipation factor (1 KHz)	Curie Temp (°C)	d_{33} $Cn^{-1} \times 10^{-12}$	Relative Density	Elastic S^E_{33} Compliance $m^2N^{-1} \times 10^{-10}$	Mechanical Q
501A	2000	0.014	360	400	0.96	0.19	80
401-488	1000	0.003	325	215	0.96	0.14	1000

Table II

Specimen	Sintering Conditions	Relative Density	Dielectric Constant 25°C, 1KHz	d_{33} CN^{-1} $\times 10^{12}$	Dielectric* Breakdown Strength KV m^{-1}
401-888 Tape	Air sinter	0.95	825	265	4600
401-888 Tape	Oxygen sinter	0.96	858	240	5400
401-888 Tape	HIP	0.99	802	240	6700
501A Pressed	Oxygen sinter	0.97	1109	295	7400
501A Pressed	HIP	0.98-0.99	1158	320	8000
501A Corning Extruded	Oxygen sinter	0.93-0.94	---	---	2500
501A Corning Extruded	HIP	0.97-0.98	---	---	3200

*Dielectric breakdown strength values shown are the mean of 4 or 6 samples of similar size from each specimen tested under identical conditions.

Fig. 1. The hot-isostatic press.

STEEL BOMB

FIBERFRAX

STAINLESS STEEL

ALUMINA CANS

TC1
TC2
TC3
TC4

Pт + 20% Rн FUF
WINDING

ALUMINA SUPPORT

GAS INLET
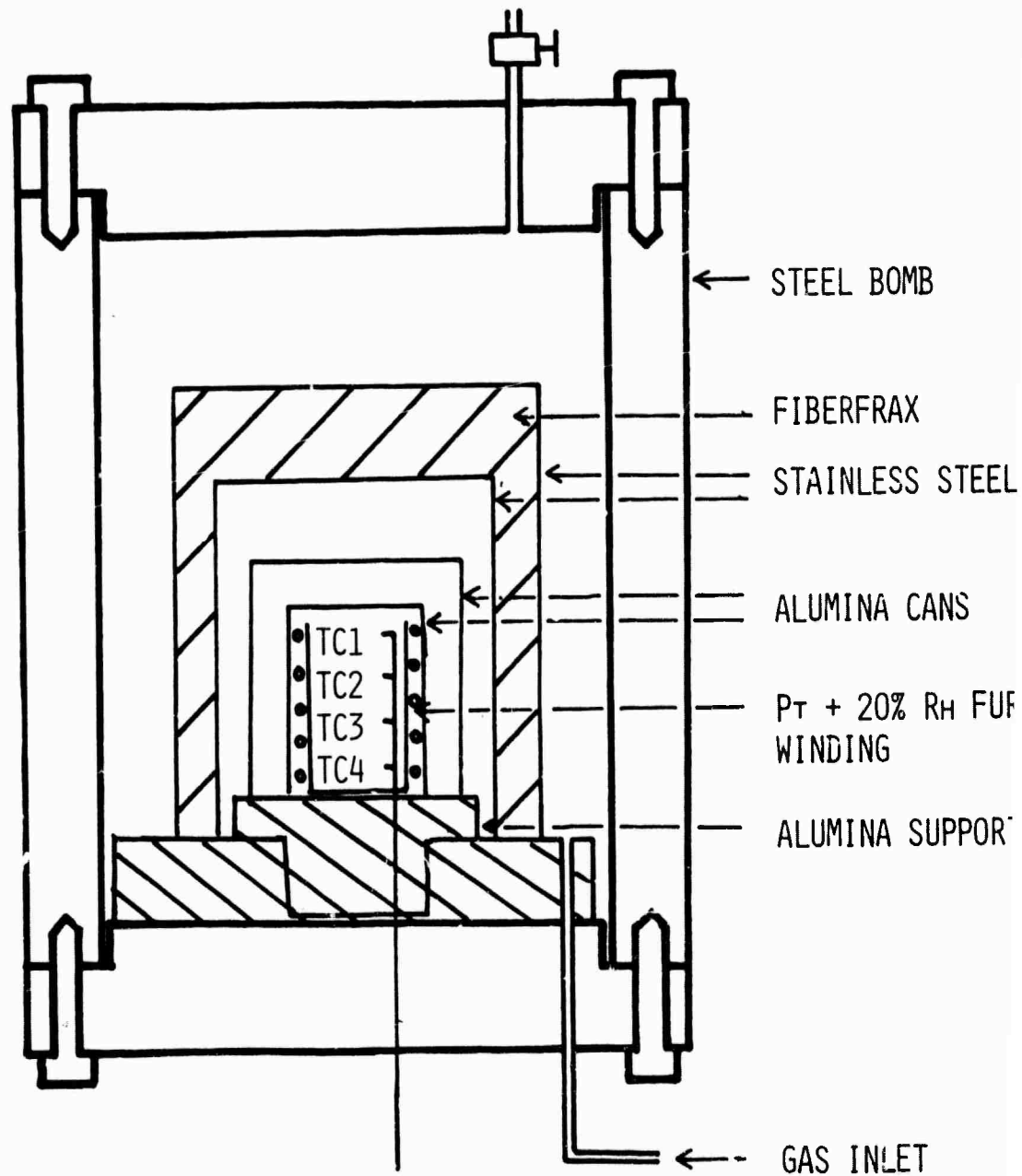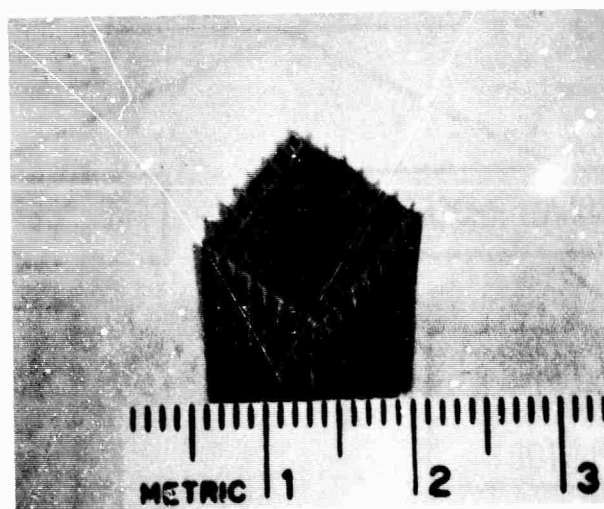
Fig. 2. A hot-isostatically pressed specimen of PZT prepared by the Corning extrusion process.

Fig. 3. Comparison of the one-step HIP and conventional sintering processes.
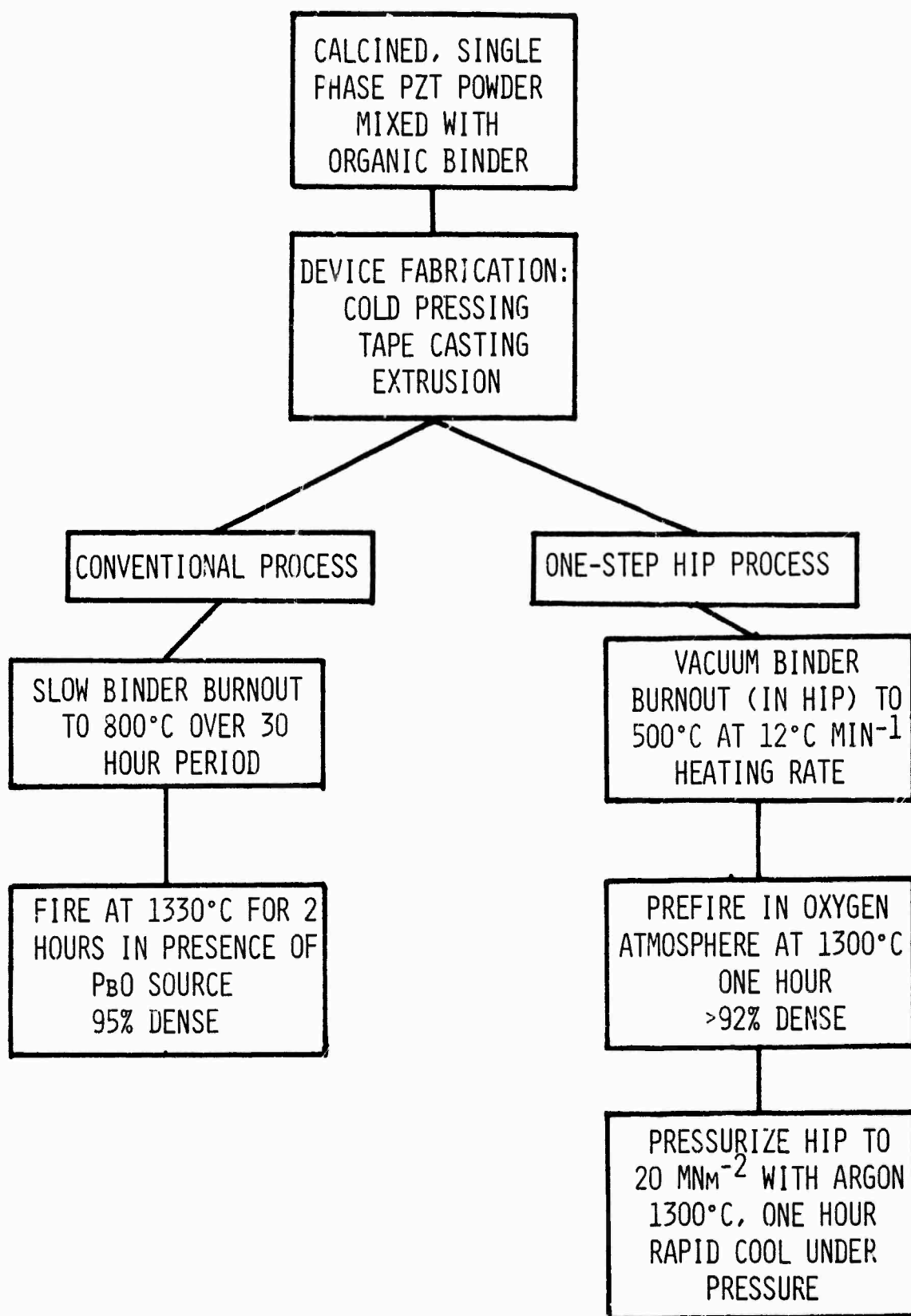
Fig. 4. Extruded PZT microstructures (a) conventionally sintered and (b) hot-isostatically pressed.

(a)   ├────300 µm────┤

├──300 µm──┤

(b)
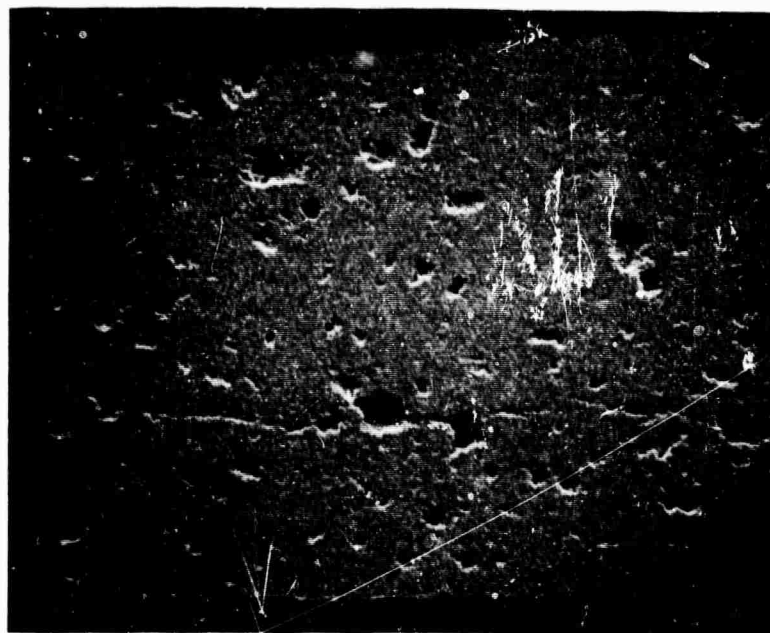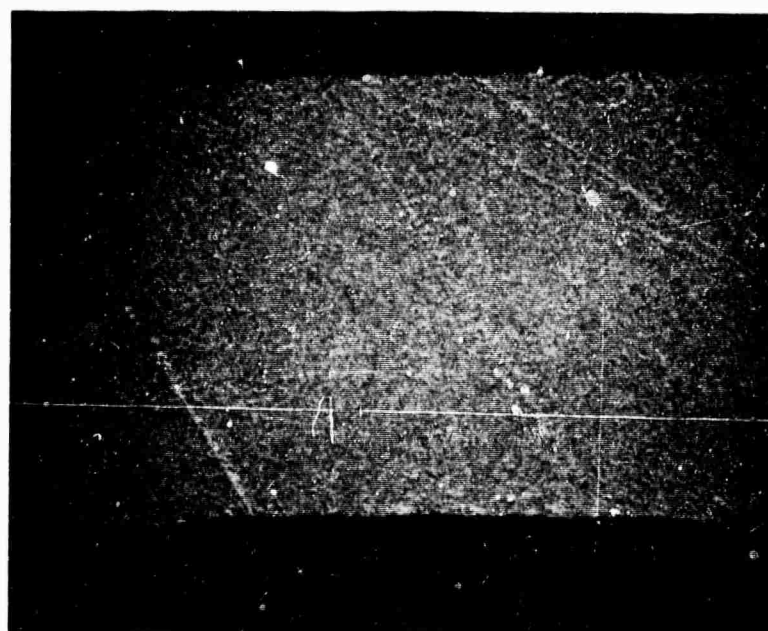
Fig. 5. Microstructures of HIP PZT.

├── 10 μm ──┤

(a) PZT 501 A.
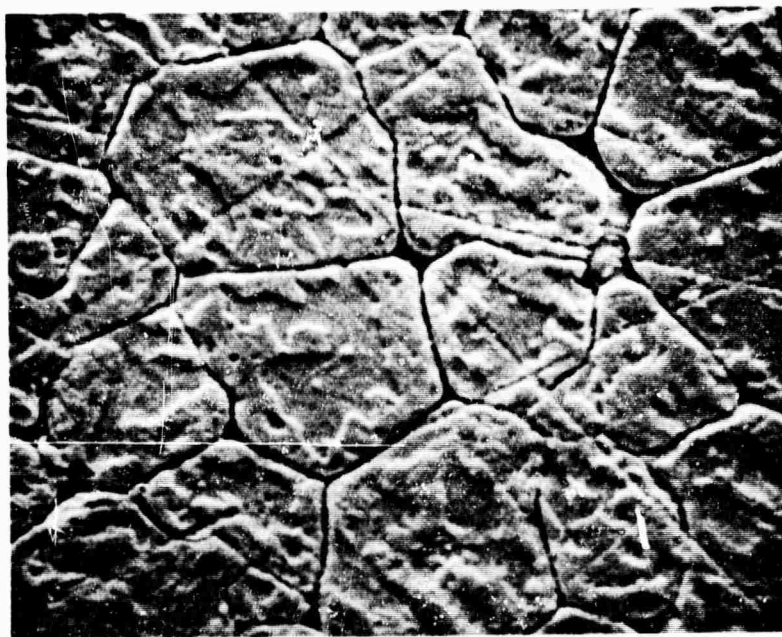
├── 10 μm ──┤

(b) $PbZr_{0.6}Ti_{0.4}O_3$
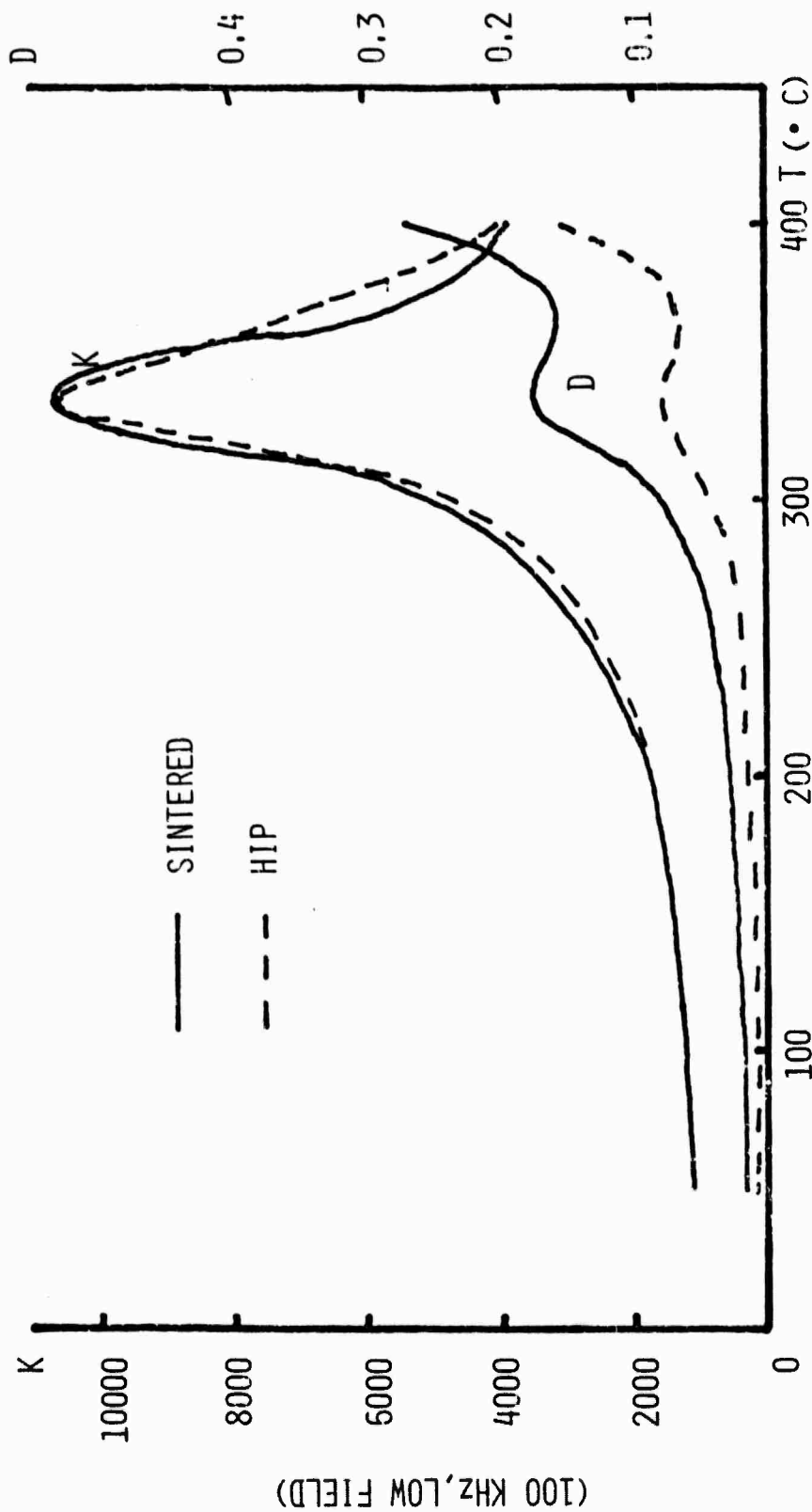
Fig. 6. Relative permittivity (K) and dissipation factor (D) as a function of temperature for conventionally sintered and HIP PZT 501A.

(a)

(b)

(c)
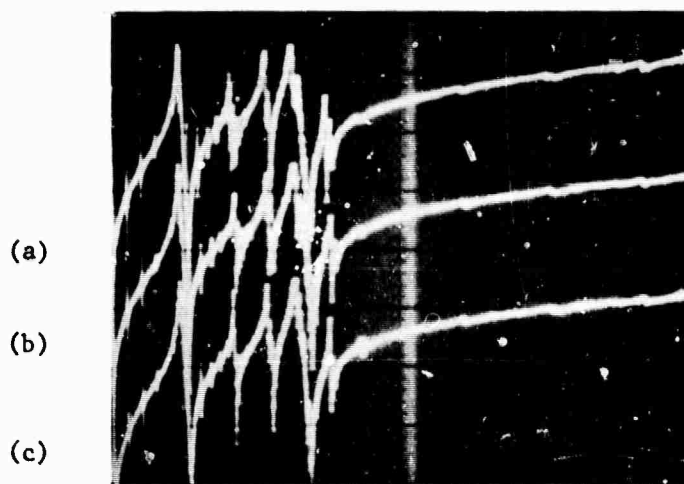
Fig. 7. Resonance spectra for (a) air-sintered,
(b) oxygen-sintered, and (c) HIP 401-888
PZT. Horizontal scale 1 MHz per divi-
sion.

APPENDIX 12

A Study of Acentricity in Complex Perovskites Based on Tellurium Oxide
Using Optical Second Harmonic Generation (SHG)

A. Sa Neto, L. E. Cross and R. E. Newnham

A STUDY OF ACENTRICITY IN COMPLEX PEROVSKITES BASED ON TELLURIUM OXIDE USING OPTICAL SECOND HARMONIC GENERATION (SHG)

A. Sa Neto, L. E. Cross and R. E. Newnham
Materials Research Laboratory
The Pennsylvania State University
University Park, PA 16802

Abstract

A large number of complex perovskites of the general formula $A^{+2}(B'^{2+}_{0.5}B''^{6+}_{0.5})O_3$ where B'' is the tellurium ion, A is Sr, Ca, or Cd and B' is Mg, Co, Zn, Cd, Sr, Ca or Mn have been synthesized as single phase powders in the perovskite structure. Using the SHG technique on powder samples only four from the 19 compounds synthesized showed any harmonic generation, namely Sr_2CdTeO_6, Sr_2CaTeO_6, Sr_2SrTeO_6 and Cd_2MgTeO_6. The results suggest that many of the phase transitions which have been identified earlier in these crystals must be into ordered antiferroelectric structures.

A number of complex mixed oxides of the general formula $A^{+2}(B^{+2}_{0.5}B''^{+6}_{0.5})O_3$ where B'' is the tellurium ion, A is one of the cations Sr, Ca, Cd and B'' is chosen from Mg, Co, Zn, Cd, Sr, Ca and Mn have been studied earlier by Politova and Venetsev (1) and shown to exhibit phase transitions to distorted structures. It is not clear from these x-ray and dielectric studies whether or not the lower temperature phases are ferroelectric, and the present study was initiated to resolve this question. Theoretical and experimental studies by DiDominico and Wemple (2,3) have shown that in oxygen octahedron ferroelectrics there is a close correlation between the spontaneous electric polarization and the optical second harmonic generation in these crystals, i.e. perovskite structure crystals which are ferroelectric at room temperature should be strong optical harmonic generators

with respect to quartz (provided of course that the crystals are transparent in the appropriate frequency range). Thus it was decided to fabricate a wide range of the tellurate based materials by simple mixed oxide techniques, to check the powders for phase purity by x-ray methods, and to then determine the SHG efficiency of the resulting perovskite phases.

An important feature of the powder SHG method (4) is that the harmonic intensity is a strong function of particle size, both for materials whose indices of refraction are such as to permit phase matching, and for non-phase matchable crystals. If one is to obtain even semi-quantitative assessment from the powder method it is thus important to compare powders of similar mean particle size. In the present study the automatic CESEMI particle sizing techniques of Johnson and White (5) were used to confirm that particles which had been seived to screen them were of the appropriate size and in a suitably narrow size distribution range. Details of the SHG apparatus and technique used have been described elsewhere (6). The results of the present study are given in Table 1 which summarizes the compounds studied, the average particle diameter, the type of structure and the SHG intensity (if any) as a fraction of the corresponding intensity from a quartz which had an average particle size of 26μ meters.

Using the criterion given by Kurtz (4) that the powder should be classified as acentric if the signal is larger than 1/100 that of quartz, Sr_2CdTeO_6, Sr_2CaTeO_6, Sr_2SrTeO_6 and Cd_2MgTeO_6 may be thus classified. However, on the expectation of the strong harmonic intensity from a ferroelectric perovskite at room temperature, it appears doubtful that such a weak intensity is a true bulk phenomenon indicative of useful ferroelectric activity.

A rather clear indication that this is probably the case is given by intercomparison with the structures determined by Politova and Venetsev given in column 5 of Table 1. In these studies both Sr_2CaTeO_6 and Sr_2SrTeO_6 were

classified as cubic m3m and therefore should not be acentric.

It would appear that these studies tend to confirm the expectation that when there are two very dissimilar cations in equal proportions in the B sites of the ABO_3 structure, these cations will order, and that the resulting order will strongly favor antiferroelectric over alternative possible ferro-electric phases.

Table 1. Complex tellurate perovskite studies summary of structural and SHG information.

Compound	Average Particle Diameter	X-ray Structure (Politova, et al.)	SHG	Intensity factor I_{Te}/I_Q
Sr_2MgTeO_6	30.2	cubic	centric	0
Sr_2CoTeO_6	26.6	monoclinic	centric	0
Sr_2ZnTeO_6	35.4	monoclinic	centric	0
Sr_2MnTeO_6	28.1	cubic	centric	0
Sr_2CdTeO_6	37.3	monoclinic	acentric	<0.02
Sr_2CaTeO_6	35.5	cubic	acentric	<0.02
Sr_2SrTeO_6	32.9	cubic	acentric	<0.02
Ca_2MgTeO_6	29.8	monoclinic	centric	0
Ca_2CoTeO_6	26.7	monoclinic	centric	0
Ca_2ZnTeO_6	25.6	monoclinic	centric	0
Ca_2MnTeO_6	29.4	monoclinic	centric	0
Ca_2CdTeO_6	28.6	monoclinic	centric	0
Ca_2CaTeO_6	30.1	monoclinic	centric	0
Cd_2MgTeO_6	31.9	monoclinic	acentric	<0.02
Cd_2CoTeO_6	34.7	monoclinic	centric	0
Cd_2ZnTeO_6	33.6	monoclinic	centric	0
Cd_2MnTeO_6	28.2	monoclinic	centric	0
Cd_2CdTeO_6	27.4	monoclinic	centric	0
Cd_2CaTeO_6	28.5	monoclinic	centric	0

References

1. Politova, E. D., Venevtsev, Yu. N., Soviet Phys. Dokl. $\underline{18}$, 264 (1973).

2. DiDomenico, D., Wemple, S., J. Appl. Phys. $\underline{40}$, 720 (1969).

3. DiDomenico, D., Wemple, S., J. Appl. Phys. $\underline{40}$, 720 (1969).

4. Kurtz, S. K., Perry, T. T., J. Appl. Phys. $\underline{39}$, 3768 (1968).

5. Johnson, G. G., White, E. W., Science $\underline{176}$, 922 (1972).

6. Newnham, R. E., Kramer, J. J., Schulze, W. A., Brindley, G. W., Phys. Chem. Min. $\underline{1}$, 379 (1977).

APPENDIX 13

RF Sputtering of $Sr_2Nb_2O_7$

A. Sa Neto and L.E. Cross

RF SPUTTERING OF $Sr_2Nb_2O_7$

A. Sa Neto and L. E. Cross
Materials Research Laboratory
The Pennsylvania State University
University Park, PA 16802

Abstract

The deposition of $Sr_2Nb_2O_7$ thin films by conventional RF sputtering has been shown to give rise to films with stoichiometry different to that of the target material. The composition offset was traced to an anomalously high re-sputtering rate from the substrate which occurs for argon, argon:oxygen or pure oxygen carrier gases. By suitably adjusting target composition at a fixed sputtering geometry and power level, stoichiometric films were produced. For films deposited onto substrates of up to 1100°C temperature, the $Sr_2Nb_2O_7$ was x-ray amorphous and showed simple linear dielectric properties with no evidence of the ferroelectricity of the corresponding crystalline form. High temperature annealing disrupted the integrity of the film before the crystalline form could be clearly identified.

Introduction

RF sputtering has been considered as a promising method for fabricating thin insulated films, and has already been applied to the fabrication of crystalline ferroelectric oxide films (1,2). Strontium pyroniobate ($Sr_2Nb_2O_7$) has recently been shown to be a ferroelectric crystal with unusually high ferroelectric Curie temperature ($T_c = 1352°C$) and is an interesting candidate for optical guided wave applications (3,4). The crystal structure appears to be a lower symmetry modification of the pyrochlore structure but the polarizability again appears to be associated with the NbO_6 octahedral arrangement. Lines (5) has pointed out that ferroelectric behavior may occur in amorphous materials and amongst the boundary conditions suggested to be important are identifiable polarizable groupings which may be preserved in the amorphous state, and a very high Curie temperature for the ordered crystalline form.

The objectives of the present work were to explore the sputtering parameters for $Sr_2Nb_2O_7$ so as to be able to deposit reproducible, amorphous stoichiometric pinhole free insulating films. To check the dielectric properties of these films for possible ferroelectric activity, and if the amorhous phase was not ferroelectric to investigate the growth of a crystalline ferroelectric form by thermal annealing.

Preparation of Sputtered Films

Sputtering was carried out in an MRC model 8502 rf diode sputtering system with a 5 cm diameter target. A sputter-down configuration was used with the substrates laid on the rotatable anode table, and a 30 mm target:substrate distance. Substrate materials included fused silica, alumina, and platinum, the area presented for the film was ∿8 mm x 2 mm. A grounded shield confined the plasma to the inner 42 mm of the target during sputtering. The sputtering gases used were argon and oxygen which were of regular commercial grade. Using pure

argon, it was evident immediately that the target became oxygen deficient and suffered physical damage after a short time. With 10% oxygen in argon oxygen reduction in the films was avoided but the targets again showed cracking. After a number of initial studies it became evident that the lifetime of the target improved with oxygen content in the sputtering gas and eventually pure oxygen was used.

The variables which were most thoroughly explored in the sputtering runs taken were the influence of target composition, particularly the ratio of SrO:Nb in the target and the partial pressure of oxygen which was varied over the range $0:100 \times 10^{-3}$ torr. A power level of 50 watts was found to produce a highly stab plasma. Typical deposition rates as a function of oxygen partial pressure are shown in Fig. 1. These very low rates, ranging from 200 to 800Å/hour lead us to examine in more detail the deposition mechanism.

The depletion of the target was measured after each of a sequence of sputtering runs, and compared in each case to the deposition on the substrate Allowing for all geometrical factors, a ratio of 6/1 was found to exist between the rate at which material was leaving the target and the corresponding amount being sputter deposited. Clearly there must be major re-sputtering from the su strate leading to deposition in other parts of the system.

Re-sputtering often occurs either through the action of energetic neutr species, through negative ions which originate at or near the cathode, or, in t case of insulating films by positive ions which have been accelerated towards t film surface as a result of a significant negative floating surface potential (bias sputtering). Measurements of the surface potential at the substrate (Fig 2) show that the potential difference is small and the positive ion mechanism could not apply. To try and separate the effects of negative ions, a bias potential was deliberately applied to the substrate. For potentials up to 100

volts no differences were detected in the sputtering rate, so we are lead to suspect that the major cause of the high re-sputtering in this sytem is the action of energetic neutral species.

Characterization of the films was carried out by x-ray secondary emission spectrometry, and by diffraction analysis. Early films showed significant departures from the $SrO:Nb_2O_5$ stoichiometry of the target and to balance the stoichiometry of the film at the $Sr_2Nb_2O_7$ composition it was found necessary to start from a $(2SrO)_{1.05}Nb_2O_5$ target. All films produced under the widest diversity of sputtering conditions, with substrate temperatures up to 1100°C were x-ray amorphous. Under the optimum conditions pinhole free samples were deposited, and by using very long sputtering times (up to two weeks) films which were sufficiently thick to part from the substrate were obtained. For high temperature dielectric studies and for annealing, small areas of the thicker films were equipped with circular evaporated platinum electrodes.

Dielectric Measurements

Dielectric permittivity was measured by evaluating the capacitance and loss tangent of a restricted area parallel plate capacitor formed by evaporating platinum electrodes directly onto both surfaces of the film. Measurements were made using a Hewlett Packard 7270A automatic bridge. The sample was contained in a Delta design environment chamber which could be controlled over the range from -100°C to +400°C. Capacitance and loss tangent were recorded at 1 kHz, 10 kHz, 100 kHz and 1 MHz. Both C and tan δ are plotted directly against the temperature recorded on a chromel:alumel couple read by a Fluke digital thermometer.

Typical data for ε as a function of temperature is shown in Fig. 3, and the corresponding tan δ values are plotted in Fig. 4. On first heating, the permittivity shows significant structure with peaks in the range 50 to 150°C.

This structure varies from sample to sample and is, we believe, some release of internal stress. All subsequent temperature runs show quite reproducible values with no hysteresis between heating and cooling, and a room temperature relative permittivity of 20. At higher temperature the response becomes markedly dispersive, and the dispersion is accompanied by a rising electrical conductivity under DC fields.

Films were annealed at fixed temperatures in the range 400°C to 1100°C, but after the initial dielectric structure was eliminated by the first anneal no further change was evident in the low temperature dielectric response. X-ray diffraction measurements confirmed that even very long annealing times at 1100°C, up to two weeks in duration, did not modify the diffraction spectra. Even short excursions of the temperature up to 1200°C did however, lead to catastrophic colla of the film with the development of a crystalline powder which exhibited well developed powder diffraction lines corresponding to the $Sr_2Nb_2O_7$ structure (Fig

Discussion

It appears that coherent pinhole free insulating films of amorphous stoichiometric $Sr_2Nb_2O_7$ can be fabricated by conventional RF sputtering. The films have linear dielectric behavior with a relative permittivity of order 20 which does not change markedly with temperature or frequency. These films exhibit no ferroelectric properties, the material does not generate harmonic ligh under optical SHG test, and attempts to pole the films to exhibit birefringence or a measurable pyroelectric response were unsuccessful. It would have been ve interesting to be able to explore the evolution of the ferroelectric response with progressive recrystallization of this stoichiometric amorphous matrix; however, unfortunately, the kinetics of annealing appear most unusual and frustrated this study. The amorphous films appear to remain stable in the amorphou

phase at 1100°C for long periods of time, however once crystallization is initiated at higher temperature it appears to propagate catastrophically and we were not able to retain coherent films which exhibited any significant recrystallization. Several studies on somewhat simpler amorphous systems have reported unusual recrystallization behavior (6,7,8) and we believe this may frustrate the use of sputtered films to explore micro-crystalline behavior in ferroelectrics.

References

1) L.I. Mendelsohn, E. D. Orth and R.E. Curran-
         J. Vac. Sci. Tech. 6, 363, 1969

2) I.H. Pratt and S. Firestone-
         J. Vac. Sci. Tech. 8, 256, 1969

3) S. Nanamatsu, M. Kimura and T. Kawamura-
         J. Phys. Soc. Japan 38, 817, 1975

4) A. Ishitani and M. Kimura-
         Appl. Phys. Letters 29, 289, 1976

5) M. E. Lines-   Phys. Rev. B 15, 388, 1977

6) R. Messier, T. Takamora and R. Roy-
         Solid State Communications 16, 311, 1975

7) C. E. Wichershaw, G. Bajar and J.E. Greene-
         Solid State Communications 27, 17, 1978

8) L. R. Gilbert, R. Messier and R. Roy-
         Thin Solid Films, 54, 129, 1978.

Figure Captions

Fig. 1.   Sputtering rates for $Sr_2Nb_2O_7$ ceramic target as a function of the sputtering gas pressure.
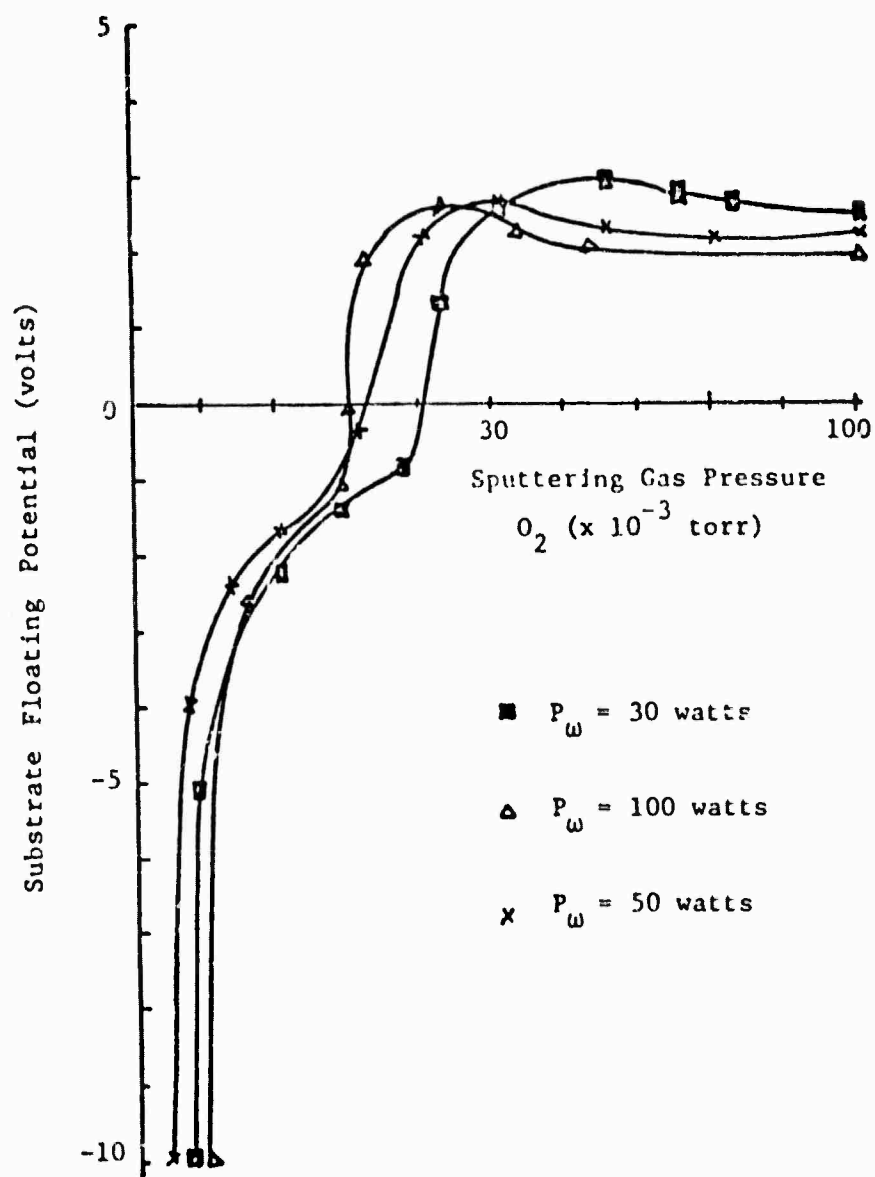
Fig. 2.   Plot of the film floating potential as a function of pressure (O_2) for fixed different operating powers.

Fig. 3   Dielectric permittivity as a function of temperature and frequency in amorphous $Sr_2Nb_2O_7$.

Fig. 4   Dielectric loss tangent δ as a function of temperature and frequency in amorphous $Sr_2Nb_2O_7$.

Fig. 5   X-ray pattern shown by the polycrystalline and amorphous $Sr_2Nb_2O_7$ sputtered films at the different annealing temperatures.

R.F. Power = 50 watts

Target to substrate distance = 30 mm

Fig. 1   Sputtering rates for $Sr_2Nb_2O_7$ ceramic target as a
function o the sputtering gas pressure.

Fig. 2   Plot of the film floating potential as a function of pressure (O_2) for fixed different operating powers.
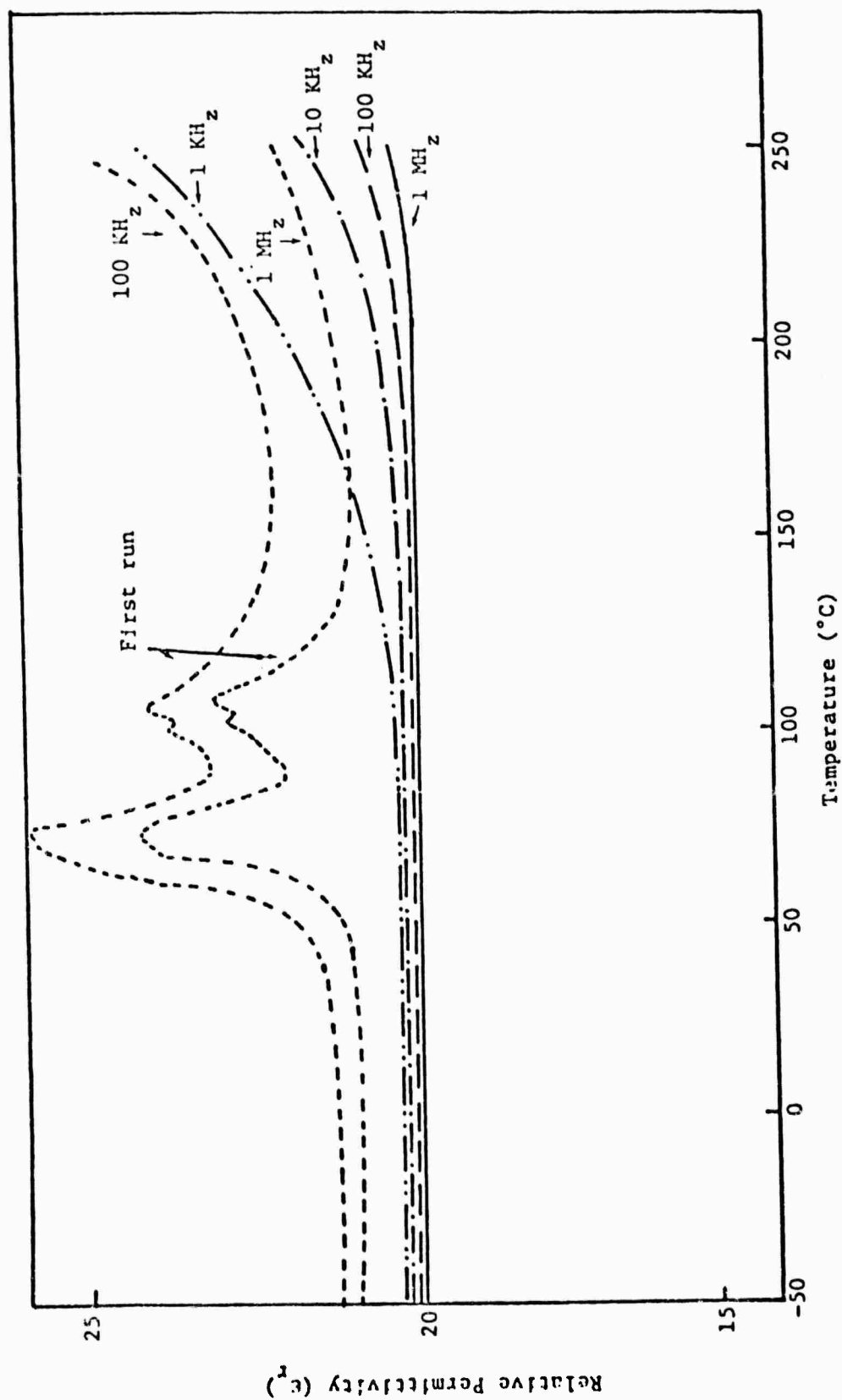
Fig.3. Dielectric permittivity as a function of temperature and frequency in amorphous $Sr_2Nb_2O_7$.
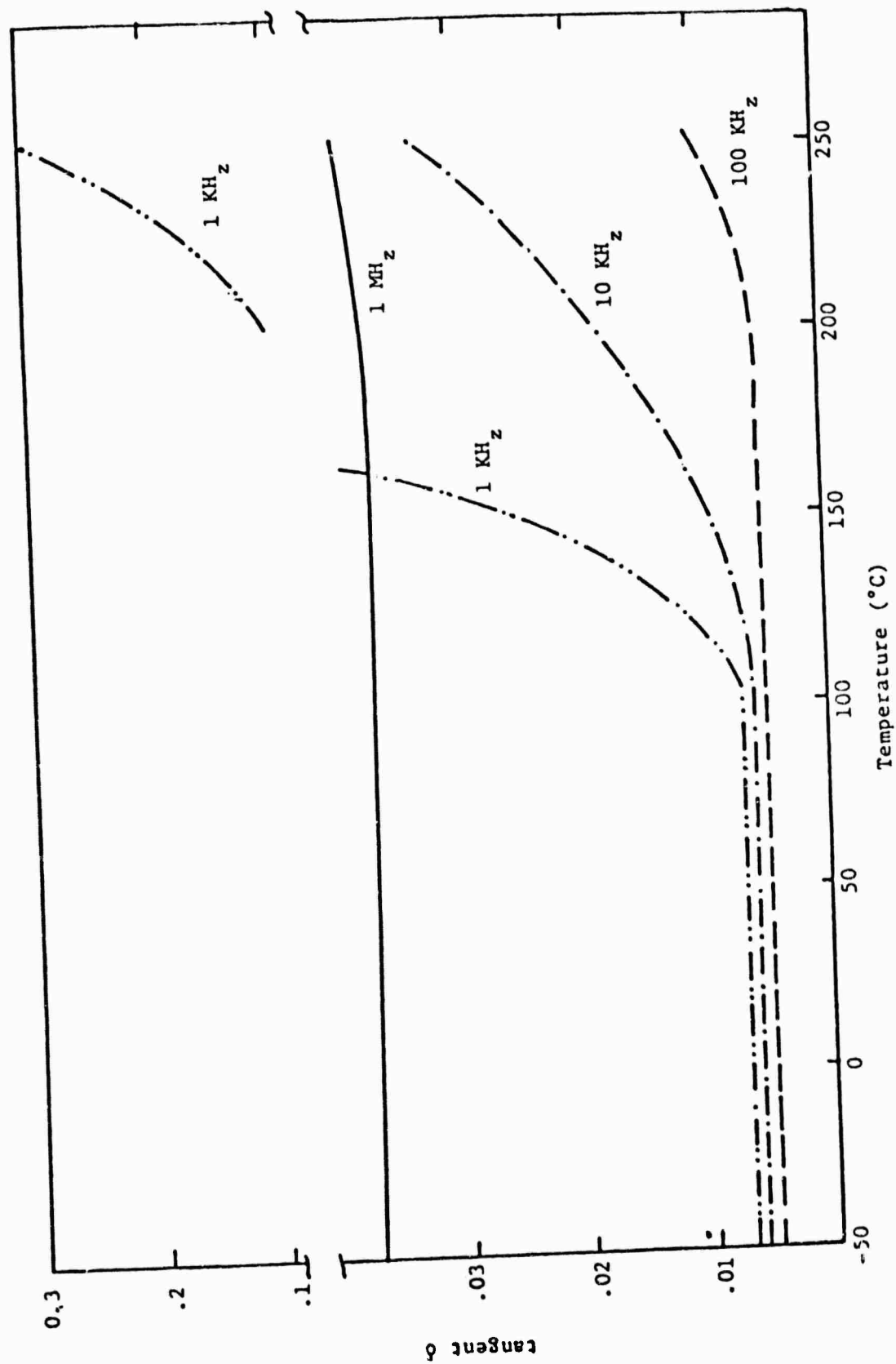
...f temperature and frequency in amorphous $Sr_2Nb_2O_7$.
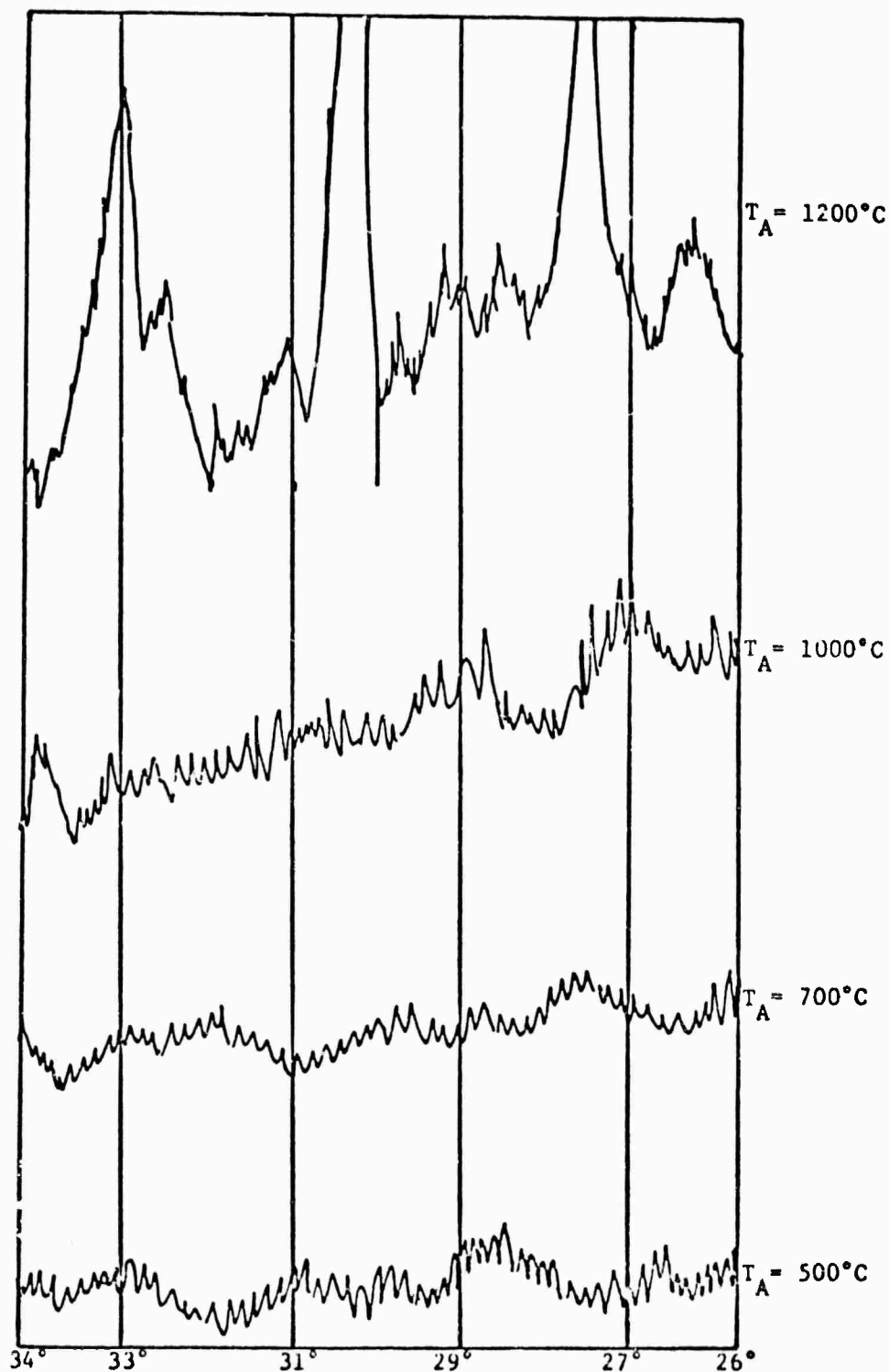
Fig.5.   X-ray pattern shown by the polycrystalline and
         amorphous $Sr_2Nb_2O_7$ sputtered films at the different
         annealing temperatures.

APPENDIX 14

Electro Mechanical Behavior of Single Domain Single Crystals
of Bismuth Titanate ($Bi_4Ti_3O_{12}$)

A. Sa Neto and L.E. Cross

ELECTRO MECHANICAL BEHAVIOR OF SINGLE DOMAIN SINGLE CRYSTALS

OF BISMUTH TITANATE ($Bi_4Ti_3O_{12}$)

A. Sa Neto and L. E. Cross
Materials Research Laboratory
The Pennsylvania State University
University Park, PA 16802

Abstract

The piezoelectric constants d_{11}, d_{22} and d_{33} for a single domain single crystal of $Bi_4Ti_3O_{12}$ have been measured at room temperature using appropriate crystal cuts on a Berlincour. d_{33} meter. From the known temperature dependence of the spontaneous polarization, lattice strain and dielectric permittivity, the equivalent piezoelectric constants have been calculated assuming a simple proper ferroelectric in which P_s is the order parameter. Constants in the plane of the perovskite like sheets in the $Bi_4Ti_3O_{12}$ structure ($d_{11}$, d_{22}) show good agreement with experimental values. The calculated constant d_{33} is more than an order of magnitude larger than that measured and gives clear indication of the 'indirect' coupling to the strain in the tetrad axial direction and the need for a more sophisticated phenomenology.

Introduction

Bismuth titanate, $Bi_4Ti_3O_{12}$, is probably the most thoroughly investi-
gated member of the very large family of mixed bismuth oxide layer structure
ferroelectrics. In spite of this however, there are no data upon the piezoelec-
tric behavior of this crystal in the most recent Landolt Bornstein (1) and we
can find no data in the literature. The advent of processing techniques to de-
velop grain oriented ferroelectric ceramics (2,3,4) have renewed interest in
the layer structure family materials as potential high temperature piezoceramics
and good single crystal data upon the d_{ij} coefficients is urgently needed. In
this study the Berlincourt d_{33} meter (5) was used to measure the piezoelectric
d_{11}, d_{22}, d_{33} coefficients of regular rectangular samples cut from large single
domain $Bi_4Ti_3O_{12}$ crystals. These measured values were then compared to values
derived by fitting a simple Landau phenomenology (6) to the available polariza-
tion, strain and dielectric data so as to derive values for the electrostriction
constants of the prototypic paraelectric phase, and from these constants and the
known permittivity to derive appropriate d coefficients.

Piezoelectric Measurements

A large suite of bismuth titanate single crystals which had been grown
for electro-optic domain switching studies were kindly made available for this
work by . E. Cummins (7). These crystals which are in the form of flat plates
with major surfaces normal to the tetragonal c axis of the prototype phase had
been subjected to thermal annealing in a weak temperature gradient to eliminate
90° type twins. Large area sections had then been pulse poled to single domain
state using surface electrodes (8). Rectangular sections with surfaces normal
to the pseudo orthorhombic axes of the ferroelectric single domain were string
sawn from these sections, and hand polished. The major difficulty in this
finishing operation is the small single domain crystal thickness ($\sim 200\mu$ meters)

which makes handling delicate and tedious.

After preparation and cleaning, samples were checked using the tilted extinction method (9) to ascertain that they were single domain.

Piezoelectric measurements of the three axial d coefficients were made on the Berlincourt d_{33} meter using point contacting electrodes. To check the efficacy of the point contact method, d_{33} was checked using larger area contacts but no measurable difference could be discerned.

From the Berlincourt meter

$$d_{11} = 39 \pm 1 \ 10^{-12} \ c/N$$
$$d_{22} = 0$$
$$d_{33} = 9 \pm 1 \ 10^{-12} \ c/N.$$

In principle the d_{33} meter could be used to measure other components of the d tensor in the single domain, however the practical limitations imposed by the crystal geometry restricted reliable measurement to just the components above.

Calculation of the Piezoelectric Constants

If it is assumed that bismuth titanate is a simple proper ferroelectric derived from the prototypic point group 4/mmm, it has been shown by Pohanka and Cross (10) that the elastic Gibbs function takes the form

$$\Delta G_1 = \alpha_1^X(P_1^2+P_2^2) + \alpha_3^X P_3^2 + \alpha_{11}^X(P_1^4+P_2^4) + \alpha_{33}^X P_3^4 + \alpha_{13}^X(P_1^2 P_3^2+P_2^2 P_3^2) +$$
$$\alpha_{12}^X P_1^2 P_2^2 + \alpha_{111}^X(P_1^6+P_2^6) + \alpha_{333}^X P_3^3 \tag{1}$$

where $P_1 \ldots P_3$ are the components of P along the orthogonal tetragonal axes and α_i are related to the dielectric stiffness and higher order stiffnesses.

Since 4/mmm is a centric group, the lowest order elasto-electric coupling which is allowed is electrostrictive. Thus to describe the crystal at finite elastic stress X, the following additional terms must be added:

$$\Delta G_1 = (\Delta G_1)_P - 1/2 \, s_{11}^P (X_1^2 + X_2^2) - 1/2 \, s_{12}^P X_1 X_2$$

$$- s_{13}^P (X_1 + X_2) X_3 - 1/2 \, s_{33}^P X_3^2 - 1/2 \, s_{44}^P (X_4^2 + X_5^2)$$

$$- 1/2 \, s_{66}^P X_6^2 + Q_{11} (P_1^2 X_1 + P_2^2 X_2) + Q_{12} (P_1^2 X_2 + P_2^2 X_1)$$

$$+ Q_{13} (P_1^2 X_3 + P_2^2 X_3) + Q_{31} (P_3^2 X_1 + P_2^2 X_1) \tag{2}$$

$$+ Q_{33} P_3^2 X_3 + Q_{44} (P_2 P_3 X_4 + P_1 P_3 X_5)$$

$$+ Q_{66} P_1 P_2 X_6 + Q_{144} (P_1^2 P_2 P_3 X_4 + P_2^2 P_1 P_3 X_5)$$

$$+ Q_{366} P_3^2 P_1 P_2 X_6 .$$

The $X_1 \ldots X_6$ are components of elastic stress,

$S_{11} \ldots S_{66}$ are the conventional elastic compliances measured at constant polarization,

$Q_{11} \ldots Q_{66}$ are the electrostriction constants in polarization notation.

The spontaneous polarizations are derived from the equations

$$\left(\frac{\partial \Delta G_1}{\partial P_i} \right)_{T, \, X = 0} = E_i = 0 \tag{3}$$

and the spontaneous elastic strains from

$$\left(\frac{\partial \Delta G_1}{\partial X_i} \right)_{TP} = - x_i . \tag{4}$$

Cummins and Cross (11) have shown that the only stable fer.oelectric

phase in $Bi_4 Ti_3 O_{12}$ has monoclinic symmetry and corresponds to solutions of (3)

in which

$$P_{1(S)} = P_{2(S)} \neq 0 \text{ and } P_{3(S)} \neq 0 . \tag{5}$$

Relation for the polarizations and dielectric permittivities in the

single domain states have been derived in reference (10).

From equations (4) with $X_i = 0$ the spontaneous strains take the form

$$- x_1 = Q_{11}P_1^2 + Q_{12}P_2^2 + Q_{31}P_3^2 \quad a$$

$$- x_2 = Q_{11}P_1^2 + Q_{12}P_2^2 + Q_{31}P_3^2 \quad b$$

$$- x_3 = Q_{13}(P_1^2+P_1^2) + Q_{33}P_3^2 \quad c$$

$$\qquad\qquad\qquad\qquad\qquad\qquad\qquad (6)$$

$$- x_4 = Q_{44}P_2P_3 + Q_{144}P_1^2P_2P_3 \quad d$$

$$- x_5 = Q_{44}P_1P_3 + Q_{144}P_2^2P_1P_3 \quad e$$

$$- x_6 = Q_{66}P_1P_2 + Q_{366}P_3^2P_1P_2 \quad f.$$

The piezoelectric polarization coefficients b_{ijk} are given by the partial derivatives

$$\frac{\partial X_i}{\partial P_j} = \frac{\partial \Delta G}{\partial X_i \, \partial P_j} \qquad\qquad\qquad (7)$$

which for the stable monoclinic ferroelectric phase may be written

$$\frac{\partial X_1}{\partial P_1} = b_{11} = b_{22} = -2Q_{11}P_1$$

$$\frac{\partial X_1}{\partial P_2} = b_{21} = b_{12} = 2Q_{12}P$$

$$\frac{\partial X_1}{\partial P_3} = b_{31} = b_{32} = -2Q_{31}P_3$$

$$\frac{\partial X_3}{\partial P_1} = b_{13} = b_{23} = -2Q_{13}P_3$$

$$\frac{\partial X_3}{\partial P_3} = b_{33} = -2Q_{33}P_3 \qquad\qquad (8)$$

$$\frac{\partial X_4}{\partial P_2} = b_{24} = b_{15} = -Q_{44}P_3 - Q_{144}P_1^2 P_3$$

$$\frac{\partial X_4}{\partial P_3} = b_{34} = b_{35} = -Q_{144}P_1 - Q_{144}P_1^3$$

$$\frac{\partial X_5}{\partial P_2} = b_{25} = b_{14} = -2Q_{144}P_1^2 P_3$$

$$\frac{\partial X_6}{\partial P_1} = b_{16} = b_{26} = -Q_{66}P_2 - Q_{366}P_3^2 P_1$$

$$\frac{\partial X_6}{\partial P_3} = b_{36} = -2Q_{366}P_3 P_1^2.$$

Obviously the b coefficients derived in this manner may be converted to the more familiar d coefficients by the relations of the form

$$d_{ij} = \varepsilon_{ik} b_{kj} \qquad\qquad (9)$$

where ε_{ik} are the appropriate dielectric permittivities. It may be noted that two higher order striction coefficients Q_{144} and Q_{366} have been included, these coefficients were inserted as without them the piezoelectric matrix for the mono-clinic phase does not contain the required non-zero terms dictated by symmetry

i.e. b_{36}, b_{25} and b_{14} would become zero.

For the required Q coefficients, the x-ray data from Subbarao (11) was used together with the monoclinic strain measurements of Cummins (12) to derive the components of the spontaneous strain in the ferroelectric phase. These strains were then used in equations (6) with the polarizations calculated by Cummins and Cross (10) to derive the Q coefficients.

In making this derivation it was assumed that the Q_{ij} are independent of temperature so that the equations (6) could be applied at a sequence of temperatures throughout the ferroelectric range. Since the number of equations then over determines the constant, a least squares fitting was used to derive 'best' values for the Q. From these calculated Q values, the equations (8) were used with room temperature (25°C) values of P_S [$P_{1(S)}$ and $P_{3(S)}$] to calculate the b constants at 25°C. These b constants were then combined with the dielectric data from Fouskova and Cross (13) using equations (7) to determine values of the d constants at room temperature.

After rotating the d matrix to correspond to the monoclinic symmetry with the mirror plane containing the 3, 1 axes, the values obtained were

$$d_{ij} = \begin{vmatrix} 44 & 18 & -48 & 0 & 1 & 0 \\ 0 & 0 & 0 & 0.8 & 0 & _md_{26} \\ -75 & -76 & 269 & 0 & 12 & 0 \end{vmatrix} \times 10^{-12} \text{ c/N}$$

where

$$_md_{26} = \sqrt{2(_td_{11} - _td_{12})}$$

here the prefixes m and t refer to monoclinic and tetragonal axes.

With the simple phenomenological theory it is not possible to derive $_td_{11}$ and $_td_{12}$ separately but only the sum $_td_{11} + _td_{12} = 43 \times 10^{-12}$ c/N.

The fitting process by which the values above are derived is quite complex, and utilizes data from many different investigators. Much of this

experimental data has been presented with no clear measure of error, so that it is very difficult to assess a level of confidence in the values derived above. If we assume arbitrarily that the x-ray lattice parameters are reliable to $\pm 0.005\text{Å}$ (relative) which is not unreasonable for good x-ray powder work, the assessed spontaneous strains may be in error $\pm 20\%$. Taking the errors in permittivity to be $\pm 2\%$ and in the polarization $\pm 10\%$, we estimate the calculated d values

$$d_{33} = (269 \pm 100)\ 10^{-12}\ c/N$$

$$d_{11} = (44 \pm 12)\ 10^{-12}\ c/N$$

$$d_{22} = 0.$$

Discussion

The surprisingly close agreement between measured and calculated d_{11} values for $Bi_4Ti_3O_{12}$ suggest that the major part of the lattice distortion in the plane of the perovskite sheets of this layer structure material is simple electrostriction originating from the spontaneous polarization in the plane of sheet which occurs at T_c. The absence of any measurable d_{22} is clearly in agreement with the symmetry requirements of the monoclinic single domain, and further confirms that the samples were completely free from 90° twins. Experimental and theoretical values of d_{33} however, are in very marked disagreement and appear well outside the range of possible error. Thus it appears unlikely that the spontaneous strains outside the perovskite sheets can be attributed to the very small tilting of P_S out of the ab plane. That the transition at T_c was more complex is also evidenced by the x-ray measurements of Newnham and Dorrian (14) which show an obvious doubling of the unit cell in the ferroelectric phase.

The fact that the in-plane properties behave in a manner so similar to a simple proper ferroelectric, whilst the 'c' axis behavior would certainly

suggest a second order parameter, aside from the polarization, does lend additional support to the concept of a triggered phase change which has been suggested by Holakovsky (15).

References

1) Landolt-Bornstein   Group III Crystals and Solid State Physics
Vol. III and Vol. IX, Ferro and Antiferroelectric
Substances. Editor K. Hellwege.

2) H. Igaraski, K. Matsunaga, T. Tanioi and K. Okazaki
Am. Ceram. Soc. Bull. 57 815, 1978.

3) T. Takenaka, K. Shoji, H. Takai and K. Sakata
Proc. Japan Cong. Mat. Res. 19 230, 1976.

4) M. Holmes, R.E. Newnham and L.E. Cross
J. Am. Ceram. Soc. (In Press).

5) D. Berlmcourt   Channel Products CPDT 3300
d_{33} meter 16722 Park Circle Drive
Chagrin Falls, OH 44022.

6) L. D. Landau and E.M. Lifshits
Statistical Physics
Pergamon Press, London 1958

7) The $Bi_4Ti_3O_{12}$ crystals supplies by S.E. Cummins included batches grown at Wright Patterson Airforce Base by Cummins and Luke, and crystals grown under Airforce contract at Sperry Rand by C.S. Sahagian.

8) S.E. Cummins and T. E. Luke
IEEE Trans. El. Dev. ED 18
761, 1971.

9) S.E. Cummins and T. E. Luke
Ferroelectrics 3 125, 1972.

10) R. Pohanka and L.E. Cross

                       Mat. Res. Bull. 6, 939, 1971.

11) S. E. Cummins and L. E. Cross

                       J. Appl. Phys. 39, 2268, 1968.

12) S. E. Cummins and T. E. Luke

                       Ferroelectrics 3, 323, 1974.

13) A. Fouskova and L. E. Cross

                       J. Appl. Phys. 41, 41, 1970

14) R. E. Newnham and J. F. Dorrian

                       Mat. Res. Bull. 6, 1029, 1971.

15) J. Holakovsky   Phys. Stat. Sol. b56, 615, 1973.

APPENDIX 15

Electrostatic Measurements of Unusually Large Secondary
Pyroelectricity in Partially Clamped LiNbO$_3$

L.B. Schein, P.J. Cressman and L.E. Cross

ELECTROSTATIC MEASUREMENTS OF UNUSUALLY LARGE SECONDARY PYROELECTRICITY IN PARTIALLY CLAMPED LiNbO$_3$

L.B. Schein, P.J. Cressman
Xerox Corporation - W114
Rochester, New York 14644

and

L.E. Cross
Materials Research Laboratory
The Pennsylvania State University
University Park, Pennsylvania 16802

ABSTRACT

Pyroelectricity has been observed in single domain, single crystal LiNbO$_3$ under _partially_ _clamped_ elastic boundary conditions using a non-contact electrostatic voltmeter. These boundary conditions were produced by the use of localized laser heating which generated a temperature change in the central 2.5 mm of a 19 mm diameter disk. These partially clamped boundary conditions have allowed (1) observation of an unusually large secondary pyroelectric effect in 2-cut crystals (the 2 or y axis perpendicular to the disk's face) whose components along the 1 and 3 axis map the radial and tangential components of the thermal stress and (2) an experimental technique for partially separating the primary and secondary pyroelectric effects.

I. INTRODUCTION

It has recently been shown[1] that non-contact electrostatic potential measurements can be used to detect, with high sensitivity and spatial resolution (10^{-2}cm), a macroscopic charge separation phenomenon in ferroelectrics associated with laser induced optical damage. It is the purpose of this paper to examine another charge separation phenomenon in a ferroelectric crystal using the non-contact electrostatic method: pyroelectricity under partial elastic clamping in $LiNbO_3$. Unusually large secondary pyroelectricity has been observed which can be attributed to the partial elastic clamping when the polar but non-pyroelectric 2 axis is normal to the disk. From the potential distribution along the 1 and 3 axes it appears possible to examine the radial and tangential components of the thermal stress, respectively. From the symmetry of the primary and secondary effects with respect to the sample inversion, it appears possible to partially separate experimentally the primary and secondary pyroelectric response.

Pyroelectricity is usually studied under elastically free boundary conditions which therefore includes charge separation due to both primary (thermal) and secondary (piezoelectric) pyroelectricity. Under totally clamped conditions, charge separation is due only to primary pyroelectricity. It might be expected that partial elastic clamping would give rise to effects intermediate between those of the free and clamped states. However, since the symmetry of the clamping stresses alters the crystal symmetry, large and qualitatively different effects can appear.

Partial elastic clamping is achieved in these experiments by laser heating a small 2.5 mm diameter area in the center of a larger 19 mm diameter thin disk of poled, single crystal lithium niobate. Clamping occurs in two dimensions (approximately) because of the elastic restraint from the unheated parts of the disk. The third dimension, perpendicular to the thin disk, is unclamped and free to expand. Experiments have been performed on crystals with the pyroelectric 3 axis both normal and in the plane of the disk.

In Section II we discuss the electrostatics which relate the measured potential differences and the pyroelectric charge separations. Section III gives a simple theoretical treatment for the secondary pyroelectricity assuming perfect partial clamping, which established the proper signs of the observed potentials. Sections IV and V discuss the experimental procedure and results. In Section VI a simplified but improved model of the thermoelastic effects is given which treats the crystal as an elastic isotropic solid. Agreement with the data is significantly improved. The conclusions are drawn in Section VII.

II. ELECTROSTATIC CONSIDERATIONS

Consider a poled ferroelectric single crystal in the form of a thin disk with the polar axis (3 axis) perpendicular to the plane of the disk (Figure 1A) resting on a ground plane. If the (normally compensated) spontaneous polarization is changed by an amount ΔP under open circuit conditions (constant D), a non-zero electric field E_3 is generated (opposite in sign to the change in

polarization) which raises the upper surface to a potential V

$$V = - \int_0^L E_3 dx = - \frac{\Delta PL}{K_3 \epsilon_0} \tag{1}$$

where K_3 is the dielectric constant for fields along the 3 axis, ϵ_0 is the permittivity of free space, and L is the disk's thickness.

If the ferroelectric axis lies in the plane of the disk (Figure 1B) and the polarization varies as a function of distance along the polar 3 axis, as for example might be induced by local laser heating under the geometry in Figure 1C, there will be a volume distribution of bound charge ρ_b given by

$$\rho_b = -\nabla P \tag{2}$$

Neglecting secondary effects and temperature gradients

$$\frac{\partial P^1}{\partial x} = \frac{\partial P^2}{\partial y} = 0 \tag{3}$$

so that ρ_b will be a function z only and (2) reduces to

$$\rho_b(z) = - \frac{\partial P_3}{\partial z} \tag{4}$$

For the case that P_3 (ρ_b) is only a slowly varying function of z, the potential V will be given by solving Poisson's equation for a uniform volume distribution of charge in a medium of relative permittivity K_1, i.e.,

$$V = - \frac{1}{2} \frac{\rho(z)L^2}{K_1 \epsilon_0} = \frac{L^2}{2K_1 \epsilon_0} \frac{\partial P_3}{\partial z} \tag{5}$$

For rapid variations in P_3 (relative to the resolution of the electrostatic voltmeter probe) a more complete electrostatic analysis would be required.

III. PYROELECTRICITY IN CRYSTALS

Charge separation phenomena in insulators (or semi-insulators) associated with thermally induced changes of electrical polarization are generally classified as pyroelectric.[2] The polarization at constant stress X for a change in temperature ΔT is given by

$$P_i^X = \gamma_i^X \Delta T \tag{6}$$

$$\gamma_i^X = \gamma_i^X + d_{ijk}^T c_{jklm}^{TE} \alpha_{lm}^E . \tag{7}$$

γ_i^X is the (primary) coefficient measured under constant strain χ and the second term represents contributions to the polarization due to secondary pyroelectricity, i.e., polarization induced piezo-electrically where d_{ijk}^T are the piezoelectric stress coefficients at constant temperature, c_{jklm}^{TE} are the elastic constants at constant temperature and electric field and α_{lm}^E are the thermal expansion coefficients measured at constant electric field. Both γ_i^X and γ_i^X have the same symmetry constraints so that under the condition that the elastic boundary conditions do not lower the symmetry of the problem (i.e., totally clamped or totally free) pyroelectricity is confined to crystals in the ten polar point symmetries.[3] It can be shown in general[4] that primary and secondary effects are of the same order of magnitude but because of the tedious requirements to measure piezoelectric, elastic, and thermal expansion in determining the secondary effect a complete separation has been effected in only a few single crystals[5-7] and poled ceramics.[8,9]

For partial elastic constraints (partially clamped conditions), the situation can become much more complex. The secondary effect

may occur along orientations other than the polar axis and may occur in additional crystal classes. The case of interest here is a thin disk absorbing radiation over a small circular region on one surface so that a small cylindrical region remote from the boundaries of the plate is raised in temperature (Figure 1C). To ascertain the nature and the approximate magnitudes of the primary and secondary effects, the following initial assumptions are made:

(1) In the direction perpendicular to the surface of the disk free expansion occurs $(X_3 \equiv 0)$.

(2) In the plane of the disk, internal stresses are developed of a magnitude sufficient to maintain the disk undeformed in this plane.

(3) The temperature profile across the disk can be calculated from the pyroelectric voltage profile on a disk cut normal to the 3 axis.

(4) Under the conditions of the experiment the elements of the d, c, and α tensors are constant.

Assumption (1) is probably legitimate; (2) will clearly overestimate the secondary effects but should give the correct signs. Since even under assumption (2) the secondary response along the 3 axis is much less than the primary, (3) is probably also valid (see Table I). Assumption (2) is replaced by a more realistic assessment of the internal stresses in Section VI. For the small temperature changes in these experiments (4) is certainly valid.

By making these assumptions, we are able to demonstrate the qualtitative behavior of the system: the elements of the secondary pyroelectric effect are shown in Table I for the 1. 2 and 3

directions of $LiNbO_3$ perpendicular to the disk (indicated by a number in parenthesis). The expected voltage profiles along each of the orthogonal crystal axes for 1, 2 and 3 cut disks are sketched in Figure 2. A rough scaling has been placed on each figure by calculating the maximum voltage, which occurs either at the center (for surface charging) or at the position of maximum gradient in P (the maximum observed temperature gradient was $31^{\circ}C/cm$ corresponding to a voltage gradient of 750 V/mm in the 3 cut crystal). The voltages were calculated by using equations 1 or 5, the values in Table I, and the constants of $LiNbO_3$ given in Reference 14. Lettering on the curves P or S indicates whether the voltage distribution is from the primary or secondary effect; the number in parenthesis indicates the voltage contributions of the primary and secondary effects.

IV. EXPERIMENTAL PROCEDURE

The $LiNbO_3$ crystals used for these experiments were purchased from Crystal Technology, Inc. in the form of polished, poled disks 19 mm in diameter, 0.75 mm thick. To obtain the partially clamped conditions, the disks were painted black on one side and irradiated with an (expanded) 2.5 mm diameter 0.6 mm argon laser beam ($4880\overset{o}{A}$). The central 2.5 mm of the black paint served as a local source of heat; the rest of the disk which was not heated tended to prevent the central 2.5 mm of the $LiNbO_3$ disk from expanding.

The side with the black paint was placed on Nesa glass (glass with a tin-oxide coating) which served as a ground plane for the electrostatic measurements. The measurements were obtained by

translating the electrostatic voltmeter (Monroe, Model 144 Volt-
meter with Model 1009CG probe having a resolution of 1 mm) across
the crystal face along the various axial directions.

The procedure used is as follows: the electrostatic voltmeter
is positioned at one of the coordinates of interest and the laser
is turned on. Within a few seconds, the electrostatic potential
reaches a steady value. The laser is turned off, the temperature
of the sample returns to ambient conditions, the electrostatic
voltmeter is translated to a new position, and the measurement
is repeated.

The temperature distribution in the disk was determined by making
this electrostatic measurement on a 3 cut crystal and using the
known pyroelectric coefficient and Equation (1) where the pyro-
electric coefficient is taken to be 8.3 x 10^{-5} coul/m^{2o}C, L = 0.75 mm,
$K_3^X = 30$. This gives 235 volts/^{o}C for the proportionality constant
between temperature and voltage. As expected, for a polarization
which produces a surface charge, the electrostatic voltage changed
sign when the sample was inverted. The data in Figure 3B indicates
that the peak temperature in the disk was 11.7^{o}C (= 2750 V/235 V/^{o}C)
and the maximum temperature gradient is 31°C/cm corresponding to
a voltage gradient of 750 V/mm. The same result was obtained when
translating the measuring head either along the 1 or the 2 axis.

V. EXPERIMENTAL RESULTS

The full family of experimental measurements are
exhibited in Figure 3 in a form which allows direct comparison
between these data and the qualitative shapes expected (Figure 2).

The measured values along the 3 axis (Figure 3B) are determined (to first approximation) by primary pyroelectricity and were used to determine the temperature distribution in the disk. In Figures 3C and 3D the data are shown for the 1 cut crystal measured along the 2 axis (C) and the 3 axis (D). Both the shape and the sign are in qualitative agreement with the predictions in 2(C) and 2(D). That the measured potentials are from bulk and not surface charges was verified by inverting the samples: the measured profiles did not change. The values along the 2 axis (Figure 3C) are determined entirely by secondary pyroelectricity and can be directly attributed to the partial clamping.

Figure 3(A,E,F,G) summarize the data for 2 cut crystal measured along the (1) and (3) axes. In Figure 2A the effect is exclusively from the secondary pyroelectricity along the z direction (i.e., a surface charging) and reverses sign when the crystal is inverted. Qualitatively, Figure 2E suggests that the pyroelectric effect measured along the 3 axis should be made up of two superimposed effects, a strong secondary pyroelectric effect due to a surface charge distribution and a smaller volume effect due to both the primary and secondary response. The resulting asymmetry about the axis of the laser (center of heating) is evident in Fig. 3E. Since t'e potential due to surface charge inverts on inverting the crystal, while that of the volume charge does not, the surface charge (the secondary effect) and the volume charge (due to the primary and secondary effect) can be separated by taking the sum and difference of the curves measured with the +2 axis up (Figure 3E) and +2 axis down (Figure 3F). These sums and differences (Figure 3G) may be

compared with the separate components of the predicted response in Figure 2E. The use of the symmetry of these effects on simple inversion therefore provides an experimental technique for partially separating the primary and secondary pyroelectric responses.

A qualitative feature of the 3 axis curve, Figure 3G, which is not predicted by the simplified treatment of perfect partial clamping discussed in Section III is that the measured potential goes to zero near the edge of the heated region and changes sign in the outer region. This behavior contrasts markedly with the measurement along the 1 direction (Figure 3A) where the sign of the potential does not change out to the edge of the crystal.

VI. SIMPLIFIED ISOTROPIC MODEL FOR THE ELASTIC STRESS DISTRIBUTION

The two most serious discrepancies between the data and the simple treatment given in Section III were the zero crossing and the magnitude of the potential along the 2 axis for the 2 cut crystal. This clearly requires a more detailed consideration of the stress distribution. Unfortunately, the problem of the temperature and stress distribution in a circular cylinder of an anisotropic crystalline solid under local axial heating does not appear to have been studied in the literature. However, for $LiNbO_3$ the elastic properties are not strongly anisotropic so that as a first approximation it is reasonable to consider the equivalent stress distribution in an isotropic disk with radial temperature variation.

Boley and Weiner[11] give expression for σ_{rr} the radial component of the elastic stress and $\sigma_{\theta\theta}$ the tangential component of the elastic stress

$$\sigma_{rr} = \alpha Y \left[\frac{1}{b^2} \int_0^b Trdr - \frac{1}{r^2} \int_0^r Trdr \right] \tag{8}$$

$$\sigma_{\theta\theta} = \alpha Y \left[\frac{1}{b^2} \int_0^b Trdr + \frac{1}{r^2} \int_0^r Trdr - T \right] \tag{9}$$

where T is the temperature (which is a function of the radial distance only), r is the radius vector, b the external diameter of the disk, α the thermal expansion coefficient, and Y Young's modulus for the material. In the case of interest here T(r) can be obtained from the pyroelectric measurement on the 3 cut crystal (Figure 3B). By graphical integration of a plot of Tr vs r the magnitude of the radial and tangential stress $\sigma_{rr}(r)$ and $\sigma_{\theta\theta}(r)$ can be determined.

For $LiNbO_3$, the only non-zero piezoelectric coefficient which couples a plane stress applied normal to 2 to an electric field along 2 is the coefficient d_{21} (or d_{211}), which is required by symmetry to equal $-d_{22}$. It follows then from the morphology of the plate, that values of the potential along the 1 axis will monitor the radial component of the thermal stress (σ_{11} along 1) while the values of the secondary component of the potential along the 3 axis will be controlled by the tangential component of the stress (σ_{11} along 3). In Figure 4 the potential calculated from the radial and tangential stress distributions are compared with the measured values, all curves being normalized to unity at the center of the heated region. Note that while the radial stress distribution is compressive across the whole axial length, the tangential stress changes from compressive in the center of the disk to a tensile stress beyond a certain critical radius. The shape of the potential distribution calculated from the radial stress

(1 axis) is quite close to the measured distribution. For the case of the tangential stress, the calculated crossover from compressive to tensile stress occurs farther from the origin than in the measured distribution.

This discrepancy along the 3 axis is most likely associated with the neglect in this treatment of the effects of anisotropy in the thermal expansion. While in $LiNbO_3$ the elastic properties are not strongly anisotropic, the thermal expansion gives $\alpha_{11} \simeq 2\alpha_{33}$. Thus, while in the isotropic case, the contours of equal strain (stress) will be circular, in $LiNbO_3$ for the 2-cut, they must be elliptical with the major axis along the 1 axis. Clearly for the thermal stress, this will have the effect of shrinking the contour separations along the 3 axis with respect to those along 1 and will tend to bring calculated and observed potentials into closer agreement.

Using Equation (1) the magnitude of the polarization along the 2 direction at $r = 0$ can be calculated. Since

$$\lim_{r \to 0} \frac{1}{r^2} \int_0^r T r dr = 1/2 \ T(o) \equiv 1/2 \Delta T \qquad (10)$$

$$\sigma_{rr}|_{r=0} = \sigma_{\theta\theta}|_{r=0} \approx -1/2 \ \alpha Y \Delta T \qquad (11)$$

(a compressive stress) and the value of the first integral in Equations (7) and (8) is small under the conditions of local heating. The polarization generated piezoelectrically through d_{21} is

$$P_2 = \sigma_{rr} d_{21} = -\frac{1}{2} \ \alpha Y \Delta T \ (-d_{22}) = \frac{1}{2} \ \alpha Y \Delta T \ d_{22} \qquad (12)$$

and the potential V is given by Equation (1)

$$V_{r=0} = \frac{1}{2} \alpha Y \Delta T \ d_{22} \ \frac{L}{\epsilon_o K_2^X}$$

(13)

Taking the thermal expansion α to be the mean of the two anisotropic coefficients α_{11}, α_{33} (1.145 x 10^{-5}/°C) gives $V_{(r-0)}$ = 272 volts, as compared with the measured 260 volts.

VII. CONCLUSION

Primary and unusually large secondary pyroelectricity has been observed in LiNbO$_3$ under partially clamped conditions. Partially clamped elastic boundary conditions were achieved by laser heating the central 2.5 mm of a 19 mm disk. Observations of the induced polarization were achieved by using a non-contact electrostatic voltmeter. The primary pyroelectricity, which was observed on the 3 cut crystals, was used to map the temperature distribution in the sample. Large secondary pyroelectricity was induced in the 2 cut crystals whose origin was the partially clamped boundary conditions. To obtain quantitative agreement with data, a detailed consideration of the stress distribution was necessary. It was found that the components of the secondary pyroelectricity along the 1 and 3 axes appear to map the radial and tangential components of the thermal stress. Both the magnitude of the signal and the observed change in sign of the potential along the 3 axis are accounted for. The symmetry of primary and secondary effects upon sample inversion was used to partially separate experimentally the secondary from the primary pyroelectric effect.

TABLE I

PIEZOELECTRICITY IN LiNbO$_3$ UNDER PARTIALLY CLAMPED CONDITIONS

On heating, the disk expands in all three directions. As a first approximation we assume that strains and stresses are generated in the plane of the disk to maintain the heated region undeformed. In the direction normal to the plane (indicated in parenthesis) the disk freely expands, giving zero restoring strain ε and stress σ, i.e., $\varepsilon_i(i) = \sigma_i(i) = 0$ for the ith direction normal. The components of the σ and P tensors are obtained by tensor multiplication

1 NORMAL	2 NORMAL	3 NORMAL
STRAIN		
$\varepsilon_1(1) = 0$	$\varepsilon_1(2) = -\alpha_{11}\Delta T$	$\varepsilon_1(3) = -\alpha_{11}\Delta T$
$\varepsilon_2(1) = -\alpha_{11}\Delta T$	$\varepsilon_2(2) = 0$	$\varepsilon_2(3) = -\alpha_{11}\Delta T$
$\varepsilon_3(1) = -\alpha_{33}\Delta T$	$\varepsilon_3(2) = -\alpha_{33}\Delta T$	$\varepsilon_3(3) = 0$
STRESS		
$\sigma_1(1) = 0$	$\sigma_1(2) = C_{11}\varepsilon_1 + C_{13}\varepsilon_3$	$\sigma_1(3) = C_{11}\varepsilon_1 + C_{12}\varepsilon_2$
$\sigma_2(1) = C_{11}\varepsilon_2 + C_{13}\varepsilon_3$	$\sigma_2(2) = 0$	$\sigma_2(3) = C_{12}\varepsilon_1 + C_{11}\varepsilon_2 = \sigma_1$
$\sigma_3(1) = C_{13}\varepsilon_2 + C_{33}\varepsilon_3$	$\sigma_3(2) = C_{13}\varepsilon_1 + C_{33}\varepsilon_3$	$\sigma_3(3) = 0$
$\sigma_4(1) = -C_{14}\varepsilon_2$	$\sigma_4(2) = C_{14}\varepsilon_1$	$\sigma_4(3) = C_{14}\varepsilon_1 - C_{14}\varepsilon_2 = 0$
$\sigma_5(1) = 0$	$\sigma_5(2) = 0$	$\sigma_5(3) = 0$
$\sigma_6(1) = 0$	$\sigma_6(2) = 0$	$\sigma_6(3) = 0$
PIEZOELECTRICITY		
$\gamma_1(1) = 0$	$\gamma_1(2) = 0$	$\gamma_1(3) = 0$
$\gamma_2(1) = d_{22}\sigma_2 + d_{15}\sigma_4$	$\gamma_2(2) = -d_{22}\sigma_1 + d_{15}\sigma_4$	$\gamma_2(3) = -d_{22}\sigma_1 + d_{22}\sigma_2 = 0$
$\gamma_3(1) = d_{31}\sigma_2 + d_{33}\sigma_3$	$\gamma_3(2) = d_{31}\sigma_1 + d_{33}\sigma_3$	$\gamma_3(3) = d_{31}\sigma_1 + d_{31}\sigma_2$

REFERENCES

1. L.B. Schein, P.J. Cressman, Frederick M. Tesche, Journal of Applied Physics, 48, 4844 (1977); L.B. Schein, P.J. Cressman, and L.E. Cross, Journal of Applied Physics, 49, 798 (1978).

2. D. Brewster, J. Sci., 1, 208 (1824).

3. W. Cady, Piezoelectricity, Dover, New York, p. 699 (1964).

4. J.F. Ney, Physical Properties of Crystals, Oxford University Press, London, p. 189 (1957).

5. S.T. Liu, Pyroelectric Coefficients, Landolt-Bornstein, New Series III/II, edited by H. Hellwege.

6. H. Jaffe, Phys. Rev., 75, 1625 (1949).

7. S.B. Lang, Phys. Rev. B4, 3603 (1971).

8. T.A. Perls, T.J. Diesel, W.I. Bobrov, J. Appl. Phys., 29, 1297 (1958).

9. J.L. Wentz, L.Z. Kennedy, J. Appl. Phys., 35, 1767 (1964).

10. A.M. Warner, M. Onoe, and G.A. Coquin, J. of the Acoustical Society of America, 42, 1223 (1966).

11. B.A. Boley and G. Jerome W. Weiner, Theory of Thermal Stresses, John-Wiley & Sons, New York London & Sydney (1960), page 289.

12. J.T. Milek & M. Neuberger, Handbook of Electronic Materials, V8, published by IFI Plenum N.Y. Washington & London (1972).

13. Tomoaki Yamada, Nobukazu Niizeki, a Hiroo Toyoda, Jap. Journal of Applied Physics 6 151 (1967).

14. Constants of $LiNbO_3$ used in paper were obtained from Refs. 10,12 and 13: $\alpha_{11} = 1.54$, $\alpha_{33} = 0.75$ (both $\times 10^{-5}$ °C^{-1}); $C_{11} = 2.03$, $C_{12} = 0.53$, $C_{13} = 0.75$, $C_{14} = 0.09$, $C_{33} = 2.45$, $C_{44} = 0.60$, $C_{66} = 0.75$ (all times 10^{11} N/m^2); $d_{15} = 6.8$, $d_{22} = 2.1$, $d_{31} = -0.1$, $d_{33} = 1.6$ (all $\times 10^{-11}$ coul/N); $Y = 0.192 \times 10^{12}$ N/m^2; $K_3^x = 30$, $K_1^x = K_2^x = 84$; and $\gamma_3^x = -8.3 \times 10^{-5}$ coul/m^2°C.

FIGURE CAPTIONS

Figure 1:   Polarization (due to pyroelectricity) can cause
either (A) a surface charge or (B) a bulk charge
in the disk. Schematic diagrams of the resultant
electrostatic potentials are shown. (C) As a first
approximation we have assumed that the laser heats
the crystal only in the region directly in line with
a laser beam.

Figure 2:   Schematic of the predicted electrostatic voltages
along the three axis for the 1, +2 and +3 axis of
the $LiNbO_3$ disk up. The + direction is indicated
on the schematic diagrams   P (S) indicate that
primary (secondary) pyroelectricity dominates the
observed polarization.

Figure 3:   Observations of electrostatic voltages for the
various axes of $LiNbO_3$ perpendicular to the disk.

Figure 4:   Calculated and experimental potentials for the 2 cut
crystal along the 1 and 3 axis. The calculated curves
(dashed curves) were based on a model assuming iso-
tropic elastic properties. The experimental curves
were taken from Figure 3.
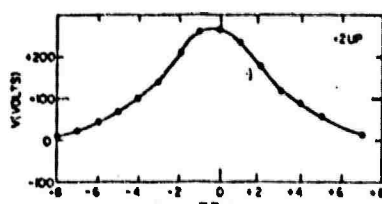
SURFACE
CHARGE

BULK
CHARGE

(A)

(B)
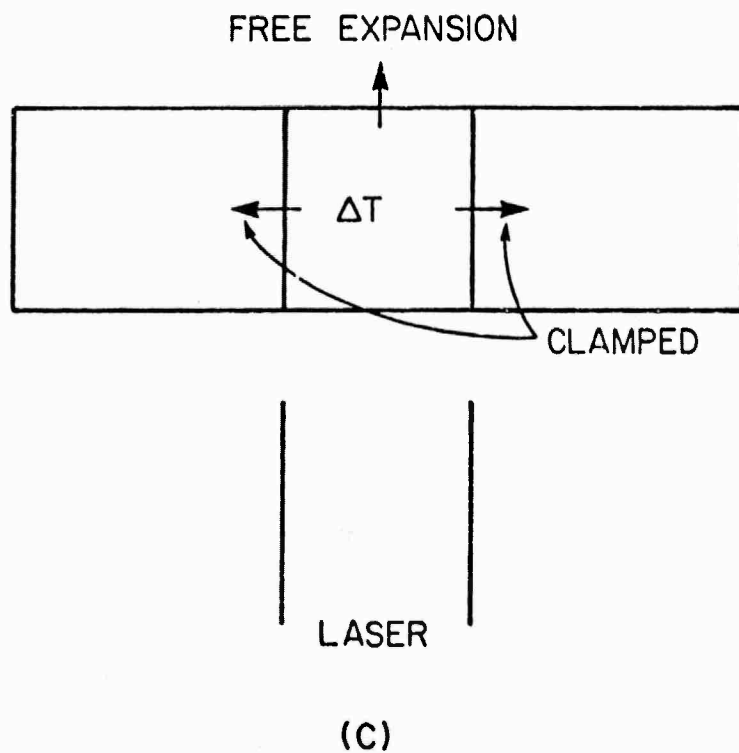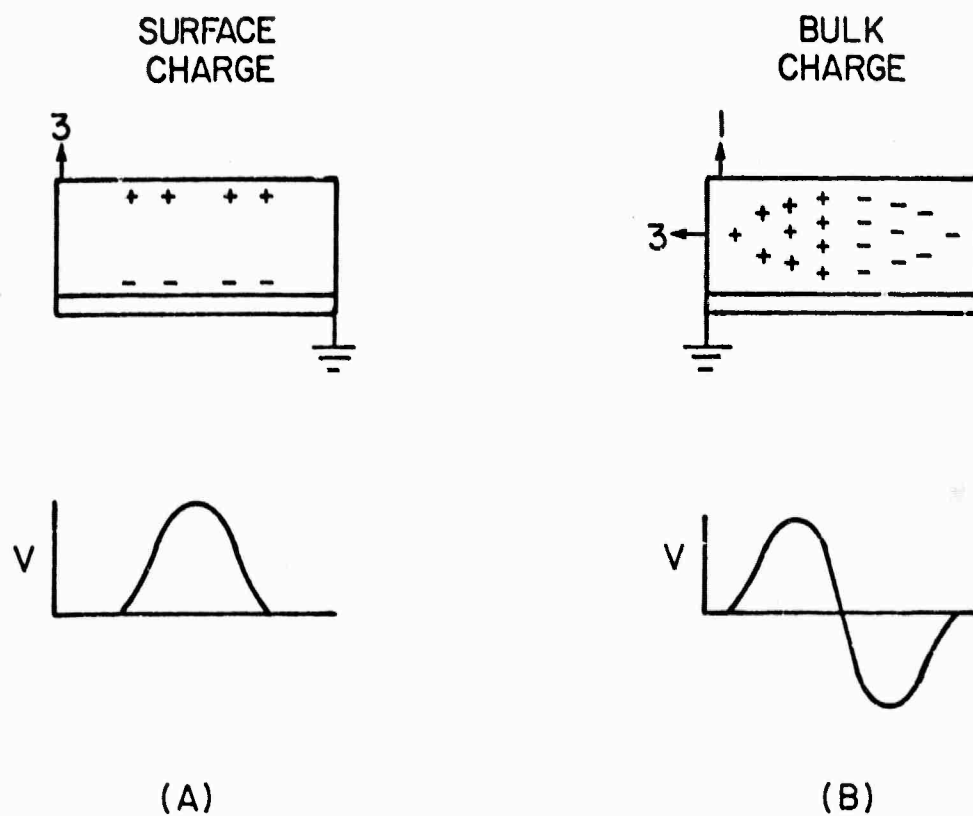
Fig. 1

Fig. 2

P-PRIMARY PYROELECTRICITY
S-SECONDARY PYROELECTRICITY

AXIS UP
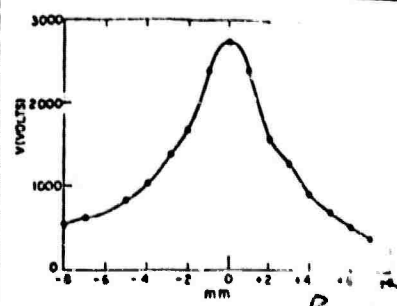

Fig. 3
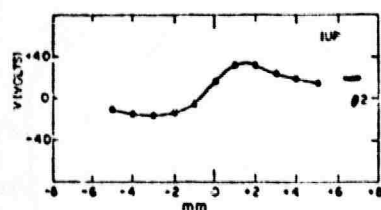
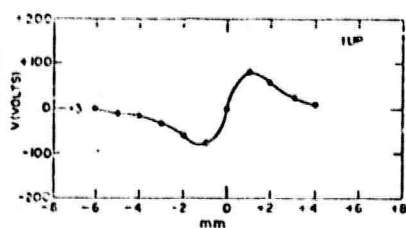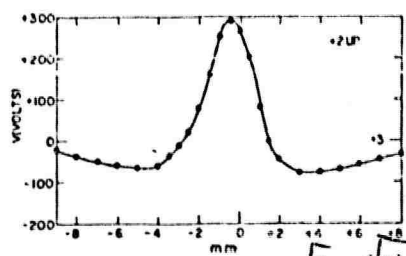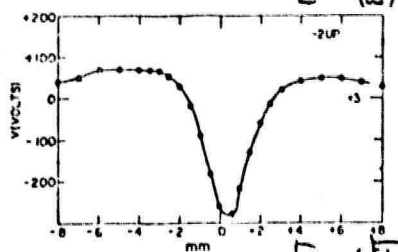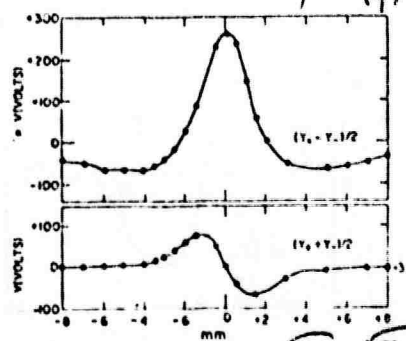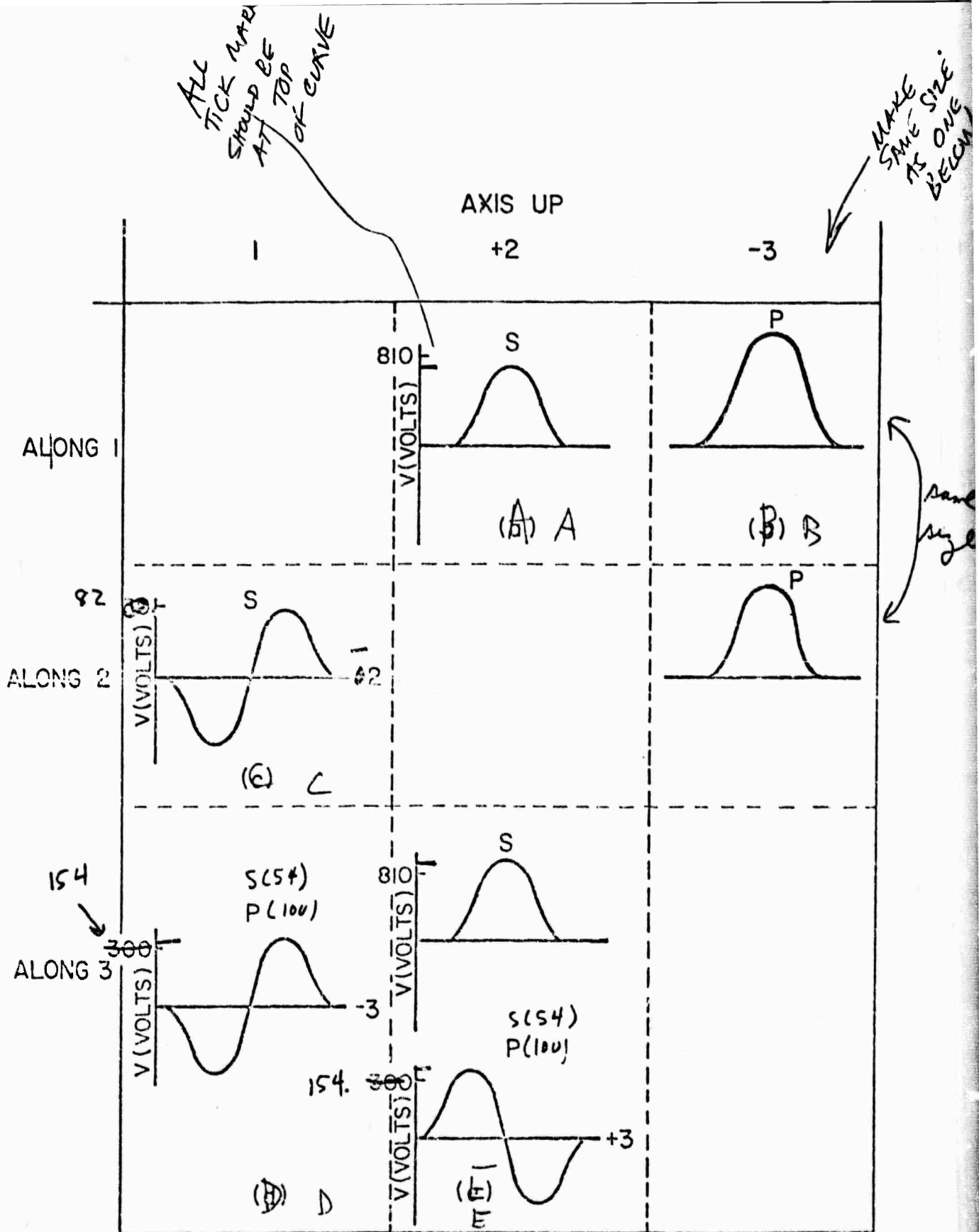AXIS UP

| 1 | +2 | −3 |

ALONG 1

810

V(VOLTS)

S

P

(A) A

(B) B

82

V(VOLTS)

S

82

ALONG 2

P

(C) C

154

300

ALONG 3

S(54)
P(100)

V(VOLTS)

−3

810

V(VOLTS)

S

S(54)
P(100)

154. 300

V(VOLTS)

+3

(D) D

(E) E

Fig. 2

P−PRIMARY PYROELECTRICITY
S−SECONDARY PYROELECTRICITY

Fig. 3

PREDICTED ALONG I AXIS
MEASURED ALONG I AXIS
(FIG. 11)

PREDICTED ALONG 3 AXIS
MEASURED ALONG 3 AXIS
(FIG. 10)
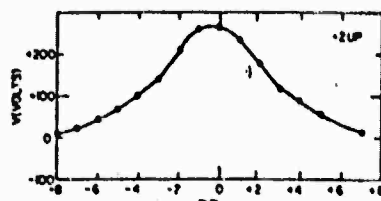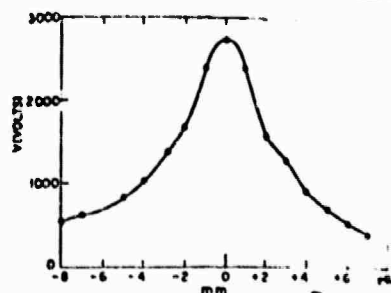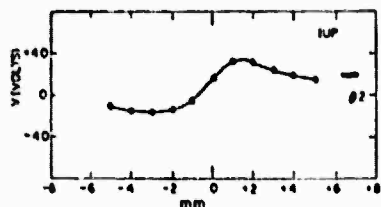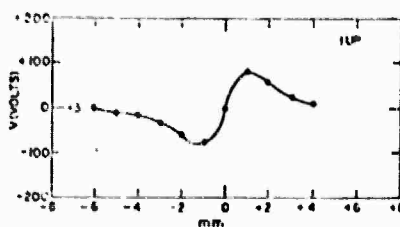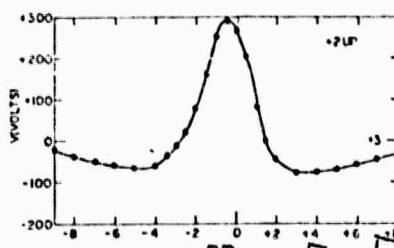
Fig. 4

APPENDIX 16

Electrostatic Measurements of Tertiary Pyroelectricity
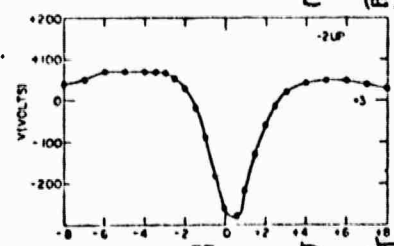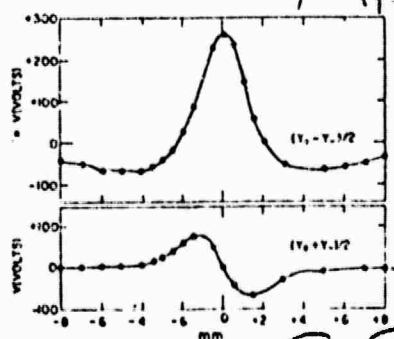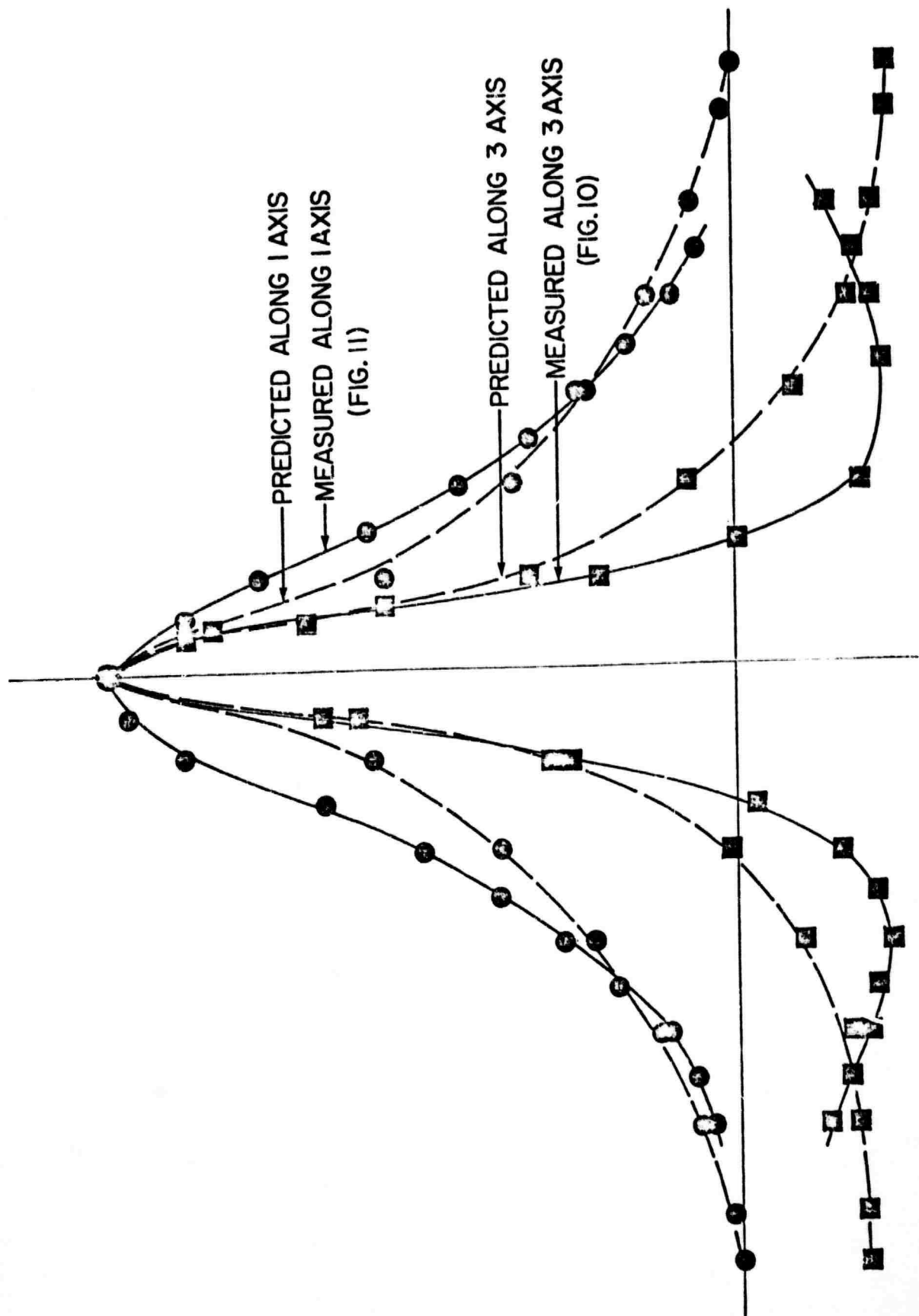in Partially Clamped LiNbO$_3$

L.B. Schein, P.J. Cressman and L.E. Cross

ELECTROSTATIC MEASUREMENTS OF TERTIARY PYROELECTRICITY
IN PARTIALLY CLAMPED LiNbO$_3$

L.B. Schein, F.J. Cressman
Xerox Corporation - W114
Rochester, New York 14644

and

L.E. Cross
Materials Research Laboratory
The Pennsylvania State University
Univeristy Park, Pennsylvania 16802

ABSTRACT

One of the first observations of tertiary pyroelectricity is reported. Tertiary pyroelectricity has been observed on disks of single domain, ingle crystal LiNbO$_3$ under partially clamped elastic boundary conditions (obtained by locally laser heating the central 2.5 mm of a 19 mm diameter disk) using a non-contact electrostatic measurement. When the y axis is perpendicular to the disk's face, the observed transient effect may be traced to the time evolution of the secondary pyroelectric response. When the x axis is perpendicular to the disk's face, a true tertiary response due to a temperature gradient through the thickness of the disk was observed.

I. INTRODUCTION

It has been shown[1] that non-contact electrostatic measurements can be used to measure and separate primary and secondary contributions to the pyroelectric response in partially clamped single domain, single crysta` $LiNbO_3$. In this paper it is shown that under similar conditions of partial clamping (obtained by heating only the central region of a thin disk) the transient potentials developed on heating and cooling can be used to identify and separate (1) the time evolution of the secondary pyroelectric response and (2) a true tertiary pyroelectric response associated with the temperature gradient developed through the sample. There have been almost no reports in the literature of observations of tertiary pyroelectricity.[2,3]

In Figure 1 is shown the potential distribution observed for a 2 cut crystal (2 or y axis normal to the plate) observed along the polar 3 axis. For this orientation, the response was shown[1] to be dominated by secondary pyroelectricity (i.e., piezoelectricity) which is associated with the tangential component of the thermal stress $\sigma_{\theta\theta}$ (for this geometry σ_{11}) acting through the piezoelectric coefficient d_{21}. In the measuring procedure used to establish the potential distribution of Figure 1, the electrostatic voltage probe is positioned along the 3 axis of the 2 cut crystal and the laser is turned on. Within a few seconds, the electrostatic potential reaches a steady state value (see Figure 2). The laser is then turned off and the temperature returns to ambient as indicated by the decay of the pyroelectric voltage. The electrometer then translated to a new position and the measurement repeated until

the full voltage profile has been established. Under the condition
that the steady state value of the electrostatic potential is
zero (Figure 2), within a few seconds after switching the laser
on or off, transient peaks occur in the measured potential. It
is the purpose of this paper to relate these transient potential
changes to (1) the time evolution of the secondary response, and
(2) to tertiary pyroelectricity in $LiNbO_3$.

II. EXPERIMENTAL PROCEDURE

Poled single crystals $LiNbO_3$ used for these experiments were
purchased from Crystal Technology, Inc. in the form of polished
disks, 19 mm in diameter, 0.75 mm thick. As in the earlier studies[1]
partial elastically clamped conditions were obtained by painting
one side of the disk black and irradiating this side with an ex-
panded 2.5 mm diameter, 0.6 W argon laser beam (4880Å). The
central 2.5 mm serves as a local heat source and the rest of the
19 mm diameter crystal (which is not heated) tends to prevent the
central region of the $LiNbO_3$ disk from expanding.

The side with the black surface was placed on conducting glass
which served as a ground plane for the electrostatic measurements.
The thermally generated potentials were measured by translating an
electrostatic voltmeter (Monroe Model 144 voltmeter with Model 1009CG
probe) across the crystal face along the various axial directions.
Details of the electrostatic considerations associated with the
potentials developed both by primary and secondary components of
the pyroelectric response for different crystal orientations have
been given in Reference 1.

III. TRANSIENT EFFECTS IN 2-CUT CRYSTALS

As indicated in Figure 2 when the electrostatic probe is positioned where the steady state electrostatic potential vanishes there are strong transient signals on switching on and off the laser source. The characteristics of these signals are summarized in Fig. 3. When the positive 2 axis is up, switching on the laser (heating) produces a negative potential spike; switching off (cooling), a positive spike at either crossover point. With the sample inverted (the positive 2 axis down) heating produces a positive spike and cooling a negative spike.

It is tempting to associate these time dependent changes with a tertiary pyroelectricity (i.e., polarization due to temperature gradients). However, it appears that the proper explanation may be obtained by considering the time evolution of the temperature distribution (Figure 4). Initially after switching on the laser, the temperature distribution will be sharply peaked and the detector, which is located at the crossover of the steady state distribution, will look at a tensile stress giving a negative signal with 2 up (a) and a positive signal when 2 is down (b). This signal will rapidly decay to zero as the steady state distribution is established. Similarly, on switching off the laser, the central temperature peak will diffuse out on cooling, moving the crossover point out so that the detector (set at the equilibrium crossover) will now look at a compressive stress giving a positive potential with 2 up and a negative potential with 2 down, which will again rapidly disappear as the crystal cools back to ambient.

IV. TERTIARY PYROELECTRICITY IN 1 CUT CRYSTALS

From the elementary considerations of the transient signal seen on the 2 cut crystal it is clear that in seeking a genuine tertiary pyroelectric response it is highly desirable to use a cut for which both primary and secondary potentials are minimized so that the time evolution of these signals associated with the changing temperature distribution does not lead to confusion. It was shown in Reference 1 that for the 1 cut sample, the 3 axis generates a volume charge due to primary pyroelect. ity while the 2 axis generates a volume charge due to secondary pyroelectricity. There is, however, a radius making an angle of ~3° with the 2 axis along which primary and secondary signals approximately cancel. Measurements along this axis reveal a transient signal which is significantly smaller than that observed on the 2 cut crystal and has a shorter time constant ~ 0.4 seconds (compared to several seconds for the 2 crystal transients) and spatial characteristics illustrated in Figure 5. At the center of the heated region both transient and steady signals are zero. With the 1 axis up, along an axis making an angle of approximately 3° with the 2 axis, on the +2 side, the transient signal is positive on heating, negative on cooling. On the -2 side of the center the signal is negative on heating, positive on cooling (Figure 5). Inverting the sample did not change the character of either transient or steady state response.

We believe that the transient response, in this instance, is associated with a true tertiary pyroelectric effect. The only active piezoelectric coefficients coupling electrical signals along the 1

axis in LiNb$_3$ are d_{15} (or d_{131}) and d_{16} (or d_{112}), where $d_{16} = -d_{22}$ by symmetry. During initial heating from the lower blackened surface of the crystal the lower surface will tend to expand while the bulk of the crystal acts as a restraint to limit this expansion (Figure 6). The clamping effect will result in a stress system tending to oppose the thermal expansion which will involve a non-zero shear component σ_{12} (Figure 6b). For the axial arrangement shown, +3 would be emergent from the Figure and thus in the +2 direction σ_{12} is positive, while in the -2 direction σ_{12} is negative. The shear stress will give rise to a polarization

$$P_1 = \sigma_{12} d_{16}$$

along the 1 axis. Since $d_{16} = -d_{22}$ and d_{22} is positive in LiNbo$_3$ one predicts a positive spike on heating, as is observed. Since on the -2 side of center, σ_{12} is negative, there is a negative voltage spike on heating. Cooling would, of course, reverse the polarity of the transient signal, as is observed.

A second feature which further supports the tertiary pyroelectric model proposed is the short time constant of the observed transients (~ 0.4 seconds). If, as is hypothesized, the signal is dependent upon a temperature gradient through the sample thickness, then this signal must decay with a time constant of the order of the thermal time constant for heating through the crystal surface. For a crystal of thickness L, the time constant τ is given by

$$\tau = L^2/\alpha_T$$

where α_T is the thermal diffusivity which for $LiNbO_3$ is

$$\alpha_T = 1.4 \ mm^2/sec$$

Since the 1 cut crystal is 0.75 mm thick, this gives

$$\tau = 0.4 \ sec$$

in excellent agreement with the time constant measured on the transient pyroelectric signals.

V. CONCLUSION

One of the first observations of tertiary pyroelectricity is reported. By using partial elastic clamping in single domain, single crystal $LiNbO_3$ we have observed transient electrostatic potentials which have been associated with (1) the time evaluation of secondary pyroelectricity and (2) a true tertiary pyroelectricity in $LiNbO_3$

REFERENCES

1. L.B. Schein, P.J. Cressman, L.E. Cross, preceding article.

2. S.D. Pel'ts and A.E. Kapel'son, Soviet Physics, Solid State, 13, 2606 (1972).

3. "Source Book of Pyroelectricity," S.B. Lang, Vol. 2 of Ferroelectricity and Related Phenomena, Ed. I. Lefkowitz and G.W. Taylor (Gordon and Breach, N.Y., London, Paris) 1974.

FIGURE CAPTIONS

Figure 1 - Measurements for a 2 cut crystal with the +2 axis up, along the 3 direction. This potential is primarily due to secondary pyroelectricity which in this case creates a surface charge.

Figure 2 - Raw data from which measurements of the potentials were determined. The electrostatic voltmeter is positioned above the crystal (upper left is 0.5 mm from the center of the laser beam), the laser is turned on and the electrostatic potential reaches a steady value in a few seconds. The laser is then turned off, the temperature of the sample returns to ambient conditions, the electrostatic voltmeter is translated to a new position, and the measurement is repeated. The bottom line shows the transient response on a 2 cut crystal when the steady state value is zero: on applying heat, a negative potential is observed; on cooling, a positive potential is observed.

Figure 3 - Location and nature of the transient pyroelectric signals observed on 2 cut crystals (a) +2 axis up (b) +2 axis down.

Figure 4 - Time evolution of the secondary pyroelectric signal measured along the 3 axis of a 2 cut $LiNbO_3$ crystal indicating the origin of the heating and cooling transients in the pyroelectric signal. Left half, dotted curve, signal on initial heating; right half dotted curve, signal on cooling.

Figure 5 - Transient pyroelectric signals observed on the face of a 1 cut $LiNbO_3$ crystal along the axis at minimum steady state signal. The amplitude of the signal was ~ 4 volts which lasted ~ 0.4 seconds. For this experiment only, the laser diameter was set at 1 mm.

Figure 6 - Origin of the transient pyroelectric signals on a 1 cut $LiNbO_3$ crystal showing thermal expansion and thermal stresses on heating.

Fig. 1
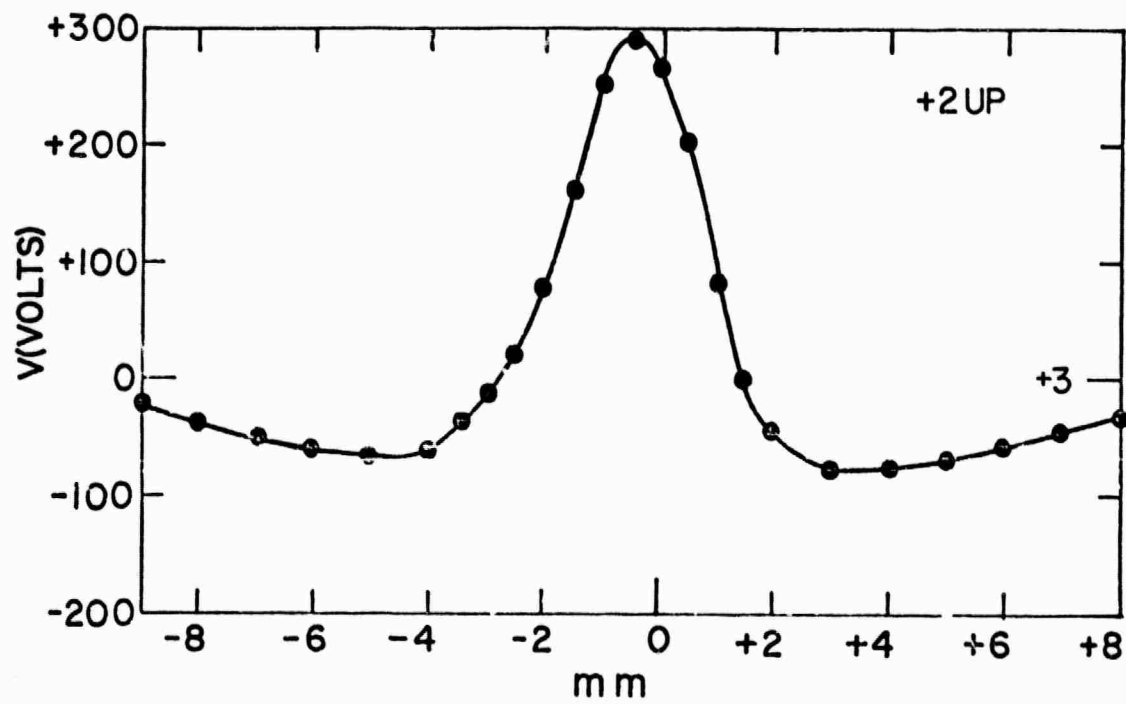
ELECTROSTATIC
VOLTMETER

LiNbO₃
BLACK PAINT

LASER

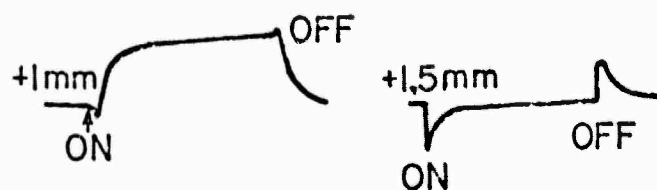STEADY STATE MEASUREMENTS

-0.5mm ... 0mm ... +0.5mm

TRANSIENT RESPONSE

+1mm ... +1.5mm
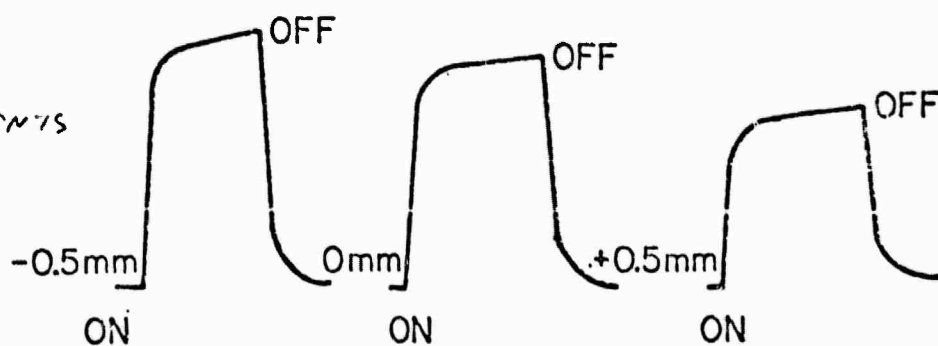
SCALE

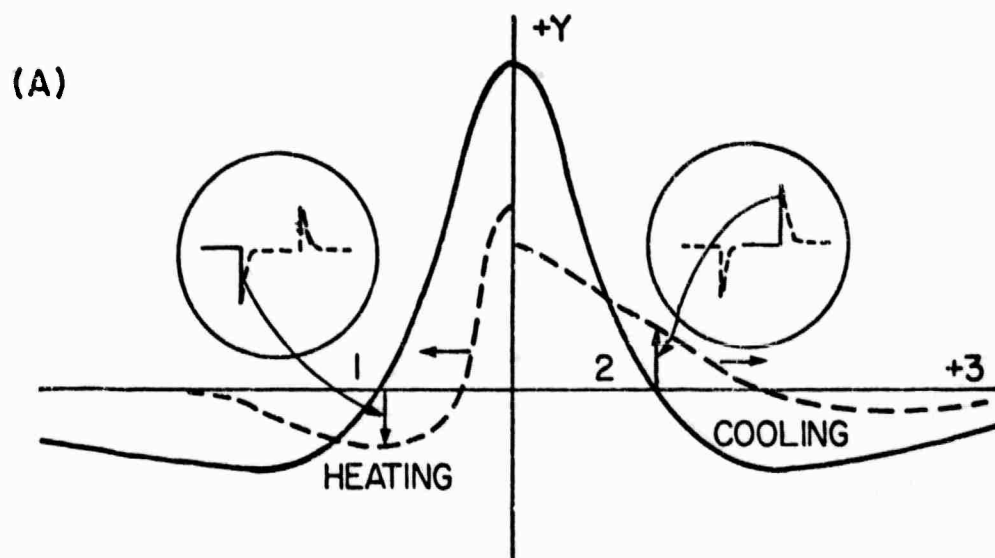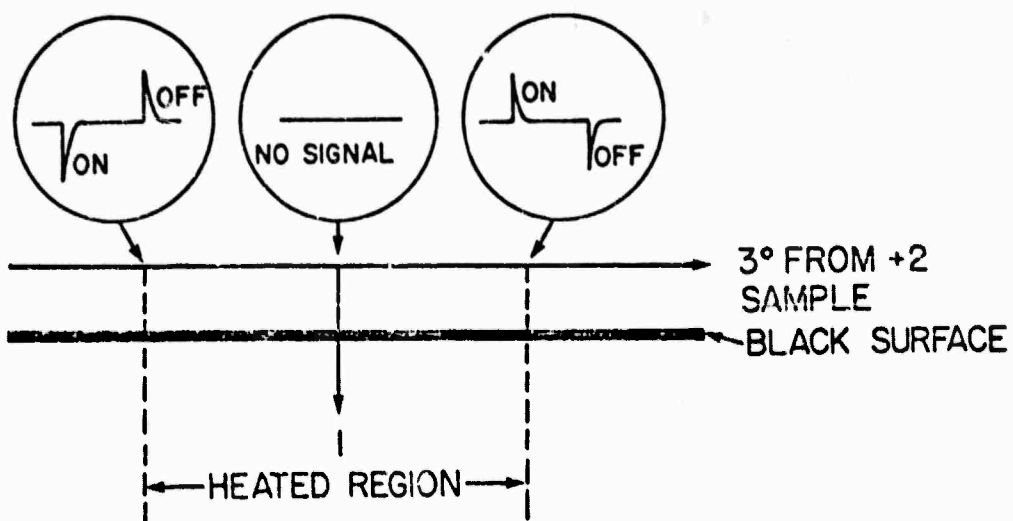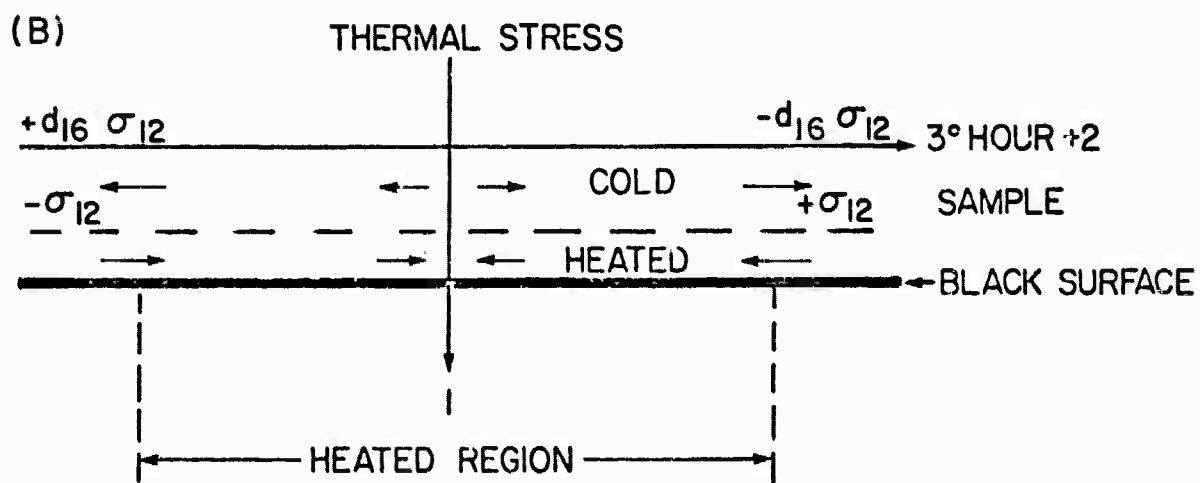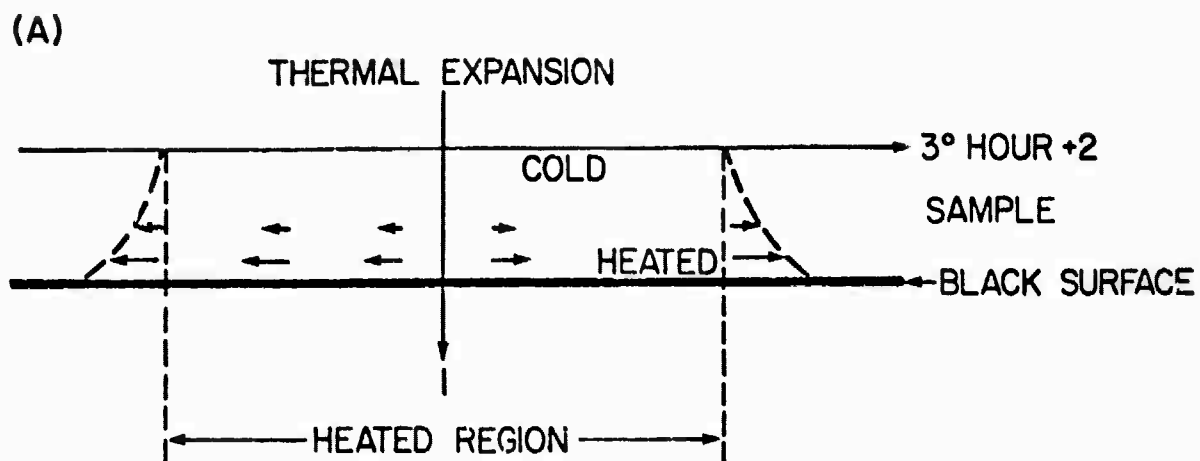20 SEC   100 VOLTS

Fig. 2
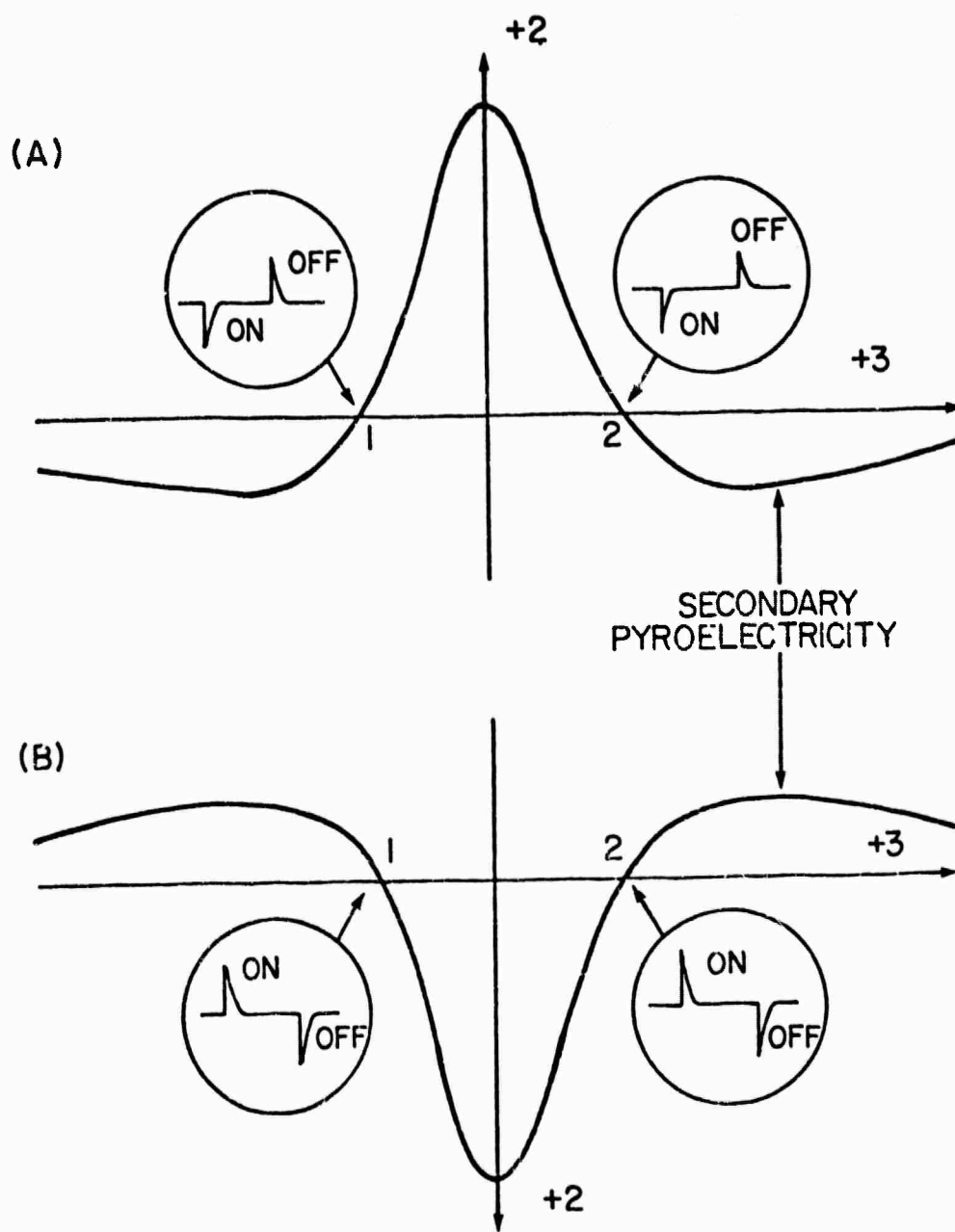
Fig. 3
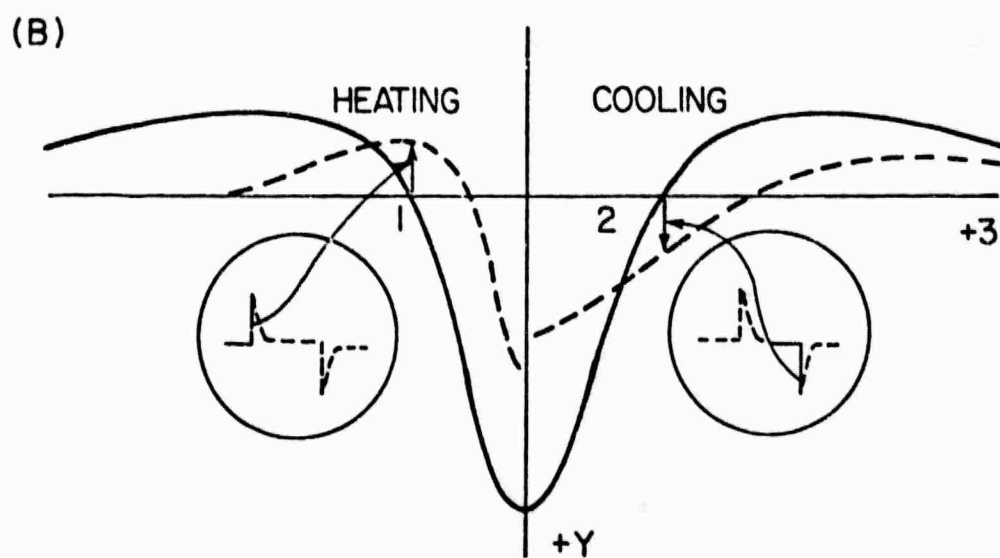
Fig. 4

Fig. 5

Fig. 6

APPENDIX 17

Crystal Growth of Antimony Sulphur Iodide

A. S. Bhalla, K. E. Spear and L. E. Cross

CRYSTAL GROWTH OF ANTIMONY SULPHUR IODIDE

A. S. Bhalla, K. E. Spear and L. E. Cross
Materials Research Laboratory
The Pennsylvania State University
University Park, Pennsylvania, 16802, USA

ABSTRACT

Single crystals of SbSI have been grown from SbI_3 flux by directional cooling through a temperature gradient. The morphology of the crystals is found to be dependent on the growth parameters: (1) composition of the mixture of Sb_2S_3 and SbI_3 flux; (ii) temperature gradient, and (iii) rate of lowering (or cooling). Single crystals highly oriented parallel to the ferroelectric c-axis can be produced by this method in the form of fine parallel needles, thin parallel plates and larger size plates. Characterization information and a brief description of some applications for the single and polycrystal forms produced are given.

Introduction

Antimony sulphur iodide (SbSI) has interesting ferroelectric, electrooptic and photoconducting properties with highly anisotropic behavior along the polar c-axis (1-4). Single crystals of SbSI have been grown by vapor phase techniques (5-10) using hydrothermal methods (11,12) from aqueous solutions (13) and by melt and flux growth techniques (14-17). In all these experiments, a needle growth morphology has predominated with the length of the needles being parallel to the c-axis of the orthorhombic crystal. Since such a wide variety of growth techniques have produced the same growth morphology, it can be deduced that the growth rate anisotropy in this crystal is a characteristic property of the material, a conclusion which is also evident from its structure. However, Nassau's (14) detailed studies with flux growth experiments showed the feasibility of growing large size single crystals.

For a number of current applications of this material in single crystal, in hot forged polycrystal (18) and in composite (19) forms, a more detailed understanding is required of the factors controlling crystal morphology in the flux growth process, so that the size, shape and spacing of the grown crystals can be controlled to suit specific device requirements. This paper describes the effect of growth parameters in relationship to the morphological features of SbSI crystals, and the factors which permit the growth of very fine closely

spaced needles, thin parallel plates, and large sized single crystals.

Materials and Apparatus

The SbI_3 and Sb_2S_3 used for this study were obtained from Gallard Schlesinger. The purity of the materials as claimed by the supplier was 99.999%. The chemicals were handled in a pure, dry nitrogen atmosphere and were sealed in quartz tubes as described in detail by Nassau [14]. Various sizes of quartz containers were used but most of the experiments were performed in quartz tubes of 2 cm ID and typically 10-12 cm in length. Some of the quartz tubes were drawn to a fine point at the bottom and various geometries were tried. The one with the small capillary (1/2 mm diameter and 1/2 cm in length) at the bottom end of the tube proved most satisfactory for initial nucleation of SbSI.

The Bridgman apparatus used in the experiment consists of a vertical two-zone platinum wound resistance furnace, details of which have been described earlier[20]. The SiO_2 glass growth tubes containing the proper ratio of the mixture of $SbI3:Sb_2S_3$ and a half an atmosphere nitrogen pressure were sealed. These tubes were supported on an alumina block inside the furnace and could be lowered through the desired temperature zone at a known rate. Precautions were taken to eliminate fluctuating heat losses, and the furnace was equipped with a temperature controller which has the capability of stabilizing and holding the temperature to better than $\pm0.1°C$ over a period of several days.

Growth Procedure and Results

In the present studies single crystals of SbSI have been grown from $SbI3$ flux by directional cooling through a temperature gradient. By choosing the suitable ratio of reactants $SbI3$ and Sb_2S_3, the desirable amount of the flux can be introduced into the SiO_2 glass crystal growth container. A 1:1 ratio would produce single phase SbSI.

The temperature profile in the growth region of the Bridgman furnace is shown in Fig. 1. By controlling the temperatures of the two heating elements any desirable temperature gradient could be obtained. Indirectly the cooling rate can also be adjusted by proper selection of the lowering rate. The crystallization of SbSI and morphology of the crystals thus obtained have been studied as a function of the following growth parameters:

   (a) Composition of the mixture of
       Sb_2S_3 and $SbI3$

   (b) Temperature gradient

   (c) Rate of pulling (or cooling)

After cooling through the temperature gradient and when the hottest part of the crystal boule was 350°C, the SiO_2 glass container was taken out of the furnace and inverted in order to remove excess flux. The tube was cut open while cool, and the crystal boule was immediately dipped into methanol and boiled to help dissolve out the excess flux. When most of the flux was removed the boule was dipped into 50% water solution of HI for a few minutes and then dried. For the final characterization studies on the samples, crystals were washed in hot dilute hydrochloric acid.

It is observed that the morphology of the crystals can be controlled (Fig.2)

by choosing the proper growth parameters as summarized in Table I. Low cooling rate (1°C/hr) and a melt containing around 38-42% Sb_2S_3 in SbI_3 favors the larger size crystals while faster cooling of melts richer in Sb_2S_3 favors the plate and needle morphologies. Melts containing less Sb_2S_3 (35% Sb_2S_3) favor the plate morphology. The thickness of the plates also depends upon the cooling rate. Slower cooling of < 5°C/hr gives thicker plates than those grown with the faster cooling rates of ∼8-12°C/hr. Plate and needle distribution in the boules was usually very uniform at the lower cooling rates with compositions of around 40% Sb_2S_3. The lengths of such single crystal materials along the c-direction can be more than several centimeters. Cross-sectional areas are given in Table 1.

Characterization Methods and Results

Dark crystals with well developed crystallographic planes were obtained. Laue back reflection photographs of the needles, plates, and bulk pieces of SbSI showed they were single crystals with orthorhombic point group of symmetry. Crystals grow parallel to the c-axis, and the major terminated surface was the (101) plane of the orthorhombic crystal structure. Powder prepared from such single crystals did not show any peaks corresponding to the flux (SbI_3). Conoscopic examination of the crystals by optical microscopy under polarized red light showed biaxial figures. Also no inclu-

FIG. 1
Temperature profiles of the crystal growth system. A and B correspond to two different systems. Dashed line at 400°C represents the M.P. of SbSI. With addition of SbI_3 flux the melting point decreases. Schematic drawing on left shows starting position (melt) and final crystallized state. Crystallization zone is represented between the temperature range 400° and 350°C.

sions or precipitates were observed under transmitted light. Crystals showed the ferroelectric Curie temperature of 20°C, optical absorption of 6300Å and have lattice parameters of a = 8.52Å, b = 10.13Å, c = 4.10Å. It was quite apparent from the morphology of the crystals as indicated by Molnar et al. (7) and Nassau et al. (14) on the basis of the structure of SbSI that the growth rate was much faster along the c-direction. The present study also indicates the qualitative relationship in the growth rate in various directions as follows:

$$[001] \gg [100] \approx [010] > [110]$$

Thus the major faces of the plates generally terminate as {110} planes, parallel to the c-direction. The (110), (100), and (010) faces are also present as facets in plates, needles and thick crystals.

Fig. 2. Various morphologies of SbSI crystals grown under varied growth parameters: (A) Thin needle morphology; (a) Top of the crystal boule (X5); (b) As grown crystal boule (XI); (c) Side view of the boule showing the bundle of fine needles oriented parallel to the c-direction; (B) Plate morphology; (d) Thin plages; (e) Thick plates and (f) Magnified area of (e) showing the larger single crystal areas in boule.

TABLE 1

Effect of composition and cooling rate on the morphology of single crystals of antimony sulphur iodide

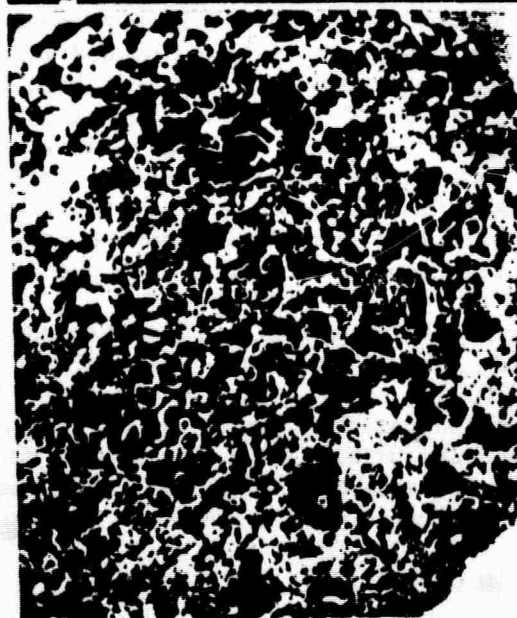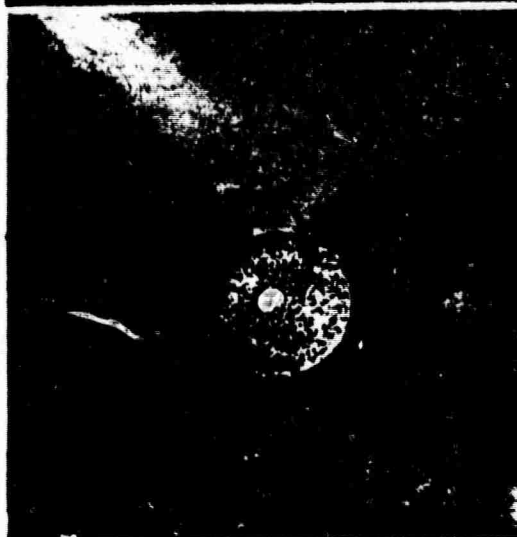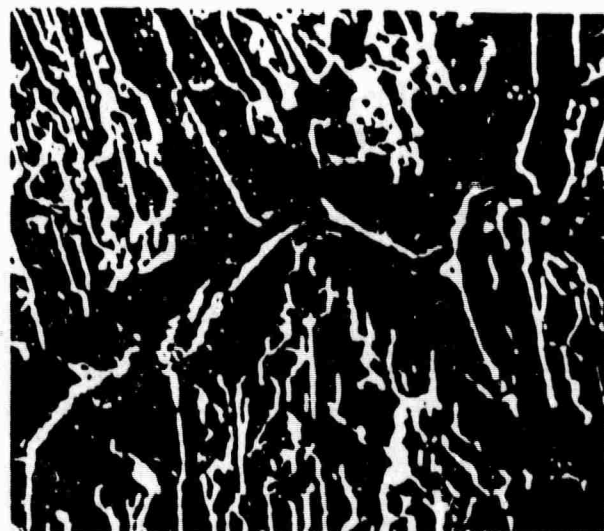| Composition of $Sb_2S_3:SbI_3$ (Mole % Sb_2S_3)	Cooling Rate (°C/hr)	Morphology, Remarks and Cross-Sectional Areas
(A) 38 to 43	0.5 – 10	Thick crystals, plates, needles
40	1	Large size crystals (5×5 mm^2)
40	5	Thick plates (5×2 mm^2)
40	10	Needles (0.5×0.5 mm^2)
42.5	10	Finer needles (0.2×0.2 mm^2)
(B) 44 to 50	1 – 10	Needles (0.1×0.1 mm^2) Thicker needles for lower Sb_2S_3 composition and lower cooling rates; thinner needles for higher Sb_2S_3 compositions and lower cooling rates; polycrystalline boule for higher compositions and faster cooling rate.
(C) 30 to 37	5 – 12	Plates
35	5	Thick plates (7×2 mm^2)
35	12	Thin plates (7×1 mm^2) Thickness of the plates increases for higher Sb_2S_3 compositions for a particular cooling rate.

The crystal boules in the form of bundles of thin parallel needles showed the presence of some SbI_3 flux which held the needles together. This flux was difficult to remove completely from the as-grown boules, but substantial amounts could be removed by heating the boule in vacuum at 170°C and then washing in methanol after cooling. At 170°C most of the SbI_3 vaporized and deposited on the cooler part of the container.

An etchant was developed to study the etch pit dislocation density on the crystals. Both concentrated HI acid as well as the dilute HI produced well defined etch pits on the SbSI single crystal surfaces. With concentrated HI and 5-10 sec etching time, good size etch pits developed at the dislocation sites, as is shown in Fig. 3. A typical dislocation density of $10^5/cm^2$ was observed on most of the crystal. Dilute hydrochloric acid (25% water solution) also etched the samples, but higher concentrations of the acid apparently decomposes the material.

Discussion

Some similar effects of composition ($Sb_2S_3:SbI_3$) on crystal growth by the
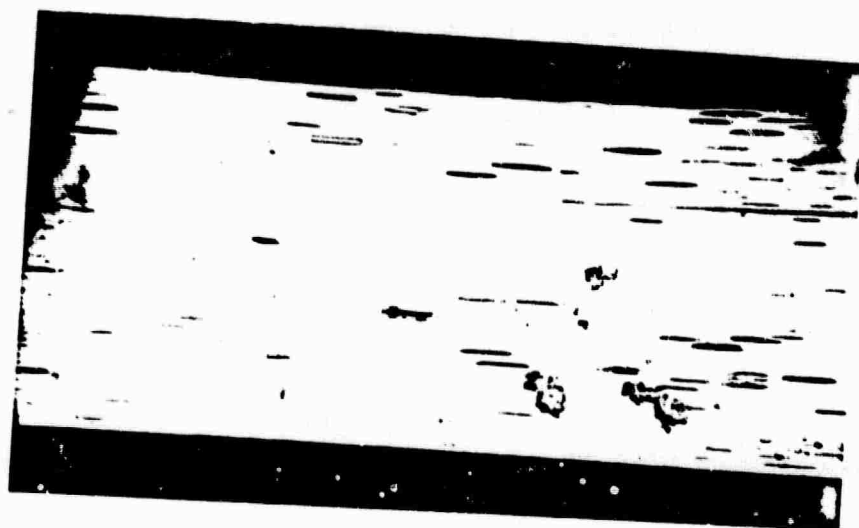
FIG. 3
Etched surface of SbSI single crystal.
Conc. HI was used as an etchant.

vapor method has been observed by Dziuba (5). The needle morphology was
observed in all the compositions but the thicker needles were obtained when
the starting material compositions changed from Sb_2S_3-rich to SbI_3-rich. Tem-
perature zones were not critical factors. No critical composition and tem-
perature limits for a particular morphology was established.

Nassau (14) made some preliminary studies on the crystallization of SbSI
as a function of melt compositions. A cooling rate of 5°C/hr was used in all
his experiments. He showed that with 10% Sb_2S_3 and 50% Sb_2S_3 compositions,
considerable supercooling occurred and resulted in sudden nucleation and the
formation of very fine needles of SbSI. Intermediate compositions produced
larger needle crystals. At 40% compositions largest size needle crystals were
obtained. In the present study various compositions and cooling rates were
used. The number of nuclei can be increased by increasing the cooling rate.
At the 40% composition, cooling rates of $\leq$ 1°C/hour produced larger size crys-
tals whereas 10°C/hour cooling rate produced a very high density of nuclei and
the needle-shaped crystals were obtained.

Crystals grown with different morphologies have potential use in the field
of piezoelectric and pyroelectric applications. The application of the hot
forging process to a dense bundle of needles aligned parallel to the c-direction
will produce a dense, well oriented polycrystal microstructure (18). The hot
forged samples are expected to have markedly improved mechanical properties and
thus can be of practical use in piezoelectric hydrophone transducer applications.
Proper control of the needle morphology has been shown to generate regular ar-
rays of closely spaced mutually parallel microcrystals. When these arrays are
"potted" in an appropriate second phase they provide interesting new composite
structures which have been shown to have advantageous properties for some
specialized pyro- and piezo-electric applications (21).

References

1. E. Fatuzzo, G. Harbeke, W.J. Merz, R. Nitsche, H. Roetschi and V. Ruppel, Phys. Rev. 127, 2036 (1962).

2. R. Nitsche, H. Roetschi and P. Wild, Appl. Phys. Letters 4, 201 (1964).

3. D. Berlincourt, H. Jaffe, W.J. Merz and R. Nitsche, Appl. Phys. Letters 4, 61 (1964).

4. K. Hamano, T.T. Nakamura, Y. Ishibashi and T. Coyane, J. Phys. Soc. Japan 20, 1886 (1965).

5. Z. Dziuba, J. Crystal Growth 35, 340 (1976).

6. A. Kikuchi, Y. Oka and E. Sawaguchi, J. Phys. Soc. Japan 23(2), 337 (1967).

7. B. Molnar, R. Johannes and W. Haas, Bull. Amer. Phys. Soc. 10, 109 (1965).

8. R. Kern, J. Phys. Chem. Solids 23, 249 (1962).

9. B.P. Grigas, Sov. Phys.-Semiconductors 2(4), 397 (1968).

10. M. Balkanski, M.K. Teng, S.M. Shapiro and M.K. Ziolkiewicz, Phys. Stat. Sol. (b)44, 355 (1971).

11. V.I. Poplitov and B.N. Litvin, Sov. Phys.-Crystallography 13(3), 483 (1968).

12. H. Rau and A. Rabenau, Sol. State Comm. 5, 331 (1967).

13. I. Lefkowitz, B. Brodman, J. Radell and M. Shields, Bull. Amer. Phys. Soc. 10, 617 (1965).

14. K. Nassau, J.W. Shiever and M. Kowalchik, J. Crystal Growth 7, 237 (1970).

15. R. Nitsche and W.J. Merz, J. Phys. Chem. Solids 13, 154 (1960).

16. T. Mori and H. Tamura, J. Phys. Soc. Japan 19, 1247 (1964).

17. L.A. Zadorozhnaya, V.A. Lyachovitskaya, E.I. Givasgizov and L.M. Belyaev, J. Crystal Growth 41, 61 (1977).

18. R. Pohanka (Private communication).

19. (a) R.E. Newnham, D.P. Skinner and L.E. Cross. Mat. Res. Bull. 13, 525 (1978).

    (b) D.P. Skinner, R.E. Newnham and L.E. Cross, Mat. Res. Bull. 13, 599 (1978).

20. V.B. Lazarev, K.E. Spear and A.V. Salov, Mat. Res. Bull. 7, 417 (1972).

21. A.S. Bhalla, et al. (to be published).

22. E. Dönges, Z. Anorg. Chem. 263, 112 (1950).

APPENDIX 18

Crystal Growth and Characterization of Lithium Metasilicate

M.R. Brun, A.S. Bhalla, K.E. Spear, L.E. Cross and R.S. Berger

Crystal Growth and Characterization of Lithium Metasilicate

M.R. Brun, A.S. Bhalla, K.E. Spear, L.E. Cross and R.S. Berger

Materials Research Laboratory
The Pennsylvania State University
University Park, Pennsylvania, 16802

The Czochralski pulling technique was used to study the crystal growth of lithium metasilicate, a potential piezoelectric and electrooptic material of the A_2BO_3 type compounds. Crystalline Li_2SiO_3 has an orthorhombic unit cell with space group $Cmc2_1$ and $(Si_2O_6)_\infty$ chains oriented parallel to the piezoelectric c-axis. Li_2SiO_3 melts congruently at 1201°C, but is highly viscous in the molten state which causes difficulties when growing large single crystal boules by pulling. In spite of difficulties with cracking in planes parallel to the chain direction, crystals of good optical quality with areas up to 5 mm x 5 mm normal to c have been grown. Growth parameters and characterization of these Li_2SiO_3 crystals are discussed.

1. Introduction

Lithium metasilicate is one member of a large family of isostructural A_2BO_3 compounds. Both the metasilicate (Li_2SiO_3) and the metagermanate (Li_2GeO_3) have the polar orthorhombic symmetry in point group mm2 and are thus of significant interest for potential piezoelectric, pyroelectric and electro-optic applications [1-4].

At room temperature, the Li_2SiO_3 structure is in space group $Cmc2_1$ with (Si_2O_6) groups as chains running parallel to the polar c axis and linked together by the small lithium ions. Though large clear transparent crystals of the germanate have been grown by Czochralski method [1], no attempts to grow single crystals of the metasilicate have been reported.

Lithium metasilicate melts congruently at 1201°C, but is highly viscous at temperatures close to the melting point. A second complication in growing high quality crystals for property studies is the presence of polar domains which have recently been observed in c-cut plates of both the metasilicate and metagermanate [5].

In this paper the various growth conditions which have been tried so as to circumvent problems of cracking and to reduce twinning will be discussed.

2. Crystal Growth

2.1 Materials

Polycrystalline silica powder of 99.97% and reagent grade lithium carbonate of 99.94% purity (both from Fischer Scientific) were used as raw materials for the synthesis of lithium metasilicate. The stoichiometric ratios of the raw materials were weighed on the Metler balance to within 1 mgm. The weighed mixture along with ethyl alcohol was ball milled for 24 hours to ensure complete mixing of the two powders. After ball milling the slurry was dried at 150°C.

The dried powder was then placed in a platinum crucible and heated gradually to 800°C. The slower heating rate (1°C/min), after 700°C, was used in order to avoid any violent activity due to the decomposition of Li_2CO_3 at 723°C. The material was calcined at 800°C for 1 - 2 hours. An x-ray pattern of the calcined powder was made to check the completeness of the reaction to form Li_2SiO_3. The calcined powder was again ball milled for 24 hours. The powder was then mixed with 3% binder and pressed into one-inch diameter pellets. The pellets were heated in the platinum crucible for 4 hours at 360°C driving off any binder present. Sintering was accomplished by heating the pellets at 1050°C for 12 hours. An x-ray pattern of the sintered powder was taken to ensure that only the Li_2SiO_3 phase was present.

Some preliminary experiments on crystal growth of Li_2SiO_3 were made earlier in this Laboratory by using the Bridgman method. Because of the very strong anisotropy in the crystal structure of Li_2SiO_3 and also the tendency of Li_2SiO_3 to supercool, a fine crystalline fibrous growth or polycrystalline boule resulted. In the present study only the Czochralski method was used.

2.2 Growth Procedure

A commercial Arthur D. Little crystal puller, equipped with a Lepel high frequency generator was utilized for these experiments. A vertical wall platinum crucible 1.5" high and 1.5" diameter was used to hold the melt. The sintered pellets of Li_2SiO_3 were melted in the platinum crucible and kept at 1300°C for 30 minutes prior to each growth run. Temperature of the melt was lowered near the melting point (1201°C) during the crystal pulling. Temperature gradients above the crucible were controlled by the use of heat shields. Initial experiments were done by nucleating the silicate on a platinum wire growing a polycrystalline boule, necking it down to get a single crystal, and finally slowing the pulling rate for final crystal growth. Most of the growth experiments,

however, were done with seeds cut from the boules obtained in the earlier runs. Usually c-seeds were used, although attempts were made with a and b oriented seeds as well. Typical growth rates of 1.5 - 3 mm/hr and rotation speeds of 6 - 30 rpm were used.

3. Results

3.1 Results of Growth Runs

In the course of the present investigation, several growth runs were made. Parameters varied were pulling rate, crystal rotation speed, heat shields above the crucible, and seed crystal orientation. Growth runs were also conducted in which attempts were made to maintain an electric potential across the liquid-crystal interface. Table 1 summarized the results of representative runs. All boules grown during this investigation ranged from 15 to 25 mm in length and 10 to 15 mm in diameter.

Pulling rates and crystal rotation were the important parameters in the growth of these boules. The reported pulling rates for each run in Table I represent the constant rates used during growth of the boule and the accelerated rates used during extraction of the boule from the melt, respectively. It was observed that increasing the pulling rates in order to extract the boules from the melt resulted in the growth of cream-colored translucent material in the rapidly grown regions of the boule. These regions disappeared when the pulling rate was kept constant and extraction was accomplished solely by increasing the temperature. The clearest boules were grown at pulling rates of 1.5 mm/hr. Growth rates lower than this are impractical on our equipment both from the standpoint of time and also when considering the sensitivity of crystal pulling at this slow rate to even very small temperature fluctuations.

Crystal rotation speed was also varied during these experiments. The first three boules were pulled at a rotation rate of 6 rpm. After observing the very high viscosity of the melt and the appearance of growth bands perpen-

dicular to the growth direction, further runs were carried out at increasingly higher rotation speeds in an effort to increase stirring of the melt. The final four runs were made at 30 rmp, which is the maximum rotation rate of the unit. The melts of experiments 7 and 8 were also stirred with a platinum rod before pulling began, but growth bands still occurred. Growth bands were not eliminated by increased seed rotation, but the frequency of their occurrence was reduced significantly.

Cracking of the boules was a recurrent problem in this investigation. During a growth run cracking was usually observed to begin at the tops of the boules, just as they cleared the top edge of the crucible. Cracking continued during cooling of the boule, smaller cracks propagating from those already present. The use of the heat shields tended to reduce cracking during growth, but did not completely eliminate it.

All boules exhibited cleavage parallel to the c-direction of growth. Several runs were made with a seed crystal oriented so that this cleavage direction was perpendicular to the new growth direction. Boules grown in this orientation also exhibited cleavage and were cracked.

Chemical etching experiments which are described in the characterization section showed the presence of domains in all the crysta. boules. Obviously changing the normal crystal growth parameters did not help in growing the desirable single domain crystals. Some special approaches were made for this purpose and are described in brief in the following section.

3.2 Special Growth Experiments

(a) The first attempt in poling a crystal during growth was made by doping the melt with 0.5% of a cation which was expected to be strongly rejected by the silicate melt. It was supposed that the rejected ions would pile up in front of the crystal-liquid interface causing a high local electro-static field, which should cause all domains to be oriented during the growth

process. Such an approach has b en successfully applied by Nassau [6] in the growth of $LiNbO_3$, using W^{+6} and Mo^{+6} as dupant ions. It was thought that Cr^{3+} would be a satisfactory ion for lithium metasilicate, as it is strongly octahedral and thus should not substitute for Si^{4+}, while its substitution for Li^+ would require the formation of two vacancies. However, when grown in air, apparently Cr^{3+} was oxidized to Cr^{6+}, as evidenced by the deep red color of the melt, and was thus substituted for silicon. The resulting crystal was red in color, and antipolar domains were still observed. Another potential candidate cation was uranium, which with high charge and larger size was expected not to be substituted in the crystal lattice. The greenish color of the crystal pulled from such a melt, however, again suggested significant solid substitution.

(b) Electrical poling of the crystals during growth was also attempted by applying a high DC field across the growth interface. For that purpose the seed was painted with platinum paint and held in a platinum pulling rod, grounded to the furnace chamber. The crucible and the melt were connected to the source of DC voltage. Because of the high conductivity of the melt and the crystal, a field of only 200 - 300 V was required to pass a 10 mA current through the interface. The resulting crystal was not poled. It is believed that the major reason was the inability to maintain very high fields across the whole assembly. All poling attempts were made with c-seeds, because of the c-polar direction in the structure of the metasilicate.

4. Characterization Studies

The as-grown crystal boules from undoped melts were colorless and optically transparent, although some small areas in the crystals were sometimes of a milky color. X-ray powder studies of small pieces from the crystal boule gave a single phase Li_2SiO_3 diffraction pat. n. Laue photographs showed the single

crystal nature of the compound. Crystals were examined for chemical composition and no indication of a second phase or of inhomogeneity in composition was observed. The lattice parameter measurements on single crystal samples gave values for the orthorhombic unit cell of a = 5.40Å, b = 9.36Å, c = 4.67Å.

The crystal boule was oriented along c direction and the clear large pieces of Li_2SiO_3 crystals were cut and polished (Fig. 1). Crystals have two cleavage planes [(100) and (110)] parallel to the c-direction and thus great difficulty was encountered while cutting and polishing the c-plates. Crystals were splitting easily into rods or plates along the cleavage planes. Such behavior was observed with the crystal grown either on a or c seeds. Optical observations indicated high quality of the crystals without any visible inclusions or presence of a second phase in the crystal. Conoscopic figures under cross polarized light showed the material was single crystal and of biaxial character.

Chemical etching experiments were done to study the domain features on c-surfaces of the crystal. Thin plates were cut and polished normal to the pyroelectric c axis of the crystal. Optical examination of these plates under crossed polarized light did not show the presence of domains. When these crystals were lightly etched with dilute acids, e.g. HCl, HF or HNO_3, the 180° domain features were revealed on the surface (Fig. 2). The polar nature of the domains was concluded on the basis of d_{33} measurements on the isostructural lithium metagermanate single crystal plates of c-orientation. On a multidomain sample of Li_2SiO_3 typical values of d_{33} ranged from $5\text{-}10 \times 10^{-12}$ C/N depending on the density of domains in the area of measurements.

Dilute hydrofluoric acid (2% HF by volume) revealed the domains very distinctly and also attacked the dislocation sites. Dislocation etch pit density was of the order of $10^5/cm^2$. Crystals grown under various growth conditions

as well as crystals grown with chromium and uranium impurities and the one example grown in the presence of electric field, all showed the characteristic domain features on chemical etching. Crystals grown with impurities were not completely colorless. The boules exhibited no noticeable solubility in water unlike its isostructure Li_2GeO_3 which has solubility in water ~ 1 gm/100 cc. Crystals of Li_2SiO_3 are relatively softer with a hardness between 3 and 4 Moh's hardness scale.

5. Discussion

Two flaws marred the perfection of the boules which were grown during this investigation. These were cracking of the boules and the presence of growth bands perpendicular to the growth direction.

Cracking of the boules was probably due to thermal shock. This is reasonable when observing that the heat shields, which lowered the thermal gradient above the melt, reduced the severity of this cracking when used during crystal growth. However, the persistent cracking of the boules even after using the heat shields, suggests that other factors may be responsible for this problem. Cracking may also be due to the fact that the material may be going through a phase transition just below the melting point. This possibility was investigated by Drafall [7], who conducted DTA and high temperature x-ray investigations on Li_2SiO_3. The DTA experiments showed a small endothermic peak at about 1030°C and then the melting point at 1200°C. High temperature x-ray diffraction patterns taken at 835°, 1060°, and 1156°C, however, showed only the expected thermal expansion of the orthorhombic unit cell. These results tend to disprove the suggestion of a phase transition taking place just below the melting point.

Banding which was observed parallel to the original liquid-crystal interface can be attributed to the instabilities in the melt. Because of the high viscosity of the melt, the degree of mixing was low, and any impurities

rejected by the crystal would not easily diffuse away from the interface. If temperature variations, or variations in the pulling rate occurred, more impurities would be incorporated in the crystal during periods of rapid growth, thus forming bands. This was particularly drastically demonstrated in the experiment done with uranium doping, where alternate colorless (pure) and green (doped) bands could clearly be observed. At faster rotation rates, banding was reduced in extent, although not completely eliminated. This again suggests that the pile-up and inclusion of impurities at the interface was responsible for banding. It has not been possible to determine whether banding was due to temperature fluctuations, or to non-uniform pulling rate.

Attempts to pole crystals during growth by doping the melt with "poison ions" or by applying an external electrical field across the interface were not successful to date. While the failure of the experiment with DC field is probably due to insufficiently large fields across the interface, the failure of the experiment using uranium as dopant could be due to the problems with non-uniform growth, as already discussed.

In spite of the difficulties with cracking in planes parallel to the chain direction, crystals of good optical quality with areas up to 5 mm x 5 mm normal to c have been obtained from the boules grown.

6. Summary

Single crystals of lithium metasilicate were grown by Czochralski pulling technique. Growth banding and cracking of the boules occurred in most of the crystal growth runs. Optically clear samples of 5 mm x 5 mm useful area normal to the c axis were obtained from the grown boules.

The single crystal nature of the material was established by optical and x-ray studies. The presence of domains was revealed by etching the crystals with diluted HF (2% HF solution in water). Attempts to grow crystals

free from polar twins by using electric field or by the addition of aliovalent ions to the melt were not successful.

References

[1] B.A. Scott, K.A. Ingebrigsten and C.C. Tsong, Mater. Res. Bull. 5(1970) 1045.

[2] V.M. Richard, P.H. Davies, K.F. Hulme, G.R. James and D.S. Robertson, J. Phys. D (Appl. Phys.) 5 (1972) 2124.

[3] H. Hirano and S. Matsumura, Japan. J. Appl. Phys. 13 (1974) 3512.

[4] T. Ikeda and I. Imazu, Japan. J. Appl. Phys. 15 (1976) 1451.

[5] A.S. Bhalla, L.E. Cross and R.E. Newnham, J. Cryst. Growth 46 (1979)(to be published).

[6] K. Nassau, J.H. Levinstein and G.M. Loicono, J. Phys. Chem. Solids 27 (1966) 989.

[7] L. Drafall (Private communication).

Table I

Growth parameters of lithium metasilicate crystal in various growth runs

Run Number	Special Conditions	Pulling Rate-mm/hr During growth	Pulling Rate-mm/hr During extraction	Crystal Rotation rpm	Comments
1	Pulled directly on the platinum wire	2	20	6	1 cm diameter boule; lower portion of the boule was of pale yellow color; highly cracked boule. The boule was used for seeds in the subsequent crystal growth runs.
2-3	c-seed	2	20	6	Boules of larger and smaller diameter; color and cracking still existed; bands perpendicular to the growth direction.
4-6	Increased rotation, decreased extraction rate	2	15	15	Transparent boules except the lower portion which was light cream color. Banding and cracked boules. Clear portions were used for optical and chemical etching experiments. Antipolar domains present on c-surface of the crystal plates.
7	Seed crystal perpendicular to c-face. Melt stirred with platinum rod before crystal pulling. Further decrease in extraction pulling rate.	2	3.5	15	Transparent but cracked boule. Less growth banding. No change in domain density.
8	Seed from run #7, oriented perpendicular to c-face, pulling rate constant throughout growth run. Heat shield was used above crucible.	1.5	1.5	30	Transparent. Cracking and growth banding were present. 5 x 5 x 5 mm^3 clear, crack-free crystal pieces were cut from the boule. X-ray and optical examination showed single crystal nature. Domain density was comparatively smaller.
9	C-oriented seed. Other conditions as in run 8.	1.5	1.5	30	Transparent boule with slight banding and fewer cracks. Big pieces of the boule were single crystal as described in run 8.

| Run Number	Special Conditions	Pulling Rate-mm/hr		Crystal Rotation rpm	Comments
		During growth	During extraction		
10	0.5% Cr^{3+} impurities added in the melt (see text). c-seed.	1.5	1.5	30	Red violet color boule. Highly imperfect boule and single crystal nature could not be established. Apparently Cr^{+3} oxidized to Cr^{+6}
11	Grown under electric field on c-oriented seed. Seed was grounded.	1.5	1.5	30	Cracked boule. Optically homogeneous and transparent, colorless crystals. Domains existed.
12	0.5% U^{+6} impurities in the melt. c-seed	1.5	1.5	30	Cracked boule. Alternate bands were clear and greenish in color. Domains existed.
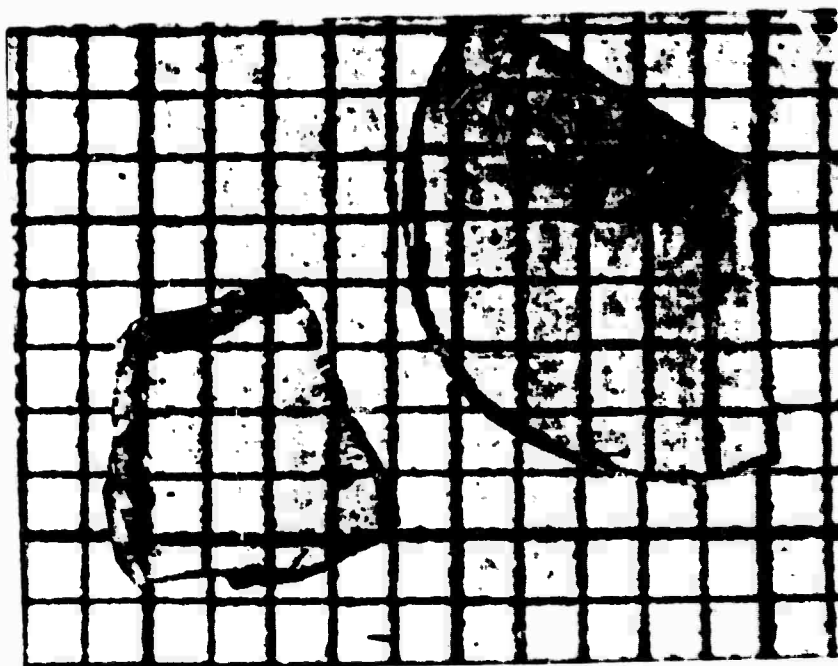
Fig. 1. Lithium metasilicate single crystals grown by the Czochralski pulling technique. Scale: each square equals 1 mm^2.
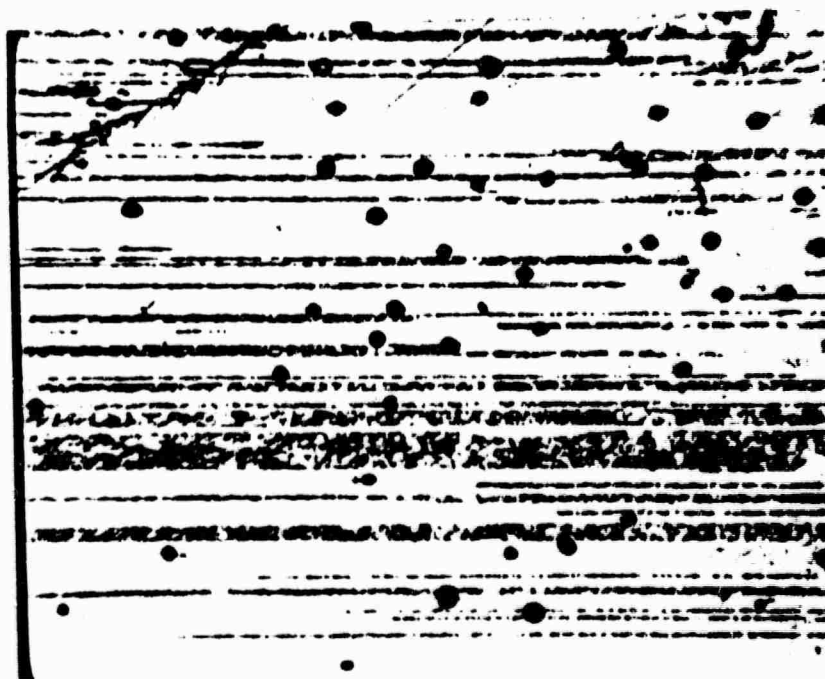

Fig. 2. 180 degrees domain pattern revealed on the C-surface of lithium metasilicate when the crystals were etched with dilute HF acid (4% HF: water solution). Etching time, 5 sec (X125).

BASIC DISTRIBUTION LIST

Technical and Summary Reports   April 1978

(12) Defense Documentation Center
Cameron Station
Alexandria, VA 22314

Office of Naval Research
Department of the Navy
800 N. Quincy Street
Arlington, VA 22217

    ATTN: Code 471
            Code 102
            Code 470

Commanding Officer
Office of Naval Research
Branch Office
Building 114, Section D
666 Summer Street
Boston, MA 02210

Commanding Officer
Office of Naval Research
Branch Office
536 South Clark Street
Chicago, IL 60605

Office of Naval Research
San Francisco Area Office
One Hallidie Plaza Suite 601
San Francisco, CA 94102

Naval Research Laboratory
Washington, DC 20375

    ATTN: Codes 6000
              6100
              6300
              6400
              2627

Naval Air Development Center
Code 302
Warminster, PA 18964
ATTN: Mr. F. S. Williams

Naval Air Propulsion Test Center
Trenton, NJ 08628
ATTN: Library

Naval Construction Batallion
Civil Engineering Laboratory
Port Hueneme, CA 93043
ATTN: Materials Division

Naval Electronics Laboratory
San Diego, CA 92152
ATTN: Electron Materials
           Sciences Division

Naval Missile Center
Materials Consultant
Code 3312-1
Point Mugu, CA 92041

Naval Surface Weapons Center
White Oak Laboratory
Silver Spring, MD 20910
ATTN: Library

David W. Taylor Naval Ship
 Research and Development Center
Materials Department
Annapolis, MD 21402

Naval Undersea Center
San Diego, CA 92132
ATTN: Library

Naval Underwater System Center
Newport, RI 02840
ATTN: Library

Naval Weapons Center
China Lake, CA 93555
ATTN: Library

Naval Postgraduate School
Monterey, CA 93940
ATTN: Mechanical Engineering
           Department

BASIC DISTRIBUTION LIST (cont'd)

Naval Air Systems Command
Washington, DC 20360
ATTN: Codes 52031
52032

Naval Sea System Command
Washington, DC 20362
ATTN: Code 035

Naval Facilities Engineering
Command
Alexandria, VA 22331
ATTN: Code 03

Scientific Advisor
Commandant of the Marine Corps
Washington, DC 20380
ATTN: Code AX

Naval Ship Engineering Center
Department of the Navy
Washington, DC 20360
ATTN: Code 6101

Army Research Office
P.O. Box 12211
Triangle Park, NC 27709
ATTN: Metallurgy & Ceramics Program

Army Materials and Mechanics
Research Center
Watertown, MA 02172
ATTN: Research Programs Office

Air Force Office of Scientific
Research
Bldg. 410
Bolling Air Force Base
Washington, DC 20332
ATTN: Chemical Science Directorate
Electronics & Solid State
Sciences Directorate

Air Force Materials Laboratory
Wright-Patterson AFB
Dayton, OH 45433

Library
Building 50, Rm 134
Lawrence Radiation Laboratory
Berkeley, CA

NASA Headquarters
Washington, DC 20546
ATTN: Code RRM

NASA
Lewis Research Center
21000 Brookpark Road
Cleveland, OH 44135
ATTN: Library

National Bureau of Standards
Washington, DC 20234
ATTN: Metallurgy Division
Inorganic Materials Div.

Director Applied Physics Laboratory
University of Washington
1013 Northeast Forthieth Street
Seattle, WA 98105

Defense Metals and Ceramics
Information Center
Battelle Memorial Institute
505 King Avenue
Columbus, OH 43201

Metals and Ceramics Division
Oak Ridge National Laboratory
P.O. Box X
Oak Ridge, TN 37380

Los Alamos Scientific Laboratory
P.O. Box 1663
Los Alamos, NM 87544
ATTN: Report Librarian

Argonne National Laboratory
Metallurgy Division
P.O. Box 229
Lemont, IL 60439

Brookhaven National Laboratory
Technical Information Division
Upton, Long Island
New York 11973
ATTN: Research Library

Office of Naval Research
Branch Office
1030 East Green Street
Pasadena, CA 91106

Technical and Summary Reports

Dr. W.F. Adler
Effects Technology Inc.
5383 Hollister Avenue
P.O. Box 30400
Santa Barbara, CA   92105

Dr. G. Bansal
Battelle
505 King Avenue
Columbus, OH 43201

Dr. R. Bratton
Westinghouse Research Lab.
Pittsburgh, PA 15235

Dr. A.G. Evans
Rockwell International
P.O. Box 1085
1049 Camino Dos Rios
Thousand Oaks, CA   91360

Mr. E. Fisher
Ford Motor Co.
Dearborn, MI

Dr. P. Gielisse
University of Rhode Island
Kingston, RI 02881

Dr. M.E. Gulden
International Harvester Company
Solar Division
2200 Pacific Highway
San Diego, CA   92138

Dr. D.P.H. Hasselman
Montana Energy and MHD Research
  and Development Institute
P.O. Box 3809
Butte, Montana 59701

Mr. G. Hayes
Naval Weapons Center
China Lake, CA 93555

Professor A.H. Heuer
Case Western Reserve University
University Circle
Cleveland, OH 44106

Dr. R. Hoagland
Battelle
505 King Avenue
Columbus, OH 43201

Dr. R. Jaffee
Electric Power Research Institute
Palo Alto, CA

Dr. P. Jorgensen
Stanford Research Institute
Poulter Laboratory
Menlo Park, CA   94025

Dr. R.N. Katz
Army Materials and Mechanics
  Research Center
Watertown, MA   02171

Dr. H. Kirchner
Ceramic Finishing Company
P.O. Box 498
State College, PA   16801

Dr. B. Koepke
Honeywell, Inc.
Corporate Research Center
500 Washington Avenue, South
Hopkins, MN   55343

Mr. Frank Koubek
Naval Surface Weapons Center
White Oak Laboratory
Silver Spring, MD   20910

E. Krafft
Carborundum Co.
Niagara Falls, NY

Dr. F.F. Lange
Rockwell International
P.O. Box 1085
1049 Camino Dos Rios
Thousand Oaks, CA   91360

Dr. J. Lankford
Southwest Research Institute
8500 Culebra Road
San Antonio, TX   78284

Library
Norton Company
Industrial Ceramics Division
Worcester, MA   01606

State University of New York
College of Ceramics at Alfred
  University
Attn: Library
Alfred, NY   14802

Dr. L. Hench
University of Florida
Ceramics Division
Gainesville, FL   32601

Dr. N. MacMillan
Materials Research Laboratory
Pennsylvania State University
College Park, PA   16802

Mr. F. Markarian
Naval Weapons Center
China Lake, CA   93555

Dr. Perry A. Miles
Raytheon Company
Research Division
28 Seyon Street
Waltham, MA   02154

Mr. R. Rice
Naval Research Laboratory
Code 6360
Washington, D.C.   20375

Dr. Robert C. Pohanka
Room 619, Ballston Tower
800 N. Quincy Street
Arlington, VA   22217

Dr. J. Ritter
University of Massachusetts
Department of Mechanical Engineering
Amherst, MA   01002

Professor R. Roy
Pennsylvania State University
Materials Research Laboratory
University Park, PA   16802

Dr. R. Ruh
AFML
Wright-Patterson AFB
Dayton, OH   45433

Mr. J. Schuldies
AiResearch
Phoenix, AZ

Professor G. Sines
University of California, Los Angeles
Los Angeles, CA   90024

Dr. N. Tallan
AFML
Wright-Patterson AFB
Dayton, OH   45433

Dr. T. Vasilos
AVCO Corporation
Research and Advanced Development
  Division
201 Lowell Street
Wilmington, MA   01887

Mr. J.D. Walton
Engineering Experiment Station
Georgia Institute of Technology
Atlanta, GA   30332

Dr. S.M. Widerhorn
Inorganic Materials Division
National Bureau of Standards
Washington, DC   20234

Dr. S.A. Bortz
IITRI
10 W. 35th Street
Chicago, IL   60616

Mr. G. Schmitt
Air Force Materials Laboratory
Wright-Patterson AFB
Dayton, OH   45433

Dr. D.A. Shockey
Stanford Research Institute
Poulter Laboratory
Menlo Park, CA   94025

Dr. W.G.D. Frederick
Air Force Materials Laboratory
Wright-Patterson AFB
Dayton, OH   45433

Dr. P. Land
Air Force Materials Laboratory
Wright-Patterson AFB
Dayton, OH   45433

Mr. K. Letson
Redstone Arsenal
Huntsville, AL   35809

Dr. S. Freiman
Naval Research Laboratory
Code 6363
Washington, DC   20375

Director
Materials Sciences
Defense Advanced Research Projects
  Agency
1400 Wilson Boulevard
Arlington, VA 22209

Dr. James Pappis
Raytheon Company
Research Division
28 Seyon Street
Waltham, MA   02154

Major W. Simmons
Air Force Office of Scientific
  Research
Building 410
Bolling Air Force Base
Washington, DC   20332

Dr. P. Becher
Naval Research Laboratory
Code 6362
Washington, DC   20375

Mr. L.B. Weckesser
Applied Physics Laboratory
Johns Hopkins Road
Laurel, MD   20810

Mr. D. Richarson
AiResearch Manufacturing Company
4023 36th Street
P.O. Box 5217
Phoenix, AZ   85010

Dr. H.E. Bennett
Naval Weapons Center
Code 3818
China Lake, CA   93555

Mr. G. Denman
Air Force Materials Laboratory
Code LPJ
Wright-Patterson AFB
Dayton, OH   45433

Dr. D. Godfrey
Admiralty Materials Laboratory
Polle, Dorset   BH16 6JU
UNITED KINGDOM

Dr. N. Corney
Ministry of Defense
The Adelphi
John Adam Street
London WC2N 6BB
UNITED KINGDOM

Dr. L.M. Gillin
Aeronautical Research Laboratory
PO Box 4331
Fisherman's Bend
Melbourne, VIC 3001, AUSTRALIA

Dr. G. Ewell
MS6-D163
Hughes Aircraft Co.
Centinela and Teale Streets
Culver City, CA   90230

Dr. R.E. Tressler
Ceramic Scien ⌐ Section
226 Steidle B. g
The Pennsylvania State Univ.
University Park, PA 16802

Dr. R.E. Newnham
Materials Research Laboratory
The Pennsylvania State Univ.
University Park, PA 16802

Dr. K.D. McHenry
Honeywell, Inc.
Corporate Technology Center
10701 Lyndale Avenue South
Bloomington, MN   55420

Dr. R.A. Queeney
Prof. Engr. Mech.
Hammond Bldg
The Pennsylvania State Univ.
University Park, FA 16802

Dr. George W. Taylor
Princeton Resources, Inc.
PO Box 211
Princeton, NJ   08540

Dr. Herb Mose
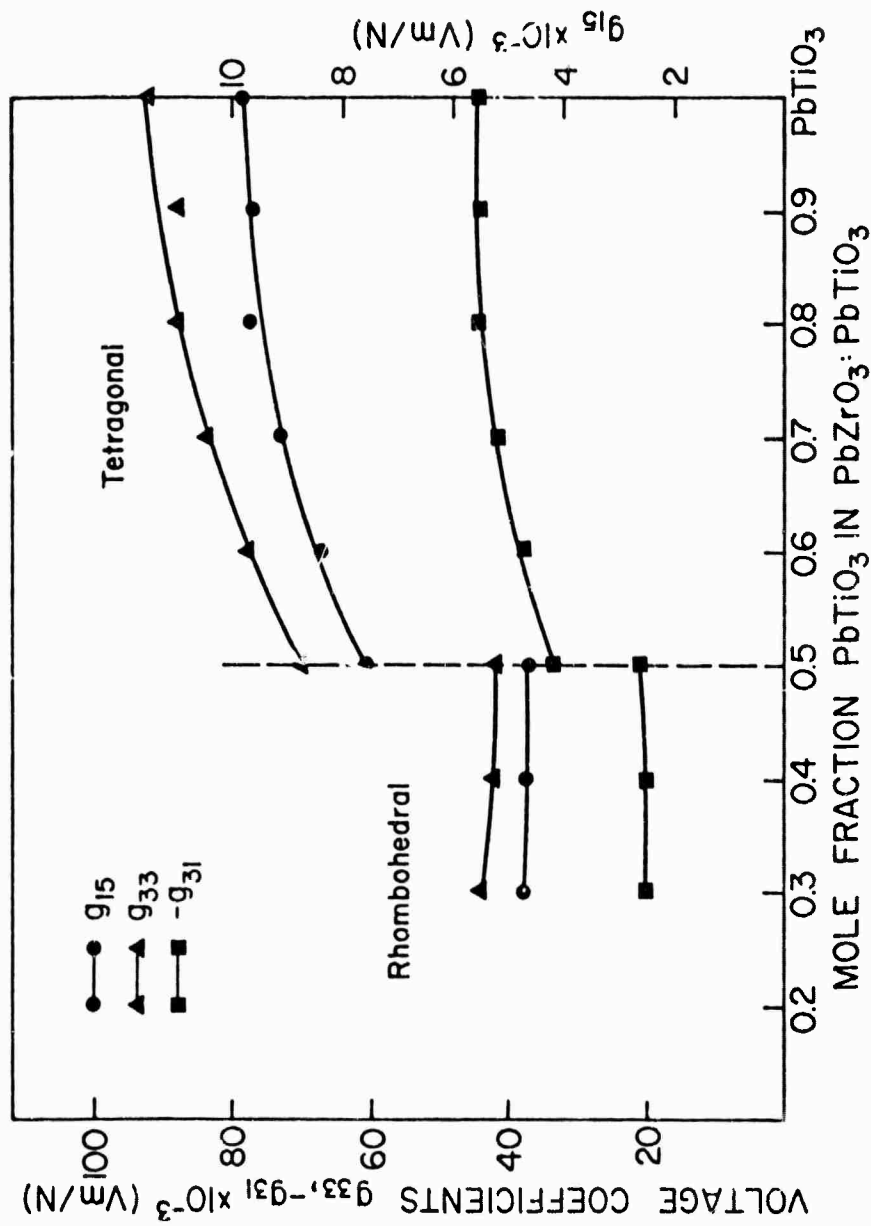RCA Laboratories
Princeton, NJ   08540

Fig. 21. Piezoelectric g coefficients calculated for single domain single crystals of PZT at 25°C.